Monitoring des binaires X et des novae avec le Burst Alert Telescope à board du satellite Swift

Fabio Senziani

UNIVERSITE TOULOUSE III - PAUL SABATIER
U.F.R. PHYSIQUE CHIMIE AUTOMATIQUE

T H E S E

en vue de l'obtention du

DOCTORAT DE L'UNIVERSITE DE TOULOUSE
délivré par l'Université Toulouse III - Paul Sabatier

Ecole doctorale :
« **Sciences de l'Univers, de l'Environnement et de l'Espace** »
Discipline : Astrophysique des hautes énergies

présentée et soutenue
par
Fabio SENZIANI

le 1 Février 2008

Monitoring of X-ray binaries and novae with the Burst Alert Telescope on board the *Swift* satellite

Directeur de thèse italien : **Giovanni Fabrizio BIGNAMI**
Directeur de thèse français : **Gerald Keith SKINNER**

JURY

Peter	VON BALLMOOS	Professeur, UPS Toulouse	Président
Giovanni Fabrizio	BIGNAMI	Professeur, Université de Pavia	Directeur de thèse
Gerald Keith	SKINNER	Professeur, UPS Toulouse	Directeur de thèse
Andrea	GOLDWURM	Docteur, CEA-Saclay	Rapporteur
Giorgio	PALUMBO	Professeur, Université de Bologne	Examinateur
Giorgio	BENDISCIOLI	Professeur, Université de Pavia	Examinateur

C.E.S.R., 9, avenue du Colonel Roche, 31028 Toulouse (FRANCE)
Universitá degli Studi di Pavia, D.F.N.T., Via Bassi 6 - 27100 Pavia (ITALY)

Acknowledgements

I would like to express my gratitude to all who believed in me. Most importantly, I would like to address special thanks to Gerry and ADL for their help, personableness, support, advice, and endless patience.

Je tiens á remercier Pierre Jean pour tout le temps qu'il m'a dédié pendant ces ans et Jürgen pour son soutien. Je remercie également tous les doctorants du CESR pour leur amitié et Julien Malzac pour son hospitalité.

Desidero inoltre ringraziare Prof. Bignami e la Dott.ssa Caraveo per avermi offerto questa opportunitá e Tomaso Belloni per i preziosi consigli. Un grazie speciale a Gió per il lavoro "gomito-a-gomito", al Gruppo BAT di Pavia e a tutti quanti gli astrofisici di Pavia e dello IASF di Milano.
Ringrazio inoltre la famiglia, tutti gli amici vicini e lontani e, di cuore,
Valeria.

THESIS SUMMARY

The Burst Alert Telescope (BAT) on board the Swift satellite is a very useful tool for hard X/gamma-ray astronomy. Thanks to its good sensitivity, huge field of view, and pointing strategy covering all the sky, BAT is a suitable instrument to monitor known hard X-ray sources as well as to catch and study new transients. In this thesis, new procedures to analyse the BAT survey data are described with details and the first astrophysical results on galactic accreting sources discussed. Three X-ray binaries were observed and studied : the microquasar GRO J1655-40 during its 2005 outburst, the SFXT IGR J08408-4503 during its third recorded outburst and the symbiotic LMXB 4U 1954+319. A search for prompt gamma-ray emission due to downgraded decay of radioactive elements from novae was also performed. The emission of RS Oph, possibly due to shock heating, led to a detection. The probability of detecting a nova during the Swift lifetime was estimated using a Monte Carlo approach.

RESUME DE THESE

Le Burst Alert Telescope (BAT) à bord du satellite Swift est un instrument très performant pour l'astronomie des rayons X-durs/gamma. L'énorme champ de vue, la bonne sensibilité et la stratégie de pointage couvrant tout le ciel font de BAT un instrument adapté pour observer des sources connues et pour étudier les nouveaux objets variables. Dans cette thèse une description détaillée des nouvelles procédures pour analyser les données de survey de BAT est fournie et les premiers résultats astrophysiques de sources galactiques en accrétion sont discutés. Trois binaires X ont été étudiées : le microquasar GRO J1655-40, le SFXT IGR J08408-4503 et le LMXB symbiotique 4U 1954+319. L'émission gamma due à la décroissance des éléments radioactifs des novae a été aussi recherchée. L'émission de RS Oph, probablement liée au chauffage par choc, a été détectée. La probabilité de détecter une nova durant le temps de vie de Swift a été estimée en utilisant une approche Monte Carlo.

RIASSUNTO DELLA TESI

Grazie alla buona sensibilità, all'enorme campo di vista e alla strategia di puntamento coprente tutto il cielo, il Burst Alert Telescope (BAT) a bordo del satellite Swift è un telescopio adatto per monitorare sorgenti conosciute e studiare nuovi transienti nella banda X-duri/gamma. In questa tesi è fornita una descrizione dettagliata di nuove procedure per analizzare i dati di survey di BAT e sono discussi i primi risultati sull'astrofisica di sorgenti galattiche in accrescimento. Tre binarie X sono state studiate : il microquasar GRO J1655-40 durante l'outburst del 2005, il SFXT IGR J08408-4503 e la simbiotica LMXB 4U 1954+319. È stata anche effettuata una ricerca dell'emissione

gamma dovuta al decadimento di elementi radioattivi nelle novae. L'emissione di RS Oph, probabilmente legata al riscaldamento da shock, è stata rivelata. Infine è stata stimata la probabilità di rivelare una nova durante il tempo di vita di Swift usando un approccio Monte Carlo.

Contents

Acknowledgements **iii**

Thesis Summary **v**

Table of contents **vii**

List of Figures **xi**

List of Tables **xv**

Structure of the thesis **xvii**

1 The physics of the accreting X-ray binary sources **1**
1.1 Introduction 1
1.2 The physics of the accretion 2
1.2.1 Accretion modes 2
1.2.2 Disc formation 3
1.2.3 Accretion onto magnetised objects and BHs 5
1.3 Observational properties of the X-ray binaries 7
1.3.1 High- and Low-Mass X-ray Binaries 7
1.3.2 Pulsars 7
1.3.3 Non-pulsing objects 10
1.4 Some X-ray binary systems 11
1.4.1 Black Hole Binaries 12
1.4.2 Supergiant Fast X-ray Transients 15
1.4.3 Symbiotic LMXBs 15

2 The *Swift* mission **17**
2.1 Science goals of the mission 17
2.2 The Burst Alert Telescope (BAT) 19
2.2.1 Technical description 19
2.2.2 BAT operating modes 22
2.3 The X-ray Telescope (XRT) 25

2.4 The Ultraviolet/Optical Telescope (UVOT) 26

3 *Swift*/BAT survey data analysis software 29
3.1 A pipeline for time resolved spectroscopy (Pipeline 1) 30
3.1.1 Preliminary data selection and preparation 30
3.1.2 Imaging analysis and source detection 31
3.1.3 Spectra and response matrices generation 33
3.1.4 Spectral analysis 33
3.2 A pipeline for sensitive imaging (Pipeline 2) 35
3.2.1 Preliminary data selection and preparation 35
3.2.2 Source selection 35
3.2.3 Light curves production 36
3.2.4 Imaging analysis and source detection 37

4 Testing Pipeline 1 with the Crab and GRO J1655-40 39
4.1 BAT as a monitor: calibration with the Crab 40
4.1.1 Data selection 40
4.1.2 Results I: flux evaluation 41
4.1.3 Results II: stacking multiple DPHs 46
4.2 Systematic effects and evaluation of upper limits 49
4.3 Monitoring a strongly-variable source: the case of GRO J1655-40 53
4.3.1 BAT data analysis 55
4.3.2 *RXTE* data analysis 56
4.3.3 Results 56

5 GRO J1655-40: the hard-X ray emission during the rise of its 2005 outburst 63
5.1 GRO J1655-40 63
5.2 Observations and data reduction 64
5.2.1 *INTEGRAL* data reduction 64
5.2.2 *RXTE* data reduction 66
5.2.3 Swift data reduction 66
5.3 Results 68
5.3.1 Light curve 68
5.3.2 Spectral Modeling of the X and gamma-ray data 70

6 IGR J08408-4503: a new recurrent supergiant fast X-ray transient 81
6.1 IGR J08408-4503 82
6.2 Data Analysis 82
6.3 Results 83
6.3.1 Flare light curves 83
6.3.2 Flare spectra 85
6.4 A SFXT with very low intrinsic absorption 86

7 4U 1954+319: a new symbiotic low mass X-ray binary system 91
7.1 4U 1954+319 . . . 92
7.2 Observations and data analysis . . . 92
7.2.1 Spectral analysis . . . 93
7.2.2 Timing analysis . . . 94
7.3 The Neutron Star with the slowest spin period . . . 97

8 Search for prompt gamma-ray emission from novae 99
8.1 General characteristics of novae . . . 100
8.1.1 Classification . . . 100
8.1.2 Observational properties of novae . . . 103
8.1.3 Thermonuclear Runaway . . . 107
8.1.4 Withe dwarf composition . . . 108
8.2 Gamma-rays from Novae . . . 108
8.2.1 How a nova can produce gamma-rays . . . 109
8.2.2 How many gamma-rays can be produced by a Nova . . . 109
8.2.3 Past attempts to detect gamma-rays from novae . . . 112
8.3 Results with BAT . . . 113
8.3.1 BAT sensitivity . . . 114
8.3.2 Method . . . 115
8.3.3 RS Ophiuchi . . . 116
8.3.4 Classical Novae . . . 130
8.4 Future prospects . . . 143

Conclusions 145

Bibliography 151

List of Figures

1.1 Equi-potential lines generated by two point masses in the Roche approximation 4
1.2 NS spin vs orbital period plot for a sample of accretion-powered pulsars[1] 9
1.3 Configuration of the accretion flow in the five spectral states of a BH binary as a function of the total mass accretion $\dot{m}$ 14

2.1 The Swift satellite 18
2.2 A schematic view of the Burst Alert Telescope 20
2.3 Picture of the BAT coded aperture mask before the *Swift* launch 21
2.4 The D-shaped BAT FOV 22
2.5 Representation of a Detector Plane Histogram (DPH) 24

4.1 Dispersion of Crab detection coordinates around the nominal source position 42
4.2 Crab count rate per detector in the 10-100 keV energy band as a function of the coded fraction, as estimated by the source detection technique 43
4.3 Crab flux in the 10-100 keV energy band (upper panel) and spectral photon index (lower panel) as a function of the coded fraction, as estimated with the mask-weighting technique using Crab detection coordinates 44
4.4 Crab flux in the 10-100 keV energy band (upper panel) and spectral photon index (lower panel) as a function of the coded fraction, as estimated with the mask-weighting technique using celestial Crab coordinates 45
4.5 Crab flux in the 10-100 keV energy band as a function of the coded fraction for rejected DPHs, as estimated with the mask-weighting technique using Crab coordinates 46
4.6 Flux difference using detection coordinates and nominal coordinates as a function of coordinate difference 47

4.7 Correlation between the image values and the upper limits (30-100 keV) extracted using mask-weighting technique at the same coordinates 51
4.8 The orbital periodicity of the total BAT counts detected in the 50-100 keV energy band 53
4.9 Daily periodicity of the total BAT counts detected in the 50-100 keV energy band 54
4.10 GRO J1655-40 complete 2005 outburst as seen from *Swift*/BAT, *RXTE*/HEXTE, *RXTE*/PCA, and *RXTE*/ASM 57
4.11 Left panel: zoom of the first part of the GRO J1655-40 outburst as seen by BAT and HEXTE. The right panel represents the PCA count rate and hardness ratio as obtained from the (*http://tahti.mit.edu/opensource/1655/)* web site 58
4.12 Zoom of the central part of the GRO J1655-40 outburst as seen by BAT and HEXTE 58
4.13 Zoom of the final part of the GRO J1655-40 outburst as seen by BAT and HEXTE 59
4.14 Spectral photon index evolution of the GRO J1655-40 outburst as obtained by fitting a power law independently to BAT and HEXTE spectra 60
4.15 Zoom of Figure 4.14 for the central part of the outburst 61

5.1 ASM (1.5-12 keV) and SPI (23-51 keV) light curves of GRO J1655–40 during the rising phase of the 2005 outburst. The evolution of the hardness from ASM in the 3-12 keV energy range is also plotted 69
5.2 Spectra of GRO J1655–40 from PCA, SPI and HEXTE data fitted simultaneously with the model described in Table 5.3 . . . 74
5.3 Spectra of GRO J1655–40 from PCA, SPI and HEXTE data fitted simultaneously with the model described in Table 5.3 . . . 75
5.4 Evolution of the high energy cutoff derived from the model given in Table 5.3, as a function of the radio flux measured by VLA at 8.460 GHz[2] 78

6.1 IBIS/ISGRI (flare 1,2) and *Swift* (flare 3) light curves 84
6.2 Combined XRT and BAT spectra of flare 3 86

7.1 The 4U 1954+319 RXTE/ASM light curve in the 1.5–12 keV energy band. 93
7.2 Broad-band spectrum of 4U 1954+319, fitted with an absorbed BB Gaussian line, and cutoff PL 95
7.3 BAT light curve (15–50 keV) of 4U 1954+319 and period evolution as measured with BAT and ISGRI 96

8.1 Maximum accretable mass $M_{env}(crit)(\equiv \Delta M_{ig})$ as a function of $< \dot{M}_{WD} >$ and M_{WD} 102

8.2 Apparent magnitude at maximum versus distance[3] 105
8.3 Histogram of the novae discovered in 5 years intervals from 1901-2005, and per year from 1995-2005 106
8.4 Predicted gamma-ray light curve of the three possible lines, compared with visual light curve in arbitrary units. Temporal evolution of CO and ONe nova spectra at a distance 1 kpc 110
8.5 lightcurves in four energy bands for a 1.25 $M_\odot$ ONe-type and a 1.15 $M_\odot$ CO-type nova 111
8.6 The flux from RS Oph in the bands 14-25 keV and 25-50 keV observed with *Swift*/BAT 118
8.7 RS Oph image before $t_{discovery}$ and after $t_{discovery}$ 119
8.8 BAT-XRT joint fit 122
8.9 Six RS Oph spectra at different epochs obtained with PCA . . . 123
8.10 All band (∼1.5-12 keV) RS Oph ASM light curve 125
8.11 Kolmogorov Smirnov test for two distributions of significance values from the 'all' band (∼1.5 - 12 keV) light curve obtained with the *RXTE*/ASM 126
8.12 Kolmogorov Smirnov test for pre-outburst ($-103 < t < -2$) and post-outburst ($11 < t < 108$) periods 127
8.13 XRT fluxes in the 0.7-10 keV band. PCA fluxes in the same energy band are also plotted 129
8.14 Distribution of the significances in all energy bands for all the novae of Table 8.3 132
8.15 Flux versus timebin duration diagram for the nova V2362 Cyg . 134
8.16 Expected flux versus assumed distance diagram for the nova V2362 Cyg 136
8.17 Distribution of the distances from the Sun of the simulated novae 140
8.18 Distribution of the distances from us of the novae detected in gamma-rays in the Monte Carlo simulation 143

List of Tables

1.1 The two main classes of strong Galactic X-ray sources[4] 8

2.1 Swift Mission Characteristics[5] 18
2.2 Burst Alert Telescope Characteristics[5] 19
2.3 X-Ray Telescope Characteristics[5] 25
2.4 UltraViolet/Optical Telescope Characteristics[5] 27

4.1 Number of DPH rows of the Crab sample rejected after the filtering stage 41
4.2 Distribution of the Crab location in the FOV for the processed sample of DPH rows 41
4.3 Catalogue and detection coordinates percent difference 43
4.4 Flux and power law statistic of Crab dataset 45
4.5 Crab flux loss for two DPH stacked as a function of the DPH pointing offset 48
4.6 Best-fit parameters obtained by fitting Gaussian distributions on the groups of DPH upper limits 52

5.1 The *INTEGRAL*observations of GRO J1655–40. The simultaneous BAT data are also indicated 65
5.2 Details of BAT data observations 67
5.3 Flux of GRO J1655–40 measured by SPI during different *INTEGRAL* revolutions and for several energy bands 68
5.4 PCA, SPI and HEXTE data fitted simultaneously using the XSPEC multicomponent model PHABS*(GAUSSIAN + DISKBB + POWERLAW) 71
5.5 PCA, HEXTE and SPI data fitted simultaneously using the XSPEC multicomponent model PHABS*(PEXRAV + GAUSSIAN + DISKBB) 73
5.6 PCA, HEXTE and SPI data fitted simultaneously using the XSPEC multicomponent model PHABS*(COMPTT + GAUSSIAN + DISKBB) 76

6.1 IGR J08408–4503 spectral parameters using a power-law model with an exponential high energy cut-off 87
6.2 Stellar parameters for HD 74194 derived from[6] 88

8.1 The different classes of novae as shown in Table 2 of Darnley *et al.*[7] 103
8.2 Expected fluxes of a 1.25 M⊙ ONe-type and a 1.15 M⊙ CO-type nova at 1 kpc assuming the nuclear reaction rates of Coc *et al.*[8] and Hernanz *et al.*[9] respectively 112
8.3 The sample of the 18 novae adopted for the search for gamma-ray emission 117
8.4 Summary of RS Oph XRT observations and spectral fits 121
8.5 Summary of RS Oph PCA observations and spectral fits 124
8.6 Summary of the results obtained from BAT data for 17 Classical novae 138
8.7 Models of the nova spatial distribution in the Galaxy used for the Monte Carlo simulation[10] 139
8.8 Expected detection rates of novae with BAT in four energy bins 141

Structure of the thesis

Our knowledge of the X-ray binary systems was recently improved by the new discoveries of the *INTEGRAL* satellite. The Burst Alert Telescope (BAT) on board the *Swift* satellite is a powerful tool for hard X/gamma-ray astronomy which can make the scenario clearer. The huge amount of data collected by the BAT while waiting for new detections of gamma-ray bursts may complete the *INTEGRAL* view of the hard X-ray sky. Indeed, due to its very large field of view (FOV), good sensitivity and pointing strategy, BAT can be exploited as an efficient monitor for X-ray binaries as well as for novae, for which the detection of the predicted gamma-ray emission still remains an intriguing challenge.

In this thesis, new software tools devoted to the analysis of the *Swift*/BAT data were developed and tested, and the instrument performance was calibrated. Results obtained using the *Swift*/BAT data on different classes of galactic accreting sources are presented.

- Chapter 1 provides an introduction to the thesis. Some of the most important characteristics of the accreting X-ray binaries hosting a Neutron Star or a Black Hole are summarised. The phenomenology and the physics of accretion are briefly reviewed. Particular emphasis is given to the classes of sources which are the object of this thesis.

- In Chapter 2 an overview of the *Swift* mission is given. A detailed description of the BAT technical performance and its operating modes is presented. A concise description of the other two instruments on board *Swift*, the X-ray Telescope (XRT) and the Ultraviolet/Optical Telescope (UVOT), is also given.

- Chapter 3 gives details on the new software tools for the analysis of the *Swift*/BAT survey data that were developed as part of this thesis. The software consists of two new pipelines: the first one (Pipeline 1) is a new procedure entirely based on public tools which allows the extraction of spectra and light curves in physical units (i.e. ergs/cm^2/s) of a given source. The second one (Pipeline 2), composed of public tools and non-standard products, yields at once count rate light curves for several

sources, minimizing the contamination from bright sources in the FOV (courtesy of Prof. Skinner).

- In Chapter 4 detailed tests performed to verify the reliability of the results of Pipeline 1 are presented. The steady and bright Crab is used to check the reliability of spectral results as a function of the source position within the BAT FOV, as well as of different observing conditions. Next, the case of a fainter, and strongly variable, source is studied taking advantage of the availability of contemporaneous data collected by a different satellite. The 2005, 9 month long outburst of the Black Hole Binary GRO J1655-40 was systematically monitored with the Rossi X-ray Timing Observatory (*RXTE*). This allows for a robust cross-calibration of the BAT results with those obtained - independently and simultaneously - by a well-calibrated instrument such as HEXTE on board *RXTE*. The BAT light curve of the outburst is in good agreement with the *RXTE* one, thus proving the capabilities of BAT as a monitor for strongly variable sources.

- In Chapter 5 the first application of Pipeline 1 to an astrophysical case is illustrated. The analysis of the spectral evolution of GRO J1655–40 during the rising phase of the 2005 outburst is presented. The wide temporal coverage of the source, serendipitously obtained by BAT, was crucial to follow the transition from the Low Hard State to the High Soft State. The evolution of the high energy cutoff during this transition is also well determined.

- In Chapter 6, Pipeline 1 is used to study the third recorded outburst of IGR J08408-4503, which was discovered by *Swift*/BAT. This, together with the a posteriori discovery of a second outburst in the *INTEGRAL* archive, allowed the source to be identified as a Super Fast X-ray Transient. The spectra of the three outbursts were used to constrain the Neutron Star magnetic field, the system orbital period and the circumstellar medium.

- In Chapter 7, Pipeline 1 is again used to unveil the nature of 4U 1954+319, a flaring X-ray binary composed of a Neutron Star and a late type star. A periodic signal and a clear spin-up trend are found by the timing analysis performed over the huge amount of BAT survey data, serendipitously collected in more than one year. Such period was identified with the Neutron Star spin, making 4U 1954+319 a new symbiotic low mass X-ray binary, hosting the Neutron Star with the slowest spin period known so far.

- Chapter 8 is devoted to the search for prompt gamma-ray emission from novae. Novae, fully described in the Chapter, are predicted to be relatively strong gamma-ray emitters, but no positive detections were found

so far with observatories launched before *Swift*. Pipeline 2 is used to search in the BAT data for evidence for gamma-ray emission from the direction of 18 novae at around the time of their explosion. RS Ophiuchi alone yields a positive detection in the 14-25 keV band, the emission being probably due to shock heating. For all other novae, upper limits were estimated. Finally, the probability of detecting a nova during the *Swift* operating lifetime is calculated using a Monte Carlo approach.

Chapter 1

The physics of the accreting X-ray binary sources

1.1 Introduction

Since the discovery of the first X-ray source (Sco X-1,Giacconi *et al.*[11]), it was suggested that the strong galactic X-ray sources were accreting Neutron Stars (NSs) or Black Holes (BHs) in binary systems. The existence of such objects was first confirmed by Schreier *et al.*[12], who discovered that the source Cen X-3 is regularly pulsing (thus: a NS), and is member of an eclipsing binary system. Then, from optical observations of Cyg X-1[13,14] a mass for the compact object $> 3M_{\odot}$ was deduced, suggesting an indirect evidence for the existence of BHs. Thanks to a broad, deep exploration of such objects during the last ~ 40 years, our knowledge of the astrophysics of the final stages of stellar evolution and the physics of matter at extreme physical conditions has greatly improved. Periodic pulsations in the X-ray light curve of spinning NSs[15] as well as X-ray bursts due to thermonuclear flashes on NS surfaces[16] were discovered in the first three decades after the Sco X-1 discovery. For a number of systems it was possible to measure the masses of the compact objects, thus providing the strongest evidence for the existence of BHs. The good performance of the X and gamma-ray telescopes launched during the last ten years (*RXTE*, *Beppo*SAX, the *Chandra* X-ray Observatory, *XMM-Newton*, and *INTEGRAL*) increased the number of observational properties of accreting compact objects and allowed many interesting behaviours to be understood. Such objects were monitored from the radio to gamma-rays, leading, for example, to the discovery of highly relativistic jets[17] and to the possible identification of NSs with masses close to the Chandrasekhar limit[18]. Many other behaviours, such as the rapid variability phenomena that occur at the dynamical timescales outside the NS surface and the BH horizon[19], were observed and other proofs of the validity of the General Relativity, such as the blue- and red-shift of atomic lines in the vicinity of compact objects, were found[20].

In this chapter some of the most important characteristics of the accreting X-ray binaries hosting a NS or a BH are summarized. All the binary systems containing an accreting White Dwarf (WD) are members of the so-called Cataclysmic Variables class (CVs). Although X-rays were observed from those WD whose magnetic field is strong enough ($\sim 10^8$ G), the X-ray flux above 2 keV is comparatively less than that observed for a NS or BH. Non-magnetic CVs, such as classical and recurrent novae, are predicted to be relatively strong emitters of gamma-rays (above a few tens of keV) during their explosions, but such emission has not yet been detected. As CVs show properties markedly different from those of NS and BH binaries, this class will be discussed separately (see Chapter 8).

1.2 The physics of the accretion

A large number of binary systems composed of a collapsed object (often defined as the "primary star") and a losing-mass companion star (the "secondary star") were discovered and studied in the X-ray domain. In most cases the efficient production of radiative energy is due to the accretion of matter from the secondary star in the strong gravitational field of the collapsed objects. Up to 10-42% (depending on the compact object) of the rest-mass of the accreting flow can, in principle, be converted into radiation, the bulk energy of which falls in the X-ray band[21].

1.2.1 Accretion modes

Stellar wind accretion

Early-type stars, such as that of type O or B, are known to lose mass in the form of an intense stellar wind (mass loss rate of $\sim 10^{-6} - 10^{-5} M_\odot/yr$) having velocities v_w comparable with the superficial escape velocity $v_{esc} = \sqrt{2GM_p/R_p} \simeq 10^3$ km s^{-1}, where M_p and R_p are the mass and the radius of the star respectively. When a compact object with mass M_x is moving through a strong stellar wind with velocity v_{rel} and sound speed c_s, it gravitationally captures matter from a roughly cylindrical region with axis along the relative wind direction. This region represents the volume where wind particle kinetic energy is less than the gravitational potential one[22,23,24]. Such cylinder has a radius, called the accretion radius (r_{acc}), given by

$$r_{acc} = \frac{2GM_x}{v_{rel}^2 + c_s^2} \tag{1.1}$$

where $v_{rel}^2 = v_{orb}^2 + v_w^2$, and v_{orb}^2 is the compact object orbital velocity. The net amount of specific angular momentum carried by the gas stream and captured by the accreting object is mainly due to the asymmetry of the accretion. Shapiro *et al.*[25] have shown that a density and velocity gradient are always

present on the cylindric surfaces because of the difference in the amount of particles captured at the far-side and at the near-side surface. Taking into account only the radial density gradient in the spherically symmetric stationary expansion of the stellar wind, the captured angular momentum per unit mass J with respect to the compact object is approximately given by $J = (1/2)\Omega_{orb} r_{acc}^2$, where Ω_{orb} is the orbital angular velocity.

Also systems containing a Be star and a NS behave in this way. Often such systems have highly eccentric orbits because tidal forces have not yet circularised the binary after the supernova explosion that originated the NS. In this case, accretion occurs during the phases of the orbit in which the NS passes closer to the Be star, where its stellar wind is denser.

Roche-Lobe Overflow

Low mass and late type stars usually have stellar winds less prominent than O-B stars, except for stars that are in the red-giant phase of their evolution. In the former case mass transfer occurs mainly through Roche-lobe overflow. Three assumptions are made in the Roche approximation: the two stars move in a circular orbit around their center of mass, they co-rotate with the binary system, and their gravitational field can be described by that of two point masses. Under these conditions, the gravitational plus centrifugal potential of the system and their corresponding equi-potential surfaces can be analytically derived (see Figure 1.1).

Close to each object, the potential is dominated by the gravitational potential of the star, thus the surfaces are almost spherical. As one moves farther from a stellar center, the tidal effect, which causes an elongation in the direction of the companion, and the flattening, due to the centrifugal force, become important. The inner Lagrangian point L_1 splits the equipotential surface passing through it into two volumes called Roche lobes of the respective stars. Stars which fill their Roche lobe transfer mass through L_1 to their companion. Mass transfer can occur either owing to star expansion (due to its own evolution) to the point that it fills its Roche lobe, or to orbital shrinking, due to systematic angular momentum losses. The specific angular momentum J with respect to the orbiting compact object is given by[26] $J \approx \Omega_{orb}(a - r_L^2)^2$, where a is the orbital separation and r_L the Roche lobe radius. All the matter from the companion star is assumed to leave the critical lobe near L_1.

1.2.2 Disc formation

The accreting matter forms a disc when its specific angular momentum J is too large to hit the accreting object directly. This happens when the circularisation radius $R_{circ} = J^2/GM_x$ (where the matter would orbit if it lost energy but no angular momentum) is larger than the effective size of the accretor. By substituting the expression found for J in section 1.2.1 and 1.2.1 it is possible to obtain the size of the expected radius at which a disc begins to form in

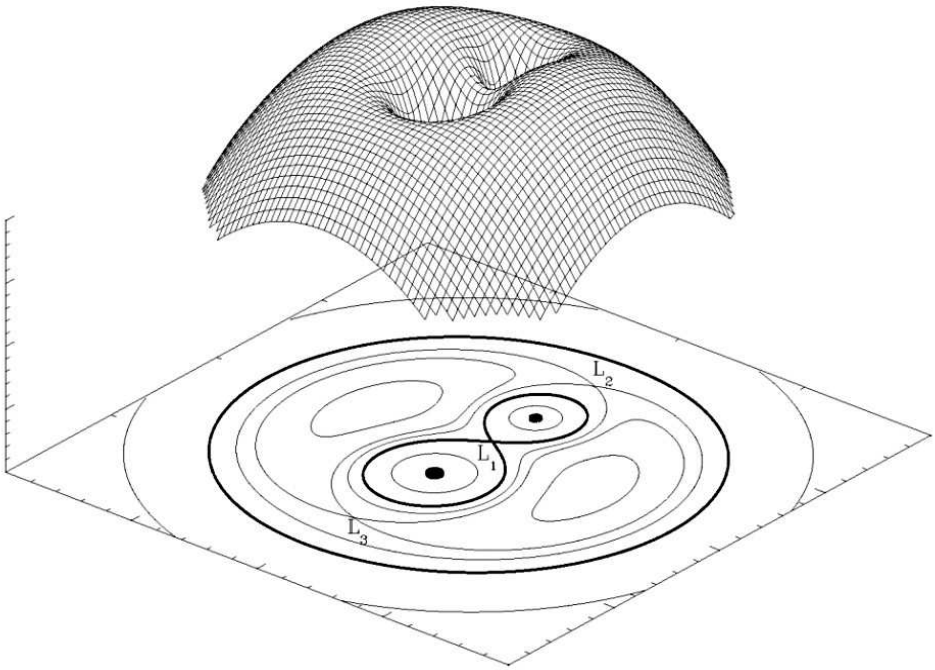

Figure 1.1: *Equi-potential lines generated by two point masses (black points) in the Roche approximation. The marked eight-shaped line determines the Roche lobes of the two stars. L1, L2 and L3 are the Lagrangian equilibrium points. Mass can flow through the saddle point L1 from one star to its companion, if the star fills its Roche lobe. In the top of the figure, a suggestion of the gravitational potential wells of the two stars is shown.*

a wind accretion and Roche lobe overflow system respectively. If accretion occurs via Roche lobe overflow, R_{circ} is greater than the radius of the compact object for typical orbital parameters, so a disc will form. If accretion occurs via stellar wind, the condition for the formation of a disc is not always kept.

The matter in an accretion disc can orbit at R_{circ} and accretion can only take place through a sequence of almost Keplerian circular orbits with gradually decreasing J (see Frank *et al.*[23] and references therein; King[24]). Most of the original angular momentum is carried outwards beyond R_{circ} and it is typically returned to the secondary star's orbit through tides. Energy dissipation and angular momentum transport are generated by viscosity which provides a torque between the shearing orbits. As a result the matter in the disc moves deeper and gets hotter as it sinks into the gravitational potential well of the compact object.

1.2.3 Accretion onto magnetised objects and BHs

If the disc extends down to the surface of the accreting star, the matter enters a region, called boundary layer, over which gas moving at Keplerian velocities is decelerated to match the star angular velocity. In this region the matter of the disc releases a large amount of energy and gives up its angular momentum to the compact object.

Systems containing strongly magnetised compact objects show different behaviours. The presence of the magnetic field plays an important role in the dynamic of the gas flow as it approaches the surface of the collapsed star leading to the disruption of the disc. The at least partially ionised gas falling towards a magnetised star will at some point have its motion affected by the magnetic field. The magnetosphere is usually defined as that volume within which the field strongly affects the dynamical properties of the infalling flow, such as the trajectory, the energy and the angular momentum (for a review see Vasyliunas[27], Henrichs[22]).

For spherically symmetric infall, the magnetospheric radius r_m is usually determined from the balance of magnetic pressure $B^2(r)/8\pi$ and ram pressure of the infalling gas $\rho v_{in}^2(r)$, where B is the magnetic field of the compact object, ρ the disc density and v_{in} the velocity of the infalling matter[28]. A significant magnetic behaviour is seen when r_m is greater than the compact object radius. Together with r_{acc} and r_m, there is a third characteristic length scale, called the co-rotation radius r_{co}, which is the distance at which the rotation velocity of the compact object matches the Keplerian one. Several physical regimes can be defined depending on the relative size of r_{acc}, r_m, r_{co} and r_L as well as the magnetic field strength[29,30].

- $r_{acc} > r_m$ and $r_{co} > r_m$:

  the gas of the disc flows from the accretion radius down to the magnetospheric radius, where a collisionless shock stops it. The gas then penetrates the magnetosphere till a point where it is forced to follow the

magnetic field lines towards the star surface (direct accretion). For values of B greater than $10^{10}G$ matter falls in a small region located near the polar caps of the compact object. In such case a large amount of X-ray radiation is released and, from the point of view of the Earth, it arrives modulated by the star rotation period P. For B values less than $10^{8}G$, matter can get through the magnetosphere without be forced to follow the magnetic field lines and accretion occurs at all star latitudes.

- $r_{co} < r_m < r_{acc}$:

  the material penetrating through the accretion radius is stopped at r_m and cannot advance any further because the drag exerted by the magnetic field is super-Keplerian. Some or all the material might be ejected beyond r_{acc} via the propeller mechanism (centrifugal inhibition of accretion). If the material accumulates at or nearby the magnetospheric more rapidly than ejection rate, a buildup of material outside the magnetosphere may occur[31].

- $r_m > r_{acc}$:

  in such a case the disc formation may be inhibited. The gas will flow around the obstacle presented by the star magnetosphere. The fraction of the material which penetrates r_m is very low (magnetic inhibition of accretion).

- $r_m \geq r_L$ and/or $r_m \geq a$:

  in this scenario the gas leaving the secondary star is expected to be attached to the field lines of the magnetised object for its entire interstellar trajectory. Depending on the location of the threading region in the magnetic field, the matter may be fed towards either one or both polar regions.

The accretion onto a BH shows different properties. The extreme gravitational field near a BH does not allow stable particle orbits, so the disk is truncated at the radius that corresponds to the innermost stable circular orbit (ISCO)[32,33]. Such radius (R_{ISCO}) can be expressed as a function of the Schwarzschild radius of the BH ($R_g = GM/c^2$). For a Schwarzschild BH R_{ISCO} =$6R_g = 90$ km$(M/M_\odot)$, whereas for an extreme Kerr BH $R_{ISCO} = R_g$. The event horizon, the surface surrounding the BH in which the spacetime cannot communicate with the exterior, lies at $R_{e.h.}$ =$2R_g$ = and $R_{e.h.} = R_g$ for a Schwarzschild and an extreme Kerr BH respectively. $\sim 90\%$ of the binding energy of the matter falling into the gravitational potential of the BH is radiated within about $20R_g$ of the center.

1.3 Observational properties of the X-ray binaries

X-ray binaries show different behaviours depending on the nature of the compact object, on the type of the secondary star and on many other parameters. In this section, the most important observational properties of such objects are briefly summarized.

1.3.1 High- and Low-Mass X-ray Binaries

As explained in section 1.2.1, a compact object can accrete matter from a companion which loses mass in the form of stellar wind. The companion star is known to emit a strong stellar wind when its mass is greater than $\geq 10 M_{\odot}$, making the compact star a bright X-ray source. In this configuration, the optical luminosity of the companion star (typically a early type (O-B) star) dominates the total emission from the system and the rate of mass transfer is determined by the strength and the speed of the wind and the orbital separation. Such systems are called High-Mass X-ray Binaries (HMXBs).

Moreover, there is a class of X-ray binaries containing a late type (K,M), low mass donor star. For such systems, stable mass transfer through the inner Lagrangian point occurs when the companion fills its Roche lobe (see section 1.2.1). Mass is driven by angular momentum loss due to gravitational radiation (for very small masses and orbital separations) and magnetic breaking (for orbital $\leq$ 2 days) or by the evolution of the companion star (for orbital periods $\geq$ 2 days). The luminosity of these sources is stronger at X-ray rather than optical wavelengths. Such systems are called Low-Mass X-ray Binaries (LMXBs).

These two classes of systems differ under many aspects. The lifetimes of HMXBs are short ($\sim 10^5$-10^7 yr), as these depend on the evolution of the high-mass companions, whereas LMXBs last longer ($\sim 10^7$-10^9 yr) depending on the mass-transfer process. For this reason, HMXBs are typically spread along the galactic plane, where young stellar populations are present, and LMXBs are mostly concentrated in the galactic center, where older stars are located. Table 1.1 summarizes the most important differences between HMXBs and LMXBs

1.3.2 Pulsars

X-ray periodic pulsations are seen in those systems containing a strongly magnetized NS for which the radiation beam intercepts our line of sight. As explained in section 1.2.3, the strong magnetic field plays a key role in channelling the ionised matter along its field lines towards the polar caps, where X-rays are produced. Instead, magnetic fields fainter than $\sim 10^8$G result in an accretion occurring at all star latitudes, so no pulsations are seen. In the case of accreting BHs, the presence of the event horizon does not allow for any stable

Table 1.1: *The two main classes of strong Galactic X-ray sources*[4]

	HMXB	LMXB
X-ray spectra:	$kT \geq 15$ keV (hard)	$kT \leq 10$ keV (soft)
Type of time variability:	regular X-ray pulsations no X-ray bursts common X-ray eclipses	only a very few pulsars often X-ray bursts rare X-ray eclipses
Accretion process:	wind (or atmos. RLO) small disk, if any	Roche-lobe overflow disk
Timescale of accretion:	10^5 yr	$10^7 - 10^9$ yr
Accreting compact star:	high $\vec{B}$-field NS ($\sim 10^{12}$G) or BH	low $\vec{B}$-field NS ($\sim 10^7$-10^8G) or BH
Spatial distribution:	Galactic plane	Galactic center and spread around the plane
Stellar population:	young, age $< 10^7$ yr	old, age $> 10^9$ yr
Companion stars:	luminous, $L_{\rm opt}/L_x > 1$ early-type O(B)-stars $> 10\,M_\odot$ (Pop. I)	faint, $L_{\rm opt}/L_x \ll 0.1$ late-type K(M) stars $\leq 1\,M_\odot$ (Pop. I and II)

feature to be anchored to the rotation of the compact object. Even in this case no pulsations are visible.

The matter interacting with a strongly magnetized NS can be channelled along the field lines or rejected, depending on the spin frequency of the NS (see section 1.2.3). If the stellar spin frequency is smaller than the orbital frequency of the matter at the interaction radius, then the accreting material is forced into co-rotation with the star and is channelled onto the magnetic poles. This system is called accretion-powered pulsar. If the stellar spin frequency is larger than the orbital frequency of matter at the interaction radius, then the material cannot overcome the centrifugal barrier in order to accrete onto the star and probably escapes the NS in the form of a wind (propeller regime).

The NSs also react differently to the accretion of matter depending on its magnetic field strength, its spin frequency, and the mass accretion rate. Magnetic field lines, which rotate at the spin frequency of the star, transfer angular momentum from the accreting material to the NS, if the former is spinning faster than the latter, vice versa in the opposite situation. In an accreting system, both situations occur simultaneously because the orbital frequency of matter decreases with increasing radius. The net result is a torque on the NS, which can be either positive (spin-up) or negative (spin-down). The strength of such torque on the star is an increasing function of the mass accretion rate and magnetic field strength[34,35].

The accretion-powered pulsars are systems for which the spin frequencies and the magnetic field strengths of NSs can be studied in some detail. Such pulsars can be divided into two distinct classes, depending on their spin period: the slow pulsars and the millisecond pulsars. The former are generally found in HMXBs as one can see in the "Corbet diagram" which correlates the spin of

the NS to the system orbital period for a sample of pulsars (Figure 1.2).

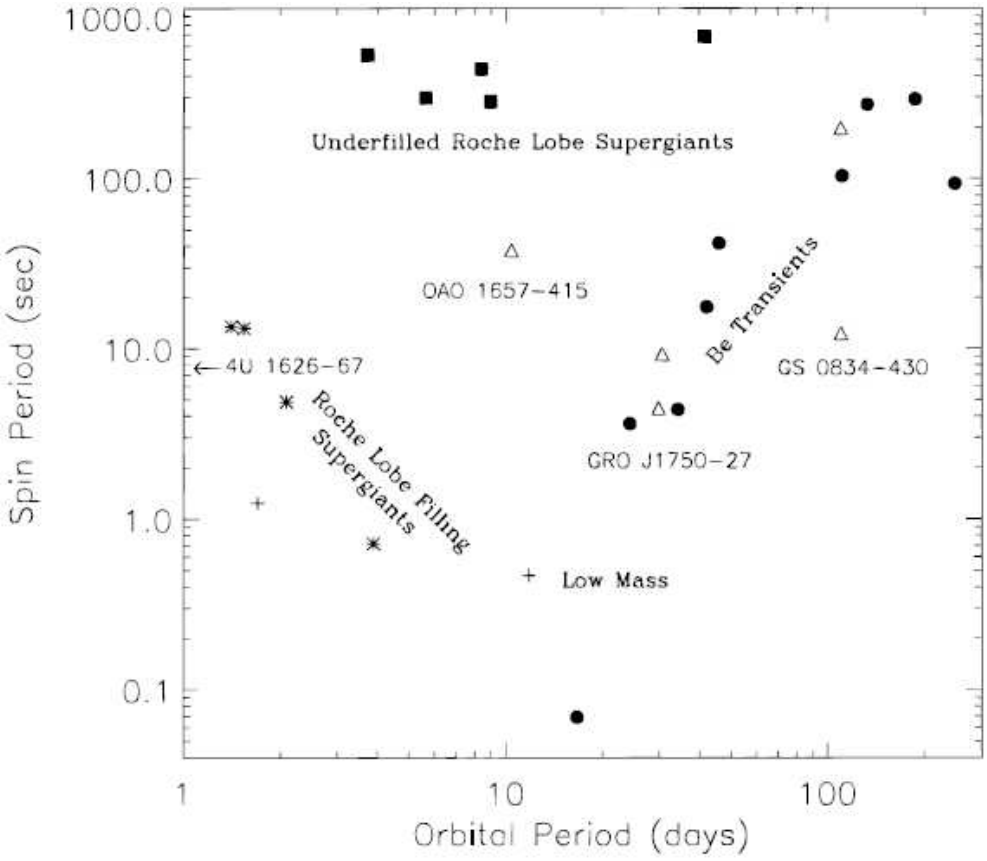

Figure 1.2: *NS spin vs orbital period plot for a sample of accretion-powered pulsars*[1]

About half of the slow pulsar systems contains main-sequence Be stars, whereas the remaining contains evolved O-B supergiants. The spin evolution of a NS can be determined by the mode of mass transfer onto it. The long-term aspect of this dependence is visible in Figure 1.2. Systems with Roche lobe filling supergiants have short spin periods, anticorrelated with the orbital periods. Systems with underfilling supergiants have long spin periods not correlated with orbital periods. Finally, the Be transient systems have long orbital periods correlated to the orbital periods. Such correlations might depend on the mode and efficiency of mass transfer. Considering transient accretion-powered pulsars at the limit of very low mass accretion rate, the NSs are expected to spin down, because the magnetic field lines that couple to the slower accretion flow remove spin angular momentum from the NS. Instead, persistent disk-fed pulsars show episodes of spin-up and spin-down at timescale that vary from $\sim$ 10 days (e.g., Cen X-3) to $\geq$ 10 yr (e.g., GX 1+4). The millisecond pulsars are generally found in LMXBs. The very short spin periods are thought to be the result of a long evolution during which accreting mass

at high rates spun-up the NS.

1.3.3 Non-pulsing objects

This class of binary systems is composed of both persistent and transient sources. The formers were almost always detectable and showed variability of X-ray flux over timescales ranging from milliseconds to months, whereas the latters show periods of inactivity of the order of months up to decades that are interrupted by short outbursts.

In the case of the persistent sources, the X-ray flux typically shows variations by factors of two over periods ranging from months to fraction of seconds. The reasons of such variability can be found in the wide range of characteristic timescales involved in the processes concerning the high-energy emission. One of these reasons is that the transfer of mass from the companion star to the compact object is expected to vary at timescale comparable to the orbital period (from hours to days). Moreover, matter spirals inwards in the disk at the viscous timescale, which is slower than the Keplerian orbital frequency at any radius. The time needed for the matter to diffuse inwards ranges from days, at the outer edge of the disk, to fractions of a second, close to the compact object.

The transient sources are in most cases BHs that show in quiescence a luminosity fainter than NSs in non-pulsing transient binaries. Such difference can be explained by the different mass ratio of the members of the binary systems between the two populations and by the presence of the event horizon in BHs which hides a large fraction of the accretion luminosity. For transient sources, the most accepted model is the disk instability model of illuminated accretion disks[36,37]. Such model states that accretion flows which extend to large radii ($>10^9$ - 10^{10} cm) from the compact object have temperatures $< 10^4$ K. At such temperatures the anomalous opacity related to the ionisation of the hydrogen causes thermal instability in the disk. During the quiescent phase, the disk is stable and material piles up at the outer edge of the accretion disk with a very low accretion rate on the compact object. When the disk becomes unstable, the accretion flow is driven to the central object at the viscous timescale, and the system begins the outburst phase.

By performing X-ray timing studies of non-pulsing objects, quasi-periodic oscillations (QPOs) were discovered at all timescales[38]. In some cases several variable-frequencies QPOs were observed simultaneously, suggesting that accretion flows can get only a small number of characteristic frequencies at which to vary preferentially. The current models of QPOs tend to associate some of the observed frequencies with dynamic frequencies in the accretion flows, such as, for example, which ones related to the azimuthal orbital motion of plasma or to Lense-Thirring precession. Such models require the presence of a characteristic radius, across which the properties of the accretion disk change considerably. For example, in BHs the ISCO is responsible, in different models, for the saturation of the observed QPO frequencies with accretion

rate[39]. In this scenario, these frequencies correspond to regions very close to the NS surface or the BH event horizon, thus providing useful probes into the physical conditions close to the compact objects. An interesting property typical of some accreting BHs is the presence of relativistic jets as seen in Active Galactic Nuclei. Their non-thermal polarised radio spectra indicate the presence of shock-accelerated relativistic electrons emitting synchrotron radiation [40]. Large flux ratios between the approaching and receding sides of the jets are also shown as expected for relativistic flows[17]. Corbel *et al.*[41] show that the presence of jets is clearly correlated to the X-ray spectral state of the accretion flows: jets appear when the X-ray spectra of the source indicate emission from hot electrons ($\sim$ 100 keV), whereas they are absent when the source spectra are typical of cold, geometrically thin accretion disks. Among the non-pulsing binaries, those containing a weakly magnetised NS can be identified by typical thermonuclear flashes, called Type I X-ray bursts (see Lewin *et al.*[42]). The material accreted on the surface of such NSs may be compressed to densities and temperatures for which the thermonuclear burning of helium is unstable. As the helium begins to ignite, rapid ($\sim$ 1 s) increase in the X-ray luminosity of the NS, followed by a slower ($\sim$ tens of seconds) decay is seen. The most energetic bursts, called Eddington-limited bursts, show a rapid expansion of the surface layers of the NS, caused by the radiation pressure that balances gravity. Eddington luminosity is reached in such phase and the remaining energy of the explosion is converted into kinetic and potential energy of the expanding layers[43]. Since the maximum observed flux roughly depends on the mass of the star, its radius, and its distance, the fact that the mass and the radius of a NS span a very narrow range allows the estimation of its distance by measuring the X-ray flux[44]. Moreover, thanks to *Beppo*SAX and *RXTE* capabilities, a new type of burst was discovered, the so-called "superburst"[45]. These bursts have long durations ($\sim$hr) and recurrence times ($\sim$ hr) and are believed to be caused by unstable carbon burning in layers that are deeper than those responsible for the Type I bursts.

1.4 Some X-ray binary systems

In the previous section, the main characteristics of the X-ray binary systems discovered before the beginning of this millennium were summarized [46]. Hundreds of bright X-ray binaries were discovered and studied thanks to the good capabilities of observatories such as the Compton Gamma-ray Observatory (*CGRO*), the *RXTE*, *Beppo*SAX, the *Chandra* X-ray Observatory and *XMM-Newton*. The *INTEGRAL* satellite[47], launched on October 17, 2002, significantly changed the scenario of X-ray binaries. Due to its large FOV (29°$\times$ 29°) and very good sensitivity in the 15-300 keV band, the Imager on Board *INTEGRAL* Satellite (IBIS, Ubertini *et al.*[48]) detected $\sim$300 previously-known sources and discovered $\sim$200 new sources during its first four years lifetime (see Bodaghee *et al.*[49],Bird *et al.*[50], and Bird *et al.*[51]).

A regularly updated list of all the new *INTEGRAL* sources is available at *http://isdc.unige.ch/∼rodrigue/html/igrsources.html*. It detected similar numbers of Galactic X-ray binary systems and extra-Galactic sources (mainly Active Galactic Nuclei), the former being mostly HMXBs and LMXBs. Among the new X-ray binaries, a few LMXBs were found whereas many HMXBs were discovered, some of which belonging to new classes, such as the Supergiant Fast X-ray Transients (SFXTs) and the highly absorbed pulsars.

Roughly half of all the new *INTEGRAL* sources are still unclassified. Some of that are too faint to allow their nature to be unveiled while some other are transients with long period of inactivity followed by short emissions. Although the *INTEGRAL* pointing strategy mainly concentrates in the Galactic plane, the IBIS FOV is not large enough to allow a good temporal coverage of all such sources, therefore their short flaring activity can be probably missed. An instrument with high sensitivity in the same energy band and a very large FOV may help in unveiling the nature of such objects as well as discovering new sources. The Burst Alert Telescope (BAT) on board the *Swift* satellite (see Chapter 2) is an excellent choice for such kind of researches. In fact, it has a very large FOV (∼2 sr), a good sensitivity in the 15-150 keV band and a serendipitously pointing strategy covering almost uniformly the sky. With such characteristics, it provides a better temporal and spatial coverage of a given celestial direction.

One of the aims of this thesis is to show that *Swift*/BAT is a suitable instrument to monitor bright X-ray sources: several interesting results will be shown in support of that. In this section a short description of the main properties shown by the X-ray binary systems treated in this thesis is presented. As one can see in the following chapters, BAT was able to follow the entire 2006, 9-months long outburst of the known BH binary GRO J1655-40 and to observe it with good detail during a phase transition. Thanks to its serendipitously collected observations, it was also able to observe the third recorded short flare of IGR J08408-4503, a new member of the SFXTs recently discovered by *INTEGRAL*. To emphasise the importance of using BAT, it is worth remarking that, at that epoch, *INTEGRAL* was pointing elsewhere and missed the event. Finally, the good temporal coverage of a given direction of the sky allowed a detailed timing study of 4U 1954+319 to be performed using BAT data covering more than one year. The derived ∼5 h periodicity, with a spin-up timescale of ∼25 years, was possibly identified as the NS spin period implying that this is the slowest established wind-accreting X-ray pulsar. The spectral and timing characteristics of the source suggest that it is the second confirmed member of the emerging class dubbed "symbiotic low mass X-ray binaries" to host a NS.

1.4.1 Black Hole Binaries

Black Hole Binaries are interesting systems which usually exhibit a complex spectro-temporal variability with the variation of the accretion rate. The

changes in their properties allow the state of the source to be characterised (see McClintock & Remillard[52] and references therein, for a complete description). Five are the states, defined in the 1-10 keV band, which are shown by such systems. The first one is the High Soft State (HSS), for which the soft X-ray emission ($\leq$ 10 keV) dominates the spectrum in the form of a blackbody component whose oringin can be ascribed to the thermal component from a standard accretion disk. Usually, the temperature of the thermal component is in the range 0.7-1.5 keV.

From the HSS the system shows a transition in the so-called Low Hard State (LHS). Such a state is characterised by a relatively low flux in the soft X-rays ($\lesssim$1 keV) and a high flux in the hard X-rays ($\sim$100 keV) which is usually interpreted (e.g. Shapiro *et al.*[25], Narayan & Yi[53]) as the Comptonization of the soft X-ray photons emitted by a hot plasma surrounding this accretion disk. The hard component is generally described by a power-law with a photon index of 1.4-1.8, and an exponential cutoff around 100-200 keV. In addition, a Fe K line at $\sim$6.4 keV and a Compton reflection bump peaking at $\sim$30 keV may exist. These are signatures of the irradiation of the cold optically thick disk by the hard X-rays from a corona[54]. The LHS is characterised by radio emission which was shown to be consistent with a mildly relativistic (v $\simeq$ 0.6c) jet[55].

Before entering into the HSS, the source may go through transitional states also called intermediate states. Homan & Belloni[56] divide the intermediate state into the hard intermediate state (HIMS) and the soft intermediate state (SIMS) which depend on the power density spectra and the spectral index. The jet starts to be quenched from this intermediate state (e.g. Corbel *et al.*[57]). There is another state, called Very High State (VHS), in which the system becomes very bright and the X-ray spectrum again displays non-thermal radiation which can constitute 40-90% of the total flux. In such case the photon index is typically $\Gamma \geq 2.4$ which is steeper than that of the LHS, and no high-energy cutoff is present. This state can be interpreted as strong Comptonization of disk photons by a non-thermal corona. The last state of a BH binary is the quiescent state (QS). Such state is dominated by faint, power-law emission.

An attempt to unify such states in a physically coherent scheme was made by Esin *et al.*[58]. The approach is schematically shown in Figure 1.3. The geometry of the accretion flow changes as a function of the mass accretion rate $\dot{m}$ expressed in Eddington units. In the three states at lower $\dot{m}$, the flow consists of two zones (the disk and a hot ($T_e \sim 100$ keV) advection-dominated accretion flow[59,60]). For the last two states, the disk extends down to the ISCO. In all the states, a corona surrounds the disk. Such model obtained a good success in describing the spectral evolution of several BH binaries.

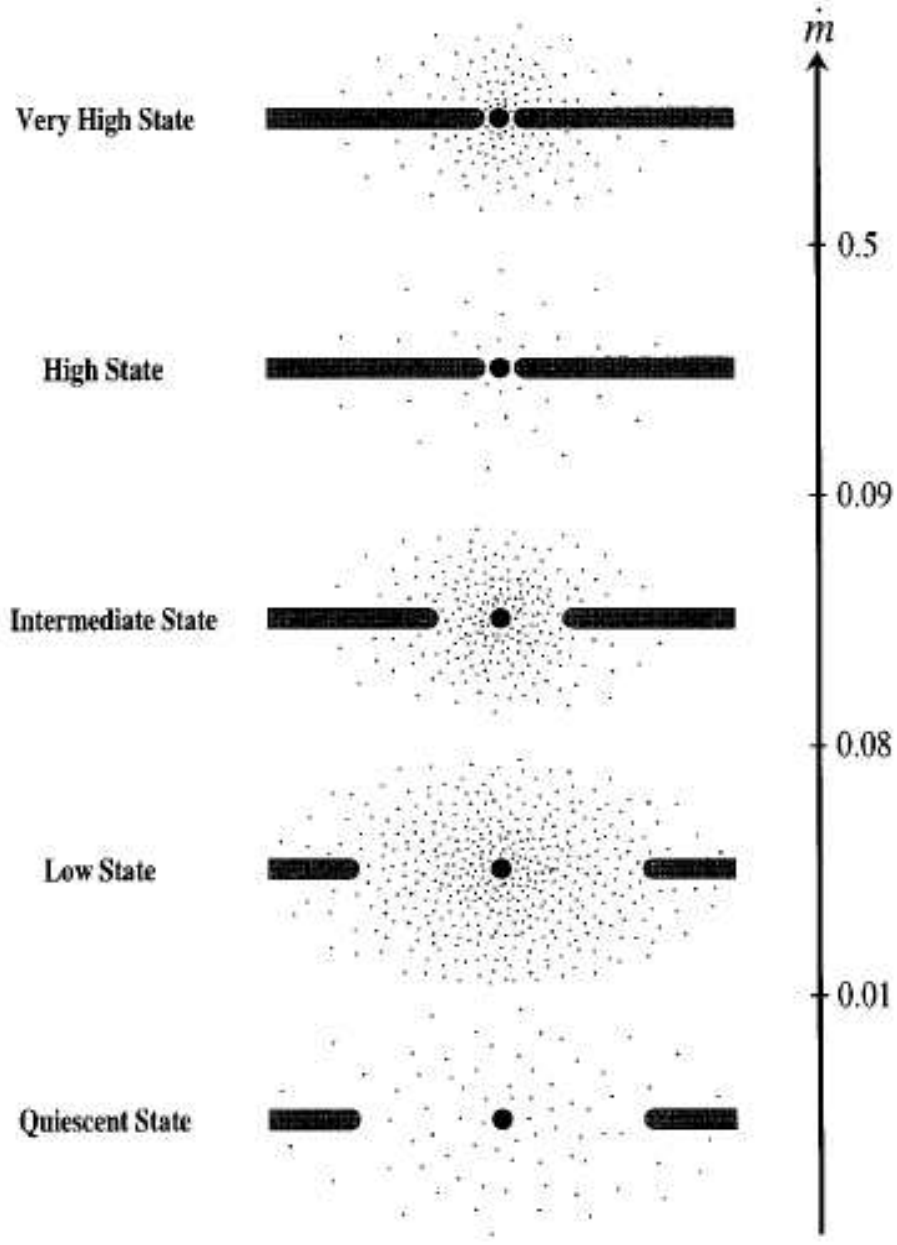

Figure 1.3: *Configuration of the accretion flow in the five spectral states of a BH binary shown schematically as a function of the total mass accretion* $\dot{m}$*. Dots and horizontal bars indicate the advection-dominated accretion flow and the thin disk respectively*[58].

1.4.2 Supergiant Fast X-ray Transients

Supergiant Fast X-ray Transients (SFXTs), consisting of a wind accreting compact object and an O-B supergiant donor star, are a new subclass of supergiant X-ray binaries (SGXBs) discovered only recently by *INTEGRAL*[61]. While SGXBs are known to be persistent bright sources with X-ray luminosity in the range $10^{35} - 10^{36}$ erg s^{-1}, SFXTs spend most of the time in a quiescent state, with X-ray luminosities of the order of $10^{32} - 10^{33}$ erg s^{-1}. Sporadically SFXTs go into outburst reaching luminosities of $10^{36} - 10^{37}$ erg s^{-1} [62,63,64,65]. The outbursts or strong flaring activities are characterised by very short time scales, i.e. from minutes to hours. For such new class of X-ray sources many unresolved fundamental questions remain open. The lack of confirmed orbital or pulse periods complicates the determination of the system parameters as well as of the compact object nature. Up to now IGR J11215-5952 alone shows regularly recurrent outbursts every $\sim$ 330 days, most likely linked to its orbital period[66]. To account for the accretion process that causes the short outbursts, it was proposed that the clumpy wind in early-type stars could be captured by the compact object producing the X-ray flares on the observed time scale[63]. However, this scenario has still to be well understood and confirmed for O-B stars in binary systems.

1.4.3 Symbiotic LMXBs

LMXBs containing evolved giant secondary stars are the current state or probable progenitor of most low-mass NS binaries with orbital period $\geq$2 days[67]. When the secondary star fills its Roche lobe matter is transferred to the NS until the donor envelope is exhausted and a WD is formed. During its existence, such envelope exerts tidal torques that circularize the orbit. Many systems are known to evolve in this way, such as Cyg X-2 which have a long orbital period ($\sim$ 9 days) and a F- or G-type giant companion star. Tens of low-mass binary radio pulsars with wide circular orbits and WD companions were also observed. Some of these radio pulsar binaries showed very long orbital periods ($\gg$ 10 days), comparatively longer than the widest known LMXBs. The progenitors of such systems might be LMXBs accreting from highly evolved (K- or M-type) giant donors and are expected to be rare to observe, since the duration of the K/M giant lifetimes is short and the mass transfer stage expected for Roche lobe overflow LMXBs with orbital period $\geq$ 2 days is unstable[68]. Such a system was observed for the first time by Davidsen *et al.*[69] (GX 1+4) and classified as symbiotic binary hosting a NS.

Symbiotic binaries consist of a K/M giant and a hot secondary surrounded by an emission-line nebula which is the result of the photoionization of the red giant's wind by the secondary[70]. More than 100 symbiotic binaries were observed. Their spectra are composed of strong emission lines superimposed on the cool molecular absorption spectra of the highly evolved primary. Except GX 1+4, a second probable symbiotic LMXB might be 4U 1700+24[71], thus

providing a new emerging subclass of LMXBs. During the last 3 decades, GX 1+4 alternated periods of high hard X-ray states and low soft X-ray states. Over the same time period the source was seen alternatively spin-up and down. From the theory of standard magnetic accretion torque for X-ray pulsars accreting from a disk[34], such behaviour implies a very strong ($\sim 10^{14}$G) magnetic field for the NS.

Chapter 2

The *Swift* mission

2.1 Science goals of the mission

The *Swift* mission[5], fruit of an international collaboration involving teams mainly from the USA, the United Kingdom, and Italy, is a multi-wavelength observatory successfully launched on November 20, 2004 (general characteristics are summarized in Table 2.1). The instruments on board *Swift* are the Burst Alert Telescope (BAT), operating in the soft gamma-ray domain, the X-ray Telescope (XRT) and the Ultraviolet/Optical Telescope (UVOT). A schematic view of the three co-aligned instruments on the spacecraft is given in Figure 2.1.

Swift is specifically designed to study the Gamma-ray Bursts (GRBs) and their afterglow. The wide-angle BAT monitors the sky awaiting for a new GRB and, whenever the system on board triggers it, an autonomous rapid spacecraft slew is performed to bring the burst into the narrower XRT and UVOT fields of view. Due to such an autonomy and to the very large BAT FOV ($\sim$2 sr), *Swift* is able to perform X-ray and UV/optical observations of > 100 bursts per year within 20-70 seconds of a burst detection. The *Swift* nominal lifetime is 5 years with a predicted orbital lifetime of ~ 10 years. The number of GRBs and their relevant afterglows that is predicted to be observed during the mission should be enough to determine their origin and to pioneer their usage as probes of the early universe.

Thanks to the gamma-ray telescope BATSE on board the Compton Gamma-Ray Observatory (*CGRO*), launched on April 5, 1991, GRBs are known to be uniformly distributed over the sky and to appear at the rate of ~ 1 per day, lasting from seconds to a few hours at gamma-ray wavelengths (for a detailed description see for example Piran[72]). Thus, while waiting for new GRBs, the BAT spends a large fraction of time collecting a huge amount of data on the hard X-ray sky. Indeed, a sensitive all-sky survey in the 15-150 keV energy range will be one of the major outcomes of the *Swift* mission. With an expected limiting flux of ~ 0.2 mCrab at high Galactic latitude and ~ 3 mCrab at low

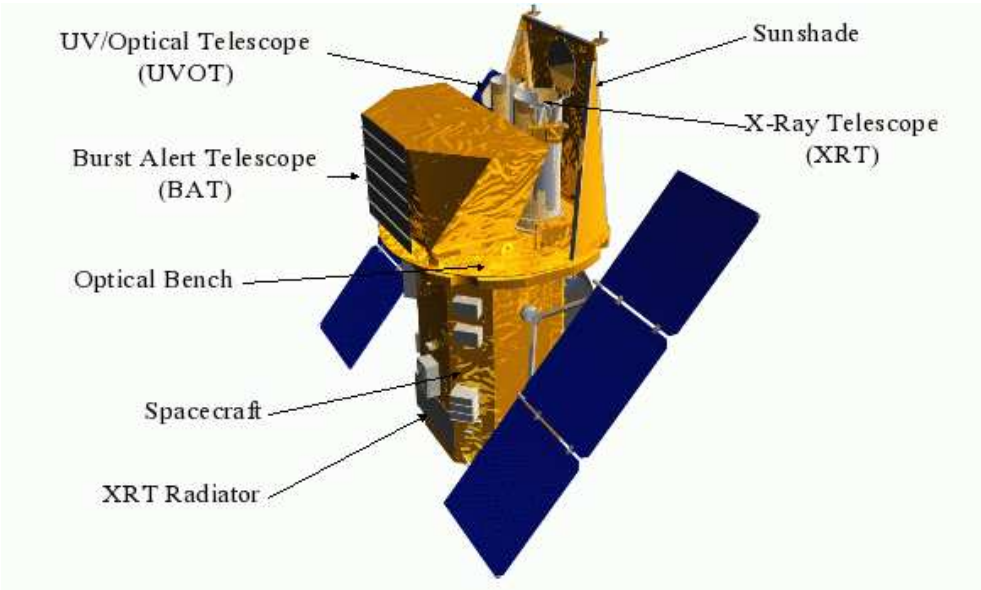

Figure 2.1: *The Swift satellite.*

Table 2.1. Swift Mission Characteristics[5]

Mission Parameter	Value
Slew Rate	50° in < 75 s
Orbit	Low Earth, 600 km altitude
Orbit Duration	96 min
Inclination	22°
Launch Vehicle	Delta 7320-10 with 3 meter fairing
Mass	1450 kg
Power	1040 W
Launch Date	early 2004

Table 2.2. Burst Alert Telescope Characteristics[5]

BAT Parameter	Value
Energy Range	15-150 keV
Energy Resolution	~ 7 keV
Aperture	Coded mask, random pattern, 50% open
Detection Area	5240 cm^2
Detector Material	CdZnTe (CZT)
Detector Operation	Photon counting
Field of View (FOV)	1.4 sr (half-coded)
Detector Elements	256 modules of 128 elements/module
Detector Element Size	$4 \times 4 \times 2$ mm^3
Coded-Mask Cell Size	$5 \times 5 \times 1$ mm^3 Pb tiles
Telescope PSF	$< 20 arcmin$
Source Position and Determination	1-4 arcmin
Sensitivity	$\sim 10^{-8}$ erg cm^{-2} s^{-1}
Number of Bursts Detected	> 100 yr^{-1}

Galactic latitude (with a 4-year dataset), the *Swift* survey is expected to be ∼10 times deeper than the HEAO1 A4 reference all-sky hard X-ray survey[73], performed more than 25 years ago. Preliminary results, based on 3 months of data, were published by Markwardt *et al.*[74]. The non-GRB science also includes a study of Active Galactic Nuclei (AGNs) as well as a monitoring of transient hard X-ray sources (see Gehrels *et al.*[5] for a detailed description).

2.2 The Burst Alert Telescope (BAT)

The BAT[75] is a highly sensitive, large FOV instrument designed to perform a detailed study of GRBs as well as a hard X-ray all-sky survey. It is a coded-mask telescope (see Caroli *et al.*[76] for a detailed description of this kind of instruments) operating in the 15-150 keV energy range, with a possible non-coded response extension up to ∼200 keV. BAT has a Point Spread Function (PSF) of ∼20 arcmin and can provide the position of a source with a 1-4 arcmin uncertainty. The parameters of the instrument are summarized in Table 2.2. A schematic view of the BAT is shown in Figure 2.2.

2.2.1 Technical description

The coded aperture mask

Since it is not possible to produce an image in the gamma-ray domain using traditional focusing optics, especially over a large FOV as for the BAT, the only way to create an image is to use the coded-aperture method (see Dicke[77], Skinner *et al.*[78]; see also Caroli *et al.*[76] and references therein for a complete

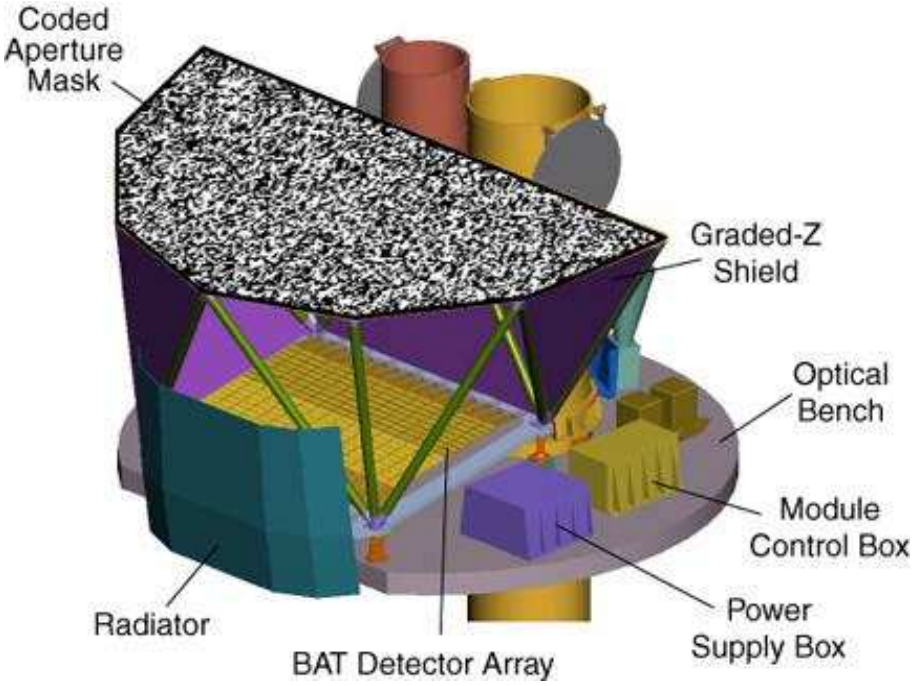

Figure 2.2: *A schematic view of the Burst Alert Telescope. The D-shaped coded mask, the CZT detector array, and the graded-Z shield are visible.*

description). Basically, a coded-mask telescope consists of a mask overheading a position sensitive detector. The mask is composed of elements transparent and opaque to the radiation assuming a selected pattern. Given a gamma-ray source illuminating the mask, the portions of the aperture blocked by the opaque elements absorb the gamma-rays, and the not blocked portions allow the rays to pass through. As a result, a shadow of the pattern, which depends on the position of the source, is projected on the detector array below. Starting from the map of illuminated detector pixels and the mask aperture, an image of the source can be reconstructed by a deconvolution process. If many sources are present in the FOV, different shadows overlap on the detector plane obstructing the image reconstruction. Thus, the aperture pattern must be carefully selected in order to allow each distinct source to cast a unique shadow pattern on the detector array. Moreover, when a source is on-axis, the aperture shadow fully illuminates the detector array, and so it is *fully coded*. As the source moves farther off axis, only a portion of the aperture shadow illuminates the detector array. The fractional illumination is called the *partial coding fraction* and obviously imply a sensitivity loss as compared with the on-axis case.

The BAT has a D-shaped coded mask, made of $\sim 54,000$ lead tiles ($5 \times 5 \times 1$ mm) mounted on a 5 cm thick composite honeycomb panel. Such tiles are opaque to radiation in the 15-150 keV energy range and become progressively transparent above 150 keV reducing the coding response. The BAT coded

Figure 2.3: *Picture of the BAT coded aperture mask before* Swift *launch.*

mask is located 1 meter above the CZT detector plane and uses a completely random, 50% open-50% closed pattern (see Figure 2.3). The mask is 2.4 × 1.2 m (considering the D-shape, it is 2.7m^2), which yields a 100° × 60° FOV (half-coded).

The BAT partial coding map is shown in Figure 2.4. It can be seen that only a small region around the centre of the BAT FOV is 100% coded whereas the partially coded region is wider. The BAT FOV with coded fraction greater than 10% is about 2.2 sr (>50%, 1.5 sr ; >90%, 0.5 sr).

The detector plane

The BAT detector plane is composed of 32768 pieces of 4 × 4 × 2 mm CdZnTe (CZT), forming a 1.2 × 0.6 m sensitive area. For electronic control, event data handling, and fabrications reasons, these pixels are grouped following a hierarchical structure. Groups of 128 detector elements are assembled into 8 × 16 arrays, each one connected to a different readout electronic circuit. Detector modules, each containing two such arrays, are further grouped by eights forming 16 blocks. For fabrications reasons, there is a gap between two adjacent pixels: it was restricted to be an integer multiple (2 or 3) of the basic pixel dimension, so that the image reconstruction process could easily handle it. Considering that a coded-mask telescope cannot derive the direction of any photon arriving at the detector, such a hierarchical structure is optimised to

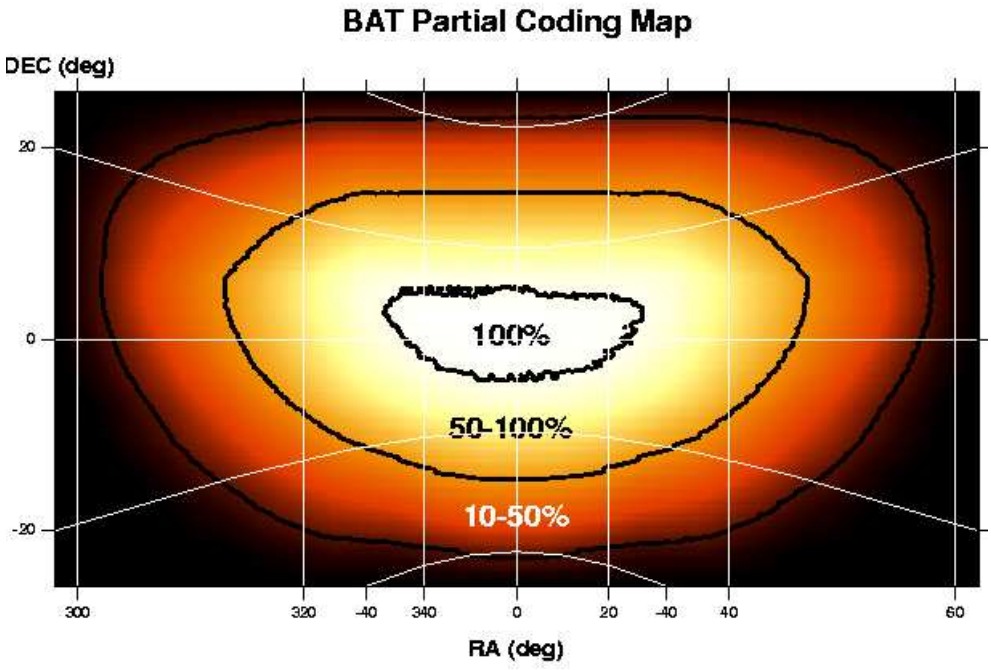

Figure 2.4: *The D-shaped BAT FOV. Fully coded (100%), half-coded (50%) down to the 10% coded fraction contours are indicated.*

allow BAT to tolerate the loss of individual pixels, detector modules, and even whole blocks without losing the ability to detect bursts and determine locations. There is, of course, a loss in burst-detection and the survey sensitivities.

The Fringe Shield

A graded-Z Fringe Shield, composed of Pb, Ta, Sn, and Cu, is located on the side walls between the Mask and the Detector Plane and under the Detector Plane in order to reduce the event rate in the detector plane. Due to its performance, the isotropic cosmic diffuse flux and the anisotropic Earth albedo flux are reduced by 95%.

2.2.2 BAT operating modes

BAT can work in two distinct operating modes: the so-called "Burst mode" and "Survey mode". Most of the BAT time is spent in Survey mode, waiting for a GRB occurring in the FOV. Events are accumulated in the detector plane and searched by the on board algorithm for increases in the count rate over a range of time scales. If no special triggers are found, all these events are binned into eighty energy bins and integrated over ∼5 minutes (survey data) because there is not enough on board storage or down-link capacity to send them all to the ground. Instead, when the trigger algorithm is satisfied, the

Burst mode is enabled and photon-by-photon data are produced and sent to the ground.

Burst mode

The algorithm on board BAT, which search for a GRB, is composed of two processes. First, it looks for excesses in the detector count rate above the expected background and constant sources count rate. During a 96-minute low Earth orbit, the detected background rates can vary by more than a factor of two. Moreover, the duration of the gamma-ray emission from GRBs ranges from milliseconds to minutes. For such reasons the triggering algorithm was written in order to be able to extrapolate the background and compare it to the measured count rate over a variety of timescales and in several energy bands. If at least one trigger is found, the algorithm switches to the second process. Another independent trigger criterion is implemented to search for slow rising GRBs and transients: it consists in an image analysis of the detected count rate performed every 64 sec. Such images are scanned for point sources which are then cross-checked against an on board catalog. The detection of any new source produce a GRB alert, whereas any known source above a given level initiates the interesting-source response procedure. The second process begins whenever the trigger algorithm detects a count-rate excess in the detector. In this case the data are analysed to discover if this excess is due to a GRB. The system on board extracts source and background data based on the energy range and time intervals flagged by the trigger. Such data are converted to a sky map which is then searched for excesses. If a significant excess is detected in a position that not match any source of the on board catalog, then a GRB is declared. The imaging process is fundamental to confirm the reality of the previous count rate detection. Thus, in order to eliminate false triggers, the trigger threshold was set to an opportune level. Finally, when a GRB alert is produced, the system on board decides if it is worthy to begin a spacecraft slew to point the source, depending on the merit of the burst and the observing constraints (e.g. the Earth limb does not cover a large fraction of the FOV).

When a GRB is declared, several products are constructed, the most significant of these being a dump of all event data included in the trigger time, with a total duration of about 10-15 minutes. Each event is tagged with an associated time of arrival, detector number and energy. This allows event data to be used for the extraction of light curves of all the sources in the FOV with different timescales and energy bands. These data can also be used to extract spectra of a given source. The BAT also produces several products all the time, regardless of whether there is a GRB or not. These are typically various array rates, spacecraft attitudes, housekeeping values, and trigger diagnostics.

Figure 2.5: *Representation of a Detector Plane Histogram (DPH). It is three dimensional in the sense that there are two spatial dimension (that of the detector plane) and one spectral dimension.*

Survey mode

Most of the time is spent by BAT waiting for a GRB occurring in the FOV (Survey mode). Photons interacting with the detector are processed (events) and then are tagged with an associated time of arrival, detector number and energy. Such information is stored on board in a memory buffer which may contain ∼10 minutes of data (depending on the actual count rate). If the burst trigger algorithm described above fails, the event data from the array are collected on board into Detector Plane Histograms (DPHs). DPHs are three dimensional histograms: for a given buffer set, every cell contains the number of events received in one of the 32768 pixels of the detector plane and in one of 80 energy channels. The energy bin widths are variable from one energy bin to the next, but have remained always the same since the *Swift* launch. Figure 2.5 shows a representation of a survey DPH.

Such histograms are accumulated over a typical 5 minutes time interval and then stacked as independent rows in a "Survey" data file. In some cases the duration of a DPH row can be longer or shorter depending on operational reasons (e.g., telemetry reduction or to get diagnostic information about the instrument). Also, DPH row integration times are truncated whenever the spacecraft begins a slew or enters the South Atlantic Anomaly (SAA). Generally speaking, the survey data cannot be used to search for time variations on

Table 2.3. X-Ray Telescope Characteristics[5]

XRT Parameter	Value
Energy Range	0.2-10 keV
Telescope	JET-X Wolter 1
Detector	E2V CCD-22
Effective Area	110 cm^2 @ 1.5 keV
Detector Operation	Photon counting, integrated imaging, and timing
Field of View (FOV)	23.6×23.6 arcmin
Detection Elements	600×602 pixels
Pixel Scale	2.36 arcsec
Telescope PSF	18 arcsec HPD @ 1.5 keV
Sensitivity	2×10^{-14} erg cm^{-2} s^{-1} (1 mCrab) in 10^4 s

time scales shorter than 5 minutes.

Other useful products are obtained on board, such as the Rate Data and the Maps. The former are lightcurves of the overall detected counts with different time scales, used by the on-board software for trigger searching. Housekeeping maps, useful for BAT analysis, are also produced. Among these, detector enable/disable maps and gain/offset maps are the most important. The former represent those detectors which were automatically disabled because noisy, whereas the latter record the approximate pulse-height-to-energy calibration for each detector. Gain/offset maps, in combination with ground calibration files, are used to produce calibrated event lists and survey files.

Together with auxiliary files (which contain all spacecraft-related information for a given observation), they are the standard basic products for BAT non-GRB science.

2.3 The X-ray Telescope (XRT)

The XRT[79] is designed to measure fluxes, spectra, and lightcurves of GRBs in the 0.2-10 keV energy range. It can locate a typical GRB to 5-arcsec accuracy within 10 seconds of target acquisition and it can observe it beginning 20-70 seconds from burst discovery and continuing for days to weeks. The XRT is a focusing X-ray telescope with a 110 cm^2 effective area, 23 arcmin FOV and 18 arcsec resolution (half-power diameter). Table 2.3 summarizes the XRT parameters.

The XRT uses a grazing incidence Wolter 1 telescope to focus X-rays onto a performant CCD detector. Designed for the EPIC MOS instruments on the XMM-Newton mission, the CCD has an image area of 600×602 pixels (40×40

mm) and a storage region of 600×602 pixels (39×12 mm). The FWHM energy resolution of the CCD decreases from $\sim$ 190 eV at 10 keV to $\sim$ 50 eV at 0.1 keV, where below $\sim$ 0.5 keV the effects of charge trapping and loss to surface states become significant.

The XRT can work in three readout modes in order to cover the dynamic range and rapid variability expected from GRB afterglows. The telescope autonomously selects which mode is the best to use during an observation. The first mode is the "Imaging Mode" which produces an integrated image measuring the total energy deposited per pixel and does not permit spectroscopy. Usually this mode is used to position bright sources up to $\sim$37 Crab. The "Windowed Timing Mode" is selected whenever a high time resolution (2.2 ms) and bright source spectroscopy is required at expenses of the position information. This mode is very useful for sources with flux below $\sim$5 Crab. Finally, "Photon-counting Mode" uses sub-array windows to allow full spectral and spatial information to be obtained for source fluxes ranging from 1 mCrab to 45 mCrab

2.4 The Ultraviolet/Optical Telescope (UVOT)

The UVOT[80] is a 30 cm clear aperture Ritchey-Chrétien telescope with a primary f-ratio of f/2.0 increasing to f/12.72 after the secondary. It operates as a photon-counting instrument and carries two redundant detectors. Each detector has a filter wheel which allows low-resolution grism spectra of bright GRBs, and broadband UV/visible photometry. It is mounted in front of the detector carrying the following elements: a blocked position for detector safety; a white light filter; a field expander; two grisms; U, B, and V filters; and three broadband UV filters centred on 190, 220 and 260 nm. The two detectors are CCDs with 384×288 pixels, 256×256 of which are usable for science observations. Each pixel corresponds to 4×4 arcsec on the sky, providing a 17×17 arcmin FOV. Table 2.4 summarizes the UVOT parameters.

The UVOT can work in six different operating modes: slewing, settling, finding chart, automated targets, pre-planned targets, and safe pointing targets. When a GRB or a new target is triggered, the spacecraft is slewed to allow it to be within the UVOT FOV. During the slew, the UVOT is switched off in order to protect it from bright sources slewing across its FOV and damaging the detector. When the object is within ten arcminutes of the target, the UVOT begins the observation. Since the spacecraft is still settling, the target is moving rapidly across the FOV and the positional accuracy is only known to a few arcmin based on the BAT's centroided position. When the spacecraft is settled with small pointing errors, the UVOT begins a 100 second exposure in the V filter to produce a finding chart with positional accuracy of $\sim$ 0.3 arcsec. This aids the ground-based observers in localising GRBs. Then, an automated sequence of exposures, which uses a combination of filters, is executed (Automated Targets). When no Automated Targets are produced, observations

Table 2.4. UltraViolet/Optical Telescope Characteristics[5]

UVOT Parameter	Value
Wavelength Range	170-600 nm
Telescope	Modified Ritchey-Chrétien
Aperture	30 cm diameter
F-number	12.7
Detector	Intensified CCD
Detector Operation	Photon counting
Field of View (FOV)	17×17 arcmin
Detection Elements	2048×2048 pixels
Telescope PSF	0.9 arcsec FWHM @ 350 nm
Colors	6
Sensitivity	B = 24 in white light in 1000 s
Pixel Scale	0.5 arcsec

of planned targets such as follow-up of previous automated targets, targets-of-opportunity, and survey targets begin. When observing constraints do not allow observations of automated or pre-planned targets, the spacecraft points to predetermined locations on the sky that are observationally safe for the UVOT.

The UVOT data can be collected in two modes which can be run contemporaneously: "Event" and "Imaging". The Event mode consists on tagging the arrival time of each photon with a resolution equal to the CCD frame time (~ 11 ms). In Imaging Mode, photon events are summed into an image for a time period ≤ 20 s. The advantage of Imaging Mode is that it minimizes the telemetry requirements when the photon rate is high, but at the expense of timing information.

Chapter 3

Swift/BAT survey data analysis software

Due to its large FOV, high sensitivity and good angular resolution, BAT could perform an efficient monitoring of high-energy sources. Indeed, count-rate light curves (in the 15-50 keV energy range) for more than 400 known sources, updated on a single orbit basis, recently were made available on the web at the "BAT Hard X-ray transient monitor" facility of the Goddard Space Flight Center (*http://swift.gsfc.nasa.gov/docs/swift/results/transients/*)[81]. To fully exploit the data collected by BAT, however, a procedure aimed at following the spectral and flux evolution of high-energy sources is required. BAT survey data can be analysed using the public tools available at the Heasarc-U.S. web site (*http://heasarc.gsfc.nasa.gov/cgi-bin/W3Browse/swift.pl*) each of which performs a single analysis step required for a coded mask instrument (see section 2.2.1). An useful description of such tools is available at *http://swift.gsfc.nasa.gov/docs/swift/analysis/bat_swguide_v6_3.pdf*, but no information about how to build a complete pipeline for the BAT survey data analysis is given either in this on-line guide or in the literature. In this chapter two sets of software devoted to this aim are described. The former is a new procedure entirely based on public tools which provides spectra and light curves in physical units (i.e. ergs/cm^2/s) for a given source at a time. After the selection of the data, a filtering stage is performed in order to obtain a good-quality dataset. The so called "Mask-weighting" technique is then adopted to extract spectra of the source which are then analysed to obtain the flux and the spectral parameters of the model used for the fit. The procedure can run both on a single DPH row basis (corresponding to the shortest temporal interval for survey data) and on groups of DPHs having similar pointings. Thus, such procedure is suitable in monitoring both the temporal and spectral variability of a given source with the desired timescale. Since it is a new procedure, many calibration tests were performed using both a stable, bright source and a variable, fainter one (see Chapter 4)[82].

The second algorithm, composed of public tools and non-standard products,

was developed and tested by Prof. Skinner at the CESR of Toulouse (France). It is based on an imaging rather than spectral approach. Such procedure can analyse many sources at a time, providing light curves in arbitrary units, and can be run both on a single DPH row basis and on entire DPHs. Unlike the previous procedure, the resulting light curves have no contamination from the subtracted bright sources in the FOV.

3.1 A pipeline for time resolved spectroscopy (Pipeline 1)

The pipeline described in this section is aimed at producing flux light curves and extracting spectral information for one source at a time. After an initial filtering of the selected dataset to reject bad data, spectra of the source are produced. The spectral and flux evolution of the source is obtained by fitting such spectra within XSPEC with a dedicated model which depends on the source under study. The pipeline can work both on single DPH rows (which provide the shortest time interval for "survey data") and with combinations of rows (which allow a better sensitivity on target). With the current software release (*Swift* release 2.7 - June 15, 2007) no provision was made on the tools to take into account and correct the effects of the other sources, so results can be potentially affected by the presence of strong sources in the FOV. A simple procedure to make images in a given energy band for source detection is also implemented.

3.1.1 Preliminary data selection and preparation

In this section the prescription used to select a good-quality, reliable dataset is described.

1. Data collected in the desired time interval, with the target inside the BAT FOV are selected. Data, including housekeeping and auxiliary files, may be searched and retrieved through the *Swift* data archive (see *http://heasarc.gsfc.nasa.gov/cgi-bin/W3Browse/swift.pl*).

2. The energy scale for each detector in each DPH is corrected using gain offset maps. Gain offset files, stored among housekeeping files, are not supplied for each OBS ID. The most recent available file is selected for each observation (the mean time between the file and the next is ∼3h). The dedicated tool *baterebin* is used to perform the correction.

3. Bad datasets are rejected. Data filtering is performed using information stored both in housekeeping and attitude files:

    - Attitude information. Data for which the star tracker is not locked and the spacecraft is not in pointing mode are rejected.

- Number of enabled detectors. To optimise imaging capability and detector performance, a minimum number of enabled detectors is required. DPH collected with less than 24000 enabled detectors are rejected.
- Background noise. DPHs with anomalously high background noise may be identified by checking the total detector count rate. If such a value exceeds 18000 counts s^{-1} in the 14-190 keV energy band, data are discarded.
- Avoidance angles and occultations. Data for which the angle between the pointing direction and the Earth limb is less than 30 degrees, or the spacecraft is in the South Atlantic Anomaly (SAA) are discarded. Time intervals during which the source under study is occulted by the Earth, Moon and Sun may be identified using the dedicated *batoccultgti* tool.
- Overall data quality. DPHs for which data quality is acceptable are identified by checking the appropriate flag stored in each DPH file, allowing observations affected by bad telemetry to be discarded.

Each of the above criteria yields a Good Time Interval (GTI) table. The intersection of all such GTIs yields a table that can be used to screen for bad data. The resulting GTI table is possibly unnecessarily restrictive. Often good data may be discarded because of a few seconds of bad GTI intersection. In order to avoid such a problem, on both sides of each GTI time interval a small allowance of 10% of the time interval is added. If such a value exceeds 10 seconds, the allowance is set to 10 s. Next, all DPH times are checked against resulting GTIs using the *batbinevt* tool, both for the entire DPH and for a combination of DPH rows. Only the data for which the time intervals totally intersect the GTIs modified by the allowance will be considered for further analysis.

4. The attitude information is updated. A new attitude file based on the median pointing direction, as evaluated considering only the observation GTI, is generated using the *aspect* tool.

3.1.2 Imaging analysis and source detection

In this section details on a simple procedure used to extract an energy resolved image of the sky and to search for the source of interest as well as for new ones is described. The image formation for the coding mask instruments can be briefly summarized as follows: assuming a two-dimensional object distribution in the sky $S(x, y)$ and an aperture transmission function $A(x, y)$ (the mask pattern), the spatial distribution of the detected flux is given by

$$D(x, y) = A(x, y) * S(x, y) + B(x, y), \tag{3.1}$$

where $*$ is the convolution operator and $B(x, y)$ is a signal-independent noise term. An estimate $\hat{S}(x, y)$ of the object S can thereafter be obtained by filtering the shadowgram D with a suitable decoding function $G(x, y)$:

$$\hat{S}(x, y) = G(x, y) * A(x, y) * S(x, y) + G(x, y) * B(x, y). \tag{3.2}$$

Therefore, the quality of the object reconstruction depends on the choice of the aperture $A(x, y)$, the decoding function $G(x, y)$, and on a good estimation of the background $B(x, y)$[83,84,85].

1. A Detector Plane Image (DPI) is created ($D(x, y)$). DPIs are obtained from the DPH by adding, for each detector, the total counts recorded. Energy selections may be performed a priori in order to have energy-resolved DPIs. Such operations may be performed using the *batbinevt* tool.

2. A detector mask is generated starting from the map of enabled/disabled detectors stored in the housekeeping files. As for the case of gain offset files, detector masks are not supplied for each observation. They are supposed not to change rapidly, so the nearest available file is used. Hot pixels are then searched for and identified using the special task *bathotpix*. A bad pixel map is obtained, and it is combined with the original map to produce the final detector mask.

3. A pure background map $B(x, y)$ for each DPI is generated, not accounting for sources inside the FOV, using the *batclean* tool, the detector mask, and the default background model. Here below the basic scheme of how *batclean* works. The tool creates a simple eighteen parameter background model, then creates a background exposure map based on that model. The tool then uses a singular value decomposition method to fit the source exposure and background exposure maps to the data from the DPI. The fit coefficients are then used to create a model background DPI. This is then subtracted from the original input DPI to produce a cleaned DPI.

4. A sky image $\hat{S}(x, y)$ is produced from each DPI, together with the associated background map $B(x, y)$, corrected attitude file and merged detector mask, using the task *batfftimage*. Such tool constructs a sky image by deconvolving the observed detector plane image $D(x, y)$ with the BAT mask aperture map $A(x, y)$. The result is a background-subtracted image of the sky, including all the sources within the instrument FOV. This tool is used to estimate the positions and intensities of previously unknown sources on the sky by exploiting the so called Fast Fourier Transform technique.

5. A map of the coded fraction across the instrument FOV can be obtained using the *batfftimage* tool using the same inputs as above. This map represents the fractional exposure of the sky for a given detector/aperture

configuration, and is similar to the vignetting profile for imaging telescopes. The values vary from 1 for a fully coded region to zero at the edge of the FOV.

6. The source detection algorithm is run. The dedicated task *batcelldetect* is used to perform a source search on the sky images. A list of sources above a desired signal-to-noise and partially-coded fraction thresholds is generated, including sky and image coordinates, signal-to-noise, count rate, coded fraction and other useful pieces of information for each source.

The procedure outlined above may be run either on a single-row DPH, or on the merged rows of a DPH.

3.1.3 Spectra and response matrices generation

Here the procedure used to extract the source spectrum using the mask-weighting approach, as well as to generate appropriate response matrix is described. Such an approach consists in assigning to each detection element a weight (from -1 to +1), depending on the fraction of the detector which is shadowed by the mask with respect to the source position.

By applying such a weight map to a DPH, it is then possible to extract a background-subtracted spectrum for a source of known position (see *http://swift.gsfc.nasa.gov/docs/swift/analysis/bat_swguide_v6_3.pdf*).
The source coordinates must be known a priori (either from source detection, or from independent measurements). This section of the pipeline uses as input either a single-row DPH, or a merged DPH.

1. The weight map for the source under study for each DPH is generated. The dedicated tool *batmaskwtimg* is employed, using a detector mask as well as the corrected attitude files described above.

2. The source background-subtracted spectrum from each DPH is extracted. This is done with the *batbinevt* tool, using an energy-corrected, GTI-filtered DPH together with the corresponding weight map.

3. A dedicated response matrix (including effective area information) for each spectrum is generated using the task *batdrmgen*.

4. Systematic errors are added to the spectrum. The spectrum extracted as described above does not include systematic errors, which may be relevant at low energy (<25 keV). The *batphasyserr* tool may be used to add dedicated (as stored in the CALDB) systematics to each spectrum.

3.1.4 Spectral analysis

This section of the pipeline is devoted to the automatic spectral analysis of a source strongly variable both in flux and in spectral shape.

1. Evaluation of the target signal-to-noise.
   As a first step, the source signal-to-noise for each spectrum is estimated. This is simply done by selecting a suitable spectral range, which has to be optimised on a case by case basis, and checking the source count rate together with its associated error. If the ratio between the count rate and the error is null or negative, the spectrum (and the corresponding DPH group) is discarded. If such a ratio is positive, then further steps are performed.

2. An initial guess of the spectral shape using hardness ratio is required in order to optimise an automatic, "blind" spectral analysis. For the case of a strongly variable source, the hardness ratio is used to select an appropriate starting point. Such an approach may allow the choice between different source states, and/or the identification of the presence and relative contribution of different spectral components. The resulting hardness ratio values allow one to choose the spectral model to be used to fit the source spectra, and/or to select an appropriate energy range to perform spectral analysis.

3. Evaluation of the source flux.
   Before running a complex spectral fit, a preliminary fit with a simplified model (reducing, e.g., the number of free spectral parameters) is performed to obtain the source flux with its associated error. The flux/error ratio is used as a criterion to decide if the data quality warrant a more complex spectral model. In particular, a preliminary power law fit with a photon index fixed to -3 is performed and the source flux is evaluated. A flux/error ratio threshold of 4 is used to discriminate between low and high S/N spectra.

4. Low S/N spectra.
   Spectra with poor S/N are used to set an upper limit to the source emission using the simplified model.

5. Further analysis of low S/N spectra.
   An attempt to recover spectral information is made, by summing low S/N spectra extracted from consecutive groups of DPHs, up to a maximum of 10 contiguous spectra. The corresponding response matrices are also combined. The resulting spectra are then analysed through the same steps of the automated pipeline.

6. High S/N spectra.
   Spectra with an adequate S/N are studied in detail within Xspec. After spectral fitting, the best spectral parameters, as well as the source refined flux in a given energy band, are computed together with their uncertainties.

3.2 A pipeline for sensitive imaging (Pipeline 2)

The pipeline described here (courtesy of Prof. Skinner) produces light curves of many sources at a time in multiple energy bins. An initial filtering step is performed on the selected dataset as for the pipeline described in section 3.1. Then, given a list of sources to be fitted and to be subtracted, mask-weight maps for each source from the lists included in the FOV are calculated. Such maps are fitted together with energy dependent background maps and detector masks in order to obtain a light curve for each fitted source and energy bin, and a best-fit background model and detector mask for each energy band. The resulting light curves, expressed in arbitrary units, are background-subtracted and not contaminated by the subtracted, bright sources in the FOV. The pipeline can work either on single-DPH rows (which provide the maximum time resolution for "survey data") or on whole DPHs (which allow the sensitivity to be increased). Images together with significance and variance maps in the given energy bands can also be produced.

3.2.1 Preliminary data selection and preparation

The prescription used in this pipeline to select a good-quality dataset is identical to that described in section 3.1.1, with only two exceptions:

- The number of sources the pipeline can analyse at a time is greater than one, so the *batoccultgti* tool is replaced further in the pipeline by *batoccultmap*, which provides the map of the occultations for the entire FOV (see section 3.2.2 below).
- Following the selection of the energy bins in which the data will be analysed, the *baterebin* tool is used to correct the DPH energy scale as in pipeline 1 and to reduce the original eighty energy channels to the selected energy bins.

3.2.2 Source selection

In this section the procedure used to identify the sources in the FOV from an input list of sources is described. The sources to fit and those to subtract are placed in two separate lists.

1. First, a Detector Plane Image (DPI) is created in the selected energy bands. This operation is performed using the *batbinevt* tool.
2. As in section 3.1.2, a detector mask is generated starting from the map of enabled/disabled detectors stored in the housekeeping files. As for the case of gain offset files, detector masks are not supplied for each observation. They are supposed not to change rapidly, so the nearest available file is used. Hot pixels are then searched for and identified

using the special task *bathotpix*. A bad pixel map is obtained, and it is combined to the original map.

3. As in section 3.1.2, a pure background map for each DPI is generated, not accounting for sources inside the FOV, using the *batclean* tool, the detector mask, and the default background model.

4. A non-standard program is used to identify the sources in the FOV from an input list. Given a list of sources which the user is interested in fitting, the program is able to identify which are in the FOV for a given DPH and attitude file and to save them in a sub-list. Such procedure is repeated to identify the sources in the FOV from a second input list containing the sources which the user is interested in subtracting. The quality of the fit of the sources contained in the former list can be improved if the contribution of strong sources in the FOV is removed.

5. A new detector mask is generated, accounting for radiation arrived at the detector not coded by the mask. There is an interstice between the mask and the body of the telescope through which radiation can pass without being coded by the mask, so the presence of strong sources near to the edge of the FOV is a potential source of noise. To avoid this, the weight map, in which detectors possibly affected by radiation from strong sources entering through the gap are marked, is generated with the *batmaskwtimg* tool, assuming the mask aperture stored in the CALDB files. A detector mask containing the contributions of all the source to subtract is generated and then merged with the previous one.

6. A temporary image is generated using *batfftimage*. This step is necessary to run *batocculmap* and obtain the map of the occultations of the BAT FOV due to the earth, moon and/or sun. *Batoccultmap* assigns to each pixel of an image the fraction of the exposure during which the celestial direction corresponding to that pixel was unocculted.

3.2.3 Light curves production

In this section the procedure adopted to obtain light curves of the sources to be fitted (that included in the former sub-list described in point 5 of section 3.2.2) is described.

1. For each DPH, the weight maps for the sources to be fitted included in the FOV are generated. The *batmaskwtimg* tool is used to do this, using as input the DPI as well as the catalog of sources to be fitted. No detector masks are needed.

2. For each DPH, the weight maps for the sources to be subtracted included in the FOV are also generated. This step is the same as the previous one,

except that the input catalog of sources used in the one that contains the sources to be subtracted.

3. This step consists in the source fitting and is performed by a non-standard program. For each energy bin, the mask-weight maps from the lists of sources to be fitted and to be subtracted, as described in the two previous steps, are fitted together with the occultation map and the energy dependent background maps and detector masks described above. For each fitted source, an amplitude (no physical unit) in a given energy band together with its uncertainty, the correction factor accounting for occultations, the χ^2, and the degrees of freedom of the fit plus other useful information are saved in a log file. An empirical correction factor is calculated to account for an additional flux loss that is known to occur and that is a function of the offset angle and the energy. The value obtained is also shown in the log file. The amplitudes of each source are background-subtracted and not contaminated by the subtracted, bright sources in the FOV. Other useful products, such as a best-fit background model and detector mask for each energy band, are also given.

4. By extracting the amplitudes with their uncertainties and the times of a given source from each log file, a light curve is generated.

3.2.4 Imaging analysis and source detection

As for the pipeline described in section 3.1, an image is generated with standard software and a source detection can be run (see section 3.1.2):

- An image of the sky together with a significance and variance maps for each energy bin are created using the *batfftimage* task. In this case, for a given energy bin, the DPI, the corrected attitude file, the background map, and detector mask obtained at the point 3 of section 3.2.3 are used as input.

- The source detection algorithm can be run on each sky image searching for new sources (i.e. those not included in the catalog used as the input of this pipeline). For this purpose, the *batcelldetect* task is used.

Chapter 4

Testing Pipeline 1 with the Crab and GRO J1655-40

Before using Pipeline 1 described in section 3.1 for scientific purposes, the procedure was carefully checked and optimised. Tests were made to verify the reliability of the results achieved through this method, focusing on the spectral performance of the BAT instrument. In this chapter a detailed description of the results of such tests is given. First of all, a systematic analysis of a large number of observations of the Crab nebula (and its pulsar), the classical calibration source for X-ray instruments, under different observing conditions was performed. The tests on the Crab are reported in section 4.1, focusing on the reliability of spectral results as a function of the source position within the BAT FOV. The requirements to combine different BAT datasets are spelled out in section 4.1.3, while the background influence on upper limit evaluations is discussed in (section 4.2). Next, after the reliability of the pipeline described in section 3.1 using the very bright and steady Crab as a reference source was assessed, a detailed study of the 2005, 9-month long outburst of the galactic BH binary GRO J1655–40 was performed. Such event was also carefully monitored with the narrow field instruments PCA and HEXTE on board the Rossi X-Ray Timing Explorer (*RXTE*), allowing the cross-check of the BAT results with those obtained simultaneously by an independent well calibrated instrument. The *RXTE* spectral analysis is described in section 4.3.2. Finally, BAT and *RXTE* spectral results are compared, thus assessing the performance of the pipeline in order to use the BAT data to monitor the behaviour of a strongly variable source (section 4.3.3)[82].

4.1 BAT as a monitor: calibration with the Crab

BAT has a very large FOV. In order to fully exploit this capability - which is crucial when using BAT as a monitor for the hard X-ray sky - it was needed to assess the stability of the source flux as reconstructed by the procedure described in section 3.1 as a function of the source position within the FOV. Indeed, different positions within the instrument FOV correspond to different mask coded fractions (see Figure 2.4). To this aim, a large sample of observations of the bright and steady Crab, the source used to calibrate the BAT spectral response, was studied. This provided a crucial test to assess the ability of our method to extract spectral and flux information across the whole instrument FOV.

To such study, products for each single DPH row were extracted following the steps described in sections 3.1.1, 3.1.2 and 3.1.3. The selected DPHs were processed to compute the source flux. Such an analysis can be carried out following, at least, two different approaches. The first one, which will be indicated as the "Imaging approach", is based on the deconvolution of the whole DPH to produce an image of the BAT FOV in sky coordinates. Such an image is then used to perform a source detection and to extract information on the source spectrum (for a detailed description, see section 3.1.2). The second possibility, called "Mask-weighting" technique, is based, instead, on the "mask-weight map", accounting for the fraction of the detector which is shadowed by the mask with respect to the source position. The application of such a mask to the DPH yields a background-subtracted spectrum of the source (for a detailed description, see section 3.1.3). Both approaches were tested on the Crab, and the results were compared.

As a final step, the possibility of combining different DPHs in order to increase the exposure time (and thus the source signal to noise) beyond the typical ~ 5 min integration of a single DPH was investigated. A careful check of the effects of DPH pointing offsets was performed, in order to assess the maximum offset allowed to minimize flux loss in the combined DPH.

4.1.1 Data selection

The Crab data set encompasses all observations, with the source within the BAT FOV, collected between 2005/01/01 and 2005/06/30. The sample includes 365 observations, including a total of 4626 DPH rows (for a total observing time of $\sim$1.46 Ms). The data set is larger than the one presented in the public BAT Digest pages[1] describing details on the instrument calibration (44 grid locations in the BAT FOV). After the data screening stage (section 3.1.1), 1014 rows ($\sim 20\%$) were rejected. Details on the impact of each specific filtering criterion are given in Table 4.1.

[1] *http://heasarc.nasa.gov/docs/swift/analysis/bat_digest.html*

Detectors not enabled	36
Earth contamination + SAA	121
Star tracker unlocked	264
Pointing unstable	317
High count rate	328
Earth/Moon/Sun source occultation	297

Table 4.1: *Number of DPH rows of the Crab sample rejected after the filtering stage.*

Deg off-axis	Processed rows
0-5	306
5-10	0
10-15	0
15-20	108
20-25	33
25-30	299
30-35	908
35-40	253
40-45	816
45-50	295
50-55	323
55-60	207
60-..	0

Table 4.2: *Distribution of the Crab location in the FOV for the processed sample of DPH rows. The source position is given in degrees from the center of the BAT FOV.*

Moreover, 34 rows ($< 1\%$) could not be processed because of the lack of the relevant housekeeping files. ~ 3600 good DPH rows remained which were used for image, as well as for spectral, analysis. Of course, the Crab position varied greatly within the BAT FOV. Table 4.2 provides the statistic of the source position in the good BAT data set.

4.1.2 Results I: flux evaluation

Imaging approach

For each DPH row, an image of the BAT FOV was produced, and the standard source detection was performed as described in section 3.1.2. The Crab detection was performed on all the images adopting a signal to noise ratio threshold of 3.8 and a partially-coded fraction threshold of 0.001 in the *batcelldetect* tool. All other parameters were left to default values, including all the required corrections in order to obtain - in output - uniform, consistent values of the target count rate, independent on its position within the FOV (i.e.

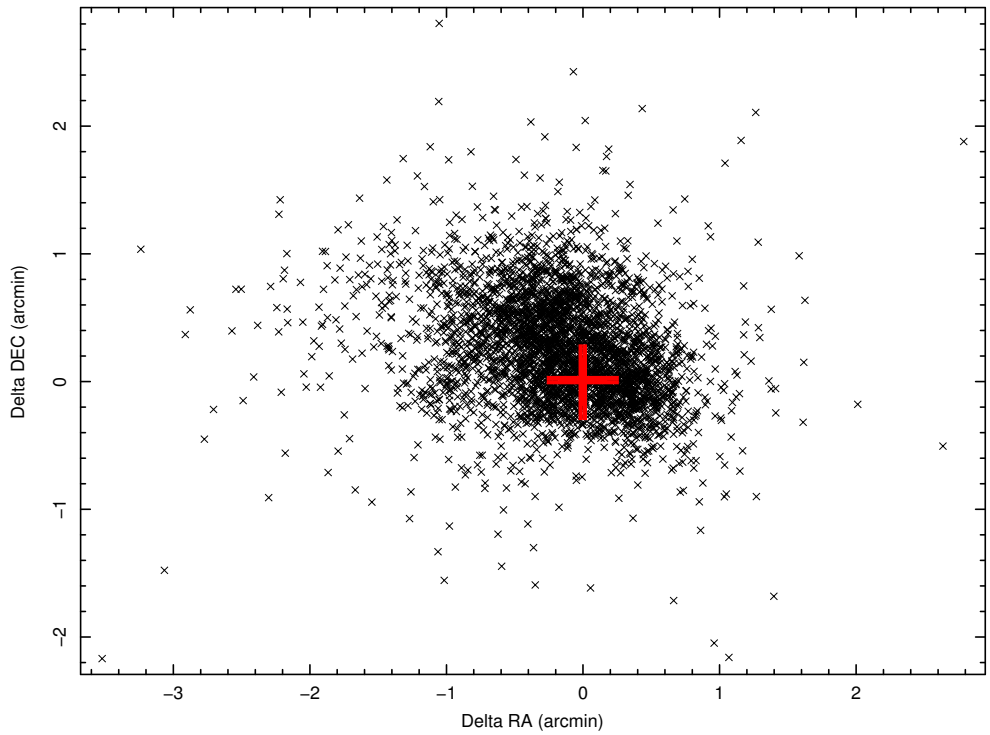

Figure 4.1: *Dispersion of Crab detection coordinates around the nominal source position (red cross). The coordinate dispersion is not perfectly centred on the Crab nominal position. Probably this is related to systematic image centroid shifts as a function of the position in the FOV (see BAT Digest pages* http://heasarc.nasa.gov/docs/swift/analysis/bat_digest.html*), as well as to the distribution of the Crab detector coordinates in our dataset.*

the pipeline should yield the target count rate as if it was observed on-axis). The Crab was detected in all but 39 cases. The target detection coordinates agree well with the known Crab position and the dispersion around the nominal source coordinates is very small, as shown graphically in Figure 4.1 and numerically in Table 4.3.

Fig. 4.2 shows the Crab count rate (as estimated with the source detection algorithm) as a function of the coded fraction (see Figure 2.4). It is immediately evident that the count rate is not stable over the entire FOV. A deficit of $\sim$20% is apparent for coded fraction below $\sim$0.2 (i.e. when the source is between 40-50 and 60 degrees from the pointing direction, corresponding to $\sim$45% of the entire BAT FOV). Thus, over a large fraction of the FOV the count rate estimated by the simple source detection algorithm described in section 3.1.2 seems to be biased by systematic effects. Such results are not completely satisfactory for the above purposes. Better results can be obtained with a more sophisticated analysis, such as that presented in section 3.2, which exploit image cleaning procedures and count rate reconstruction algorithms different

	Coded fraction > 0	Coded fraction > 0.1
$< 1 arcmin$	84.8%	90.9%
$< 2 arcmin$	98.6%	99.4%
$< 3 arcmin$	99.9%	100.0%

Table 4.3: *Catalogue and detection coordinates percent difference.*

from those included within the *Swift* software public release. At this stage, a further investigation on the origin of such a systematic effect and on the possibilities to fix it was discarded. Using the public release of *Swift* analysis software, good results may be obtained using the mask-weighting approach.

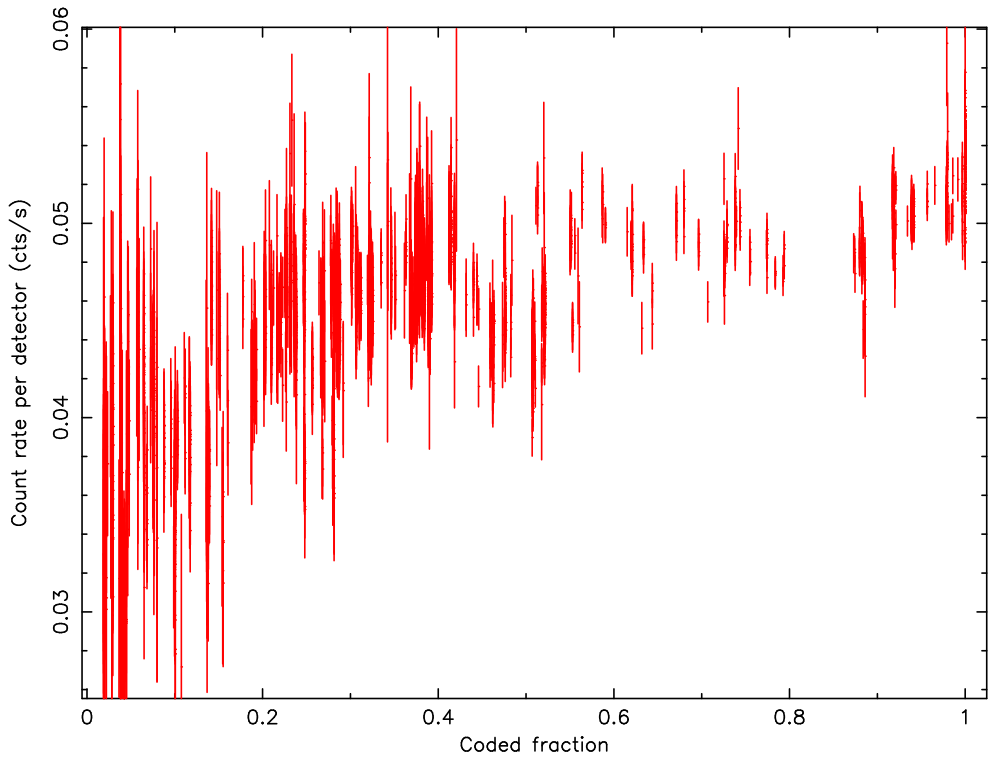

Figure 4.2: *Crab count rate per detector in the 10-100 keV energy band as a function of the coded fraction, as estimated by the source detection technique. Fluxes and error bars are taken from the output list produced by* batcelldetect *tool.*

Mask-weighting approach

The Crab mask-weighed spectrum was extracted in all cases using the target coordinates as estimated by the source detection algorithm described in section 3.1.2.

All Crab spectra were fitted with a power law in the 10-100 keV range. Best fit photon indices and normalization factors, as well as observed fluxes, were computed.

A plot of the Crab 10-100 keV flux in physical units (erg cm^{-2} s^{-1}) as a function of partial coding fraction is shown in Fig. 4.3 (upper panel). A similar plot with the values of the photon index is shown in the lower panel of the same figure. Both the flux and the photon index are in good agreement with

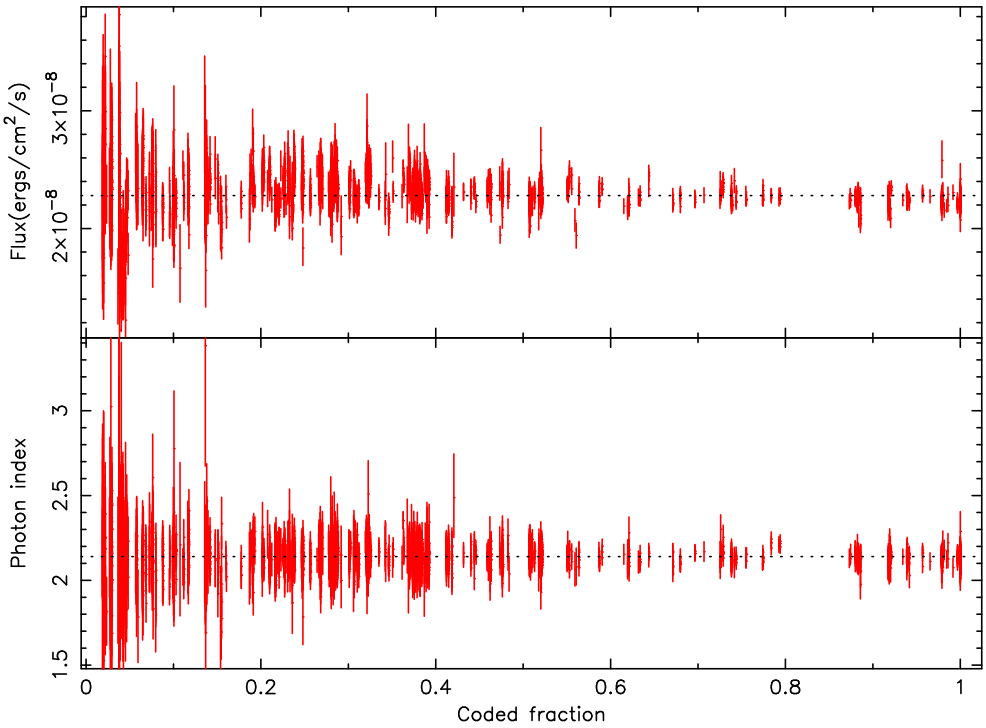

Figure 4.3: *Crab flux in the 10-100 keV energy band (upper panel) and spectral photon index (lower panel) as a function of the coded fraction, as estimated with the mask-weighting technique using Crab detection coordinates. The horizontal dotted lines represent the best fit to the constant model (see Table 4.4 for details).*

the values assumed for the BAT instrument calibration [2]. Both the flux and photon index values are very stable as a function of the source location within the BAT FOV. As shown in Table 4.4, the spread of the values is within 8%, and is further reduced to 5%, if only the coded fraction >0.1 are selected. A similar analysis, using the nominal source coordinates instead of the detection ones, yielded results almost undistinguishable (See Figure 4.4 and Table 4.4).

The same analysis was repeated, where possible, with the discarded fraction of dataset. In such a case the flux is not stable as in the previous one: the

[2] *http://heasarc.nasa.gov/docs/swift/analysis/bat_digest.html*

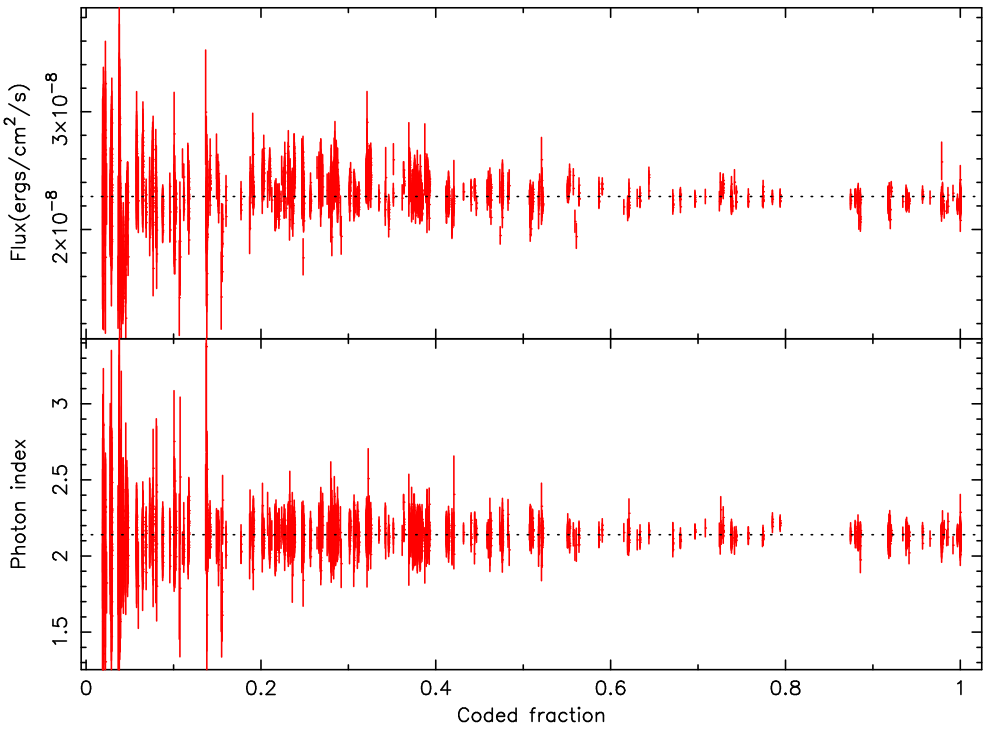

Figure 4.4: *Crab flux in the 10-100 keV energy band (upper panel) and spectral photon index (lower panel) as a function of the coded fraction, as estimated with the mask-weighting technique using celestial Crab coordinates. The horizontal dotted lines represent the best fit to the constant model (see Table 4.4 for details).*

	Detection Coordinates		Catalogue Coordinates	
	FLUX			
Coded fraction	Mean	rms	Mean	rms
> 0	2.28E-08	7.7%	2.28E-08	8.1%
> 0.1	2.28E-08	5.0%	2.28E-08	5.9%
	PHOTON INDEX			
> 0	2.14	0.09	2.14	0.11
> 0.1	2.14	0.07	2.14	0.08

Table 4.4: *Flux and power law statistic of Crab dataset. Fluxes in the 10-100 keV energy band are expressed in ergs $cm^{-2}s^{-1}$ units.*

mean flux over the full range of coded fraction (a total of 915 points) is $\sim 2 \times 10^{-8}$ ergs cm^{-2} s^{-1}, with a RMS of 33.3%.

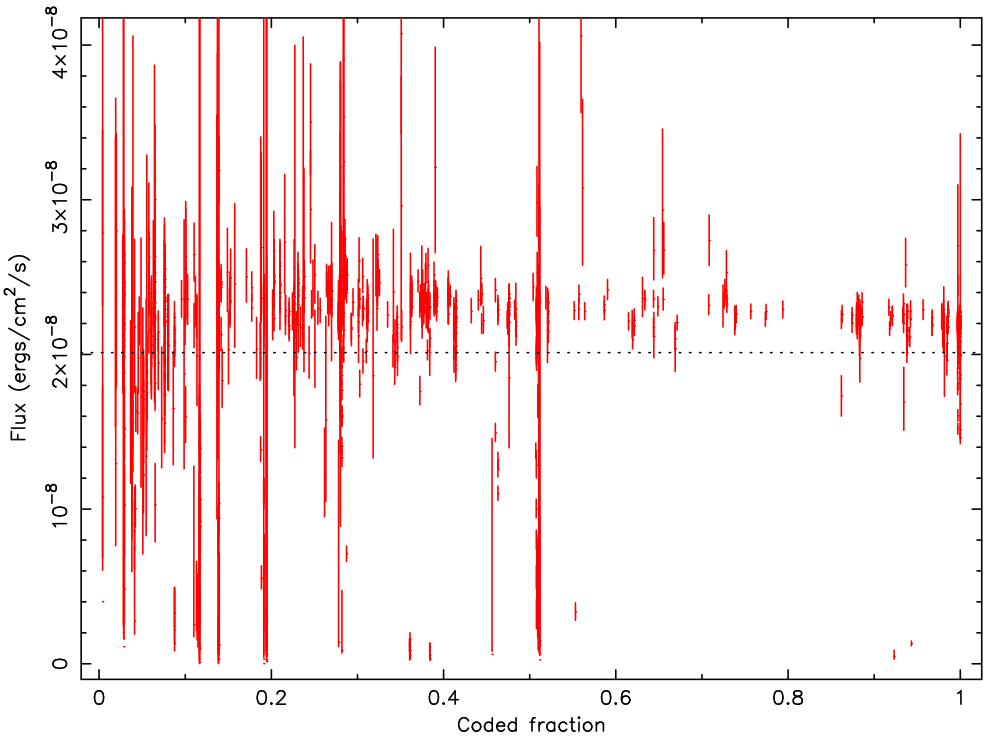

Figure 4.5: *Crab flux in the 10-100 keV energy band as a function of the coded fraction for rejected DPHs, as estimated with the mask-weighting technique using Crab coordinates. The horizontal bar represents the best fit of the constant model ($\sim 2 \times 10^{-8}$ ergs cm^{-2} s^{-1}, with a RMS of 33.3%).*

The difference arising when using nominal or detection coordinates to extract spectral information was also investigated. Figure 4.6 shows the flux difference as a function of the offset between the real Crab coordinates (in red) and those provided by the detection algorithm (in black). Considering all the Crab data, 96.0% of the detections lie within 3 arcmin of the source celestial coordinates and that their flux values differ by, at most, ±5%. Considering only flux values extracted from observations with a coded fraction greater than 0.1, the ±5% threshold is met in 98.5% of the cases.

4.1.3 Results II: stacking multiple DPHs

DPH have a typical integration time of 5 minutes. A single-DPH row analysis may be desirable in order to maximize time resolution. However, especially when dealing with faint sources, it may be important to increase the statistics, at the expense of time resolution, by merging several DPH rows. In general, different DPHs are collected with different mean satellite attitudes. Such a

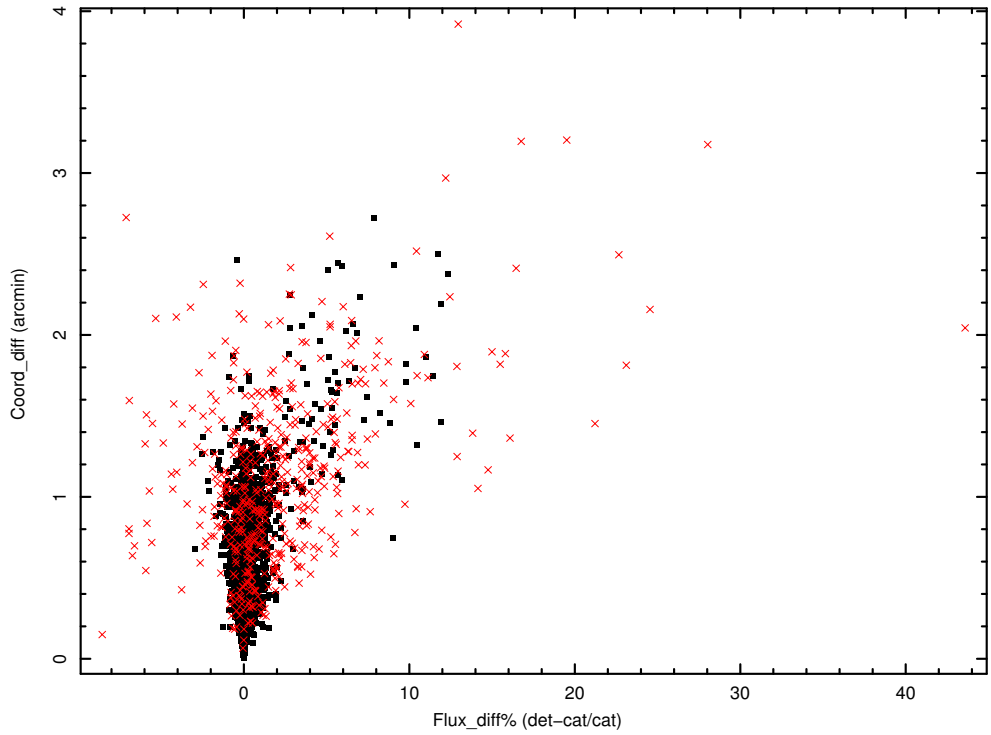

Figure 4.6: *Flux difference using detection coordinates and nominal coordinates as a function of coordinate difference. Black squares represent the rows for which Crab was located at a coded fraction greater than 0.1, whereas red crosses are those for which the coded fraction was smaller than or equal to 0.1 . The use of detection coordinates induces a slight source flux overestimate which can be quantified as ∼0.5 %.*

Offset (arcmin)	Flux loss
Pcode = 1	
1	0.1%
2	0.3%
3	1.9%
5	5.7%
7	11.1%
Pcode = 0.5	
1	1.2%
2	3.6%
2.7	5.2%
4	19.4%
Pcode = 0.1	
2	7.7%

Table 4.5: *Crab flux loss for two DPH stacked as a function of the DPH pointing offset. Different positions of the Crab in the FOV were considered.*

difference must be carefully checked before proceeding with the merging, since any offset may cause a partial loss in the reconstructed source flux. In order to quantify such an effect as a function of the pointing offset, a simple test with the Crab data was performed. Among the data set described in section 4.1.1, DPHs where the Crab happened to be in three different FOV regions (at coded fraction 1, ∼0.5, ∼0.1) were selected. For each region, a reference DPH was selected together with a group of nearly co-aligned DPHs, having ROLL angles within 1 arcmin of the reference one, as well as pointing offsets (in R.A. and Dec.) within 7 arcmin of the reference one. Then, each of the selected DPH rows was summed to the reference one, obtaining stacked DPH pairs, each being characterized by a "pointing offset" ranging from 0 to 7 arcmin. For each of such stacked pairs, a spectral analysis was performed and the Crab flux extracted, to be compared with the one obtained from the reference DPH. Details on the handling of different attitude files for the construction and analysis of a pair are given in the next subsection. The resulting flux-losses with respect to the reference DPH, as a function of the offset, for different coded fractions, are given in Table 4.5.

Although such investigation is far from complete, results suggest that significant flux losses ($> 5\%$) may occur, especially for target position at low coded fractions, when stacking different DPHs with a pointing offset larger than 2 arcmin.

Attitude information for stacked DPHs

In order to understand the previous section dealing with the stacking of different DPH, focused on the maximum allowed misalignement between the observations, a brief explanation of the *aspect* tool, handling the attitude information on DPHs, is necessary. *Aspect* calculates the mean pointing for a given atti-

tude file as follows: the algorithm first creates a two-dimensional histogram of the amount of time spent at each RA and DEC, then selects the bin with the largest time and calculates the mean RA, DEC and ROLL angle of the spacecraft axes while RA and DEC angles were in this bin. The default binsize for such a histogram is 0.01 degs and usually a large fraction of the integration time of a DPH refers to a single bin of such size. This means that, if we stack two DPHs with an offset larger than 0.01 degs, the resulting pointing coordinates as obtained with *aspect* will be the same as the fraction of DPH accounting for the peak in the above described histogram. In the case of two histogram bins with the same amount of time, aspect calculates the mean of the relevant coordinates. If the offset is smaller than 0.01 degs (or than the selected binsize), *aspect* calculates the mean of the coordinates, as described above. The approach adopted in the following section was to leave fixed the default *aspect* binsize value and to choose, for each of the three coded fraction regions selected above, a reference single DPH row with 450 s exposure time: any other selected DPH row with the same exposure time was stacked on it.

4.2 Systematic effects and evaluation of upper limits

Although the mask-weighting technique is a very powerful tool to evaluate the flux of bright sources, in most cases one aims at fainter sources, close to the limit of BAT sensitivity. In order to distinguish between a real faint source and a background fluctuation, it is crucial to estimate the sensitivity for different coded fraction values achieved when using Pipeline 1. While an exhaustive study of the BAT background is beyond the scope of this work, it is important to evaluate a rough, order of magnitude, background flux as a function of the coded fraction and the exposure time to be compared with the flux values measured when analysing real sources.

First of all, to perform such study, a large amount of data of the Crab dataset presented in section 4.1.1 was used. In particular, DPHs containing the largest number of rows were selected to allow different integration times with the same pointing to be obtained. Such selection yielded 28 multi-row DPHs corresponding to different epochs, the mean temporal separation between them being $\Delta t \sim 3$ days. For each DPH, 99 spectra were extracted from source-free directions in the following way: for each DPH, directions corresponding to the same image coordinates were used. A group of 33 directions, each one spaced by 0.12 deg, for each one of three different coded fraction values (1, $\sim$0.5, and $\sim$0.2) was selected. Thus, 99 "pure-background" spectra were obtained, i.e. 33 spectra for each coded fraction value. For each DPH, the merging of 450 s rows was also performed, in order to obtain spectra with longer integration times: finally, 28$\times$99 spectra were obtained with exposure times of 450, 900, 1800, 3600 and 7200 seconds. For each spectrum an upper limit in the 30-100

keV energy range was extracted, using the same procedure described in section 3.1.4.

For a given coded fraction value and exposure time, the 33 upper limits of each DPH show a large dispersion (by a factor ~ 3). Since the difference between contiguous directions is 0.12 deg, such a spread reflects small-scale noise. This is reminiscent of the small-scale noise which is seen in the deconvolved sky images produced by *batfftimage* (see section 3.1.2). Non surprisingly, a clear correlation between the upper limit values calculated with the mask-weighting technique and the pixel values on the deconvolved sky images is found for a given set of directions (see Figure 4.7). For a given coded fraction value and exposure time, both the normalisation factor and the slope of such a correlation does not change significantly as a function of the epoch (i.e. for different DPHs). The normalisation factor of the correlation changes as a function of the exposure time.

Moreover, the variation of the upper limit values as a function of the coded fraction value, the exposure time, and the DPH epoch was also investigated by calculating the relevant mean and the standard deviation over each set of 33 upper limits. It was found that the upper limit values do not show significant changes at different epochs, while a non negligible variation is observed as a function of the coded fraction value and of exposure time. Therefore, in order to obtain statistically significant samples, upper limits from different DPHs were grouped. For each coded fraction value and exposure time, the distributions of hundreds of upper limits were fitted with Gaussian distributions and the best fitting parameters are listed in Table 4.6.

All the results presented so far are based on observations of the Crab field. The same strategy was adopted to observations of GRO J1655-40, a source located in a different field of the sky. From the GRO J1655-40 dataset (see section 4.3 below), 4 multi-row DPHs at different epochs were selected (the mean temporal separation between a pair of DPHs was $\Delta t \sim 54$ days) and a similar analysis was performed, extracting the spectra exactly from the same source-free directions as above. The correlation between upper limits and pixel values on the deconvolved sky images is similar to that found for the Crab: the correlation slope does not change, whereas the normalisation varies as a function of both the exposure time and the coded fraction value. Considering the upper limit spread, values compatible with those shown in Table 4.6 are found, the differences being as small as $\pm$5-10%.

The range of the upper limit values should be ascribed to systematic noise, possibly related to coding mask effects. A possible correlation between upper limit mean values and BAT total count rate periodicities was also investigated. The total number of counts detected by BAT in a given energy band is modulated both by the $\sim$90 minutes *Swift* orbital period as well as by the Earth rotation. Such modulation is induced by the South Atlantic Anomaly (SAA) orbital passes. Although *Swift* instruments are switched off during the SAA passes, a higher count rate follows each passage (see Figure 4.8) inducing a 90

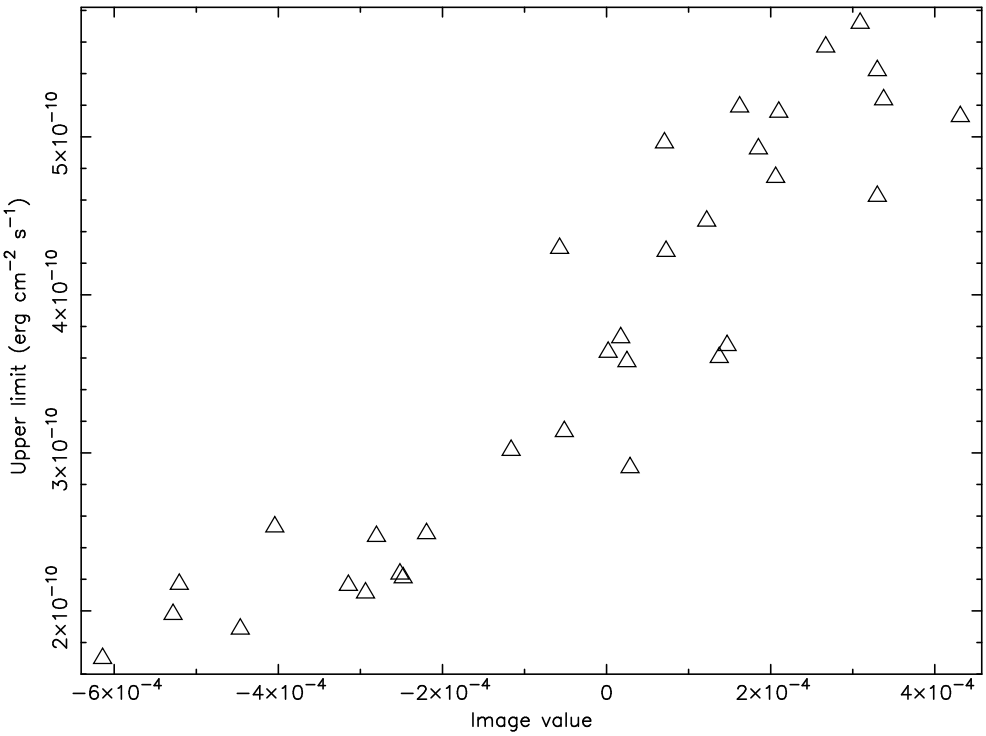

Figure 4.7: *Correlation between the image values and the upper limits (30-100 keV) extracted using mask-weighting technique at the same coordinates. 33 free-source on-axis directions in the Crab field were used.*

Exposure (sec)	Mean (ergs/cm^2/s)	St.Dev. (ergs/cm^2/s)	N of upper limits
Pcode = 1			
450	3.51e-10	1.01e-10	924
900	2.36e-10	7.73e-11	924
1800	1.58e-10	5.76e-11	825
3600	9.34e-11	4.14e-11	526
7200	5.93e-11	3.24e-11	327
Pcode = 0.5			
450	7.98e-10	2.61e-10	924
900	6.00e-10	2.00e-10	924
1800	4.55e-10	1.77e-10	825
3600	3.36e-10	1.56e-10	528
7200	2.52e-10	1.74e-10	327
Pcode = 0.2			
450	1.56e-09	4.45e-10	924
900	1.21e-09	3.54e-10	924
1800	9.61e-10	2.62e-10	825
3600	7.56e-10	2.20e-10	528
7200	6.18e-10	2.20e-10	330

Table 4.6: *Best-fit parameters obtained by fitting Gaussian distributions on the groups of DPH upper limits: mean and standard deviation are shown as a function of the exposure time and the coded fraction region. All upper limits were obtained with mask-weighting technique in the 30-100 keV energy range at fixed source-free directions.*

minutes orbital periodicity in the mean BAT count-rate. In addition, orbital precession due to the Earth rotation modifies the satellite paths inside the SAA, yielding a $\sim$ 1 day periodicity in the overall count rate (see Figure 4.9).

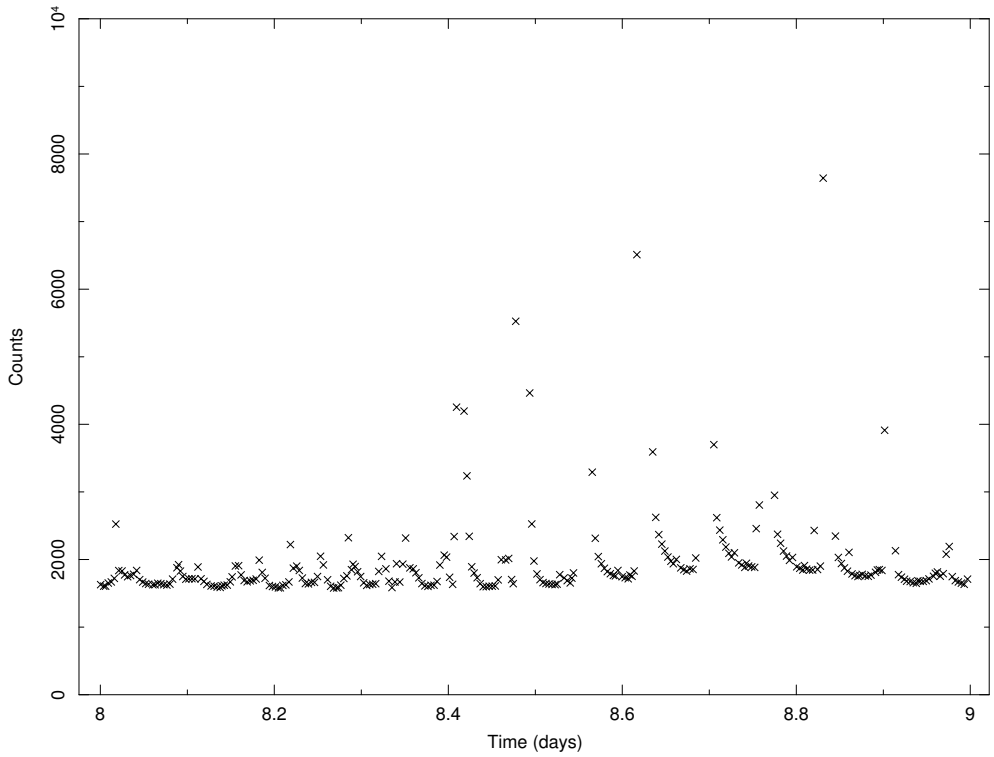

Figure 4.8: *The orbital periodicity of the total BAT counts detected in the 50-100 keV energy band. High counts observations are immediately following the gap during which BAT is turned off because of the spacecraft passage in the SAA.*

However, no correlation between upper limit mean values and BAT total count rate periodicities was found.

4.3 Monitoring a strongly-variable source: the case of GRO J1655-40

Having assessed the overall correctness and reliability of the pipeline described in section 3.1 on the bright Crab, the further step was the study of the BH binary GRO J1655–40, a source fainter than the Crab and one known to be strongly variable, both in flux and in spectral shape. GRO J1655-40 underwent a large outburst in 2005. The event started in the middle of February (it was discovered on February 17.99 during Galactic bulge scans with the *RXTE*/PCA instrument[86]) and lasted for more than 9 months. In what follows it was take advantage of the very large database serendipitously collected

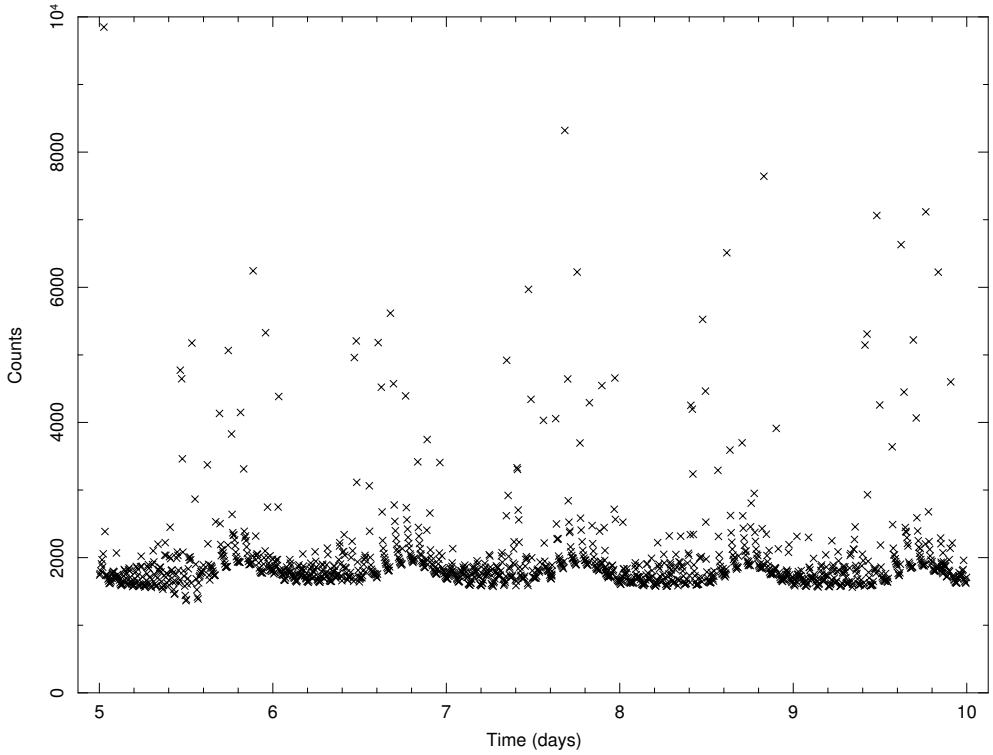

Figure 4.9: *Daily periodicity of the total BAT counts detected in the 50-100 keV energy band. See text for details.*

by the BAT instrument during the whole outburst event as well as of the systematic monitoring performed by the *RXTE* satellite. This allowed the comparison of the BAT results with quasi-simultaneous results obtained with the well calibrated instruments on-board *RXTE*. Such a cross-check yielded a very robust assessment of the capabilities of the analysis method described in section 3.1 as well as of the potentiality of BAT as a monitor of a (relatively) bright, strongly variable source.

4.3.1 BAT data analysis

All BAT observations covering the field of GRO J1655-40, collected between 2005/01/22 and 2005/11/11, were retrieved. The complete dataset includes 796 observations, for a total of 8724 DPHs, corresponding to ∼2.6 Ms observing time. As a first step, good data were selected, according to the prescription described in section 3.1.1. A total of 2080 (∼24%) DPHs were discarded after data screening. This percentage is compatible with that found for the Crab dataset in section 4.1.1. Next, well-aligned, contiguous DPHs were combined for up to a maximum integration time of 1 hour. Following the considerations exposed in section 4.1.3, it was decided conservatively to stack DPHs only if their pointings were within 1.5 arcmin. As a result, 1650 merged DPHs were obtained. Then, from each data block, a spectrum were extracted with the mask-weighting technique, and the appropriate response matrix were produced (see section 3.1.3).

An automatic spectral analysis was then carried out in XSPEC as described in section 3.1.4. After evaluating the source signal-to-noise ratio, spectra with no signal (S/N=0) were discarded. This resulted in the rejection of 378 spectra ($\sim$ 23% of the total). Low S/N spectra (with source detection below $\sim$ the 4σ level) were used to set an upper limit to the source flux. Contiguous, low-S/N spectra were summed, as well as their response matrices, in an attempt to increase the statistics, and the spectral analysis repeated on such combined spectra. High-S/N spectra were used for a complete spectral fit using a power law model. The normalization was evaluated at 40 keV in order to minimize correlation with the photon index[87]. GRO J1655-40 shows a strong, variable thermal component, dominating the source spectrum below 10 keV, while up to $\sim$ 100 keV the spectrum is well reproduced by a power law ([88];[89]). Sometimes the thermal component yields a very significant (or even dominant) contribution up to more than 20 keV. In order to simplify the spectral analysis using a single-component model, the hardness ratio test was used to select the energy range minimizing the thermal contribution. In particular, the hardness ratio between the 16-22 keV and 20-70 keV energy ranges was considered. Spectra with a high count rate in the soft band were studied in 30-100 keV energy range, otherwise the 10-100 keV band was used.

4.3.2 *RXTE* data analysis

RXTE monitored the whole outburst of GRO J1655-40 since its discovery [86]. The dataset is composed of 490 observations, performed between 2005-02-26 and 2005-11-11. Each observation has a typical integration time of ∼1.5 ks, for a total observing time of ∼664 ks. Spectral data extracted from the complete dataset have been made available to the community by the MIT group [3]. Spectra for both source and background as well as response matrices and effective area files were retrieved from their web site. In order to ease comparison of the results between different instruments, the same choices of energy range and spectral model were adopted. Thus, only data from the HEXTE instrument (operating in the 20-200 keV energy range) were used for the spectral fits. The spectral analysis was performed with an automatic pipeline based on the same algorithm adopted for BAT (as described in section 3.1.4). 53 low quality spectra (S/N<3.5) were discarded.

As a further step, data from the PCA instrument (operating in the 2-60 keV energy range) were used to extract a simple light curve (cts s^{-1}) in the soft (20-30 keV) energy range. An analogous light curve for the hard range (30-100 keV) was also extracted from HEXTE data and a hardness ratio plot was produced. In addition, public *RXTE* All Sky Monitor (ASM) data collected during the whole GRO J1655-40 outburst were downloaded and a count rate light curve in the 2-10 keV range was extracted.

4.3.3 Results

The complete light curve of the outburst of GRO J1655-40 as seen by BAT (in erg cm^{-2} s^{-1}) is shown in Figure 4.10 (top panel). HEXTE measurements are also shown, to allow for a direct comparison. In the same figure, the light curves extracted from the PCA data (count rate in 3-20 keV, central panel) and from the ASM data (count rate in 2-10 keV, bottom panel) are plotted. Errors are at the 1σ level.

Zooms of sections of the light-curve are shown in Figures 4.11, 4.12 and 4.13, where the light-curves and hardness ratio plots obtained with the PCA instrument (taken from *http://tahti.mit.edu/opensource/1655/*) are also given. In spite of the different time coverage of such a strongly variable source, the agreement between the BAT and HEXTE light curves is remarkably good.

It is difficult to perform a direct quantitative comparison since BAT and HEXTE observations are not strictly simultaneous and the source shows a large variability on short timescales. Generally, BAT and HEXTE measurements appear to be fully consistent within errors. Considering time windows for which the BAT and HEXTE observations are frequent and close in time, a difference not larger than ∼10-15% is apparent when the source flux is above 1-2 $\times 10^{-9}$ erg $cm^{-2}s^{-1}$, or ∼ 90 mCrab. Generally, a good agreement (within errors) is found when the S/N in BAT spectra is greater than 4. The actual

[3] *http://tahti.mit.edu/opensource/1655/*

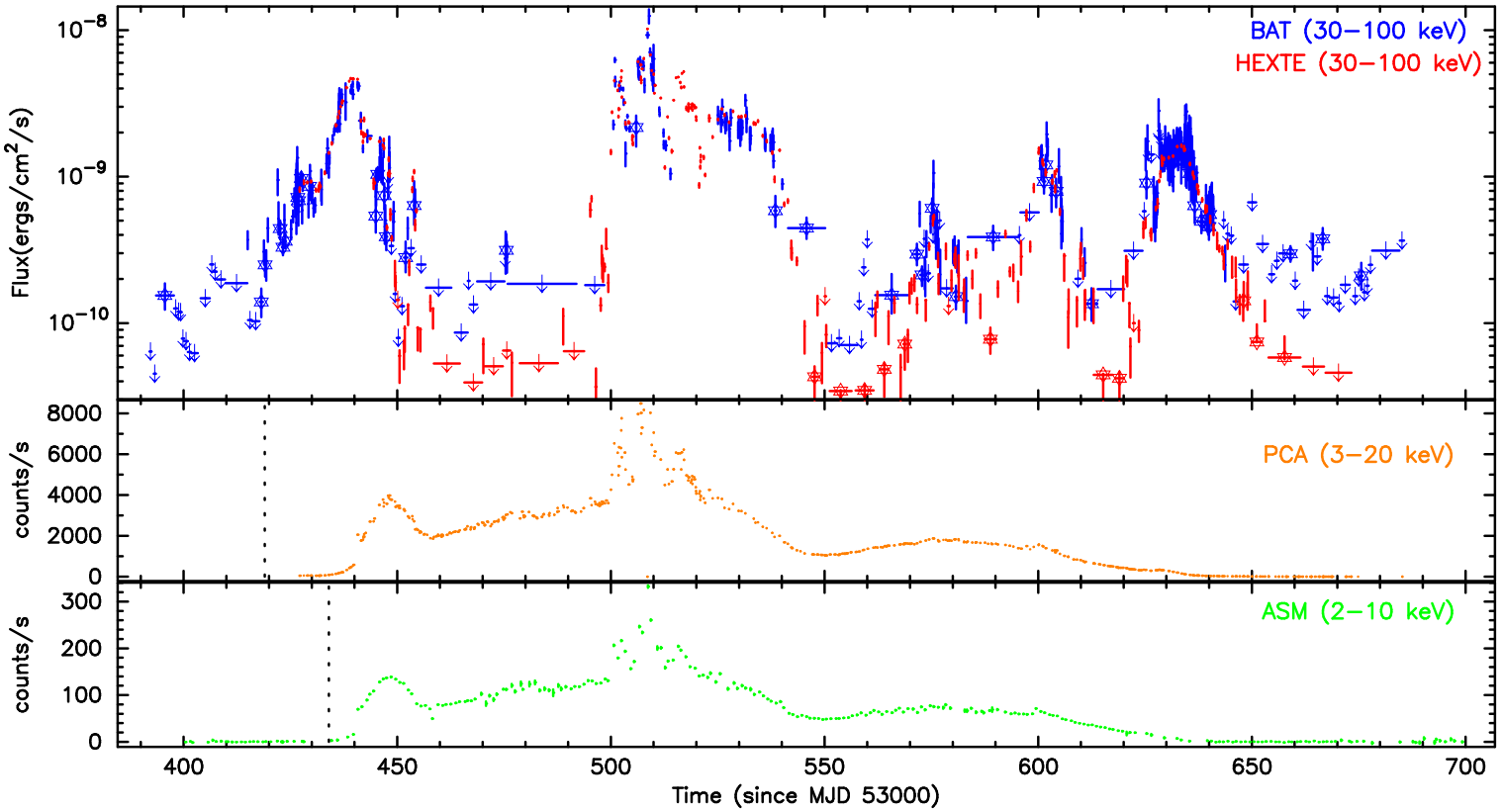

Figure 4.10: *GRO J1655-40 complete 2005 outburst as seen from* Swift*/BAT and* RXTE*/HEXTE (upper panel),* RXTE*/PCA (central panel), and* RXTE*/ASM (lower panel). In the upper panel, stars mark BAT and HEXTE points corresponding to averaged spectra. 3σ upper limits are also plotted, marked by arrows. Vertical dotted bars in the central and lower panels represent the time of the first detection of the outburst obtained with PCA and ASM respectively.*

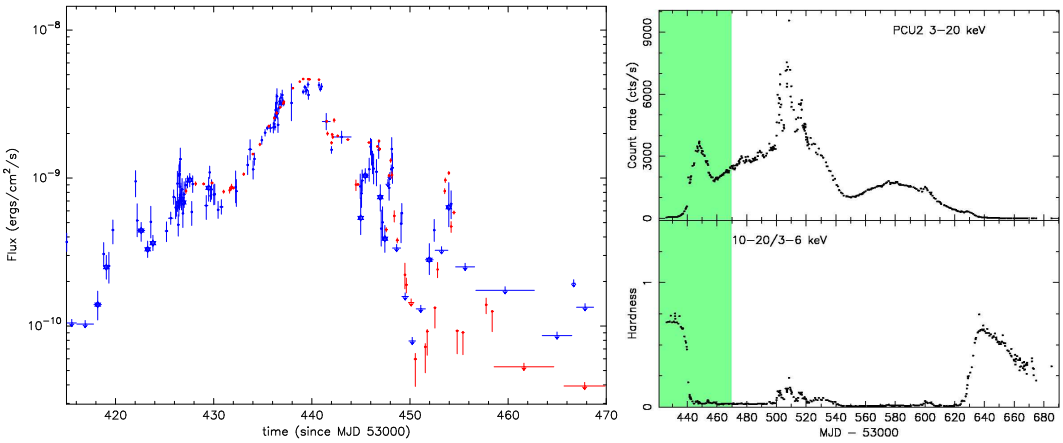

Figure 4.11: *Left panel: zoom of the first part of the GRO J1655-40 outburst as seen by BAT (blue) and HEXTE (red) (symbols as in Figure 4.10). The right panel represents the PCA count rate and hardness ratio as obtained from the (*http://tahti.mit.edu/opensource/1655/*) web site. The green box highlights the time span covered in the left panel.*

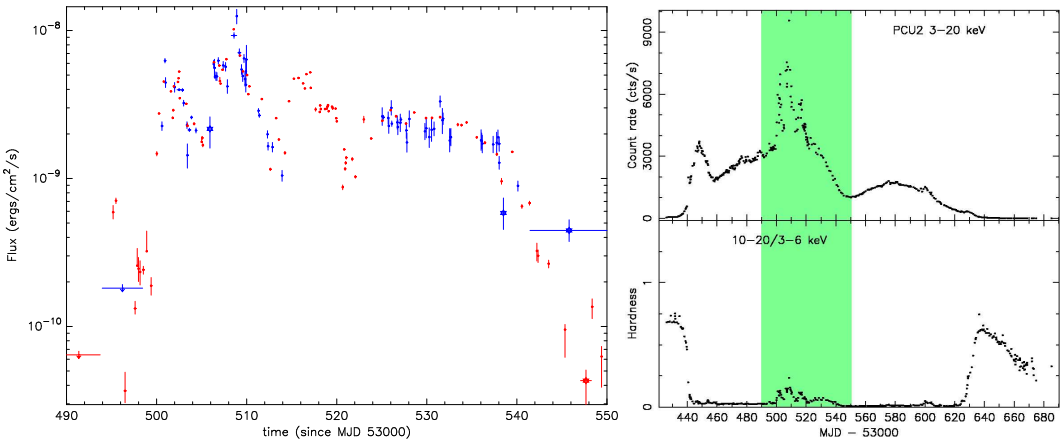

Figure 4.12: *Zoom of the central part of the GRO J1655-40 outburst as seen by BAT (blue) and HEXTE (red).*

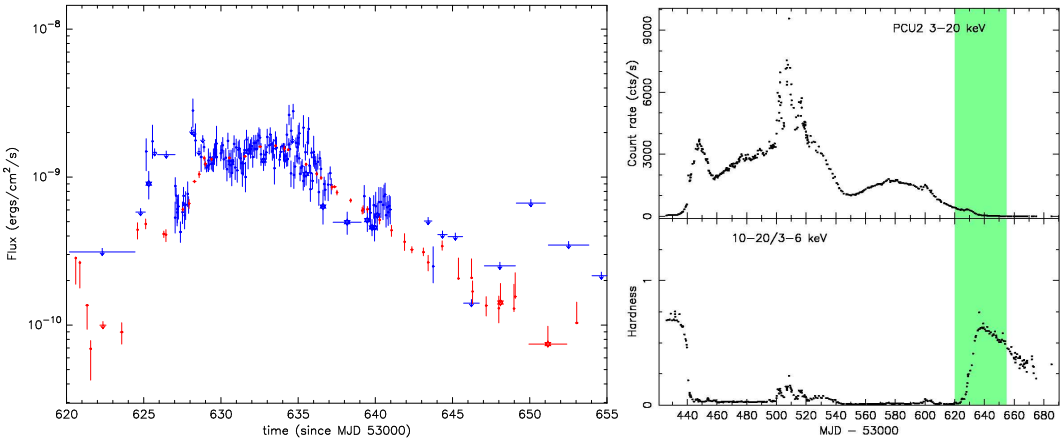

Figure 4.13: *Zoom of the final part of the GRO J1655-40 outburst as seen by BAT (blue) and HEXTE (red).*

flux yielding such a S/N obviously depends on the position of the target within the FOV. Indeed, in one hour exposures, the 3σ sensitivity with such approach is $\sim 10-20$ mCrab for an on-axis source, while it is a factor ~ 10 worse at a coded fraction of 0.2 (see Table 4.6). Thus, if the target lies within the half-coded region, such approach yields significant spectral measurements (consistent with HEXTE) in the 30-100 keV range down to $(5-6)\times 10^{-10}$ erg $\mathrm{cm}^{-2}\mathrm{s}^{-1}$, or ~ 50 mCrab (see e.g. Fig 4.13, around MJD 53640). The study of sources fainter than ~ 50 mCrab would require a different and more complex approach.

A good agreement between the power law photon index values as measured by BAT and HEXTE is also apparent in Figure 4.14. This is particularly evident if considering the time intervals corresponding to the highest source flux (above $\sim 2 \times 10^{-9}$ ergs cm^{-2} s^{-1}), as shown in Fig. 4.15, where BAT and HEXTE values agree to within $\sim$13% with no apparent correlation between spectral shape and flux discrepancy. Fig. 4.10 is a clear proof of the good capabilities of the method described in section 3.1 in extracting flux and spectral information for bright hard X-ray sources. Combining such good performance with the huge BAT FOV, which covers each day $\sim$50% of the sky, one realizes the instrument's potential to frequently monitor the temporal and spectral evolution of numerous bright, hard-X ray sources.

BAT serendipitous coverage yielded a monitoring with a time coverage fully comparable to that obtained through a systematic campaign with *RXTE*. It is worth noting that BAT, because of its good sensitivity over a very large FOV, caught the outburst from the very beginning, while the detection of the source activity by HEXTE and PCA was due to a planned observational campaign of the Galactic center region (PCA Galactic bulge scans). Had GRO J1655-40 been located outside the galactic bulge region scanned by *RXTE*, its outburst would have been detected by ASM with a >15 day delay with respect to BAT

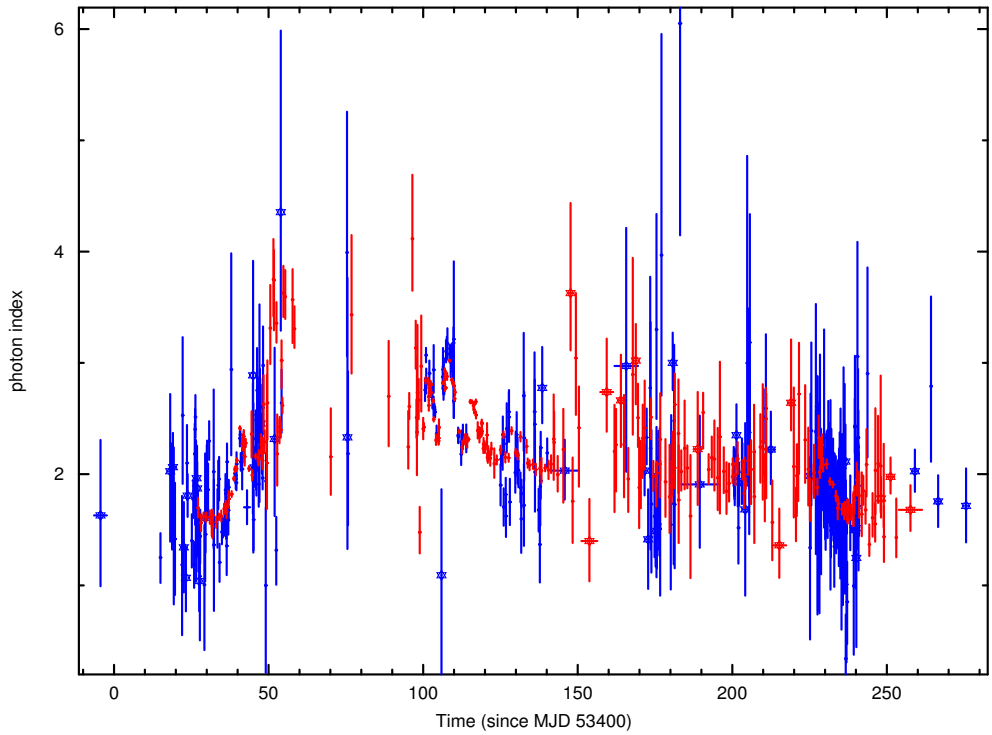

Figure 4.14: *Spectral photon index evolution of the GRO J1655-40 outburst as obtained by fitting a power law independently to BAT (blue) and HEXTE (red) spectra. Errors are given at a 1σ level. The star labeled BAT and HEXTE points correspond to averaged spectra.*

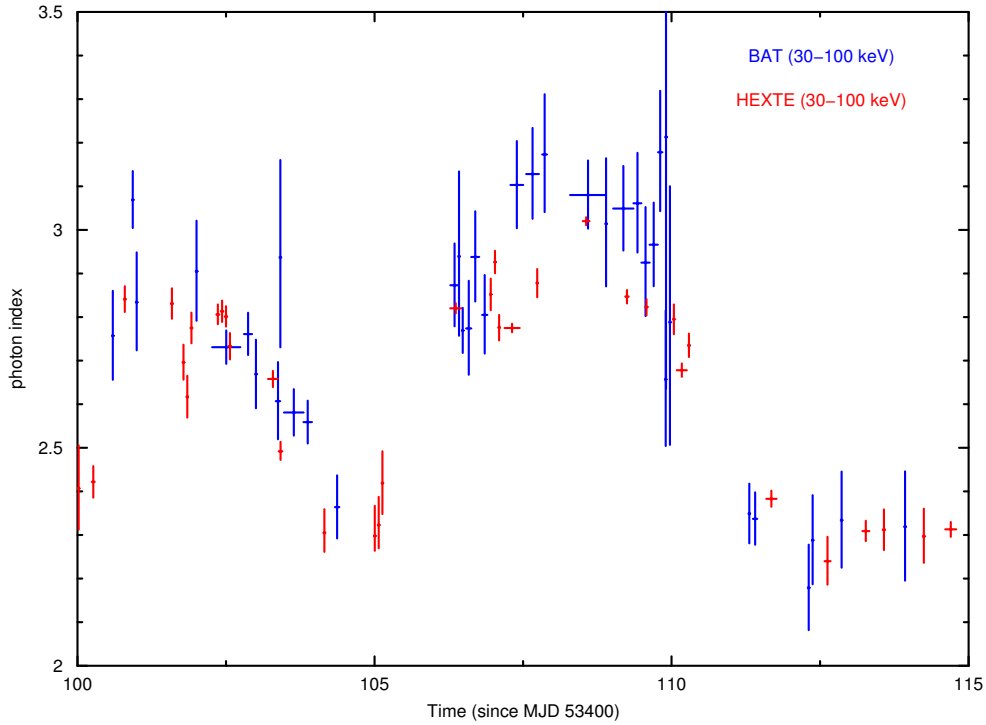

Figure 4.15: *Zoom of Figure 4.14 for the central part of the outburst.*

(see Figure 4.11). Thus, while scanning the sky waiting for GRBs, BAT can be used both for detecting emission from hard X-ray transients and for monitoring the temporal and spectral evolution of known sources.

Chapter 5

GRO J1655-40: the hard-X ray emission during the rise of its 2005 outburst

In this chapter the analysis of the spectral evolution of the BH binary GRO J1655–40 during the rising phase of the 2005 outburst is presented. For this kind of analysis, the ability of Pipeline 1 (see section 3.1) to extract good-quality spectra was crucial. Moreover, the wide temporal coverage of the source serendipitously obtained by BAT allowed a detailed study of the spectral evolution of the BH binary during the outburst to be performed. Although data from other observatories (*INTEGRAL* and *RXTE*) were analysed, only the BAT data allowed the transition from the Low Hard State to the High Soft State of the source to be clearly observed. It is worth noting that, unlike BAT, *INTEGRAL* and *RXTE*, although both observing the outburst, did not obtain a temporal coverage wide enough to constrain the high energy cutoff during the intermediate state.

5.1 GRO J1655-40

GRO J1655–40 is a transient Galactic X-ray binary. Since its discovery on July 27, 1994 with BATSE[90] on-board the Compton Gamma-ray Observatory (*CGRO*), the source underwent several outbursts (i.e. : in 1995 see Zhang *et al.*[88], in 1996/1997 see Kuulkers *et al.*[91] and Mendez *et al.*[92]). It is likely to be a low mass X-ray binary and the compact object in this system is probably a black hole[93] with a mass estimated of 6.3 $M_{\odot}$ [94] and a distance of 3.2 kpc[95] from which the calculation of the Eddington Luminosity L_{edd} of the source will be based in this chapter. A recent work by Foellmi *et al.*[96] places an upper limit of 1.7 kpc to the distance, but this upper limit is still under debate. Radio jets were discovered in the mid-1990s and revealed apparent superluminal motion in opposite directions[97].

The analysis of the spectral evolution of GRO J1655–40 during the rising phase of the 2005 outburst is presented in this chapter. GRO J1655–40 was observed by *INTEGRAL* starting from MJD 53425 (*INTEGRAL* revolution 289 on 2005 February 24) to MJD 53448 (*INTEGRAL* revolution 296 on 2005 March 19). The spectral and timing evolution of the source from the Proportional Counting Array (PCA) on board the Rossi X-ray Timing Explorer (*RXTE*) in the 3-30 keV energy range was studied in detail in Shaposhnikov *et al.*[2] from MJD 53419 up to MJD 53445. Brocksopp *et al.*[98] presented the data from the BAT in the 14-150 keV energy range from MJD 53430 up to MJD 53435. In this chapter the broadband spectral evolution is presented using the Spectrometer on board the *INTEGRAL* (SPI, Vedrenne *et al.*[99]) in the 23-600 keV energy range combined with all the publicly available data from the PCA and HEXTE detectors on board the *RXTE* observatory, as well as the BAT detector in order to cover the 3-200 keV energy range.

One of the main interest in studying such a source during the LHS to the HSS transition (see section 1.4.1) is to follow the evolution of the high energy cutoff. Its value as well as its significance during the rising phase of the outburst will be quantified[1].

5.2 Observations and data reduction

GRO J1655-40 started a new outburst on February 17, 2005 (MJD 53418) observed by Markwardt & Swank[86] with the PCA detector on board the *RXTE* observatory. This reactivation was confirmed by Torres *et al.*[100] who reported the near infrared activity of the source on February 21, 2005. The source was followed by pointed *INTEGRAL* observations from MJD 53425. Table 5.1 gives the details of each *INTEGRAL* revolution and corresponding quasi simultaneous *RXTE* observations used in this analysis.

5.2.1 *INTEGRAL* data reduction

The data from the SPI detector were reduced as explained in section 2.1.1 of Joinet *et al.*[101] except that only 17 detectors were active compared to 2005. The SPIROS V6 algorithm was used in order to derive the position of sources detected in the FOV of GRO J1655–40. Only pointings for which GRO J1655–40 was at a distance less than 12 degrees from the central axis were taken into account for the analysis. Pointings affected by a solar flare or by exit/entry into the radiation belts were excluded. 458 ks of useful data during the observation period covered by the revolutions 289 up to 296 (see Table 5.1) were obtained. The temporal variability of each source was estimated (see section 5.3.1) on the basis of both their intensity and their known temporal behaviour. The background flux is stable within each of the considered revolution except for

[1] Joinet, A., Kalemci, E., & Senziani, F. 2007, submitted to ApJ

Rev.	SP_{start}	SP_{stop}	Δt_{sp} (ks)	ID	RX_{start}	RX_{stop}	Exp.(ks)
289	53425.14	53427.36	133	90058-16-04-00	53425.06	53425.10	3.7
				90428-01-01-00	53426.04	53426.28	20.6
				90058-16-05-00	53427.02	53427.06	3.1
290	53428.13	53430.36	134	90428-01-01-03	53428.14	53428.20	5.1
				90428-01-01-04	53428.86	53429.12	22.5
				90428-01-01-02	53429.71	53429.97	22.6
291	53432.85	53433.47	29	90428-01-01-10	53432.79	53433.00	17.97
292	53434.80	53436.42	36	91404-01-01-02	53433.91	53434.09	16.14
				91404-01-01-03	53434.69	53434.73	2.80
				91404-01-01-01	53435.61	53435.64	2.37
				91404-01-01-04	53436.16	53436.17	1.41
292_{sw}-A,B	53434.89	53436.45	17.75				
293a	-	-	-	91702-01-01-00	53436.72	53436.81	7.4
293_{sw}	53436.48	53436.49	14.89				
293b	53437.11	53438.34	51	91702-01-01-03	53438.05	53438.08	2.2
294a	-	-	-	91704-04-01-00	53439.61	53439.65	3.4
294b	-	-	-	91704-04-01-01	53439.74	53439.78	3.6
294_{sw}-A	53439.05	53439.65	13.29				
294-A	-	-	-	91702-01-02-00	53440.68	53440.77	7.6
294_{sw}-B	53440.72	53441.87	4.42				
294-B	-	-	-	91702-01-02-01	53441.51	53441.54	2.3
294-B	-	-	-	91702-01-02-02	53441.59	53441.60	1.4
294-B	-	-	-	91702-01-02-03	53441.98	53442.01	2.2
294-C	-	-	-	91702-01-02-04	53442.06	53442.07	1.8
294-C	-	-	-	91702-01-02-05	53442.12	53442.14	1.5
294-C	-	-	-	91702-01-02-06	53442.58	53442.66	6.9
295-A	-	-	-	91702-01-03-00	53443.54	53443.80	22.5
295-B	53445.07	53445.44	23	91702-01-04-01	53444.49	53444.50	0.6
295_{sw}	53444.92	53445.13	1.24				
296	53446.16	53447.71	52	91702-01-05-01	53446.62	53446.73	9.2

Table 5.1: *The INTEGRAL observations of GRO J1655–40. For each INTEGRAL revolution (Rev.), the beginning (SP_{start}) and the end (SP_{stop}) of the INTEGRAL observations are given in MJD. Δt_{sp} is the useful duration for INTEGRAL observations. ID is the identification program number of RXTE observations. RX_{start} and RX_{stop} are the beginning and the end of RXTE observations taken quasi simultaneously with INTEGRAL observations. Exp. is the exposure time for PCA. The simultaneous BAT data are also indicated: the symbol "sw" is attached to the number of the revolution. The details of the BAT observations are given in Table 5.2. The observation periods for which the source harboured the same X-ray state (see section 5.3.1 and Figure 5.1) are separated with a line. This will be done for all the Tables in this chapter.*

revolutions 292 and 293 for which a timescale variability of one pointing (with a duration of 30-40 minutes) was used. Only one normalization parameter per orbit with an uniformity map determined for the 17 detectors configuration was considered. The SPI data were limited in the energy range from 23 to 600 keV and a 3% systematic error was added to all spectral channels.

5.2.2 *RXTE* data reduction

The public data from the PCA and HEXTE detectors on board the *RXTE* observatory[102,103] were also analysed. Table 5.1 summarizes the set of *RXTE* observations performed contemporaneously with the *INTEGRAL* data observation periods except for the revolution 294 for which there are no *INTEGRAL* data available. This observation period was divided into three. Several *RXTE* observations were merged in order to correspond to one integrated *INTEGRAL* revolution (see Table 5.1). For both instruments, the data reduction was performed using the FTOOLS routines in the HEAsoft software package distributed by NASA's HEASARC (version 6.0.4). All available PCUs of the PCA[102] detector were used for the data extraction. A systematic error of 0.8% was added up to 7 keV and of 0.4% above 7 keV (for the details of how systematic uncertainties were estimated, see Tomsick *et al.*[104]) For HEXTE, the response matrix created by the FTOOLS was used, and the necessary dead time correction[103] were applied. The HEXTE background is measured throughout the observation by alternating between the source and background fields every 32 s. The data from the background regions are merged. The energy range was limited from 3 to 25 keV, and 16 to 227 keV for the PCA and HEXTE data respectively. HEXTE channels were grouped by 2 for channels 16-31, by 4 for channels 32-59, by 10 for channels 60-99 and by 64 for channels 100-227.

5.2.3 Swift data reduction

All the publicly available data from the BAT detector on board the *Swift* observatory covering the rising phase of the 2005 outburst were also analysed (see Table 5.2).

Some of them were simultaneous with the *INTEGRAL* revolutions (292, 295-B and 296). The revolution 292 was divided into two datasets composed of 7 BAT pointings with a duration of 10.09 ks for the first one (292_{sw}-A) and of 7.66 ks for the second one (292_{sw}-B). The *Swift*BAT data, covering the observation period between the *INTEGRAL* revolution 292 and 293 (293_{sw}) and between revolution 293 and 295-B (294_{sw}-A and 294_{sw}-B), were also used.

The same reduced data as obtained in section 4.3 were used. For the spectral analysis, the energy range was limited from 16 to 150 keV. For both the *RXTE* instruments and the BAT, the normalization factor was set free with respect to SPI normalization for all fits.

Rev.	ID	Sw_{start}	Sw_{stop}	Exp(ks)
292_{sw}-A	00106709002	53434.89	53434.91	1.35
	00106709003	53435.23	53435.24	1.35
	00030009002	53435.42	53435.50	2.94
	00106709004	53435.76	53435.78	0.90
	00055750001	53436.08	53436.09	0.90
	00055750002	53436.15	53436.16	1.30
	00055750003	53436.21	53436.23	1.35
292_{sw}-B	00106709005	53436.23	53436.25	1.35
	00055750004	53436.28	53436.30	1.35
	00058739002	53436.30	53436.32	1.66
	00055750005	53436.35	53436.35	0.64
	00058739002	53436.37	53436.38	1.04
	00055750006	53436.41	53436.42	0.64
	00058739002	53436.44	53436.45	0.98
293_{sw}	00055750007	53436.48	53436.49	0.64
	00055750008	53436.54	53436.55	0.45
	00107547001	53436.62	53437.17	18.30
294_{sw}-A	00107547002	53439.05	53439.65	13.29
294_{sw}-B	00058736001	53440.72	53440.93	1.80
	00058746001	53440.98	53441.00	1.80
	00058746002	53441.07	53441.87	0.82
295_{sw}	00055800001	53444.92	53445.13	1.24
296_{sw}	00111063001	53446.14	53446.88	12.60
	00058752001	53447.06	53447.21	1.49

Table 5.2: *Details of BAT data observations. The observation ID number, the beginning (Sw_{start}) and the end (Sw_{stop}) of the BAT observations are given in MJD. Exp is the net exposure time.*

rev	Φ [23-51 keV]	Φ [51-95 keV]	Φ [95-160 keV]	Φ [160-270 keV]
289	42 ± 2	64 ± 6	81 ± 7	59 ± 16
290	49 ± 4	74 ± 9	89 ± 7	87 ± 21
291	50 ± 14	116 ± 30	88 ± 30	167 ± 70
292	125 ± 8	159 ± 19	245 ± 25	187 ± 50
293_{sw}	241^{+3}_{-4}	320^{+7}_{-6}	403 ± 12	-
293	280 ± 7	327 ± 13	358 ± 14	214 ± 37
294_{sw}-A	328 ± 5	357 ± 7	382^{+14}_{-12}	-
294_{sw}-B	367^{+6}_{-7}	347^{+11}_{-10}	332 ± 17	-
295_{sw}	58 ± 6	122^{+26}_{-23}	122 ± 47	-
296_{sw}	88^{+5}_{-4}	46 ± 16	47 ± 11	-

Table 5.3: *Flux (expressed in mCrab) of GRO J1655–40 measured by SPI during different INTEGRAL revolutions (rev) and for several energy bands.*

5.3 Results

5.3.1 Light curve

The flux extraction of GRO J1655–40 from SPI observations was performed taking into account the hard X-ray sources detected in the FOV of the source. A timescale of one pointing (whose duration is about 3600 s) was used for 4U1700–377 and OAO 1657–415 and of 2 pointings for GX 340+0 and 4U 1705–322. Other sources (GRO J1655–40, 1E 1740–2942, 4U 1630–47, GX337+00 and GX349+2) with a constant flux within each revolution were also considered. As the significance of sources decreases above 150 keV, only 2 sources with a timescale resolution of 3600 s for 4U1700–77 and of one revolution for GRO J1655–40 were considered to extract fluxes in the 150-600 keV energy range. The light curve of the source from revolution 289 up to revolution 296 in the 23-51 keV energy range is shown in Figure 5.1.

As the source was in the border of the SPI FOV between *INTEGRAL* revolutions 293 and 295-B, the *RXTE* and the BAT observations (294_{sw}-A, 294_{sw}-B) were used to achieve a coverage of this period. The Table 5.3 gives the SPI and BAT fluxes in different energy bands.

The light curve obtained by the *RXTE* All-Sky Monitor (ASM) were also extracted in the 1.5-12 keV energy range in the same period of observation (data taken from the public XTE database [2]). The different states harboured by the source were determined by Shaposhnikov *et al.*[2] on the basis of the X-ray properties from the PCA observations and are summarized in Figure 5.1. The source was in the LHS from revolution 289 up to revolution 292, it then entered

[2] *http://xte.mit.edu/lcextrct/asmsel.html*

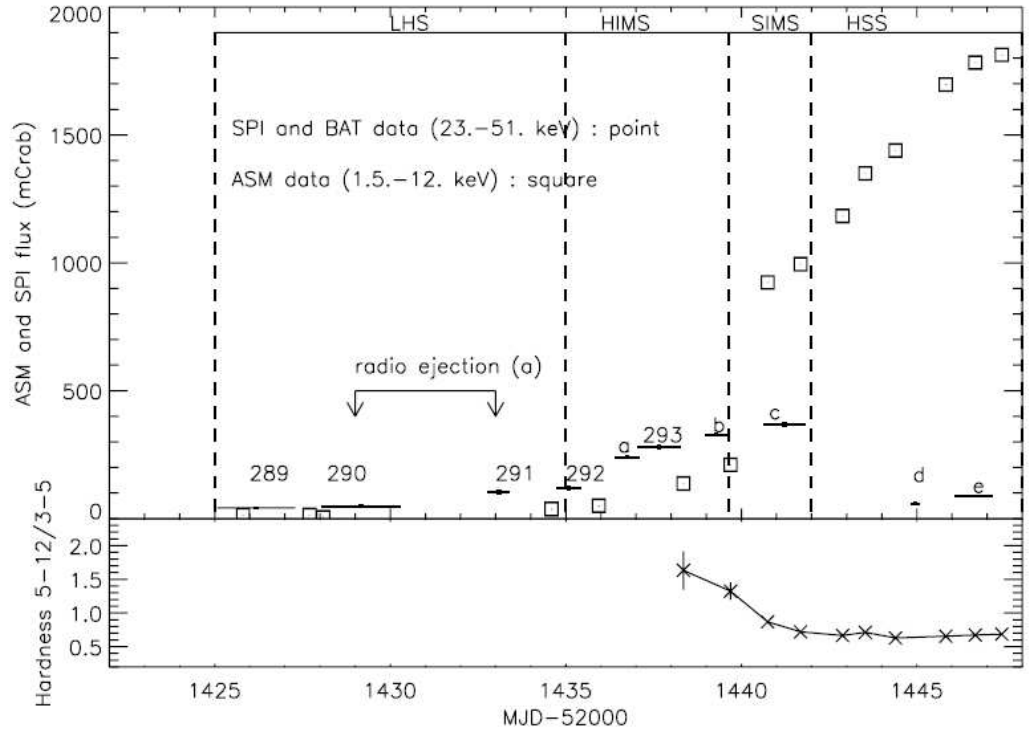

Figure 5.1: *Upper panel : ASM (1.5-12 keV), SPI (23-51 keV) light curves of GRO J1655–40 during the rising phase of the 2005 outburst. The legend of letters are: a=293_{sw}, b=294_{sw}- A,c=294_{sw}-B, d=295_{sw}, e=296_{sw} . The flux of points a,b,c,d,e was extracted from BAT observations. The different states harboured by the source are summarized on the graph (see section 1.4.1 for the definition): LHS=Low Hard State, HIMS= Hard Intermediate State, SIMS = Soft Intermediate State, HSS=High Soft State. Lower panel : the evolution of the hardness from ASM in the 3-12 keV energy range which is defined as the ratio of the ASM fluxes in two energy ranges [5.-12. keV]/ [3.-5. keV]. Two arrows indicate (a) the period associated to a radio flare event (see text).*

the HIMS from revolution 293 (also observed by the BAT detector : datasets 293_{sw} and 294_{sw}-A), the SIMS during the revolution 294-A and was in the HSS from revolution 295-A. Revolution 294 was divided into three *RXTE* datasets (294-A, 294-B and 294-C) in order to follow the evolution of the high energy cutoff during the SIMS. As seen from the SPI light curve (Figure 5.1), the 23-51 keV flux increased by a factor of 2.5 between MJD 53425 (42 ± 2 mCrab) and MJD 53433 (121 ± 7 mCrab) while the source was in the LHS. A radio ejection was observed during MJD 53429-53433 with a radio peak at 5 GHz [2]. After this ejection, the X and gamma-ray flux increased exponentially up to *INTEGRAL* revolution 293 or MJD 53437-53438 (280 ± 7 mCrab), during which the source was into the HIMS. As the flux in the 3-25 keV energy range measured from PCA data increased by a factor 3.9, the flux in the 23-51 keV energy range decreased by a factor 5.6 between revolution 293 and revolution 295-B, indicating the LHS to the HSS transition.

5.3.2 Spectral Modeling of the X and gamma-ray data

The spectra corresponding to each set of data in Table 5.1 and 5.2 were fitted with various models available in the standard XSPEC 11.3.1 fitting package [105]. In all fits, the iron emission line was modelled by a narrow Gaussian line fixed at an energy of 6.4 keV with a free width. For all models, the inner disk inclination was fixed at 70 [106]. The emission from a multicolour disk blackbody (DISKBB in XSPEC, Mitsuda *et al.* [107]) was also considered. The interstellar absorption (PHABS in XSPEC) was accounted for using a hydrogen column density N_H of 0.5 and 0.7 × 1022 cm^2 which is based on the values constrained by XMM-Newton observation during the 2005 outburst [108].

Power-law with a cutoff

First, a power-law component is added to the base model described above. The best fit parameters are presented in Table 5.4.

During the LHS (revolutions 289, 290, 291, 292), a constant spectral index of 1.47 was found (with a reduced χ^2 ranging from 1.7 up to 2.0). During revolutions 289, 290 and 291, the fits are significantly improved, as seen from the reduced χ^2 values, (with an F-test probability less than 10^{-9}) by adding a high energy cutoff component (see Table 5.4). A constant spectral index of about 1.33-1.36, which is roughly the same value found by Shaposhnikov *et al.* [2] (1.35 ± 0.03), was found. The high energy cutoff of 231^{+94}_{-50} keV is consistent with the range value of 163-214 keV presented in Shaposhnikov *et al.* [2] for the revolution 289. Unlike the work done in Shaposhnikov *et al.* [2], in this chapter its value was constrained and its evolution during the rising phase of the outburst precisely described using the SPI data, together with the BAT and the *RXTE* ones. For revolution 292, it is constrained to a value of 187^{+22}_{-20} keV with an increase of the F-test by several order of magnitude with respect to previous observations. BAT data were combined with the simultaneous

rev	T_{in} keV	N_{in}	Γ	E_c keV	W_{Fe} eV	χ^2(dof)	F-test	Φ_p/Φ_b
289	1.29 ± 0.12	$0.80^{+0.37}_{-0.23}$	1.47 ± 0.02	–	76^{+67}_{-60}	1.86 (79)		
289	$1.41^{+0.08}_{-0.14}$	$1.41^{+0.49}_{-0.17}$	1.36 ± 0.04	231^{+94}_{-50}	75^{+42}_{-48}	0.95(78)	3.62E-10	9.6
290	$1.20^{+0.10}_{-0.05}$	$1.05^{+0.58}_{-0.31}$	1.47 ± 0.01	–	75^{+36}_{-50}	2.04(79)		
290	$1.40^{+0.08}_{-0.09}$	$1.21^{+0.33}_{-0.22}$	1.33 ± 0.03	259^{+62}_{-41}	76^{+42}_{-40}	0.86(78)	1.85E-16	9.6
291	$1.04^{+0.14}_{-0.15}$	$2.64^{+3.27}_{-1.15}$	1.46 ± 0.01	–	75^{+36}_{-50}	1.60(79)		
291	$1.40^{+0.12}_{-0.16}$	$1.37^{+0.82}_{-0.32}$	$1.34^{+0.03}_{-0.04}$	253^{+76}_{-48}	78 ± 42	0.85(78)	1.42E-12	8.7
292	1.09 ± 0.08	$4.32^{+1.87}_{-1.24}$	1.48 ± 0.01	–	113^{+72}_{-82}	4.48(77)		
292	$1.27^{+0.09}_{-0.08}$	$4.49^{+1.42}_{-1.12}$	1.29 ± 0.02	187^{+22}_{-20}	177^{+88}_{-81}	0.85(76)	2.27E-29	7.5
292 + 292_{sw}	$1.27^{+0.09}_{-0.08}$	$4.50^{+1.42}_{-1.12}$	1.29 ± 0.02	186^{+22}_{-18}	76^{+42}_{-40}	0.68(223)		
293_{sw} + 293a	0.93 ± 0.06	22^{+9}_{-6}	1.53 ± 0.01	–	145^{+75}_{-52}	3.85(118)	–	–
293_{sw} + 293a	1.07 ± 0.05	22^{+5}_{-4}	1.33 ± 0.02	173^{+21}_{-17}	315^{+93}_{-57}	1.35(117)	1.19E-28	7.4
293	$1.60^{+0.05}_{-0.01}$	$4.87^{+1.52}_{-0.76}$	1.62 ± 0.05	–	388^{+46}_{-39}	5.30(77)		
293	1.00 ± 0.03	45^{+21}_{-15}	$1.37^{+0.02}_{-0.03}$	131^{+13}_{-11}	386^{+80}_{-52}	1.15(76)	3.46E-27	5.3
294_{sw}-A + 294a,b	0.67 ± 0.03	286^{+17}_{-14}	$1.82^{+0.03}_{-0.02}$	–	166^{+28}_{-38}	14.32(118)		
294_{sw}-A + 294a,b	1.01 ± 0.03	121^{+17}_{-14}	$1.41^{+0.03}_{-0.02}$	87^{+4}_{-5}	646^{+67}_{-46}	1.37(117)	–	4.4
294-A + 294_{sw}-B	0.94 ± 0.01	944^{+81}_{-82}	2.26 ± 0.01	–	555^{+47}_{-42}	2.64(118)		
294-A + 294_{sw}-B	0.97 ± 0.01	1025^{+79}_{-80}	2.03 ± 0.01	156^{+9}_{-5}	811^{+58}_{-79}	1.06(117)	3.58E-25	1.61
294-B	0.96 ± 0.01	1859^{+62}_{-68}	2.08 ± 0.02	–	627^{+36}_{-41}	1.70(62)		
294-B	0.98 ± 0.01	1681^{+67}_{-60}	$2.08^{+0.04}_{-0.05}$	320^{+223}_{-98}	672^{+49}_{-48}	1.35(61)	8.33E-04	0.41
294-C	1.02 ± 0.01	1686^{+54}_{-67}	2.15 ± 0.01	–	522^{+174}_{-108}	1.96(62)		
294-C	1.02 ± 0.01	1676^{+61}_{-57}	$2.08^{+0.02}_{-0.04}$	439^{+418}_{-153}	538^{+35}_{-49}	1.81(61)	1.49E-02	0.29
295-A	1.09 ± 0.01	1709^{+60}_{-47}	2.02 ± 0.01	> 800	340^{+38}_{-37}	1.40(62)		0.15
295-B + 295_{sw}	1.15 ± 0.01	1454^{+63}_{-29}	$1.85^{+0.07}_{-0.05}$	> 261	103 ± 50	1.03(135)		0.05
295-B + 295_{sw}	1.15 ± 0.01	1464^{+37}_{-27}	$1.87^{+0.04}_{-0.05}$	–	110^{+91}_{-80}	1.02(136)		0.05
296 + 296_{sw}	1.25 ± 0.01	1252^{+20}_{-9}	2.10 ± 0.01	–	64^{+21}_{-25}	1.18(118)		0.12

Table 5.4: *PCA, SPI and HEXTE data fitted simultaneously using the XSPEC multicomponent model PHABS*(GAUSSIAN+DISKBB+POWERLAW). T_{in} is the inner disk temperature and N_{in} the normalisation. A Gaussian line was fixed at an energy of 6.4 keV with a width fixed at 0.1 keV for rev 289, 290. W_{Fe} is the equivalent width. The interstellar absorption PHABS was fixed to 0.7×10^{22} cm^{-2} until the dataset 294-A and to 0.5×10^{22} cm^{-2} from the revolution 294-B. Γ is the photon index. The POWERLAW component was replaced by a CUTOFFPL component and E_c is the high energy cutoff. The F-test is calculated between the POWERLAW and CUTOFFPL models. The ratio Φ_p/Φ_b is also given, where Φ_p and Φ_b are the power-law and the blackbody flux in the 2-20 keV energy range respectively. χ^2(dof) is the reduced χ^2 with the degree of freedom (dof).*

PCA, HEXTE and SPI data corresponding to the *INTEGRAL* revolution 292 in order to check the cross calibration between all instruments. The addition of BAT parameters decreases the reduced χ^2 value from 0.85 with 76 degrees of freedom (dof) (with no BAT data) down to 0.68 (223 dof) (with BAT data, see Table 5.5).

The normalisation factors of BAT with respect to SPI are 0.90 and 1.07 for dataset 292_{sw}-A and 292_{sw}-B respectively. During revolutions 289-292, the disc component was very weak. A decrease of E_c down to 87^{+4}_{-5} keV during revolution 293 as the source is into the HIMS[2] can be noticed. The disc component also got stronger, while the power-law index remained relatively constant. By fitting simultaneously BAT, PCA and HEXTE data for revolution 294 (datasets 294-A and 294_{sw}-B), when the source has entered the SIMS, the high-energy cutoff is detected as 156^{+9}_{-5} keV. The disk component also starts to dominate the energy spectrum as shown from the clear changes in the Φ_p/Φ_b ratio (Table 5.4) (where Φ_p is the power-law flux in the 2-20 keV energy range and Φ_b the blackbody flux). This ratio decreases by a factor 12.93 between revolution 293 and 294-B due to a large increase (by a factor 21) of the disk component Φ_b. The contribution of the hard component with respect to the disk component is lower than 50% during revolution 294-B. Moreover, the photon index becomes steeper with $\Gamma \simeq 2$, indicating a transition. From both the datasets 294-B and 294-C, for which only PCA and HEXTE data are available, there is no evidence of a high-energy cutoff up to 222 and 286 keV respectively. For the datasets 294-C and 295-A, the highly reduced χ^2 (1.81(61) and 1.40(62)) is due to poor modelling of the low energy part of the spectra. A complex spectral feature around 7 keV was fitted by Díaz Trigo *et al.*[108], using *XMM-Newton* and *INTEGRAL* data. The spectra corresponding to these fit parameters (Table 5.4) are shown in Figure 5.2 and 5.3.

Reflection model PEXRAV

All data were fitted with a reflection model, PEXRAV in XSPEC[109], consisting of a power-law with a high energy cutoff and reflection from neutral medium (see Table 5.5). During the LHS, as the luminosity in the 3-600 keV energy range increased by a factor $\simeq 2.8$ from revolution 289 up to revolution 292, the spectral index is constant ($\simeq$1.3-1.4). Similar values of the spectral index and of the high energy cutoff are found using the CUTOFFPL and the PEXRAV models: it is explained by the fact that the reflection fraction is not required. The range of values for the high energy cutoff (180- 380 keV) are consistent with the results of Shaposhnikov *et al.*[2] (196 $\pm$ 48 keV) for the revolution 289. An upper limit on the energy cutoff is determined when the source is into the HSS : $E_c > 457$ keV and $E_c > 2000$ keV for the dataset 295-B+295_{sw} and 296+296_{sw} respectively (see Table 5.5). During all observations (from the LHS to the HSS), the reflection component is not constrained and do not exceed 0.2, which is lower than the values found in Shaposhnikov *et al.*[2] ($\Omega \simeq 0.5$).

rev	Γ	E_c keV	T_{in} keV	N_{in}	W_{Fe} eV	χ^2(dof)	$L_{3-600}\times 10^{-9}$ ergs cm^{-2} s^{-1}
289	$1.36^{+0.04}_{-0.08}$	237^{+143}_{-55}	$1.38^{+0.12}_{-0.11}$	$1.07^{+0.48}_{-0.27}$	80^{+65}_{-78}	0.98(77)	2.9 ± 0.1
290	$1.33^{+0.01}_{-0.06}$	255^{+108}_{-35}	$1.44^{+0.05}_{-0.11}$	$1.07^{+0.26}_{-0.15}$	71^{+55}_{-61}	0.89(77)	3.5 ± 0.1
291	$1.37^{+0.10}_{-0.02}$	316^{+232}_{-23}	$1.36^{+0.17}_{-0.26}$	$2.36^{+3.81}_{-0.90}$	< 130	0.85(77)	$6.4^{+0.5}_{-0.6}$
292	$1.29^{+0.03}_{-0.02}$	185^{+30}_{-19}	$1.27^{+0.10}_{-0.08}$	$5.73^{+1.80}_{-1.43}$	< 173	0.93(77)	$8.1^{+0.4}_{-0.1}$
293_{sw} + 293a	$1.33^{+0.07}_{-0.02}$	171^{+59}_{-15}	1.07 ± 0.05	22^{+5}_{-4}	317^{+80}_{-50}	1.36(116)	$10.6^{+0.6}_{-0.3}$
293	1.37 ± 0.05	131^{+14}_{-8}	$1.04^{+0.06}_{-0.04}$	48^{+18}_{-16}	381^{+88}_{-82}	1.22(77)	$13.9^{+0.5}_{-0.1}$
294_{sw}-A + 294a,b	1.42 ± 0.05	88^{+14}_{-8}	$1.00^{+0.06}_{-0.04}$	121^{+18}_{-16}	645^{+59}_{-56}	1.39(16)	15.35 ± 0.1
294-A+294_{sw}-B	$2.05^{+0.07}_{-0.02}$	173^{+79}_{-23}	0.97 ± 0.01	1029^{+76}_{-82}	774 ± 150	1.03(116)	$18.4^{+0.1}_{-0.2}$
294-B	$2.07^{+0.06}_{-0.04}$	428^{+676}_{-142}	1.02 ± 0.01	1674^{+63}_{-55}	538^{+250}_{-50}	1.84(60)	$19.64^{+0.1}_{-0.2}$
295-A	$2.03^{+0.05}_{-0.01}$	> 700	1.09 ± 0.01	1709^{+55}_{-56}	> 156	1.45(60)	$23.39^{+0.25}_{-0.16}$
295-B+295_{sw}-B	$1.86^{+0.04}_{-0.12}$	> 457	1.15 ± 0.01	1457^{+64}_{-32}	110^{+60}_{-61}	1.03(134)	$22.19^{+0.32}_{-0.11}$
296 + 296_{sw}	$2.10^{+0.01}_{-0.02}$	> 2724	1.25 ± 0.01	1216 ± 20	< 138	1.08(116)	$30.60^{+9.82}_{-6.48}$

Table 5.5: *PCA, HEXTE and SPI data fitted simultaneously using the XSPEC multicomponent model PHABS*(PEXRAV+GAUSSIAN+DISKBB).* Γ *is the photon index and* E_c *the energy cutoff.* T_{in} *is the inner disk temperature and* N_{in} *the normalisation. The interstellar absorption PHABS was fixed to* 0.7×10^{22} cm^{-2} *until the dataset 294-A and to* 0.5×10^{22} cm^{-2} *from the revolution 294-B. The Gaussian line was fixed at an energy of 6.4 keV.* W_{Fe} *is the equivalent width. The reflection fraction* $\Omega/2\pi$ *was found with an upper value ranging 0.1-0.2.* L_{3-600} *is the luminosity of the source in the 3-600 keV energy range.* χ^2*(dof) is the reduced* χ^2 *with the degree of freedom (dof).*

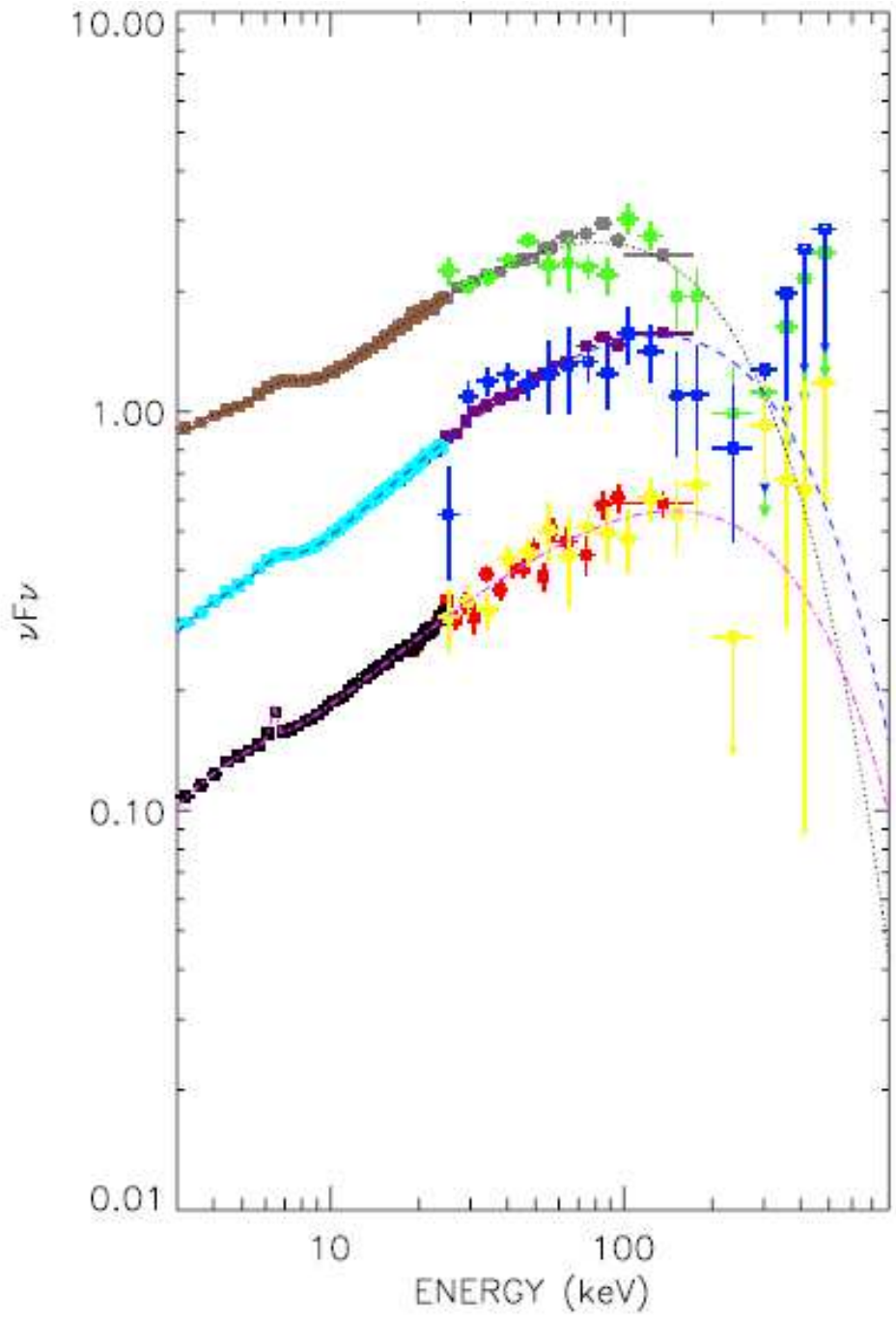

Figure 5.2: *Spectra of GRO J1655–40 from PCA, SPI and HEXTE data fitted simultaneously with the model described in Table 5.3. PCA data for revolutions 289 (black), 292(indigo), 293 (brown); HEXTE data for revolutions 289 (red), 292(violet), 293 (grey); SPI data for revolutions 289 (yellow), 292(blue), 293 (green).*

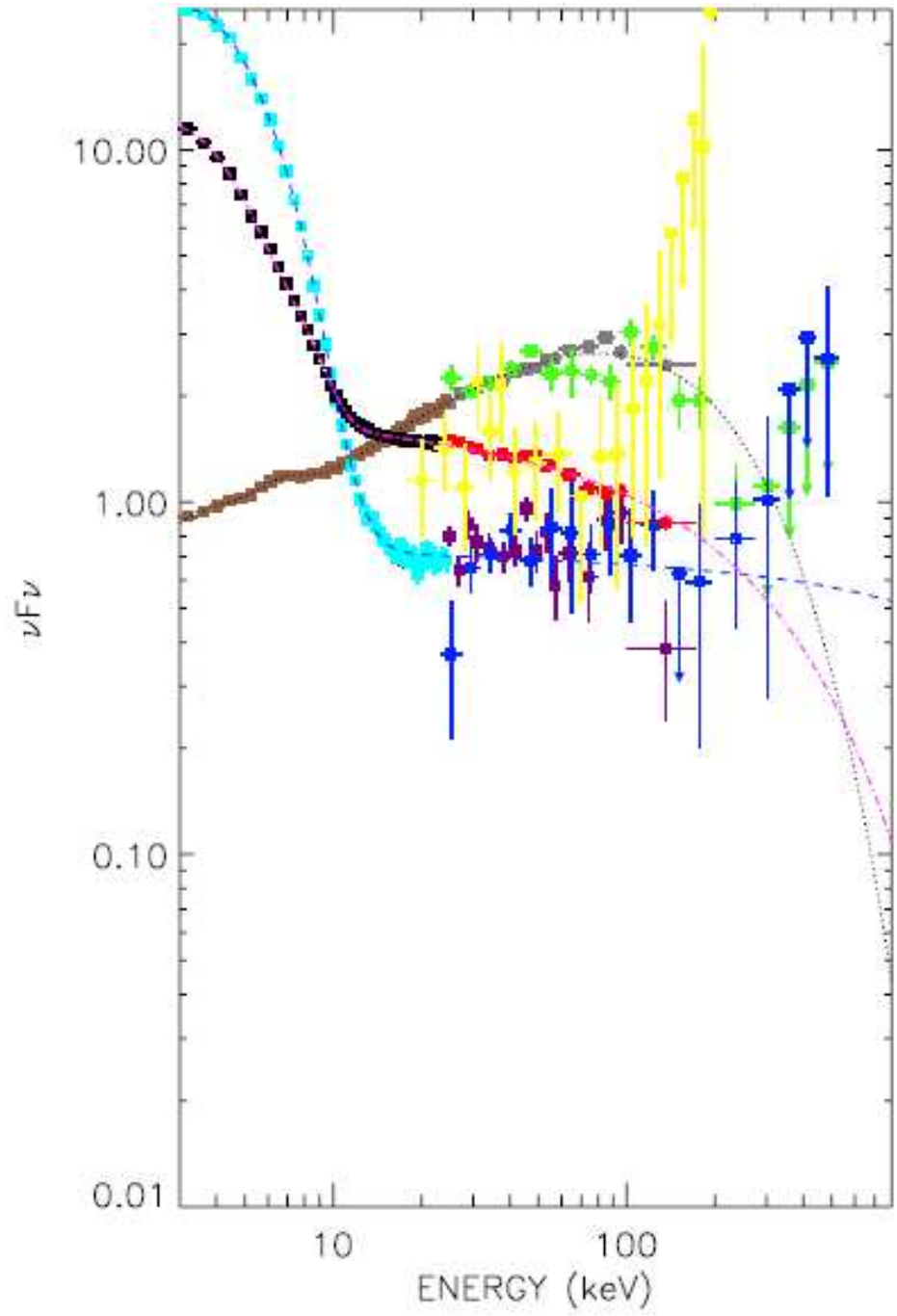

Figure 5.3: *Spectra of GRO J1655–40 from PCA, SPI and HEXTE data fitted simultaneously with the model described in Table 5.3. PCA data for revolutions 293 (brown), 294-A (black), 295-B (indigo); HEXTE data for revolutions 293 (gray), 294-A (red), 295-B (violet); SPI data for revolutions 293 (green), 295-B (blue) and BAT data for revolution 294sw-B (yellow).*

rev	kT keV	τ	T_{in} keV	N_{in}	χ^2(dof)	y
289	43^{+16}_{-8}	$1.78^{+0.26}_{-0.37}$	0.83 ± 0.04	12^{+3}_{-2}	1.04(79)	$1.07^{+0.40}_{-0.23}$
290	40^{+6}_{-4}	$1.92^{+0.13}_{-0.14}$	0.80 ± 0.03	16^{+3}_{-2}	0.93(78)	$1.15^{+0.17}_{-0.12}$
291	36^{+12}_{-6}	$2.07^{+0.15}_{-0.17}$	$0.78^{+0.07}_{-0.06}$	34^{+10}_{-21}	0.84(77)	$1.21^{+0.40}_{-0.21}$
292	35 ± 2	$2.09^{+0.10}_{-0.07}$	$0.80^{+0.02}_{-0.04}$	44^{+10}_{-4}	1.36(77)	1.20 ± 0.07
293_{sw} + 293a	31^{+2}_{-1}	2.15 ± 0.1	0.77 ± 0.02	106^{+16}_{-13}	1.63(117)	$1.12^{+0.07}_{-0.08}$
293	31 ± 2	2.01 ± 0.09	$0.74^{+0.10}_{-0.12}$	244^{+338}_{-93}	1.31(77)	0.98 ± 0.06
294_{sw}-A + 294a,b	26 ± 2	1.93 ± 0.09	$0.76^{+0.10}_{-0.12}$	457^{+338}_{-93}	2.06(117)	0.76 ± 0.06
294-A + 294sw-B	37 ± 1	$0.85^{+0.27}_{-0.65}$	$0.85^{+0.01}_{-0.02}$	2419^{+147}_{-96}	1.22(117)	0.25 ± 0.01
294-B	244^{+58}_{-84}	$0.03^{+0.07}_{-0.02}$	$0.95^{+0.05}_{-0.01}$	2064^{+94}_{-59}	1.45(61)	$0.06^{+0.04}_{-0.01}$
294-B (*)	43^{+45}_{-11}	$0.83^{+0.47}_{-0.40}$	1.02 ± 0.03	1140^{+263}_{-192}	0.83(89)	$0.27^{+0.28}_{-0.07}$
294-C	320^{+54}_{-92}	$0.02^{+0.02}_{-0.01}$	1.00 ± 0.01	1967^{+75}_{-58}	1.91(61)	$0.05^{+0.01}_{-0.03}$
294-C (*)	86^{+61}_{-38}	$0.43^{+0.51}_{-0.23}$	1.06 ± 0.03	1192^{+197}_{-172}	1.26(59)	< 0.20
295-B+295_{sw}-B	763^{+161}_{-610}	< 0.07	1.24 ± 0.01	1267^{+52}_{-37}	1.02(135)	< 0.06
296+296_{sw}	490^{+121}_{-67}	0.01 ± 0.01	1.24 ± 0.01	1239^{+28}_{-16}	1.20(117)	< 0.06

Table 5.6: *PCA, HEXTE and SPI data fitted simultaneously using the XSPEC multicomponent model PHABS*(COMPTT+GAUSSIAN+DISKBB). The interstellar absorption PHABS was fixed to 0.7 × 10^{22} cm^2 until the dataset 294-A and to 0.5 × 10^{22} cm^2 from the revolution 294-B. T_{in} is the inner disk temperature, N_{in} the normalisation, τ the optical depth and kT the plasma temperature. The Compton parameter y (see the definition in the text) was determined. (*) For the dataset 294-B and 294-C a power-law component* Γ *of* $3.77^{+0.33}_{-0.39}$ *and* $3.95^{+0.40}_{-0.35}$ *was added respectively.* χ^2*(dof) is the reduced* χ^2 *with the degree of freedom (dof).*

Comptonization model COMPTT

The hard power-law plus cutoff spectrum of the LHS is usually interpreted as thermal Comptonization in a hot ($KT_e \sim 100$ keV) optically thin plasma (the corona). A COMPTT model (in XSPEC)[110] was used in order to describe this high energy process. The temperature of the disk (T_{in}) in the multicolour disk blackbody model is forced to be equal to the soft photon temperature (T_0) of the Comptonization model. Table 5.6 shows that the optical depth is $\simeq$ 1.8 – 2.0 while the temperature decreases from $\sim$ 40 down to $\sim$ 30 keV from the LHS to the HIMS.

By freezing the temperature to 37 keV, which is the value obtained by Shaposhnikov *et al.*[2] for the dataset corresponding to the *INTEGRAL* revolution 289, an optical depth of $1.98^{+0.05}_{-0.05}$ is determined which is lower by a factor 2.2 compared to the value found in this reference. Moreover, the inner disk

temperature is higher : $T_{in} = 0.83$ keV instead of 0.60 keV[2]. This could be explained by the fact that the continuum above 100 keV constrained with the *INTEGRAL* data is different in this reference. Regardless of the fit models, the spectral evolution can be described in terms of an evolution of the geometry based on the Compton parameter $y = 4kT/m_e c^2 max(\tau, \tau^2)$ (where the electronic temperature kT and the optical depth τ are derived from a Comptonization model, Sunyaev & Titarchuk[111]). During the LHS, the Compton parameter is constant (y $\simeq$ 0.6) to within the errors bars. It starts to decrease and to strongly vary from the HIMS (revolution 293) and is correlated with the increase of the normalization of the disk component. It decreases (see value in Table 5.6) by a factor 4.3 between revolution 289 and revolution 294-A when the source is into the SIMS. The LHS to the Intermediate state (both HIMS and SIMS) transition corresponds to a gradual decrease of the inner radius of the cold accretion disk, associated with either the cold disk penetrating the hot inner flow, or the latter collapsing into an optically thick accretion disk with small active regions of hot plasma on top of it[112]. The enhanced soft photon flux from the disk tends to cool down the hot phase, leading to softer spectra. This can be directly observed from the evolution of the blackbody component with respect to the power-law component (see the Φ_p/Φ_b ratio given in Table 5.4).

High energy cutoff

For PEXRAV and CUTOFF models, the data from datasets 294-B and 294-C indicate that either the high energy cutoff increases significantly, or the cutoff vanishes completely. Such evolution was observed for GX339-4 in the HIMS[113], and now appeared in the SIMS in the case of GRO J1655–40. An attempt to describe this high energy feature was tried by adding a power-law component to the Comptonization model COMPTT. The addition of a power-law component leads to an improvement of the fit significant at the 99.9998% level for both datasets according to a F-test, with a best fit photons index of $3.77^{+0.33}_{-0.39}$ and $3.95^{+0.40}_{-0.35}$ respectively. The power-law component contributes at 25% and 20% of the 2-20 keV flux for the revolution 294-B and 294-C respectively. The extension of a power-law at high energy has already been observed in the Steep Power-Law State of GRO J1655–40 during its 1996 outburst (see Remillard & McClintock[114]). It was interpreted by the scattering occurring in a non-thermal corona, which may be a simple slab operating on seed photons from the underlying disk[115]. The origin of the Comptonizing electrons is still a subject of debate. Poutanen & Fabian[116] suggest that are regions erupting from magnetic instabilities in the accretion disk could as a possible geometry to explained such a Comptonizing media. The association of non-thermal process with state transition has already been observed[117] : indeed a power-law tail can be interpreted as the Comptonization of soft photons by accelerated electrons. The bulk-motion Comptonization model which is applied in the case when the bulk and thermal electron is included[118], produces a power-law that extends

to very high energies. Such a high energy emission could also come from an optically thick electron-positron outflow covering the whole inner region of the accretion disk[119]. The non-thermal spectrum, which was modelled with the addition of a power-law component, increases in flux as well as the equivalent width (or the flux) of the iron line. This correlation is also mentioned in Shaposhnikov *et al.*[2]. In the HSS, this non-thermal component is negligible and contributes to $< 0.2\%$. As seen from the Figure 5.4, there is a correlation between the radio intensity and the exponential energy cutoff.

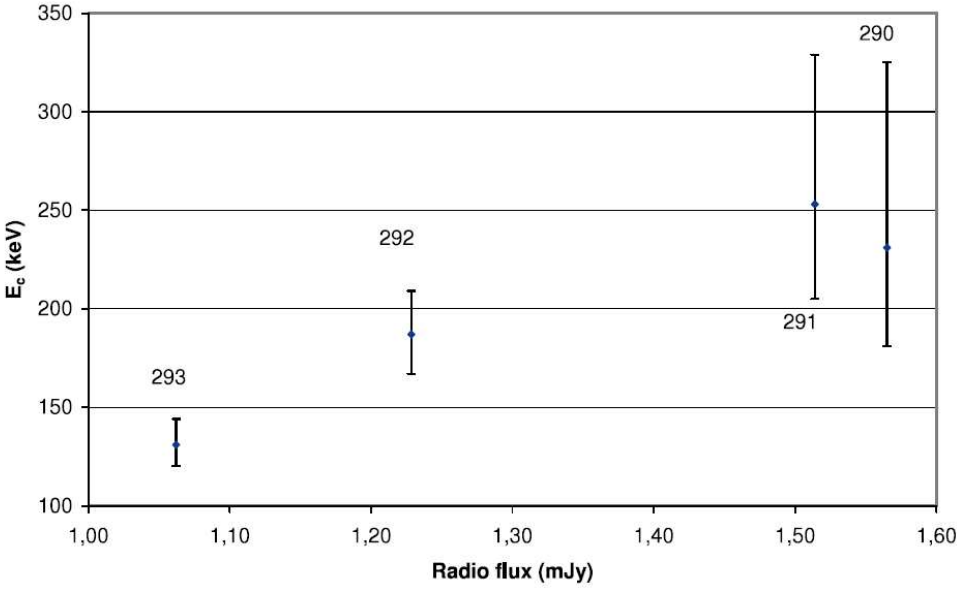

Figure 5.4: *Evolution of the high energy cutoff (E_c expressed in keV) derived from the model given in Table 5.3, as a function of the radio flux measured by VLA at 8.460 GHz*[2]*. The* INTEGRAL*revolution numbers are mentioned on the graph.*

The maximum of flux in radio is achieved when the source is in the LHS. When the source entered into the HIMS, the high energy cutoff decreases (or the plasma cools down) as well as the radio flux. Quenching of the jet in the soft states of black hole binaries is known for many sources[120,41]. Moreover, a hard spectral component with any curvature up to MeV has already been detected for the Black Hole Candidate Cygnus X-1 into its HSS[121,122,123]. A lower limit on the break energy of 690 keV was determined from OSSE (on board the *CGRO* mission) observations[121] of GRO J1655–40 during the HSS of its 1995 outburst. Here a clear evolutionary path to this quenching is shown in terms of plasma temperature, perhaps associated with the cooling and shrinking of the corona. The jet ejections usually occur at or near state transition prior to the source entering the IS[57]. A radio flare ejection, observed during the revolution 291, is accompanied by the maximum of luminosity in X and gamma-ray domain few days later (during revolution 293, see Figure 5.1 and

the details about the high energy evolution in different energy bands in Table 5.4). Such a behaviour was observed for the Black Hole Candidate H1743-322 [101] and could be linked to the corona ejection. The decrease of the Compton parameter which is linked to the decrease of the optical depth (see Table 5.6) correlated with the increase of the non thermal component (addition of the power-law component) could argue such changes in the corona geometry. Such small ejection events, related to relativistic plasma events, has also been observed during state transitions of GX339-4 [41,120]. Moreover, the small reflection fraction whereas there is a high coronal temperature (or high energy cutoff) can be explained by the model of Beloborodov [124] which argues that the corona above the accretion disk is fed by magnetic flares or by a corona with non-static or outflowing coronae [125]. GRO J1655–40 started to enter the IS from the end of the revolution 292. This state corresponds to the decay of the radio emission (Figure 5.4) which is usually dominated by the decaying optically thin synchrotron emission from the jet ejections. During this state, such an emission is decoupled from the black hole system as the emitting electrons are far from it. The radio emission is completely quenched from the SIMS (revolution 294-A).

In conclusion, a transition from the LHS to the HSS was clearly observed during the rising phase of the 2005 outburst of GRO J1655–40 between MJD 53425 and MJD 53445. The outburst was covered with SPI, HEXTE, PCA and BAT, that allowed the determination of the high energy cutoff with a high precision. During revolution 294, only data from the *Swift*/BAT and the *RXTE* observatory were available to constrain the high energy cutoff during an intermediate state. An evolution of the high energy feature was noticed during the LHS : it decreased from a value above 200 keV down to 130 keV when the source reached the maximum of luminosity in the gamma-ray domain (above 23-600 keV). During the HSS, an upper limit on the high energy cutoff was determined. However, based on the decreasing trend of the cutoff energy, and also decreasing hardness of the spectrum, it is more natural to interpret the non-detection as disappearance of the cutoff, rather than a much higher cutoff energy than the detectors could detect. This decrease corresponds to a decrease in the radio flux, and the cutoff disappeared along with the radio jet.

Finally, the relation between state transition and the emission of jet in X-ray binaries discussed above is a subject of large investigation in order to have a complete view of the X-ray geometry. It would be interesting to perform a broadband spectral fitting (from radio up to MeV) in order to discriminate the different non-thermal processes suggested in these study.

Chapter 6

IGR J08408-4503: a new recurrent supergiant fast X-ray transient

Little is known about such new class of sources: one of the most intriguing aspects is the nature of the short outbursts. Only in the case of IGR J11215-5952 the regularly recurrent outbursts were most likely linked to its orbital period. In all other SFXTs sporadic and unpredictable short outbursts were discovered after long quiescent periods. in't Zand[63] suggested a clumpy wind from the donor star captured by the compact object as a possible origin of such outbursts. In order to increase the number of detections of such outbursts, it is crucial both to check a possible periodicity and to better characterize their nature. Thanks to its very large FOV, wide temporal coverage and pointing strategy, BAT is a suitable instrument to catch and study such events. In this chapter a beautiful example of its capabilities applied to the case of IGR J08408-4503 is shown. IGR J08408-4503 is a new source recently discovered by *INTEGRAL* on May 15, 2006 thanks to a short flare. In this chapter the nature of this source is unveiled as a new SFXT, thanks to the detection of a flare on July 1, 2003 obtained by retrospectively searching in the *INTEGRAL* data archive, and to the detection of a flare on October 4, 2006 by *Swift*. It is worth noting that the latter flare was missed by *INTEGRAL* because it was pointing elsewhere, so the *Swift* detection was crucial to increase the number of detected events. The spectral analysis of the BAT data of this flare was performed using Pipeline 1, which made possible to obtain a good spectral characterisation of such an event. From all the flares, a spin period of the order of hours with a long orbital period, and a 10^{13} G magnetic field were inferred for the NS. Moreover, a low intrinsic absorption was measured during the flares. This is not consistent with the picture of the flares caused by clumps in the donor wind. Probably the flares can be associated with the sudden accretion onto the magnetic poles of matter previously stored in the magnetosphere during

the quiescent phase.

6.1 IGR J08408-4503

The number of known SFXTs has grown recently thanks to *INTEGRAL*, see e.g. IGR J16465-4507, IGR J17544-2619, or IGR J11215-5952[126,127,66]. The new SFXT presented in this section, IGR J08408–4503, was discovered in the Vela region on May 15, 2006 with *INTEGRAL* during a bright outburst lasting about 15 minutes[128]. The candidate optical counterpart was first tentatively identified as the supergiant, Ob5Ib(f), HD 74194 star[128,129] located at 3 kpc in the Vela region[130,131,132]. Successively, using the *Swift* X-ray Telescope (XRT) a refined source position ($\alpha_{J2000} = 08^{\rm h}49^{\rm m}47^{\rm s}.97$ and $\delta_{J2000} = -45°03'29''.8$ with an uncertainty of $5''.4$) was derived, strengthening the association with HD 74194[133].

Optical spectra of HD 74194 measured a few days after the outburst[134] strongly resemble the ones of the companion star of another SFXT, IGR J17544–2619[135]. In addition the radial velocity variations in the HeI and HeII absorption lines with an amplitude of about 35 km s^{-1} were measured, suggesting either a pulsating variable nature of the supergiant star HD 74194 or a possible Doppler orbital modulation[136]. IGR J08408–4503 shows the typical SFXT recurrent short flaring events. Using *INTEGRAL* archival data, an outburst was detected on July 1, 2003[137], while the last bright flare was observed on October 4, 2006 with the *Swift* satellite[138].

In this section the light curve and broad-band spectral study of all the three outbursts of IGR J08408–4503 observed up to now is presented. In addition, thanks to the knowledge of the companion star parameters, the possible wind accretion conditions are discussed[139].

6.2 Data Analysis

IGR J08408–4503 was observed twice in outburst with *INTEGRAL*[47], on July 1, 2003 and May 15, 2006, i.e. during the satellite orbits 83 and 438. This dataset includes publicly available data and part of AO3 Vela region guest observations. Hereafter the two datasets will be called flare 1 and flare 2, respectively. Data from the coded mask imaging telescope IBIS/ISGRI[48,140] at energies between 15 keV and 200 keV and from the JEM-X monitor[141] between 3 and 20 keV were used. For JEM-X the data were extracted only for flare 2, flare 1 being outside the JEM-X FOV. The data reduction was performed using the standard Offline Science Analysis (OSA) version 5.1.

Single pointings ($\sim$ 2000 s each) were deconvolved and analyzed separately. The IBIS/ISGRI 15–40 keV high energy light curve, shown in Fig. 6.1, was extracted from the images using all available pointings. Light curves with a 100 s time bin were also extracted around the outburst peaks.

The third outburst, flare 3, was observed on October 4, 2006 (14:45:42 UT) with *Swift*/BAT. Since the flare was detected with an image trigger (15–150 keV), only "Survey" data products were available from the BAT instrument. To process the data, Pipeline 1 was used, setting up a "lyne-by-line" analysis. For each DPH row the target count rate in the 14–40 keV energy range was evaluated using the XRT coordinates. The BAT data were selected 15 h before and 30 h after the trigger, and reduced using the standard software version 2.5.

Swift slewed automatically to the direction of the source and XRT[79] (0.1–10 keV) follow-up observations were performed. The XRT data were reduced using FTOOLS version 6.1.1., and processed with XRTPIPELINE version 0.10.4, using standard filtering selections. The XRT 0.1–10 keV energy band light curves were extracted by selecting a circular region of 20 pixels around the source for the Photon Counting (PC) mode, and rectangular region of 40×20 pixels for the Window Timing (WT) mode. Background light curves were extracted in source free regions in order to produce the final background-subtracted XRT/PC/WT light curves. The count rate of the source in both modes is low enough in order to avoid the pile-up in the CCD.

6.3 Results

6.3.1 Flare light curves

In Fig. 6.1 the three outburst light curves of IGR J08408–4503 observed up to now are shown. The light curves are dominated by a first bright flare that typically reaches a peak luminosity of $3-6\times10^{36}$ erg s^{-1} (see Sec. 6.3.2) in a time scale of several tens of minutes to hours. The observed flares vary from an isolated strong flare (flare 2) to a more structured flaring activity (flare 1 and 3). Moreover flare 3 shows also weaker flares with a luminosity of the order of 5×10^{35} erg s^{-1}. The three outburst durations are of the order of several hours. The flare characteristics are similar to those observed in other SFXTs, such as XTE J1739-302[62], IGR J16465-4507[142], IGR J17544-2691[63], and IGR J11215-5952[66], but resemble also those well studied in persistent wind accretion high mass X-ray binary (HMXB) sources like Vela X-1[143], 4U 1700-377[144].

Up to now only IGR J11215-5952 has shown a $\sim$ 330 days periodic outburst. Therefore, using a linear orbital function $T(n) = T_0 + nP_{\rm orb}$ an attempt to test the hypothesis of a periodically recurrent outburst also for IGR J08408–4503 was tried. $P_{\rm orb}$ is the orbital period in days and T_0 is taken from flare 2 (MJD 53780.771215). A possible orbital period is 4.2988 days (with $n_1 = 244$ and $n_2 = 33$), however, searching in the *INTEGRAL* archival data around the expected outburst time, it was not found any significant flux excess at the IGR J08408–4503 source position. One can conclude that the three observed outbursts are sporadic episodes of accretion of matter fed from the wind of the supergiant companion star.

In order to directly compare the light curves measured with different in-

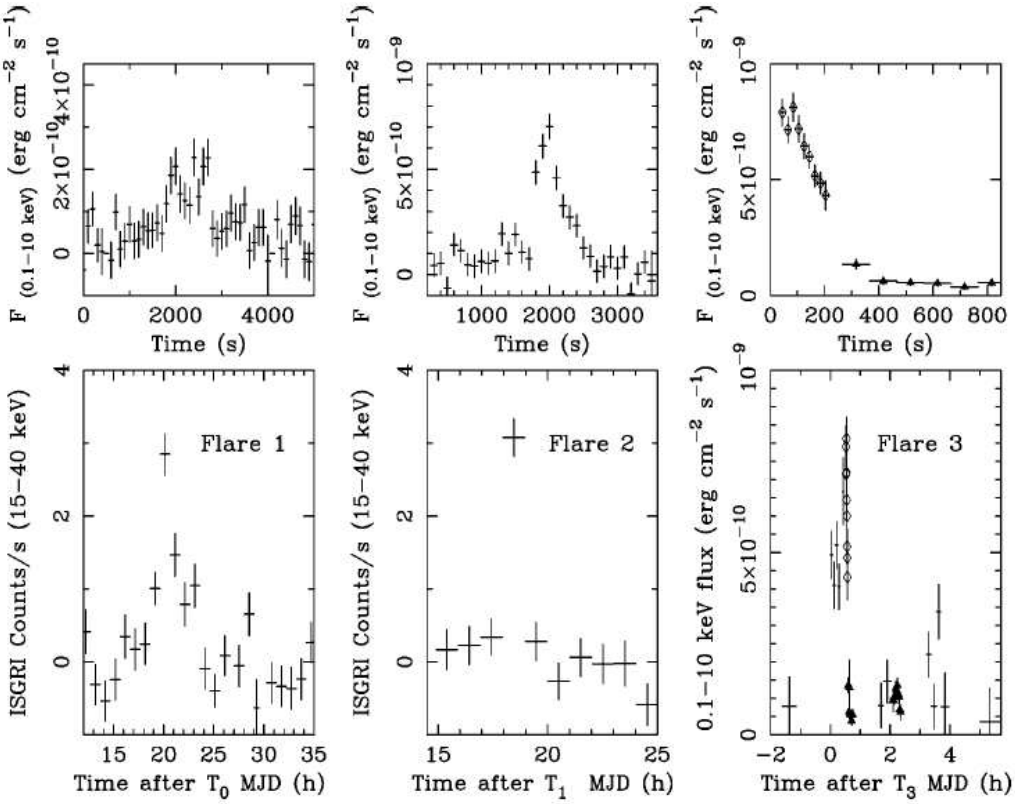

Figure 6.1: Bottom, from left: *IBIS/ISGRI (flare 1,2) and Swift (flare 3) light curves. IBIS data are binned at* ~ 2 *ks. In the last panel the crosses represent the extrapolated BAT flux, while the diamonds and triangles the XRT/WT and PC data. The time axis is expressed in hours after* T_0*=52821.0,* T_1*=53870.0, and* T_3*=54012.615 MJD, respectively. The Swift light curve shows also weak flares e.g. at t*$\sim$*3.5 h IGR J08408–4503 is detected in BAT at* $\sim 7\ \sigma$ *level.* Top: *the brightest part of each outburst is shown on a smaller time scale (100 s time bin for ISGRI).*

struments (see Fig. 6.1), all the count rates were converted to the 0.1–10 keV fluxes assuming the spectral shape derived in Sec. 6.3.2.

6.3.2 Flare spectra

The spectral analysis was performed using XSPEC version 11.3, for the ISGRI data (20–200 keV), flare 1, for the 3.5–20 keV JEM-X data with the simultaneous 20–200 keV ISGRI data, flare 2, and for the 0.3–100 keV simultaneous XRT/BAT data, flare 3. Only the brightest parts of the flares were considered. For the simultaneous data a constant factor was included in the fit to take into account the uncertainty in the cross-calibration of the instruments. All data were rebinned in order to have 3σ points and the spectral uncertainties in the results are given at a 90% confidence level for a single parameter. The source distance was assumed to be of 3 kpc.

The XRT/BAT (flare 3) broad-band (0.3–100 keV) dataset provides the widest energy coverage and the best statistics. Such data were fitted using a simple photoelectrically-absorbed power-law (PL) model which was found inadequate with a χ^2/d.o.f. $= 132.76/76$. The addition of a high-energy exponential cut-off significantly improved the fit to χ^2/d.o.f.=80.36/75, resulting in a best-fit photon index of 0.1±0.2 and a cut-off energy at 15±5 keV. The hydrogen column density, $N_{\rm H}$, was found to be $1.0 \pm 0.3 \times 10^{21}$ cm^{-2}. This value is compatible with Galactic value in the direction of the source, $N_{\rm H} = 3 \times 10^{21}$ cm^{-2}, reported in the radio maps of Dickey & Lockman[145]. An attempt to fit the low energy spectrum also with a thermal black-body model, BB, plus a PL for the high energies was tried, but a high BB temperature was found, $kT_{\rm BB} \sim 8$ keV, which is much larger than the measured values for a neutron star (NS) surface or polar cap thermal emission. Also a fit with a thermal bremsstrahlung model can be statistically ruled out by the data (χ^2/d.o.f.=183.2/76). The energy spectra during the flaring activity were hence best fitted with a high-energy exponential cut-off PL model similar to the spectra observed from persistent wind accreting HMXB hosting a NS, e.g. Vela X-1[143].

The joint JEM-X/ISGRI (3.5–200 keV), flare 2, spectrum was also fitted with the cut-off PL model used for flare 3. The best fit values are similar to the ones of flare 3, see Table 6.1. Given that it was not possible to constrain the $N_{\rm H}$ value (as the JEM-X bandpass starts above 3 keV) it was fixed to the value found from flare 3.

For flare 1 only ISGRI data (20–200 keV) were available. The data can be well fitted with a simple PL model with a photon index, Γ, of 2.5±0.5. Note that fitting flare 2 (ISGRI) and 3 (BAT) spectra in the same energy range gives consistent photon index values, namely Γ=2.8±0.3 and Γ=2.3±0.4, respectively. The apparently soft spectra derived using only the data above 20 keV show how important it is, to have a broad energy coverage in order to better characterize the spectrum of these sources. To be coherent, the same spectral model derived from the broad-band fit of flare 2 and 3 was also applied to flare 1, even if a smaller energy range was available. The slope of the power

law index was fixed to the values found (see Table 6.1) and the cut-off energy was found compatible with that found for flares 2 and 3.

In Fig. 6.1, last panel, weak flares are visible after the main peak. To infer the flux at very low mass accretion rate, a XRT/PC spectrum in the 0.1–6 keV energy band at ∼2.2 hr after the main flare was extracted (see Fig. 6.1). This is the last time interval where the source is clearly detected in the XRT images. This weak flare can be called flare 4. Using the same model found for flare 3, the source was at a bolometric luminosity of 5×10^{35} erg s^{-1}, with a marginal indication of an increase of the absorption column density.

The best fit parameters for the different flares are reported in Table 6.1. In Fig. 6.2, the broad-band unfolded spectrum and the residuals of the data to the PL with a high energy cut-off model for flare 3 are shown.

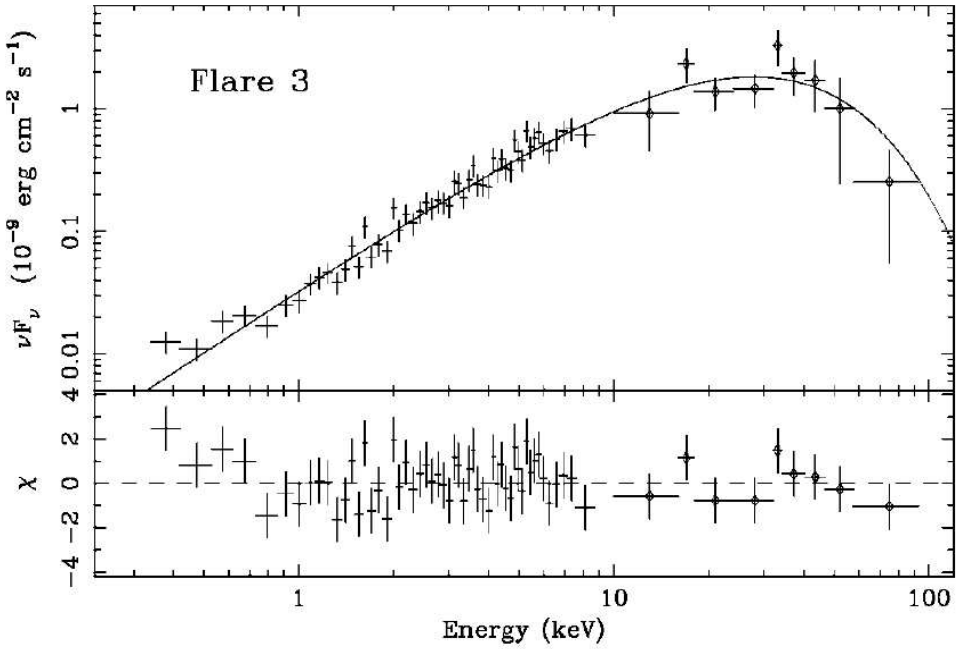

Figure 6.2: *Combined XRT (crosses) and BAT (diamonds) spectra of flare 3. The best fit* PL *high energy cut-off model and the residuals (lower panel) are shown.*

6.4 A SFXT with very low intrinsic absorption

IGR J08408–4503 is a recurrent SFXT with most likely sporadic episodes of accretion of matter from the wind of the Ob5Ib(f), HD 74194, supergiant companion star. The broad-band spectrum (0.3–200 keV) allowed an improved spectral analysis of the new source IGR J08408–4503 to be performed using XRT/BAT and JEM-X/ISGRI data. The best fit to the data required a PL with a high energy cut-off, see Table 6.1. The spectrum is typical for HMXBs

Table 6.1. IGR J08408–4503 spectral parameters using a power-law model with an exponential high energy cut-off

Dataset	Flare 1 ISGRI	Flare 2 JEM-X/ISGRI	Flare 3 XRT/BAT	Flare 4 XRT/BAT
N_H [a]	···	0.1 (f)	0.1±0.03	<0.75
Γ	0.0 (f)	0.0±0.5	0.1±0.2	0.1±0.4
E_c (keV)	12.7±2.8	11.8±2.8	15±5	15 (f)
χ^2/d.o.f	14.06/12	57.09/90	80.36/75	11.72/10
Flux$^b_{bol}$	7.0×10^{-10}	2.7×10^{-9}	6.0×10^{-9}	5.0×10^{-10}

[a]in units of 10^{22} cm^{-2}.

[b]Unabsorbed 0.1–100 keV flux in units of erg cm^{-2} s^{-1}.

hosting a NS[143] where the emergent radiation is presumably produced by accretion columns at the magnetic poles of the NS. The bolometric flare peak luminosity is of the order of $3-6\times10^{36}$ erg s^{-1}, which are typical values for wind accreting HMXBs. At low mass accretion rates, the source is observed at a bolometric luminosity of 5×10^{35} erg s^{-1}. The source quiescent luminosity is of the order of $\sim 2\times10^{32}$ erg s^{-1} [133].

During the outbursts the derived absorption of $\sim 1\times10^{21}$ cm^{-2} is compatible with the total Galactic absorption in that direction as estimated from the HI maps, indicating that the source is not surrounded by large amounts of material. Some information about the distribution of matter around an X-ray binary can be inferred from observations of the variations with orbital phase of its spectrum caused by absorption along the line of sight to the X-ray star. For IGR J08408–4503, the orbital period is not known, therefore using a simply spherically symmetric stellar wind model, the wind density[146] at the NS surface ($a >> R_*$, a is the binary separation) for a circular orbit can be approximated by:

$$N_{\rm H} \approx 1\times10^{21}\times \left(\frac{\dot{M}_w}{10^{-7}M_\odot{\rm yr}^{-1}}\right)\left(\frac{R_*}{14.5R_\odot}\right)^{-1}\left(\frac{\nu_\infty}{2000\,{\rm km\ s}^{-1}}\right)^{-1}{\rm cm}^{-2}, \quad (6.1)$$

where $\dot{M}_w$ is the HD 74194 mass loss rate and ν_∞ is the terminal wind velocity. The stellar parameters adopted for HD 74194 are reported in Table 6.2. The estimated $N_{\rm H}$ is compatible with the derived absorption from the spectral fit. On the other hand, locating the companion star at $a = 2R_*$, and using a maximal wind acceleration parameter $\beta = 1$, $N_{\rm H}$ will change by a factor $\ln(R_*) \approx 27$, i.e. $N_{\rm H} \approx 2.7\times10^{22}$ cm^{-2}. The observed $N_{\rm H}$ hints towards

Table 6.2. Stellar parameters for HD 74194 derived from[6]

Parameter	Value
$T_{\rm eff}$ (k)	33000
R_* ($R_\odot$)	14.5
M_* ($M_\odot$)	28
$\log(L_*/L_\odot)$	5.3
$\dot{M}_w$[a]($M_\odot$ yr^{-1})	2.3×10^{-7}
ν_∞ (km s^{-1})	2000±300
$\nu_{\rm esc}$ (km s^{-1})	776

[a]Calculated using Eq. 6.2.

a large binary separation and therefore a large orbital period. The measured absorption is in variance with what was observed for other SFXT[126].

The companion mass loss rate, $\dot{M}_w$, was calculated for HD 74194 using the average relation for the galactic O or B supergiants stars[147],

$$\log(\dot{M}_w) = -1.37 + 2.07\log(L_*/10^6) - \log(\nu_\infty R_*^{0.5}). \quad (6.2)$$

The $\dot{M}_w$ value is a factor 10–100 lower that what found for the persistent wind accretion HMXB, like Vela X-1 or 4U 1700-37. The free parameter to obtain a higher $N_{\rm H}$ value for IGR J08408–4503 is to have a higher mass loss rates, $\dot{M}_w$. Using Eqs. (6.2) and (6.2) it can be seen that if the terminal wind velocity is a factor 5 lower (as observed for an intrinsically obscured high energy source IGR J16318-4848[148]), one would have a higher absorption of $\sim 10^{23}$ cm^{-2}, but such a low wind velocity is not observed for HD 74194. This indicates that during the accretion of matter for IGR J08408–4503 there is no accretion wake of dense matter surrounding the compact object[149]. It was assumed that all the material within the capture radius

$$\begin{aligned} R_{\rm acc} &= \frac{2GM_{\rm x}}{\nu_{\rm x}^2+\nu_\infty^2} \quad (6.3)\\ &\approx 9.2\times10^8\left(\frac{\dot{M}_{acc}}{\dot{M}_w}\right)^{1/2}\left(\frac{M_*+M_x}{28M_\odot}\right)^{1/3}P_{\rm orb}^{1/3}\ {\rm cm} \end{aligned}$$

was accreted by the compact object[150]. $M_{\rm x}$ is the mass of the NS, $\nu_{\rm x}$ its orbital velocity, and $\dot{M}_{acc} = L_x c^{-2}\eta^{-1}$ the mass accretion rate, where $\eta \sim 0.2$ is the accretion efficiency for a NS. The rate of mass captured is then given by $\dot{M}_{\rm acc} = \dot{M}_w R_{\rm acc}^2/(4a^2)$, with $R_{\rm acc} = 9.3\times10^9$ cm. It was considered that $\nu_\infty >> \nu_{\rm x}$ and $a >> R_*$. From the measured persistent emission $L_x \sim 2\times10^{32}$ erg s^{-1}, it can be derived from Eq. (6.4) an orbital period of ∼1.5 years.

The condition for accretion to take place is that the NS magnetosphere radius is within the mass capture radius and the corotation radius, i.e. $R_{Mag} \leq R_{\rm acc}$ and $R_{Mag} \leq R_{\rm cor}$ [29]. By setting $R_{\rm acc} = R_{\rm cor}$ it can be obtained $P_{\rm spin} = 2.36 \times 10^{27}(1.4M_x)\nu_{\infty}^{-3} \simeq 7000$ s. The magnetosphere radius is given by

$$R_{Mag} = 0.1\mu^{1/3}\dot{M}_w^{1/6}\nu_{\infty}^{-1/6}M_*^{1/9}P_{\rm orb}^{2/9}, \tag{6.4}$$

where $\mu = BR_{\rm NS}^3$. Setting the accretion condition $R_{Mag} = R_{\rm cor} = R_{\rm acc}$ the magnetic field has to be $B \sim 1.1 \times 10^{13}(P_{\rm orb}/1{\rm yr})^{-2/3}$ G, for $R_{\rm NS} = 10^6$ cm. Assuming the orbital period derived above, the NS magnetic field has to be of the order of 10^{13} G. These are typical magnetic field values for young HMXBs hosting a NS, like e.g. Vela X-1 [151].

The low $N_{\rm H}$ value measured during the flares is not consistent with the picture in which they are caused by clumps in the donor wind. In an alternative scenario, the flares could be associated with the sudden accretion onto the magnetic poles of matter previously stored in the magnetosphere during the quiescent phase. However, in order to have such a mass storage, the above simplest accretion conditions have to be studied for different scenarios (e.g. $R_{\rm acc} > R_{\rm cor} > R_{\rm mag}$). One can derive these conditions by varying opportunely $P_{\rm orb}$, $P_{\rm spin}$, and B [152].

In conclusion, these recurrent sporadic very short outburst episodes, due to the accretion of matter from the wind of a supergiant companion star, imply a spin period of the order of hours with a long orbital period, and a 10^{13} G magnetic field for the NS. The determination of all the system parameters can help to solve the accretion mechanism.

Chapter 7

4U 1954+319: a new symbiotic low mass X-ray binary system

4U 1954+319 is a flaring X-ray binary hosting a NS discovered by *ARIEL* in 1981. Its nature became clearer after the recent identification[153] of its companion as an M-type giant star, suggesting the source to be the third low mass X-ray binary (LMXB) hosting a NS and a late type giant companion (symbiotic X-ray binary), after GX 1+4 and possibly 4U 1700+24. A periodic signal was recently reported from 4U 1954+319, with a quasi-monotonically decreasing period of $\sim$ 5.09 hours[154]. If such period could be associated to the NS spin period, then 4U 1954+319 would be the slowest established wind-accreting X-ray pulsar. In this chapter the identification of such periodicity with the orbit of the binary system is excluded and the nature of the source unveiled as a new symbiotic low mass X-ray binary system.

The BAT capabilities and the good performance of Pipeline 1 for this kind of research still played a fundamental role. Due to the huge amount of survey data collected in more than $\sim$1 year, a search for a periodicity as well as for a relevant period evolution from 4U 1954+319 was possible. A period of $\sim$5.17 hr and a clear spin-up trend with spin-up time scale ($P/\dot{P}$) of $\sim$ 25 years were found. Using the standard accretion torque models, a value of $B \sim 10^{12}$ G for the magnetic field was derived from the period, its derivative, and the luminosity of the source. Furthermore, it was possible to identify 4U 1954+319 as a wind accreting X-ray pulsar with the longest known spin period. This very long period can be explained in terms of the standard binary pulsar evolutionary picture, considering that a NS with a magnetic field of a few 10^{12} G can reach periods of the order of a few hours on a timescale of $\sim$ 10^8-10^9 yr, which is the age of the old companion star of 4U 1954+319 .

7.1 4U 1954+319

Since its discovery by the *ARIEL* satellite in 1981, 4U 1954+319 has appeared as a flaring X-ray source[155]. Located in the Cygnus region, this source was observed by different X-ray telescopes[156,157,158,159,160]. From the observed spectral behaviour, the source was tentatively classified as a high-mass X-ray binary system hosting a neutron star (NS). However, little was known about the system, as the optical counterpart was not identified due to the ambiguous determination of the source position. The companion star was then classified as a close M-type giant or a distant and reddened Be star[157,159].

Recently, using the *Chandra* refined source position, Masetti *et al.*[153] used optical spectroscopy to identify its companion as an M4-5 III star, which is located within 1.7 kpc. Such identification suggests the system is composed of a compact object accreting through the wind of its M-type giant companion star. This makes 4U 1954+319 the third low mass X-ray binary (LMXB) hosting a NS and a late type giant companion, after GX 1+4[161] and possibly 4U 1700+24 [162], for which, however, no coherent pulsation has been reported to date[163]. Therefore 4U 1954+319 could be attributed to the so-called "symbiotic X-ray binaries", an emerging subclass of LMXBs. These systems with an evolved giant donor are the probable progenitors of most wide-orbit LMXBs[161].

Only recently has a periodic signal been reported from this source, whit a period of $\sim$ 5.09 hours quasi-monotonically decreasing[154]. If this period can be attributed to the spin, 4U 1954+319 would be the slowest binary NS known, with the possible exception of the enigmatic source 1E 161348-5055 in the Supernova remnant RCW 103[164]. In this section several high-energy observations are used to unveil the nature of 4U 1954+319 through spectroscopic and timing analysis[165].

7.2 Observations and data analysis

The *INTEGRAL* data set was obtained using the 2003/2005 publicly available observations within $< 12^\circ$ from the source direction. 613 pointings from the IBIS/ISGRI coded mask telescope[48,140] at energies between 18 and 200 keV were analysed, for a total exposure time of 1.4 Ms. The data reduction was performed using the standard Offline Science Analysis (OSA) version 5.1. It was extracted the 20–60 keV band light curve based on the single pointings. During the *INTEGRAL* observation, 4U 1954+319 was mainly in a quiescent phase (52717–53144 MJD), and in the last part of the observation, it entered a strong outburst phase (53312–53708 MJD) with an increase in count rate of a factor 40. During the outburst phase, 4U 1954+319 is clearly detected in the mosaic image with a significance level of $\sim 45\sigma$. During the quiescent phase, 4U 1954+319 was not detected at a statistically significant level in the ISGRI data. Therefore these data were excluded from the timing and spectral analyses.

The publicly available data from the Narrow Field Instruments (NFIs) on board *Beppo*SAX were also included in the spectral analysis. The source 4U 1954+319 was observed on May 4, 1998 for a net exposure of 19 ks in the LECS[166] and for 46 ks in the MECS[167]. The average spectrum of the source was extracted from a region of 6′ in both instruments. The spectra were then rebinned in order to have at least 30 counts per channel and three channels per resolution element. Note that *Beppo*SAX observations were too short to enable the timing analysis.

The *Swift*/BAT survey data collected between December 2004 and April 2006 were also analysed. The analysis was performed using Pipeline 1. The HEASoft software (release v.6.0.5) was adopted. For each DPH row, an image in the 15–50 keV energy range was extracted and the source count rate at the *Chandra* position evaluated. Thus, a barycentered light curve containing ~ 23000 data points was obtained using the *barycorr* tool.

In Fig. 7.1 the *RXTE*/ASM light curve of 4U 1954+319 is shown, where the time interval in which the *INTEGRAL*, *Swift*, and *Beppo*SAX observations were performed are reported.

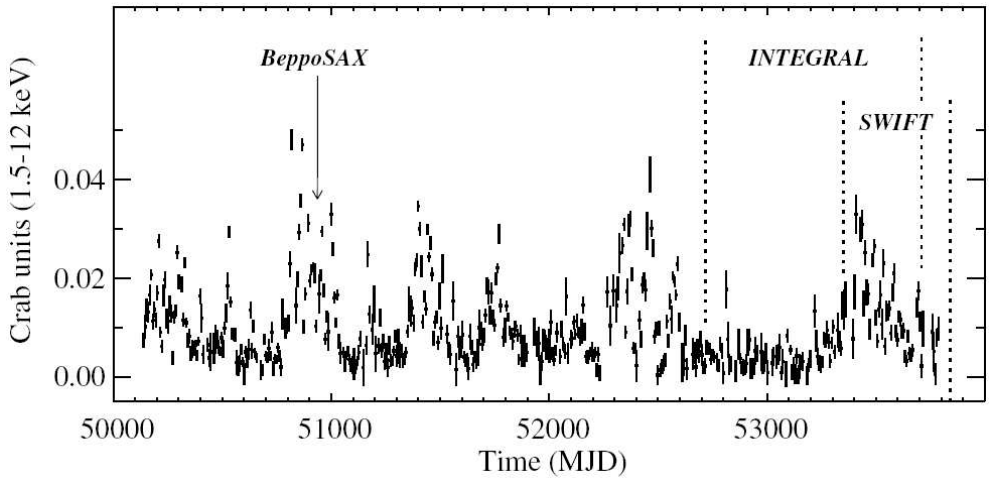

Figure 7.1: *The 4U 1954+319* RXTE*/ASM light curve in the 1.5–12 keV energy band (data-averaged over a 7-day interval). The ASM count rate were converted to flux using 1 Crab* ≈ 75 *cts/s*[168].

7.2.1 Spectral analysis

For the spectral analysis, ISGRI (18-150 keV), LECS (0.7–4.5 keV), and MECS (1.7–10 keV) data were used. The non-imaging *Beppo*SAX spectrometer PDS data (15–300 keV) could not be used due to the contamination of Cyg X–1. The analysis was done using XSPEC version 11.3[105]. All spectral uncertainties in the results are given at a 90% confidence level for single parameters.

A hardness-intensity diagram was first computed using the *RXTE*/ASM data. The hardness is the ratio of the count rates in the 1.5–5 keV to those in the 5–12 keV energy band, and the intensity is the 1.5–12 keV count rate. Each point corresponds to $\sim$ 7 days of integration time. The source shows a significant linear correlation (slope ≈ 1) between flux and hardness. Therefore ISGRI data were searched for spectral changes, dividing the observation in four different intensity levels. Each subset was fitted with a simple power-law (PL) model, but it turned out to be statistically inadequate (χ^2/d.o.f = 43/12). The best fit was found by replacing the PL with a cutoff PL model thereby obtaining a χ^2/d.o.f = 10/11. The spectral parameters for the four data sets were found to be the same within the error bars, most likely due to the low statistics during the flare, so it was not observed the same hardness-intensity correlation as observed below 12 keV with the ASM data. The best-fit values for the average ISGRI spectrum are found for a PL photon index, Γ, of 0.7 ± 0.1 and a high-energy cutoff $E_c \sim 14^{+9}_{-3}$ keV.

Then the *Beppo*SAX spectrum was fitted using a simple photoelectrically-absorbed PL model plus a black body (BB) model for the soft excess below 3 keV, as often observed in accreting pulsars[169] and a Gaussian emission line, resulting in a χ^2/d.o.f. = 132/71. The best fit was found for a heavily absorbed spectrum with $N_{\rm H} = 2.8 \pm 0.2 \times 10^{23}$ cm^{-2}, a BB temperature of kT=0.11$\pm$0.01 keV to model the soft X-ray excess, a PL index of $\Gamma = 1.5 \pm 0.5$, $E_c \sim 17 \pm 12$ keV, and an iron emission line at $\sim$6.33$\pm$0.15 keV (with the line width fixed at 0.5 keV). The quite high reduced χ^2 indicates that the soft excess is not perfectly modeled by the BB component. The hydrogen column density, $N_{\rm H}$, is found to be 30 times higher than the Galactic value reported in the radio maps of Dickey & Lockman[145].

The cutoff value is not well-constrained using the NFIs or ISGRI alone. This is due to the fact that it falls outside of the energy ranges of the individual instruments. In order to better constrain the broad-band (0.6–200 keV) spectral characteristics a joint-fit of the NFI and the ISGRI data was performed. A multiplicative factor for each instrument was included in the fit to account for the uncertainty in the cross-calibration of the instruments, as well as variability across the non-simultaneous observations. The best-fit parameters are Γ=1.1$\pm$0.1, E_c=17$\pm$2 keV, kT=0.123$\pm$0.004 keV, and a similar value of N_H, with a χ^2/d.o.f. of 138/83. The broad-band spectrum, together with the best-fit model, are shown in Fig. 7.2.

7.2.2 Timing analysis

For the timing analysis, the BAT (15–50 keV) and ISGRI (18–50 keV) light curves after solar-system barycentric correction were used.

The BAT data were searched for coherent pulsations of the source by computing a power density spectrum (PDS) in the frequency range between 2×10^{-8} and 10^{-4} Hz from fast Fourier transforms. In the resulting PDS, a signal is evident at $\nu = 5.45 \times 10^{-5}$ Hz. The peak is broad with an FWHM of 6.7×10^{-7}

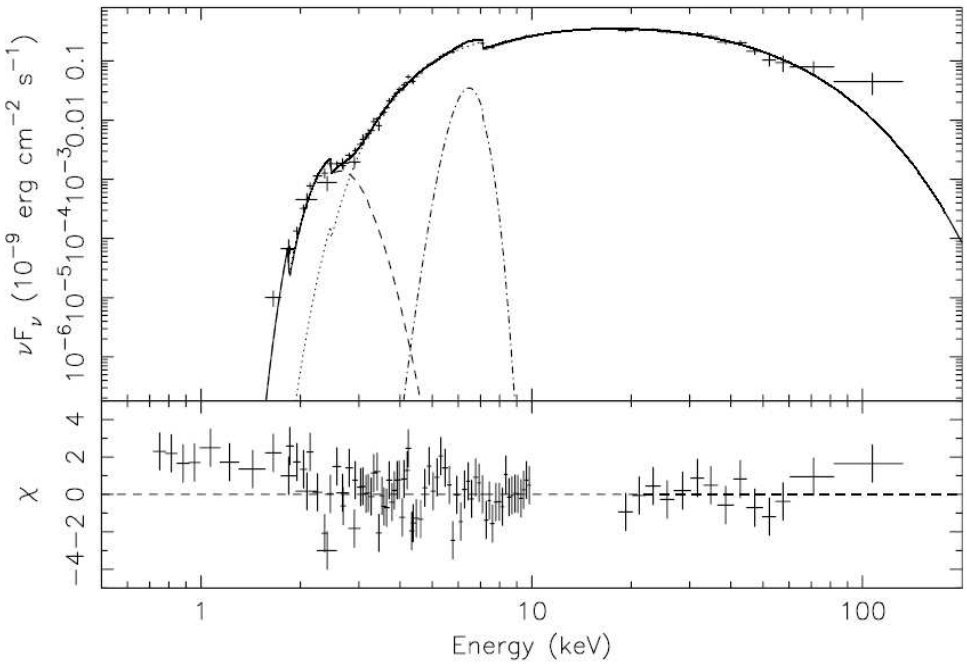

Figure 7.2: *Broad-band spectrum of 4U 1954+319, fitted with an absorbed* BB *Gaussian line, and cutoff* PL*. The data points correspond to the LECS/MECS (0.7–10 keV) and ISGRI (18–150 keV) spectra. The lower panel shows the residuals with respect to the best-fit model.*

Hz, suggesting a period evolution. Therefore the light curves were grouped into 100 cycles per time interval, and the best period was determined using an epoch-folding analysis. The distribution of the χ^2 values versus trial period were fitted as described in Leahy[170]. The resulting 14 best-fit period values clearly show a spin-up trend, see Fig. 7.3.

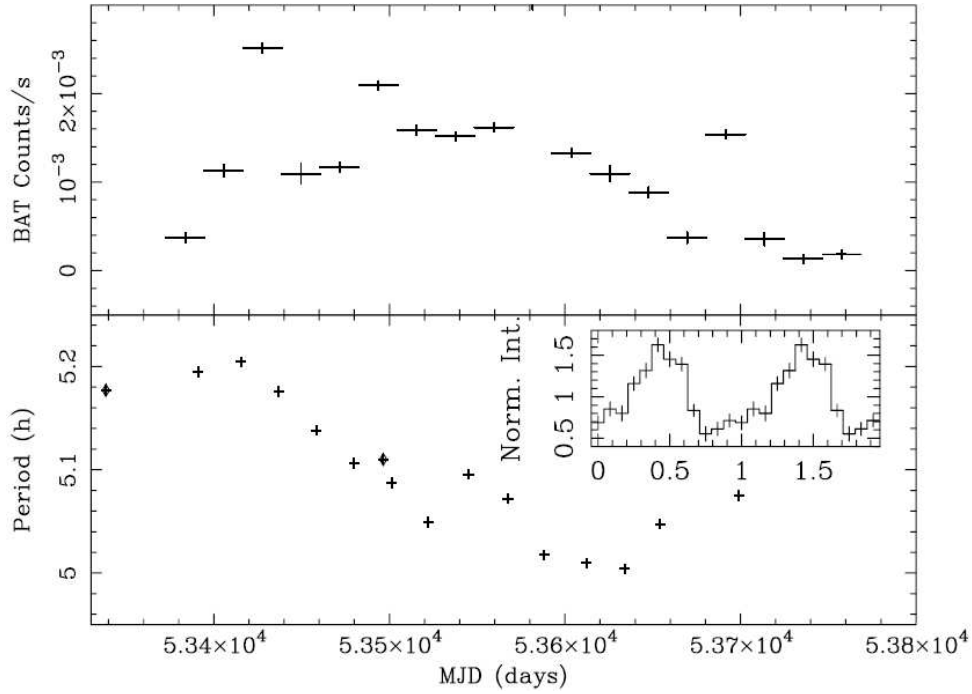

Figure 7.3: *Upper panel: BAT light curve (15–50 keV) of 4U 1954+319. The time bin size is 22 days. Lower panel: period evolution as measured with BAT (crosses) and ISGRI (diamonds). The inset represents the normalized BAT phase folded light curve between 53400 and 53500 MJD considering P and $\dot{P}$. Two cycles are shown for clarity.*

Using the ISGRI light curves, the presence of a period at ∼5.17 hr is confirmed. An attempt to search for a period change in the ISGRI data was tried; but, due to the sparse coverage using the 100 cycle time intervals, only 2 significant measurements were derived (see Fig. 7.3), which are consistent with the previous findings.

Fitting the period evolution with a linear function, the derived spin-up trend is around -3×10^{-5} s s^{-1}, which implies a spin-up time scale ($P/\dot{P}$) of $\sim$ 25 years. However, note that some scattering around this trend is present, indicating a possible local spin-down. On the other hand, a much better fit was obtained using a sinusoidal function, indicating a possible orbital period of 385±4 days and a projected semimajor axis, $a_x \sin i$, of 178±4 AU. However, since this periodicity is of the order of the time interval spanned by the data, it is difficult to identify it with a possible orbital period (see below).

7.3 The Neutron Star with the slowest spin period

The timing and broad-band spectrum of 4U 1954+319 allowed the nature of this system to be investigated for the first time. Only recently it was tentatively attributed to the emerging NS "symbiotic LMXB" class.

The ∼5 hr measured periodicity could be due either to the system orbital modulation or to the rotation of the compact object. It can be ruled out that what was measured is the system orbital period. In fact, given the typical luminosity and temperature of an M 4-5 III star[171], the stellar evolutionary models with solar metallicities[172] predict a mass of ∼1.2 $M_\odot$ for the companion. Assuming a mass within 3 $M_\odot$ for the compact object, the orbital separation would be much smaller than the donor star radius (∼80 $R_\odot$). Thus, the hypothesis of measuring the spin period of the NS hosted in the system is considered[154].

Furthermore, the observed spin-up could be attributed to the accretion torque on the magnetized NS. While suggestive of a sinusoidal trend (see Fig. 7.3 and Sect. 7.2.2), the time evolution of the period cannot be accounted for by the Doppler shift of the system's orbital motion: in this case the derived orbital parameters would imply a companion star mass of a few 10^6 $M_\odot$. Thus we can consider ∼ 400 days a lower limit to the orbital period of the system. This implies a wide orbit ($a > 2\times10^{13}$ cm) and explains the fact that the optical spectrum reported by[153] shows no signs of the influence of the X-ray source.

It was found a broad-band spectrum typical of accreting X-ray pulsars[173] and, in particular, similar to that of GX 1+4[174], and 4U 1700+24[175]. The high column density found of the order of 3×10^{23} cm^{-2} could be attributed to the local (circumstellar) absorption. In fact, this value is typical of the local environment of symbiotic stars as indicated by observations of Rayleigh scattering in their UV spectra[176]. The measured luminosity of $\sim 2 \times 10^{35}$ erg s^{-1}, assuming a 1.7 kpc source distance, points towards a wind-fed accretion system with the companion not filling its Roche lobe. Taking the period, its derivative, and the luminosity into account, one can use the standard accretion torque models[22] to derive an order-of-magnitude value for the dipolar magnetic field of the NS. It turns out to be $B \sim 10^{12}$ G, which implies a magnetospheric radius $r_m = 3 \times 10^8$ cm $(L_X/10^{37}$ erg s$^{-1})^{-2/7}(B/10^{12}$ G$)^{4/7} \sim 10^9$ cm, smaller than the corotation radius ($r_{co} = (GM_X P_{spin}^2/4\pi^2)^{1/3} \sim 1.2 \times 10^{11}$ cm, where M_X∼1.4 $M_\odot$ is the mass of the NS), allowing the accretion process. We are hence dealing with a regular wind accreting X-ray pulsar but with the longest known spin period.

The very long period measured in 4U 1954+319 can be explained by taking into account the age of the companion star[172] and the standard binary pulsar evolutionary picture[177]. In fact, a newborn NS experiences a spin-down initially due to the magnetic dipole braking (radio phase). In this case this phase lasts ∼8×10^9 yr, namely the time the donor spends on the main sequence.

Since the orbit is quite wide, the NS can spin down practically as if it was isolated. When the donor star leaves the main sequence, starting to evolve rapidly into a red giant, the star mass loss increases and there is coupling between the infalling matter stopped by the magnetosphere and the magnetosphere itself[29]. By means of these processes during its whole lifetime, a NS with a magnetic field of a few 10^{12} G can reach periods of the order of 10^4 s in $\sim 8.5 \times 10^9$ yr.

The distance where the ram pressure of the accretion flow balances the magnetic pressure is called the Alfvén radius. A further increase in the accretion rate, as the donor becomes a red giant, allows the corotation radius to overcome the Alfvén radius and the NS to start accreting, becoming observable in X-rays and spinning-up. The emerging picture is an old, hence slow, NS accreting from the slow and dense wind of an evolved M type giant on a wide orbit. The inhomogeneities of the wind can explain the observed long-term X-ray variability (see Fig. 7.1). The wide orbit also allowed the companion star not to be affected by the Supernova explosion that generated the NS thereby enabling the donor star to follow its natural evolutionary track.

In conclusion, in the framework of standard binary pulsar evolutionary models, the value found for the magnetic field, coupled to the age of the companion star, can justify the very long observed NS period without invoking any additional spin-down process. It turns out that 4U 1954+319 is the slowest accretion powered NS, and it is hosted in a "symbiotic LMXB" system. These are rare systems that could eventually evolve into wide-orbit binary systems hosting an NS and a white dwarf, but without mass transfer so hence very difficult to observe.

Chapter 8

Search for prompt gamma-ray emission from novae

In this chapter a search for prompt gamma-ray emission from novae is presented. Novae are members of the so-called Cataclysmic Variables (CVs) which are systems containing an accreting WD in a binary system. In the general scenario, the material ejected by the companion star accretes onto the WD until it reaches hydrogen ignition conditions and an explosion occurs. Gamma-rays are expected to be emitted during and immediately following a nova explosion due to the annihilation of positrons emitted by freshly produced short-lived radioactive isotopes. The expected gamma-ray emission is relatively short-lived and, as nova explosions are unpredictable, the best chance of detecting the gamma-rays is with a wide field instrument. At the time when the flux is expected to reach its peak, most of the gamma-ray production is at depths such that the photons suffer several Compton scatterings before escaping, degrading their energy down to the hard X-ray band (tens of keV).

The detection of such gamma-rays was hardly searched in the past with many instruments. None of these searches has led to a convincing detection but none was sufficiently sensitive and complete in coverage that this is surprising. Due to its wide coverage and to its good sensitivity in the 14-190 keV energy range, BAT is a very well suited instrument to the search for such gamma-rays. A retrospective search was made in the BAT data for evidence for gamma-ray emission from the direction of 18 novae at around the time of their explosion. Recent estimations of the gamma-ray flux expected from these sources point to low values, thus, in order to be sure of the detection of the source, it was crucial to clean up light curves from a possible contamination coming from the bright sources in the FOV. To this aim, Pipeline 2 (see section 3.2) was used.

This search led to a positive detection in the 14-25 keV band of the RS Ophiuchi 2006 outburst. Such emission cannot be due to downgraded radioactive decay gamma-rays. It is probably due to the shock between the material ejected from the nova and the dense stellar wind of the red giant companion star. No positive detections were found for all the other novae, so only upper

limits were evaluated. Finally, the probability of detecting a nova during the *Swift* operating lifetime was estimated using a Monte Carlo approach. Three different models of the spatial distribution in the Galaxy of the simulated novae were assumed. Moreover, typical gamma-ray fluxes from novae based on the more recent estimations of nuclear reaction rates were used. It was found that the chances of detecting gamma-rays from novae are low but not null if *Swift* will be operating for 10 years as predicted. Novae located at less than $\sim$2-3 kpc have best probabilities to be detected, although detection of novae at distances up to $\sim$5 kpc is not completely excluded.

8.1 General characteristics of novae

Historically, novae (from latin *novae stella:new stars*) were stars visible to the naked eye, appearing in a position of the sky in which prior no stars were known to exist and lasting some days before vanishing. The first known records of such events go back to c. 1500 BC and were kept by the Chinese for astrological purposes. The knowledge of such objects has greatly improved during the last 200 years thanks to the progress made in astronomical instrumentation at different wavelengths. However, a multi-wavelength study of a nova depends on its discovery which typically still occurs at optical wavelengths. Thus, the steadily increasing activities of amateurs astronomers have been crucial in enhancing the rate of discoveries. Many novae have been discovered showing different temporal and spectral behaviour. All such objects are grouped in the so-called cataclysmic variables class (CVs), sharing the common property of being interacting binary stars containing a white dwarf (WD) accreting from an orbiting companion. Matter accumulates on top of the WD until it reaches critical conditions and consequently erupts. In some CVs subclasses, the eruption causes the ejection of a fraction of the accreted mass and the emission of light at different wavelengths. After that, the nova returns in its normal state until the accreted material on top of the WD is enough to enable a further eruption.

8.1.1 Classification

According to the general classification given by Warner[178], CVs can be summarised as follows:

- *Classical novae*: novae having only one observed eruption. These can be satisfactorily modelled as thermonuclear runaways (TNR) of the hydrogen-rich material that accretes on to the surface of the WD (see section 8.1.3). The range from pre-nova brightness to maximum brightness is from 6 to 19 magnitudes and is strongly correlated with the rate at which the nova fades after maximum.

- *Dwarf novae*: these have outbursts of typically 2-5 mag, with some rare exception with up to 8 mag range. The interval between outbursts is from ∼10 d to tens of years with a well-defined time scale for each object. The duration of normal outbursts is from 2-20 d, correlated with interval between outbursts. Dwarf nova outbursts are reasonably well understood as a release of gravitational energy caused by a temporary large increase in rate of mass transfer through the disc. When gas in the accretion disc reaches a critical temperature, the disc becomes unstable and a change in viscosity occurs, resulting in a collapse onto the WD that releases large amounts of gravitational potential energy.

- *Recurrent novae*: these are previously recognized classical novae that are found to repeat their eruption on a time scale of a few tens of years. The distinction between recurrent and dwarf novae is made spectroscopically: in recurrent novae (as in CN) a substantial shell is ejected at high velocities, whereas in DN no shell is lost.

- *Nova-like variables*: these include all the CVs believed to be in the pre-nova or post-nova phase, for all of which our observational baseline (typically ∼1 century) is too short to reveal their cataclysms. Most nova-like variables have emission-line spectra, but a subgroup show in addition broad absorption lines.

- *Magnetic CVs*: these are usually included among the nova-like variables (except for the few that are already recognized as classical novae or other defined types). The magnetic fields of the WDs can disrupt the accretion disc, either partially or totally.

In this chapter classical and recurrent novae subclasses are considered (hereafter the generic term "nova" will be used to refer to such objects). Probably all classical novae are recurrent novae of long recurrence time T_R. There are no definite recurrences of classical novae from ancient records, suggesting $T_R >$ 1000 y in general. Following a nova eruption, a recurrence would be expected after a time

$$T_R = M_{env}(crit) / < \dot{M}_{WD} > \tag{8.1}$$

where $M_{env}(crit)$ is the mass of the envelope accumulated on top of the WD needed to ignite the TNR and $< \dot{M}_{WD} >$ is a long term average of the mass transfer from the companion star to the WD. From equation 8.1 the short recurrence times for recurrent novae require either or both small envelope masses and high $\dot{M}_{WD}$. Using the dependence of $M_{env}(crit)$ on M_{WD} and $\dot{M}_{WD}$ found by Fujimoto[179] (see Figure 8.1) and equation 8.1, Livio & Truran[180] deduced that $M_{WD} \geq 1.3 M_{\odot}$ and $\dot{M}_{WD} \geq 1 \times 10^{-8} M_{\odot} y^{-1}$, for $T_R < 100y$. Recurrent novae therefore represent that fraction of CVs in which accretion is occurring at a high rate onto a primary close to the Chandrasekhar mass.

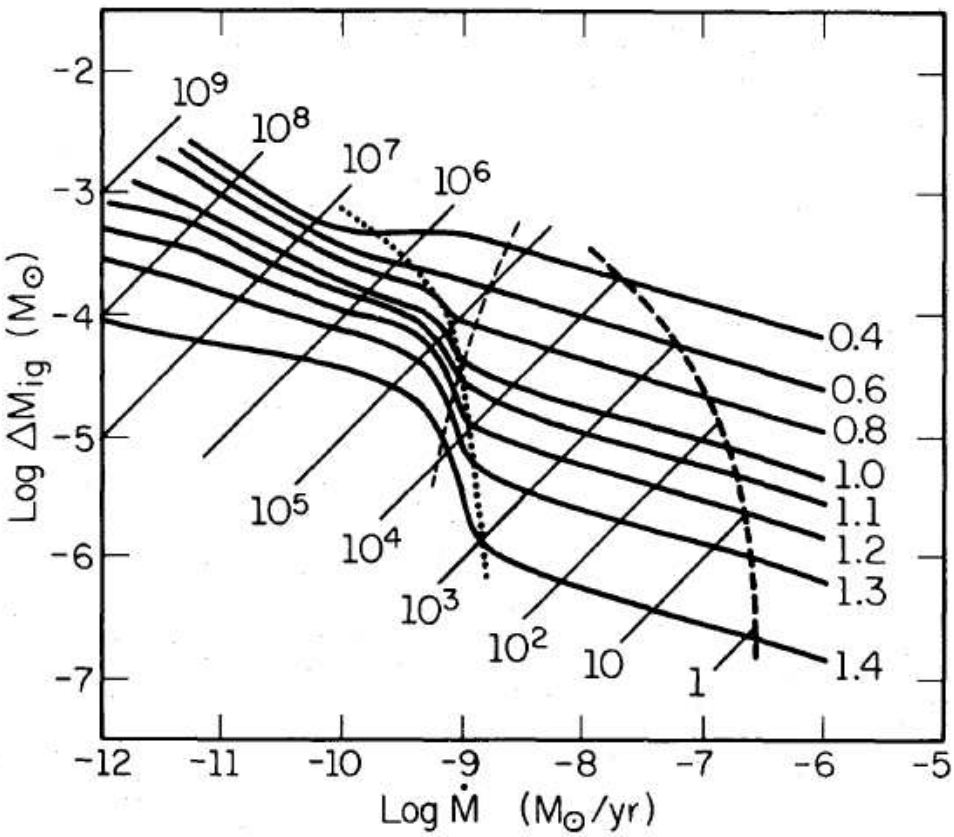

Figure 8.1: *Maximum accretable mass* $M_{env}(crit)(\equiv \Delta M_{ig})$ *as a function of* $< \dot{M}_{WD} >$ *and* M_{WD}*. Thick solid lines give the relationship and are labelled with* M_{WD} *expressed in solar masses. The heavy dashed line is the upper limit on* $< \dot{M}_{WD} >$ *above which stable H-burning occurs. The light dashed line shows where p-p and CNO reactions contribute equally to energy production. Thin solid lines are labelled with* $T_R(y)$ *from equation 8.1. From Fujimoto*[179]

8.1.2 Observational properties of novae

All novae show similar characteristics which allow certain very useful relations to be obtained. Typically a nova reaches a maximum luminosity which corresponds to a decrease of the apparent visual magnitude (m_V) of more than 9 magnitudes occurring in a few days. Then the light curve shows a decay on a timescale which is different for different nova.

It is useful to define the time t_2 (or t_3) as the time needed to decay by 2 (or 3) visual magnitudes after maximum. Using these parameters it is possible to classify the novae according to outburst speed. Table 8.1[7] shows the different classes in which a nova can fall.

Speed class	t_2 (days)
Very fast	$\leq$10
Fast	11-25
Moderately fast	26-80
Slow	81-150
Very slow	151-250

Table 8.1: *The different classes of novae as shown in Table 2 of Darnley* et al.[7]

It is found that the brighter novae have shorter decay times. Livio[181] has shown that the maximum luminosity can be roughly expressed as a function of the WD mass:

$$(L_{max}/L_{\odot}) \simeq (M_{WD}/0.6M_{\odot})^3(L_{Edd}/L_{\odot}) \tag{8.2}$$

where L_{Edd} is the Eddington luminosity. The maximum luminosity of a nova is close to the Eddington luminosity, according to observations, and nearly all the nova envelope is ejected in a time similar to t_3. Livio[181] also found the relationship

$$t_3 = 51.3 \left(\frac{M_{WD}}{M_C}\right)^{-1} \left[\left(\frac{M_{WD}}{M_C}\right)^{-2/3} - \left(\frac{M_{WD}}{M_C}\right)^{2/3}\right]^{3/2} days. \tag{8.3}$$

where M_C is the Chandrasekhar mass. By combining equations 8.2 and 8.3 it is possible to deduce an expression relating the absolute magnitude at maximum and t_3 which is called the maximum magnitude-rate of decline (MMRD). There are many calibrations of the MMRD relationship, but the most used is that of Della Valle & Livio[182] that contains a t_2(days) dependence:

$$M_v = -7.92 - 0.81 arctan\left(\frac{1.32 - log(t_2)}{0.23}\right). \tag{8.4}$$

The reason for the use of t_2 is that, for extragalactic novae, it is very often the only rate of decline which can be measured because measurements more than 2m dimmer than the peak are too difficult. Equation 8.4 can be used to estimate distances to novae, given measurements of apparent magnitude, and of t_2 and an estimate of visual extinction. This last is due to the presence of dust and gas between the source and the observer which causes the absorption and scattering of light emitted by the source. The preferential scattering of short wavelengths (bluer light) by the interstellar medium is responsible for reddening, a phenomenon which makes the stars to appear redder than their normal colours. This situation clearly contributes to generating a colour excess, that is the difference between observed and intrinsic colours expressed in magnitudes. For instance using the (B-V) Johnson colour index, one can define the colour excess as:

$$E(B-V) = (B-V)_{observed} - (B-V)_{intrinsic} \tag{8.5}$$

The combined effect of scattering and absorbtion is called interstellar extinction A and it generally depends on wavelength and the observing path through the galaxy. Outside the galactic plane, extinction decreases very rapidly. An average interstellar extinction in the V band can be estimated using equation 8.5 and is given by

$$A_V = 3.1E(B-V). \tag{8.6}$$

The equation used to estimate the distance D of a nova can be written

$$m_V - M_V = 5log(D) - 5 + A_V. \tag{8.7}$$

Figure 8.2, taken from Hernanz[3], shows the distribution of apparent magnitude at maximum of a sample of novae from 1901 and 1995[183] as a function of distance.

In order to have an idea of the frequency of the classical nova explosions in our Galaxy, it is convenient first to remember the fact that the discovery of a classical nova mainly depends on the work of amateurs astronomers who search for optical variabilities in stars. A very useful catalog is available on the web, containing all novae discovered up to February 1, 2006 (see Downes *et al.*[184] and the web-site *http://archive.stsci.edu/prepds/cvcat/index.html*). From that, all types of classical novae were selected (object type "nova","fast nova","slow nova" and "very slow nova" in the catalog; all uncertain novae were discarded). The number of novae discovered in the last century is shown in the left panel of Figure 8.3 with a binsize of 5 years.

The general rising trend of discoveries as a function of time is certainly related to the steadily increasing activities of amateurs during the last tens of years and it is quite promising if maintained in the future. The right panel of Figure 8.3 shows the number of novae discovered during the last ten years with a binsize of 1 year. It can be seen that the maximum rate of discoveries obtained up to date ($\sim 10\ \mathrm{y}^{-1}$) is still far from the predicted Galactic nova rate

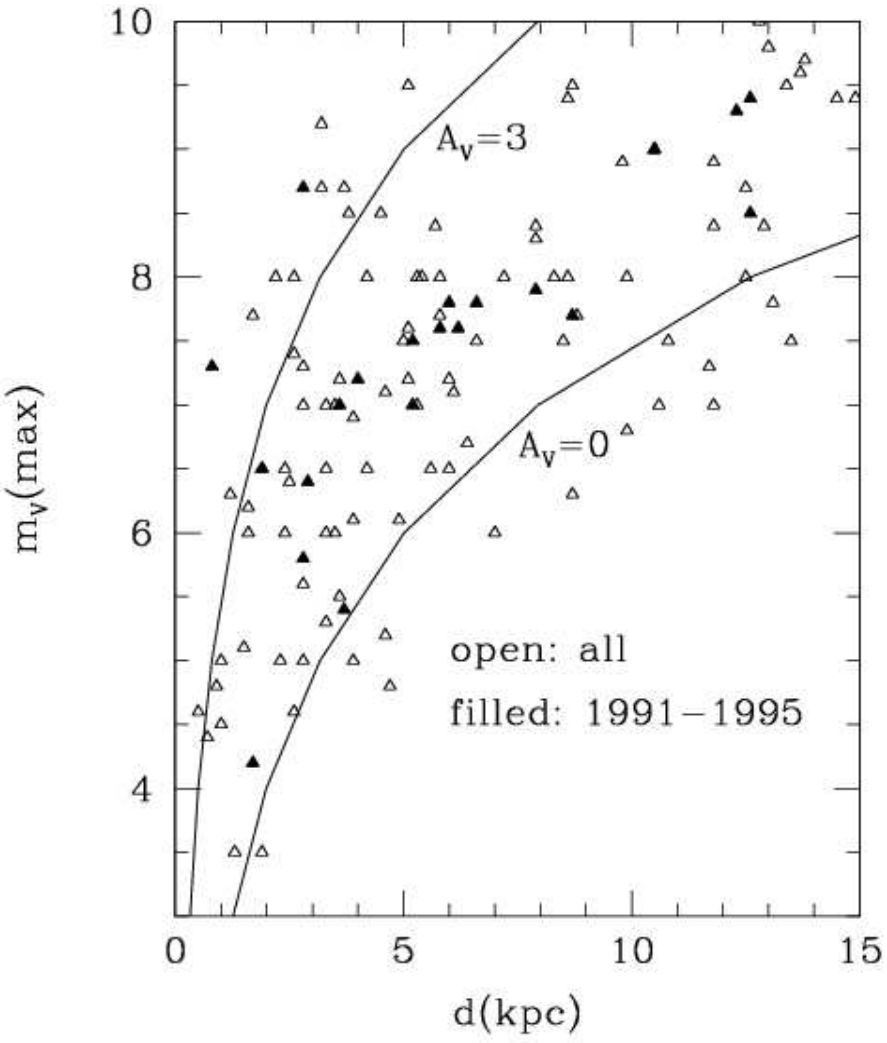

Figure 8.2: *Apparent magnitude at maximum versus distance*[3]*: the sample includes novae from 1901-1995 and the 2 curves correspond to visual extinction* $A_V = 0$ *and* $A_V = 3$ *are plotted for illustrative purposes.*

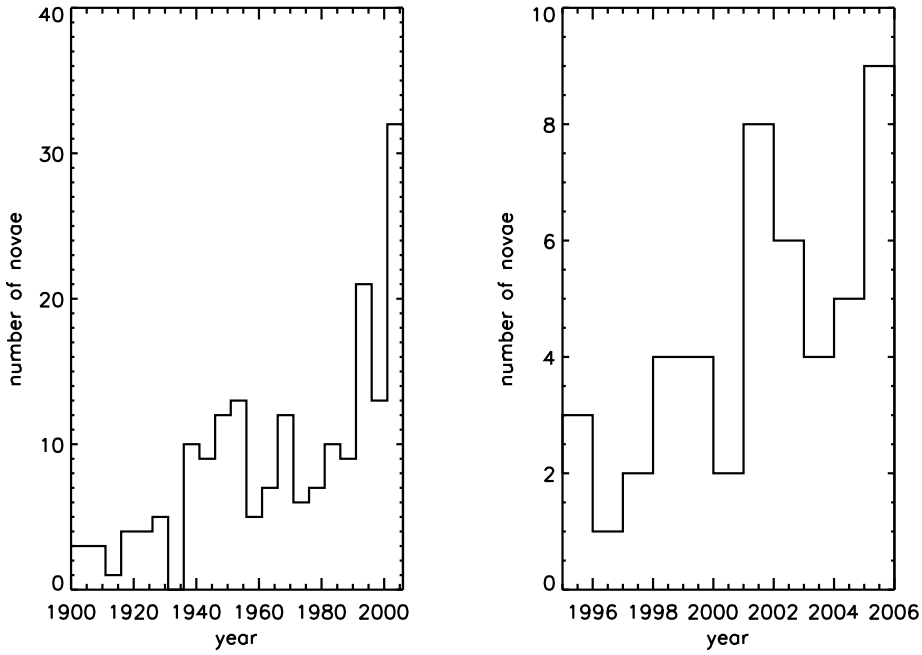

Figure 8.3: *Histogram of the novae discovered in 5 years intervals from 1901-2005 (left) and per year from 1995-2005 (right).*

of 35 ± 11 y^{-1} as estimated by Shafter[183] (see below). Interstellar extinction prevents us from directly observing more than a small fraction of the novae that explode each year. Several methods were used to estimate the nova occurrence rate. Shafter[183] extrapolated the global nova rate from the observed one, accounting for surface brightnesses of the bulge and the disc components and correction factors taking care of any observational incompleteness. With this method, a nova rate of 35 ± 11 y^{-1} was estimated. Hatano *et al.*[185] found a similar value (41 ± 20 y^{-1}) using a Monte Carlo technique with a simple model for the distribution of dust and classical novae in the Galaxy.

All classical novae discovered up to now can be well classified into one of two distinct populations: the faster and brighter disk novae, with $M_V(max) \simeq 8$, and the slower and dimmer bulge novae, with $M_V(max) \simeq 7$. A possible phenomenology which allows the former population to be distinguished from the latter is based on the strongest emission lines they display: novae which emit strong FeII lines evolve more slowly and have a lower level of ionization than novae which emits strong He and N lines. The latter also show larger expansion velocities and higher levels of ionisation. Della Valle & Livio[186] found that the He/N type novae are mainly concentrated in the galactic plane, whereas the FeII type novae preferentially belong to the bulge. Another important result obtained from nova observations concerns the enrichment in carbon, nitrogen, oxygen and neon seen in the ejecta of many objects (around 1/3 of the total).

The abundances of these elements are sometimes very large relative to solar values. The general assumption (see for instance Starrfield *et al.*[187]) is that some enrichment of the accreted matter with matter from the underlying WD core is necessary, both to power the nova explosion and to explain the observed enhanced (with respect to the solar) abundances. Depending on the WD elemental composition, Carbon-Oxygen (CO) or Oxygen-Neon (ONe), different relative abundances in the ejecta are found.

8.1.3 Thermonuclear Runaway

The mechanism by which an accreting WD makes a nova explosion is well established[188,189]. During the accretion phase the accretion timescale, defined as T_R of Equation 8.1 (which is of the order of 10^4 - 10^5 y for classical novae), is less than the nuclear timescale $\tau_{nuc} \sim C_p T/\epsilon_{nuc}$, where C_p is the specific heat, T the temperature at the base of the envelope and ϵ_{nuc} the specific rate of nuclear energy generation. During this phase the envelope mass M_{env} increases.

Since the equation of state for degenerate matter is independent of temperature ($P \propto \rho^{\gamma}$, where P and ρ are respectively the pressure and the density at the base of the envelope), if the temperature and density are sufficiently high for nuclear reactions to occur, any small increase in temperature, leading to enhanced energy generation but no increase in pressure, is amplified in an exponential runaway. This is only terminated when the Fermi temperature T_F is reached, whereupon the equation of state becomes that of a perfect gas and is wildly out of balance, so expansion occurs to reduce the overpressure. Degenerate ignition conditions are reached when the critical pressure $P_{crit} = GM_{WD}M_{env}(crit)/4\pi R_{WD}^4$ (assuming a temperature of $T \sim 2.5{\times}10^7 K$) is reached. At this stage hydrogen starts to burn at the base of the envelope where the CNO cycle is set up and the temperature continues to increase up to $2-3\times10^8 K$ because the envelope cannot expand quickly enough. In the early stage of TNR the nuclear-burning timescales for proton capture reactions ($\tau_{p,\gamma}$) is longer than the β^+-decays timescale (τ_{β^+}). But as peak temperatures are approached in the envelope, $\tau_{p,\gamma}$ becomes very short, allowing the abundances of the β^+-unstable nuclei (^{18}N, ^{14}O, ^{15}O, ^{17}F) to increase to the point where, except for H and ^{4}He, they become the most abundant nuclei in the envelope. This inversion is crucial because, under these conditions, the rate of the CNO cycle is determined by the half-lives of the β^+-unstable nuclei, which are not dependent upon the temperature or the density. Therefore, the reaction rate at a given time depends only on the abundances and half-lives of the β^+-unstable nuclei. Another key role is played by the gradient of temperature between the inner and the outer part of the envelope. In fact the difference of temperature between these two regions is so high that the time needed for carrying β^+-unstable nuclei to the surface by convection is less than the τ_{β^+}. The three main implications of the convection are: first β^+-unstable nuclei will decay after they have reached the surface and second new fresh unburned material is transported to the inner part of the envelope. The third implication is the

probable erosion of the underlying WD core (see section 8.1.4 for more details) which will enrich the accreted material with heavy elements. The decay of the β^+-unstable nuclei in the layers near the surface causes the generation of a large amount of energy (more than $5 \times 10^{47} ergs$), which heats and expands the outer layer leading to typical velocities of $10^2 - 10^3$ km/s and reducing the temperature gradient to the point where convection ends. The ejection of the outer layer is accompained by gamma-rays emission. At this stage, only a very few nuclei in the deepest layers are able to capture protons and the energy generation ceases to rise.

8.1.4 Withe dwarf composition

In order to make a nova explosion possible and to explain the large metallicities, with respect to solar values which are observed in nova ejecta, it is fundamental that the accreted envelope, mainly composed of Hydrogen, is mixed with elements of the underlying WD core. The mechanism allowing such mixing to occur is not clear. Many efforts using complex codes have been made in order to try to explain both the explosion and the abundances seen in spectra (see Kovetz & Prialnik[190] , Alexakis *et al.*[191]), but the theoretical explanations are not completely satisfactory. When a particular model is chosen, the most important parameter to set is the composition of the underlying WD core, because the nova evolution and the observable quantities (such as fluxes, abundances etc) depend significantly on it (see section 8.2.2). There are two different types of WD composition: Carbon-Oxygen WD (CO type) and Oxygen-Neon WD (ONe WD). The former is more common, whereas it was established that the latter requires massive progenitors of around $10 M_\odot$. Typically a CO WD has a mass up to $\sim$1.1 $M_\odot$ whereas that of an ONe WD can be up to the Chandrasekhar limit. It is not always possible to identify the WD in a nova by observing a nova explosion at peak: typically, to distinguish between these two classes, it is necessary to observe the emission spectrum of the ejecta many days after the explosion in order to see a clear signature of the elements. A complication that has to be taken into account is that an ONe WD has a thick CO buffer on top of its ONe core: therefore among the elements ejected from WD surface, Neon may be not present, at least until a number of successive outbursts have eroded that buffer (see José *et al.*[192]).

8.2 Gamma-rays from Novae

Clayton & Hoyle[193] were the first to mention novae as potential gamma-ray emitters. Many theoretical efforts have been made since their work in order to better understand the type and the amount of gamma-ray emitting elements in a nova explosion. One of the aims of such efforts was to obtain a better estimate of the gamma-ray flux expected during the time following the explosion. The detection of such emission would confirm our understanding of the general

scenario and put strong constraints on the models.

8.2.1 How a nova can produce gamma-rays

When a nova explodes the hydrogen burning produces several radioactive isotopes, which are responsible both for the explosion mechanism and for the emission of gamma-rays. As explained in section 8.1.3, short-lived β^+-unstable nuclei, such as ^{13}N, ^{14,15}O and ^{17,18}F, are produced in the inner layer of envelope and then carried up to the outer layer by convection. The decay of such nuclei results in a release of energy, leading to envelope expansion, huge luminosity increase and mass ejection. The longer-lived of such nuclei, ^{13}N and ^{18}F (with lifetime τ=862s and 158min respectively), are the most important contributors of the gamma-ray emission since they decay when the envelope is becoming transparent. The positrons produced in the decay annihilate with electrons, producing the characteristic 511 keV line and a continuum down to few tens of keV, due to positronium decay. Comptonization of the photon emitted in the line also provides a continuum down to low energies. The energy cutoff at low energies is due to photoelectric absorption. Besides the annihilation emission, an additional contribution to the overall emission comes from medium- and long-lived isotopes, such as ^{7}Be (lifetime τ=77days), which is mainly produced in CO novae, and ^{22}Na and ^{26}Al (with lifetime τ=3.75yrs and 10^6yrs respectively), which are produced in ONe novae. The characteristic energies of those nuclei are 478 keV from ^{7}Be decay, 1275 keV from ^{22}Na and 1809 keV from ^{26}Al. The best chances to detect prompt gamma-rays from novae are tied to the short-lived nuclei decay which are expected to generate an intense burst of gamma-ray before the nova visual maximum (see Figure 8.4 taken from Hernanz[3]).

In figure 8.4 the predicted spectral evolution of gamma-ray emission from a CO and a ONe nova at different epochs after peak temperature is shown. The duration of this type of emission depends on the time during which positrons are available and the time during which the envelope is not completely transparent. Hernanz & José[194] estimate this time to be $\sim$ 2 days for annihilation of positrons from ^{18}F and much shorter for those from ^{13}N. The gamma-rays produced by the other radioactive nuclei appear later, stay for a much longer time and are fainter (depending on the nova type).

8.2.2 How many gamma-rays can be produced by a Nova

It is clear from the scenario described above that the detection of gamma-rays from novae will give a fundamental test of many theoretical efforts made in this direction. But the challenge is still open. Recently Hernanz & José[195] have summarised their studies and estimations of gamma-ray emission from novae. They calculated the gamma-ray light curves and spectra for the two type of classical nova (CO and ONe), using a detailed hydrodynamical code which included all the relevant phases of a nova: accretion, nucleosynthesis,

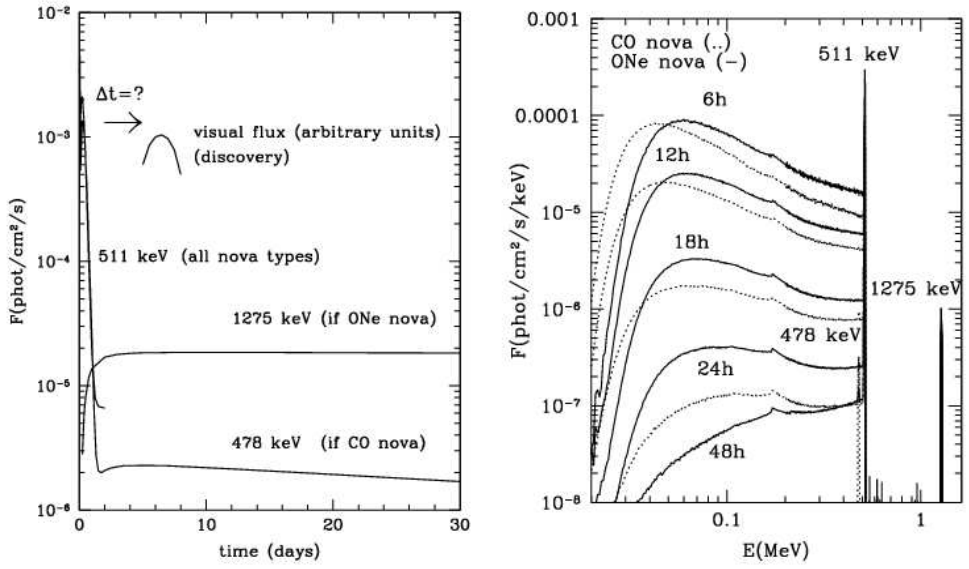

Figure 8.4: *Left panel: predicted gamma-ray light curve of the three possible lines, compared with visual light curve in arbitrary units. Right panel: temporal evolution of CO (dotted) and ONe (solid) nova spectra at a distance 1 kpc.*[3]

explosion and radiative transfer of gamma-rays photons. The conclusion was that the detection of this type of emission is very hard with the instruments now available. A source of uncertainty comes from poorly known aspects of the synthesis of radioactive nuclei: in fact the predictions depend critically on some crucial nuclear reactions whose rates are still uncertain. Until recently, the most uncertain nuclear reaction rates were those related to ^{18}F synthesis [9]. Cross sections were uncertain within a factor of $\sim$ 300. More recent measurements obtained by Bardayan *et al.*[196], De Séréville *et al.*[197], Fox *et al.*[198] and Chafa *et al.*[199] have reduced the uncertainty by a factor of $\sim$15, resulting in a decrease in the expected flux. The situation concerning ^{13}N is much more favorable since it has not been reduced by recent nuclear physics results. Hereafter only gamma-rays produced by ^{13}N and ^{18}F isotopes decay will be considered, because the detection probability of the emission from all other nuclei described above is greatly reduced at the timescale we will consider (few hours).

M.Hernanz and his collaborators (private communication) have computed expected light curves in four energy bands for a 1.25 $M_\odot$ ONe-type nova at 1 kpc assuming the nuclear reaction rates as shown in Coc *et al.*[8] (see Figure 8.5). Lightcurves for a 1.15 $M_\odot$ CO-type nova at 1 kpc were also obtained assuming the nuclear reaction rates as shown in Hernanz *et al.*[9] (see Figure 8.5). The peak at $t < 1hr$ due to decay of ^{13}N and the emission $t >= 6hr$ induced by the decay of ^{18}F are visible in Figure 8.5. The former peak is stronger and shorter then the latter. For the latter peak, the bump shape is

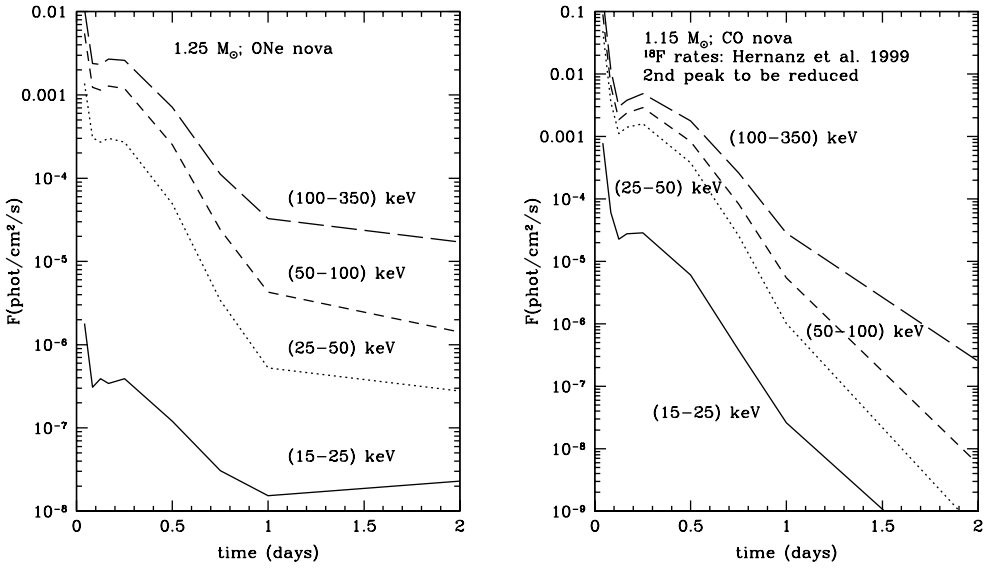

Figure 8.5: *Left panel: lightcurves in four energy bands for a 1.25 $M_\odot$ ONe-type nova assuming the nuclear reaction rates as shown in Coc* et al.[8]. *Right panel: lightcurves in four energy bands for a 1.15 $M_\odot$ CO-type nova assuming the nuclear reaction rates as shown in Hernanz* et al.[9] *(courtesy of M.Hernanz and his collaborators).*

due to the increase of the transmission while the ejecta expands and the decay rate decreases. The values of the expected gamma-ray fluxes shown in Figure 8.5 as a function of time are summarised in Table 8.2:

t	Flux (ph/cm^2/s)			
(hr)	15-25 keV	25-50 keV	50-100 keV	100-350 keV
		ONe type		
1	$1.80\ 10^{-6}$	$1.37\ 10^{-3}$	$5.49\ 10^{-3}$	$1.03\ 10^{-2}$
2	$3.07\ 10^{-7}$	$3.06\ 10^{-4}$	$1.23\ 10^{-3}$	$2.39\ 10^{-3}$
3	$3.90\ 10^{-7}$	$2.70\ 10^{-4}$	$1.14\ 10^{-3}$	$2.33\ 10^{-3}$
4	$3.41\ 10^{-7}$	$3.00\ 10^{-4}$	$1.28\ 10^{-3}$	$2.70\ 10^{-3}$
6	$3.90\ 10^{-7}$	$2.71\ 10^{-4}$	$1.19\ 10^{-3}$	$2.59\ 10^{-3}$
12	$1.20\ 10^{-7}$	$4.93\ 10^{-5}$	$2.53\ 10^{-4}$	$7.13\ 10^{-4}$
18	$3.08\ 10^{-8}$	$3.39\ 10^{-6}$	$2.41\ 10^{-5}$	$1.12\ 10^{-4}$
24	$1.54\ 10^{-8}$	$5.25\ 10^{-7}$	$4.27\ 10^{-6}$	$3.28\ 10^{-5}$
48	$2.30\ 10^{-8}$	$2.78\ 10^{-7}$	$1.42\ 10^{-6}$	$1.71\ 10^{-5}$
		CO type		
1	$7.81\ 10^{-4}$	$4.87\ 10^{-2}$	$9.08\ 10^{-2}$	$1.60\ 10^{-1}$
2	$6.06\ 10^{-5}$	$3.53\ 10^{-3}$	$6.45\ 10^{-3}$	$1.17\ 10^{-2}$
3	$2.27\ 10^{-5}$	$1.11\ 10^{-3}$	$1.87\ 10^{-3}$	$3.00\ 10^{-3}$
4	$2.78\ 10^{-5}$	$1.41\ 10^{-3}$	$2.37\ 10^{-3}$	$3.81\ 10^{-3}$
6	$2.87\ 10^{-5}$	$1.61\ 10^{-3}$	$2.89\ 10^{-3}$	$4.84\ 10^{-3}$
12	$6.03\ 10^{-6}$	$3.78\ 10^{-4}$	$8.27\ 10^{-4}$	$1.77\ 10^{-3}$
18	$3.81\ 10^{-7}$	$2.59\ 10^{-5}$	$8.30\ 10^{-5}$	$2.60\ 10^{-4}$
24	$2.60\ 10^{-8}$	$1.01\ 10^{-6}$	$5.45\ 10^{-6}$	$2.83\ 10^{-5}$
48	$4.51\ 10^{-11}$	$4.79\ 10^{-10}$	$5.65\ 10^{-9}$	$2.53\ 10^{-7}$

Table 8.2: *Expected fluxes of a 1.25 M⊙ ONe-type and a 1.15 M⊙ CO-type nova at 1 kpc assuming the nuclear reaction rates of Coc* et al.[8] *and Hernanz* et al.[9] *respectively (courtesy of M.Hernanz and his collaborators).*

These values are only a first order estimate: in the future the uncertainties due to different aspects may decrease further, yielding a more precise estimation of the fluxes. It is important to note that these results were obtained for particular values of novae mass, those used in Gomez-Gomar *et al.*[200] paper. Different values would be obtained for other WD masses, as pointed out by Hernanz *et al.*[201].

8.2.3 Past attempts to detect gamma-rays from novae

Which characteristics a telescope must have to be able to detect gamma-rays from novae requires some consideration. First of all, it is impossible to foresee the position of classical novae before their appearance: usually novae are

discovered by optical observations around or after the visible light peak. The situation is complicated by the fact that gamma-ray emission occurs some time before optical maximum and is relatively strong only for a very short time ($\lesssim$ 2 days). The best chance of detecting gamma-rays from a nova is therefore by making a retrospective search in the data from a wide field instrument after the nova has been discovered optically. Moreover, to obtain a positive detection, a telescope must have a good enough sensitivity for emission lines or continuum described in section 8.2.1.

The instruments used in the past for such searches did not detect gamma-rays from novae mainly because none was sufficiently sensitive and complete in coverage. The first attempt was made using the gamma-ray spectrometer GRS on Solar Maximum Mission (*SMM*). Leising *et al.*[202] searched for the 1.275 MeV line of ^{22}Na and Harris *et al.*[203] the 478 keV line of ^{7}Be but only upper limits were estimated. Another unfruitful effort to detect 1.275 MeV line was made later by Iyudin *et al.*[204] with COMPTEL telescope on board *CGRO*. With BATSE on board the same satellite, Hernanz *et al.*[205] searched for the 30-511 keV continuum from the annihilation of positrons emitted by ^{13}N and ^{18}F, but even in this case only upper limits were obtained. Harris *et al.*[206] used the Transient Gamma-Ray Spectrometer (TGRS) on board the *Wind* spacecraft to search for the 511 keV line generated by the annihilation of positrons and slightly blueshifted by the outburst. A more recent attempt to detect the positron annihilation was made by Smith[207] using *RHESSI*, but, as in the previous case, no positive detections were found.

8.3 Results with BAT

The ideal instrument to detect gamma-rays from novae is a wide FOV telescope which can continuously monitor the sky in the appropriate energy range and with a good sensitivity. Hernanz & José[195] have pointed out that *INTEGRAL* may have the good sensitivity requested for the gamma-rays detection. Nevertheless, they also showed that only novae closer than 0.5 kpc (i.e. very near to us) have chances to be detected by *INTEGRAL*/SPI, mainly in the ^{2}2Na 1275 keV line, emitted by ONe novae. The expected weak and long-lived emission from such line requires a very long exposure time in order to make it detectable, thus reducing the chances of success. Hernanz & José[208] presented prospects for detectability of the electron-positron annihilation continuum with IBIS/ISGRI on board *INTEGRAL*. They obtained that this type of emission could be detected when novae are at distances less than 4-5 kpc, but for observations which catch them by chance around 10 hours after T_{peak} in the IBIS FOV. The relatively small FOV of the IBIS telescope makes the chances of detection very low. However, five years since the *INTEGRAL* launch, no gamma-ray emission from novae have been detected.

Another mean to obtain a successful detection is provided by the *Swift*/BAT instrument. In fact, the BAT satisfies all the conditions described above: it

has a large FOV ($\sim$ 1 sr, larger than all the instrument on board *INTEGRAL*), it monitors every day almost the whole sky (monitoring the sky for gamma-ray bursts, whereas *INTEGRAL* concentrates mainly in the Galactic plane), it has a good sensitivity and it covers a wide energy range (14-195 keV). In "survey mode" the BAT can monitor a given source about every day with a time resolution which is typically 300s. In this section the BAT sensitivity estimates, together with the results obtained with a sample of 20 novae, are presented.

8.3.1 BAT sensitivity

The interest here is the possibility of using BAT to detect for the first time prompt gamma-ray emission from novae. The detection of a source in the lightcurves or images requires a significant increase, with respect to a background noise level. Typically, the significance of a point source in a coded mask image in a given energy band is defined as

$$S_i = \frac{f_m C_s}{\sqrt{B}} \tag{8.8}$$

where C_s is the number of counts detected from the source, B is the number of detected background events and f_m (equal to 0.73 for BAT) is a factor which takes into account the finite size of the detector pixels relative to the mask elements[209]. In principle B includes the photons detected from all the gamma-ray sources in the FOV, but for sources that are not too strong the number of such photons is much smaller than the background events (more than 1 order of magnitude). The sensitivity of a coded mask instrument varies across the FOV: in fact a source near to the center of the pointing (on-axis) illuminates the whole detector (except for the shadows cast by the mask), whereas a source towards the edge of the FOV (in the "partially coded field") can illuminate only a small fraction of the detector. Therefore it is convenient to write equation 8.8 in a more useful way:

$$S_i = \sqrt{n_{c.f.}}\frac{f_m C_s}{\sqrt{B}} \tag{8.9}$$

where $0 \leq n_{c.f.} \leq 1$ is the coded fraction, i.e. the fraction of detector area viewed by the source (ignoring the mask). In this case C_s takes the meaning of the number of counts which would be detected if the source were on-axis and B is the number of background counts in the whole detector (assumed uniform). $C_s(\Delta E)$, which is a function of energy range, can be written as $C_s(E) = F_s(E) \cdot \Delta t \cdot (A_{det}/2) \cdot \eta(E)$, where $F_s(E)$ is the flux of the source in the energy band under consideration, A_{det} the detector plane area (notice the factor 2 due to the mask blockage) and $\eta(E)$ the detector efficiency. This latter parameter is the probability that a photon in a given energy band arriving at the detector would be detected[209]. Similarly $B(E) = r_B(E) \cdot \Delta t \cdot \eta(E)$, where

$r_B(E)$ is the background count rate in the energy band under consideration. By substituting the expression obtained above, formula 8.9 becomes

$$S_i = \sqrt{n_{c.f.} \cdot \Delta t \cdot \eta(E)} \cdot (A_{det}/2) \cdot f_m \frac{F_s(E)}{\sqrt{r_B(E)}} \tag{8.10}$$

By setting a particular threshold significance level, S_{th}, for detection, equation 8.10 gives the flux threshold below which a source cannot be detected:

$$F_s(E) = \frac{S_{th} \cdot \sqrt{r_B(E)}}{(A_{det}/2) \cdot f_m \cdot \sqrt{n_{c.f.} \cdot \Delta t \cdot \eta(E)}} \tag{8.11}$$

8.3.2 Method

In the next sections the results of the search in the BAT data for gamma-ray emission from a sample of 18 novae detected from the *Swift* launch (see Table 8.3) will be shown. The method adopted for such investigation consists of the following steps:

- Data selection:
  the time at which prompt gamma-ray emission from novae occurs relative to the discovery time ($t_{discovery}$) in optical is unknown, but probably the difference not exceeds few days (see section 8.2.1). Thus, in order to be certain to include in the analysis data around such time and to provide a baseline for comparison, all data having the given nova in the FOV and covering the interval $t_{discovery}$ - 20 days $< t < t_{discovery}$ + 20 days were selected.

- Data analysis:
  the analysis was performed using the pipeline described in section 3.2 with an input catalog containing the coordinates of all novae. A "line by line" analysis was selected. In this way, for each dataset, an amplitude and a signal to noise ratio (SNR) in each of four different energy bands (14-25, 25-50, 50-100, 100-195 keV) plus other useful information were obtained.

- Searching for detections:
  the resulting lightcurves were scanned to search for high points. All points with SNR greater than 4 in a single energy band or observations having SNR greater than 2.5 in at least two energy bands were selected. For such points an image was created and searched for detections using *batcelldetect* tool with no input catalog and a SNR threshold of 3.5.

- Searching for a positive mean level:
  if the previous procedure was unsuccessful, a different approach was tried: each lightcurve was fitted with a simple constant model, in order to find in the reduced χ^2 a possible indication of the nova detection or to find a

significant positive mean level over 40 days. In order to take account of possible systematic errors, the procedure was repeated for a number of random points around each nova: these points were chosen to lay in an annulus, centered on the nova coordinates, with inner and outer radii 1 and 2 degrees. Given a lightcurve, the χ^2 is not an ideal test for a group of associated high points because χ^2 value is the same if this points are adjacent or not. For this reason many different bintimes were tried (from 1 day to 1 hour).

If the above procedure showed no evidence for a detection of a given nova, upper limits were estimated. In the next sections the results obtained for the recurrent nova RS Ophiuchi and the other novae of the sample will be presented. RS Ophiuchi was the only case in which a significant detection was made and will be discussed separately.

8.3.3 RS Ophiuchi

RS Oph is a recurrent nova characterized by a long orbital period (457 days) and a recurrence period of ∼10-20 years. The companion is an M-giant star which blows a massive stellar wind and the WD mass is considered to be very near to the Chandrasekhar limit. The distance of this object is estimated to be 1.6 kpc from X-rays observations[210], although a distance of 0.6 kpc has been suggested based on UV and optical observations[211]. RS Oph has undergone six recorded outbursts (in 1898, 1933, 1958, 1967, 1985 and 2006). The last outburst was discovered the first time ($t_{discovery}$) in 2006 February 12.83UT[212], reaching magnitude V=4.5 at this time. The previous optical observation, 1 day before, showed the source in its normal state. In the following sections the *Swift* and *RXTE* observations of RS Oph before and after $t_{discovery}$ are reported.

BAT data analysis

BAT data before and after $t_{discovery}$ were searched for gamma-ray emission from RS Oph. The data reduction was performed using the software described in section 3.2. Version 2.3 of the *Swift* software was adopted. The results are shown in Figure 8.6. The RS Oph gamma-ray outburst emission is clearly visible in the 14-25 keV band during the first 3 days from $t_{discovery}$. In an overlay of images formed from the corresponding data, standard software (*batcelldetect*) finds a 9.9σ source within 2'.5 of the position of RS Oph as the only unidentified source above 5σ, confirming the reality of this detection.

An image of the region of RS Oph before and after the outburst is shown in Figure 8.7. In the 25-50 keV band there appears to be a weaker detection immediately after the outburst, but this should be treated with caution. X or gamma-ray emission has never been seen so close to the optical discovery: this is a clear example of one of many advantages in using BAT. Moreover,

Nova	RA (deg)	DEC (deg)	$t_{discovery}$ (UTC)	Nova type	Distance from literature (kpc)	References
V2361 Cyg	302.329375	39.814694	2005 Feb 10.850	CO,FeII		IAUC #8483 #8484 #8487 #8511 #8524 #8529 #8641
V382 Nor	244.936417	-51.581417	2005 Mar 13.309	FeII		IAUC #8497 #8498
V378 Ser	267.352375	-12.999778	2005 Mar 18.345	CO,FeII		IAUC #8505 #8506 #8509 #8527 #8529
V5115 Sgr	274.246000	-25.944111	2005 Mar 28.779			IAUC #8502 #8523
V1663 Aql	286.302083	5.236667	2005 Jun 9.240	FeII	2.9 ± 0.4 5.5 ± 1 7.3-11.3	Boyd & Poyner[213] Lane *et al.*[214] Poggiani[215] IAUC #8540 #8544 #8640
V5116 Sgr	274.461542	-30.442000	2005 Jul 4.049			IAUC #8559 #8561 #8579 #8596
V1188 Sco	266.089958	-34.276583	2005 Jul 25.284	FeII(?)		IAUC #8574 #8575 #8576 #8581
V1047 Cen	200.207250	-62.630694	2005 Sep 1.031			IAUC #8596
V477 Sct	279.678875	-12.271000	2005 Oct 11.026	He/N	11 ± 3.6	Munari *et al.*[216] IAUC #8644 #8617
V2575 Oph	263.304417	-24.351972	2006 Feb 8.379	CO,FeII		IAUC #8671 #8676 #8710 #8728
RS Oph	267.555008	-6.707911	2006 Feb 12.830	RN	1.6 0.6	[210] [211]
V5117 Sgr	269.719208	-36.793083	2006 Feb 17.370	FeII		IAUC #8673 #8706
V2362 Cyg	317.885250	44.801017	2006 Apr 2.807	CO,FeII	~ 1.5 5-12	Czart *et al.*[217] Steeghs *et al.*[218] IAUC #8697 #8698 #8702 #8710 #8731 #8785 #8788
V2576 Oph	258.887500	-29.161083	2006 Apr 6.565	CO,FeII		IAUC #8700 #8710 #8730
V1065 Cen	175.793042	-58.067861	2007 Jan 23.354			IAUC #8800 #8801
V1280 Sco	254.420458	-32.343444	2007 Feb 4.854	FeII		Swank[219] Osborne *et al.*[220] IAUC #8803 #8807 #8809
V1281 Sco	254.247292	-35.363944	2007 Feb 19.859			IAUC #8810 #8812
V2467 Cyg	307.052167	41.810139	2007 Mar 15.787	FeII	1.5-4	Steeghs *et al.*[221] IAUC #8821

Table 8.3: *The sample of the 18 novae adopted for the search for gamma-ray emission. Only for 4 novae is a measure of distance available from literature. For 5 novae it was possible to identify the type as CO. For each nova references to the first few IAU Circulars are given.*

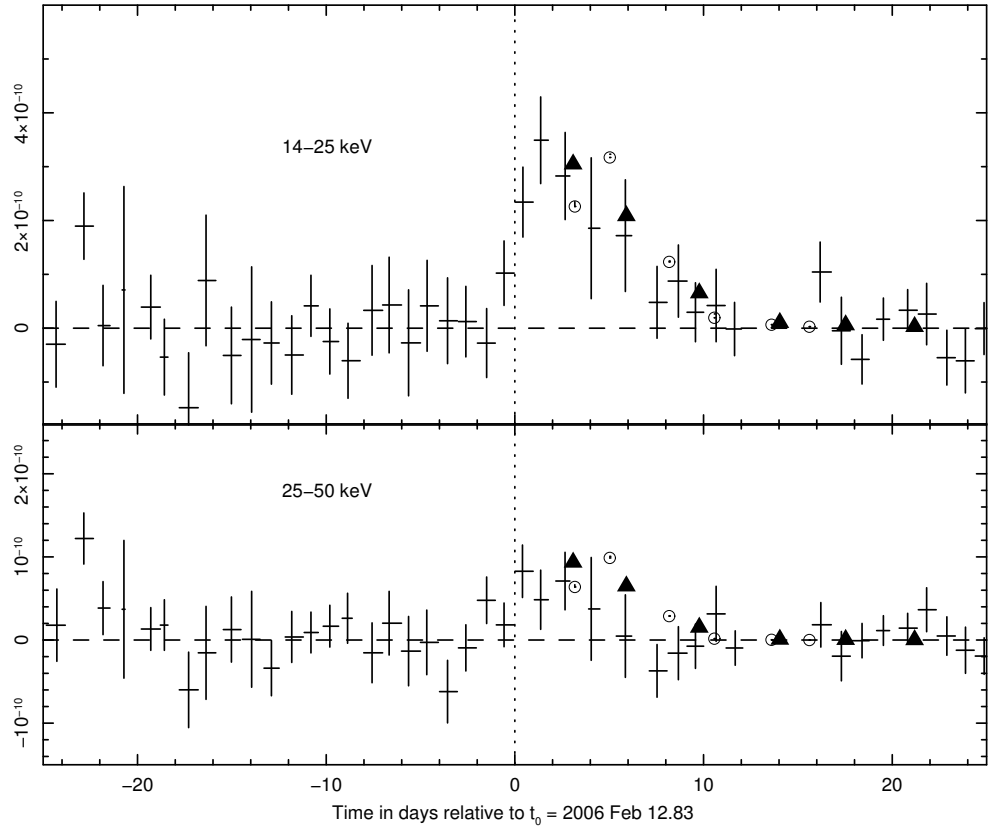

Figure 8.6: *The flux from RS Oph in the bands 14-25 keV and 25-50 keV observed with* Swift*/BAT (units are ergs* cm^{-2} s^{-1}*). Each point of the plot represent the weighted mean flux at weighted mean time, with horizontal error bar stretching from the first to the last sample included in the mean. The circles and triangles show the flux in the same energy bands from extrapolation of the models in Table 8.4 and 8.5 respectively. The dotted line is the time of the first optical detection of the outburst.*

following the discovery, an XRT target was planned and observations started 3 days later (see Table 8.4). Because of a BAT reboot, no data were available at the time of first XRT observation: data became available again after t∼4 days, but at this epoch BAT flux was too weak in order to make an useful comparison.

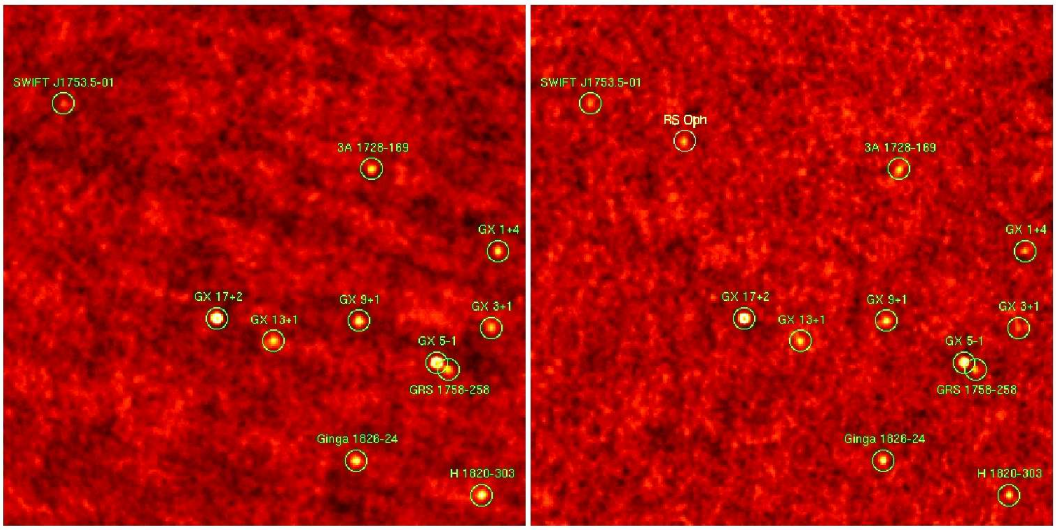

Figure 8.7: *RS Oph image before $t_{discovery}$ (left panel) and after $t_{discovery}$ (right panel). The 2 images are the overlying of February 10-12 and 13-15 BAT data respectively.*

For the spectral analysis, standard *Swift* software was used. This latter is able to extract a single source spectrum at a time so it is potentially affected by the presence of strong sources in the FOV. Spectra with 2 keV bins were extracted for each interval over which the pointing was unchanged (averaging 840 s). Systematic errors (version 2005-11-03 of the BAT CALDB) were taken into account and XSPEC (version 11.3.2) was used to fit models simultaneously to all the observations covering $\sim$ 1 day. The signal to noise ratio was never good enough to justify models with multiple free parameters and so only the normalisation was fitted. All BAT 14-25 keV spectra were fitted with the spectral model found from Obs 001 of the XRT dataset (see Table 8.4). A scale factor accounting for the two different instruments was also fitted. Satisfactory χ^2 values were always found, allowing an approximative factor to convert filtered count rates in physical units (erg cm^{-2} s^{-1}) to be found.

For comparison Figure 8.6 also shows the 14-25 and 25-50 keV fluxes from *Swift*/XRT (circles) and *RXTE*/PCA (triangles) obtained by extrapolating into these energy bands the best-fit spectral models of the first datasets available for each instrument after the beginning of the outburst. Considering that the BAT data points are averages over 24h periods and centered on slightly different times, the measured fluxes are consistent with extrapolations of corresponding XRT and PCA spectra.

A significant point around t = -23 d is also clearly visible in Figure 8.6. Although it is well far from $t_{discovery}$, a possible very short spike of emission at that epoch is not completely excluded: this might be expected from the modelling of Alexakis *et al.*[191]. In the overlay of images in the 14-25 keV band corresponding to this point, *batcelldetect* finds a 3.5σ source. An attempt to increase the signal-to-noise ratio was made by overlaying only the images whose corresponding RS Oph spectra showed a significant count rate in the 14-25 keV band. In such case the source was not detected by *batcelldetect*. By overlaying the images corresponding to the t = -23 d point in the 25-50 keV band no detection was found. Given the negative results of these tests and the large number of trials, the evidence that the t = -23 d point is associated with emission from RS Oph is weak.

XRT data analysis

In order to better understand the origin of the emission seen with BAT, a study in the X-ray domain was performed. Results from the *Swift*/XRT telescope are presented in this section, whereas results from the PCA and ASM instruments on board *RXTE* are discussed in the following sections. After pointed observations started, the XRT temporal coverage of RS Oph 2006 outburst was very good: the source was observed 8 times in the first 26 days after the outburst, allowing a detailed temporal and spectral study. The results of this study are shown in Table 8.4[222]

A Mekal, optically thin, collisionally-ionized plasma emission model was used for spectral fitting, obtaining a satisfactory reduced χ^2 in all cases. BAT spectra whose times are compatibles with XRT observations were added in the fit in order to make a joint XRT-BAT fit. The aim is to see if the model used for XRT fit is compatible with BAT spectra. The result for spectra around Obs 001 of the XRT dataset (t=3.17) is shown in Figure 8.8.

The joint best-fit shows a temperature of 8.37 keV and an absorption (above the ISM) of $2.58810 \times 10^{22} cm^{-2}$, which is in agreement with values of Table 8.4. The value of χ^2/dof is 935/888 .

PCA data analysis

The Proportional Counter Array (PCA) is one of three X-ray instrument on board Rossi XTE satellite. It works in 2-60 keV energy range with a 6500 cm^2collecting area and 1 microsec time resolution. PCA detector is composed of 5 independent proportional counters (PCUs) and it is non-imaging. RS Oph was observed 6 times (t=3,6,10,14,17,21 days), everytime at least with PCU2. Thus, in order to work with data produced by the same detector, PCU2 data only were analysed. Data reduction was performed using standard *RXTE* software. The resulting 6 spectra are plotted in Figure 8.9.

A good fit for all spectra can be obtained (reduced χ^2 ranging from 0.4 to 1.7 for the 6 observations) using a single-temperature thermal bremsstrahlung

Obs.	Date(Day)	Exposure (s)	Count rate (count s^{-1})	kT keV	$[N_H]_W$ [a] (10^{22} cm^{-2})	χ^2/dof	Unabs. Flux[b] (erg cm^{-2} s^{-1})
001	2006-02-16T00:05 (3.17)	664	14.2±0.2	$8.44^{+0.98}_{-0.91}$	2.96±0.15	460/286	2.0×10^{-9}
002a	2006-02-17T20:33 (5.03)	999	31.5±0.2	$8.54^{+0.50}_{-0.49}$	$0.62^{+0.03}_{-0.02}$	993/585	2.7×10^{-9}
002b	2006-02-21T00:10 (8.18)	844	19.8±0.2	$7.24^{+0.54}_{-0.39}$	0.25±0.02	631/436	1.3×10^{-9}
004	2006-02-23T19:37 (10.99)	950	15.5±0.2	4.38±0.23	0.25±0.02	484/327	8.9×10^{-10}
005	2006-02-26T10:18 (13.6)	897	12.3±0.1	3.30±0.15	$0.20^{+0.02}_{-0.01}$	465/289	6.8×10^{-10}
006	2006-02-28T10:31 (15.61)	1041	10.6±0.1	$2.83^{+0.10}_{-0.09}$	0.19±0.02	559/283	4.9×10^{-10}
007	2006-03-03T00:04 (18.17)	738	8.6±0.1	$2.36^{+0.11}_{-0.12}$	$0.18^{+0.03}_{-0.02}$	353/206	3.6×10^{-10}
008[c]	2006-03-10T19:38 (25.99)	1605	6.5±0.1	$1.61^{+0.03}_{-0.02}$	0.18	708/189	2.5×10^{-10}

[a] Absorption above the ISM value of 2.4×10^{21} cm^{-2}.

[b] 0.7-10 keV. Bolometric correction range from 1.5 to 1.7 for Observation 1 to 8.

[c] Fits to 0.7 - 10 keV and additional column fixed at previous value

Table 8.4: *Summary of RS Oph XRT observations and spectral fits (from Bode* et al.*[222]).*

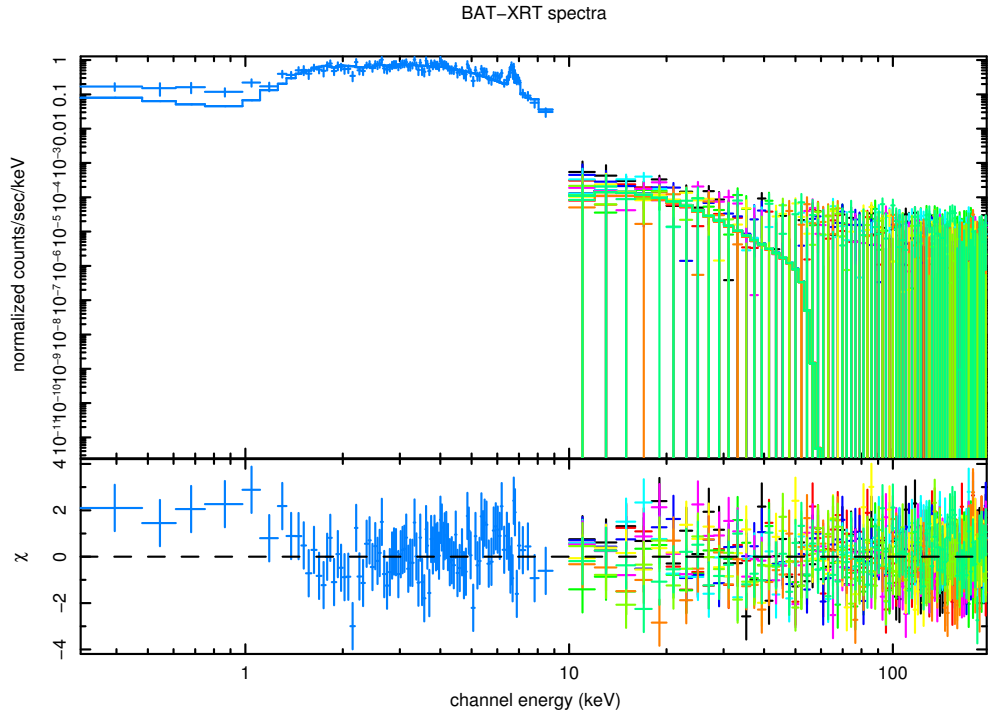

Figure 8.8: *BAT-XRT joint fit. BAT data are from t=3 days whereas Obs 001 of the XRT dataset was used.*

model plus 3 emission lines from Fe and absorption by intervening material. For all spectra a systematic error of 0.6% of the model flux was applied. The Fe lines seen in the spectra, a blending of 6.4 keV fluorescence line, 6.7 keV He-like line and 6.97 keV H-like line, imply that the X-ray emission is generated by an optically thin thermal plasma. The best-fit values are summarised in Table 8.5.

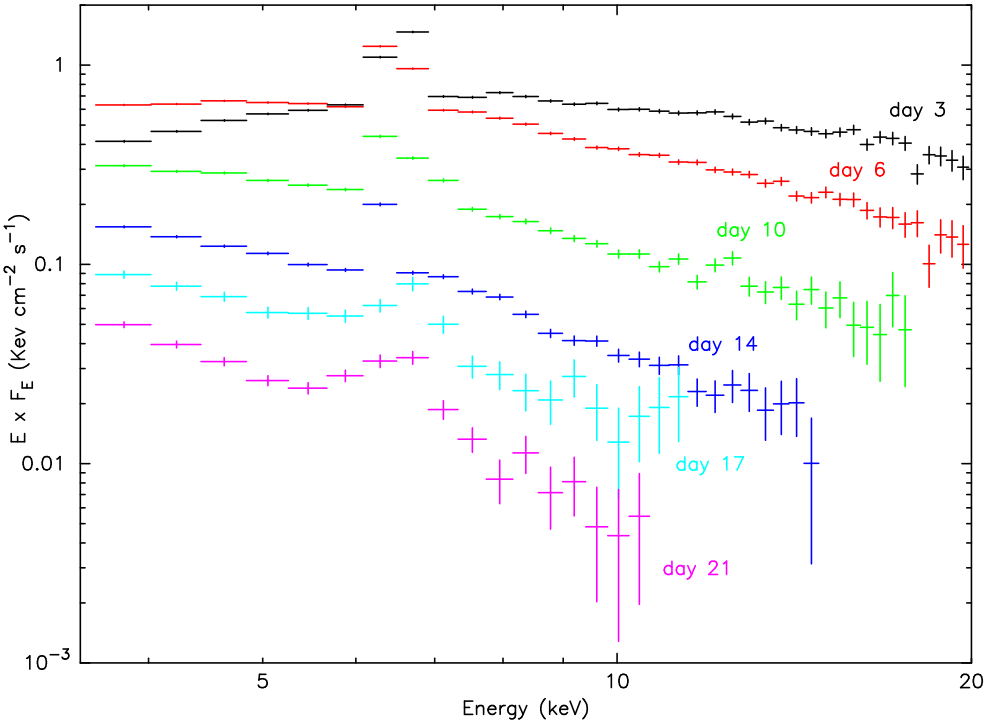

Figure 8.9: *Six RS Oph spectra at different epochs obtained with PCA. The Fe lines group around 6.7 keV is clearly visible, implying that emission comes from an optically thin thermal plasma.*

Obs.	Date(Day)	Exposure (s)	Count rate (count s^{-1})	kT keV	$[N_H]_W$ [a] (10^{22} cm^{-2})	χ^2/dof	Unabs. Flux[b] (erg cm^{-2} s^{-1})
91441-01-01-00	2006-02-15T21:47 (3.08)	1424	129.2±0.3	$9.74^{+0.21}_{-0.07}$	$5.18^{+0.35}_{-0.40}$	69/39	1.8×10^{-9}
91441-01-02-00	2006-02-18T17:28 (5.90)	2000	120.2±0.3	$6.39^{+0.08}_{-0.03}$	$0.44^{+0.08}_{-0.03}$	42/29	2.1×10^{-9}
91441-01-03-00	2006-02-22T14:09 (9.75)	1520	47.0±0.2	$3.61^{+0.15}_{-0.25}$	$0.30^{+0.16}_{-0.25}$	37/26	1.0×10^{-9}
91441-01-04-00	2006-02-26T20:21 (14.02)	3200	22.3±0.1	$2.20^{0.08}_{-0.05}$	0.0	24/21	6.4×10^{-10}
91441-01-05-00	2006-03-02T08:27 (17.52)	400	11.8±0.2	$2.03^{+0.15}_{-0.15}$	0.0	11/13	4.0×10^{-10}
92406-01-01-00	2006-03-05T23:58 (21.17)	1296	5.9±0.1	$1.45^{+0.10}_{-0.36}$	0.0	5/11	0

[a] Absorption above the ISM value of 2.4×10^{21} cm^{-2}. After t=9.75 the absorption was fixed at ISM value.

[b] 0.5-20 keV.

Table 8.5: *Summary of RS Oph PCA observations and spectral fits. The values are in agreement with those found by*[223]

ASM data analysis

The All-Sky Monitor (ASM) is another X-ray instrument on *RXTE*. It consists of three wide-angle shadow cameras equipped with proportional counters with a total collecting area of $90cm^2$. It works in the 2-12 keV energy range covering 80% of the sky every 90 minutes. Like BAT it was monitoring the region of the sky containing RS Oph at around the time of the outburst. Thus it potentially provides complementary information. RS Oph all band light curve (∼1.5 - 12 keV), starting from t=-30 to t=30 days is shown in Figure 8.10. It clearly shows a group of positive points immediately following the discovery time of RS Oph.

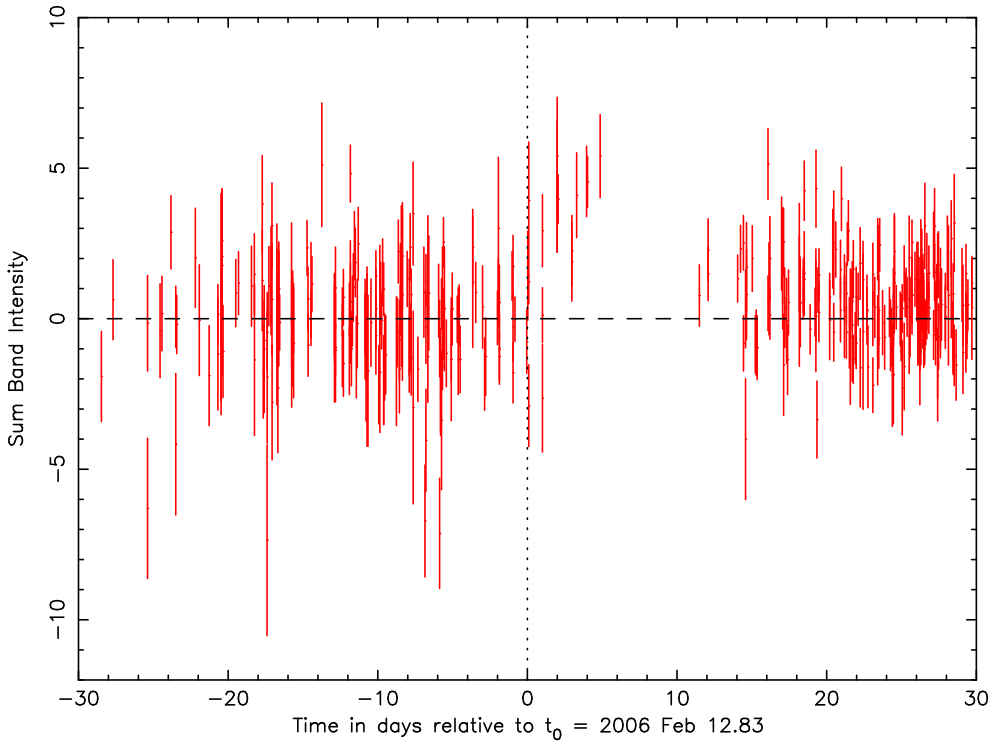

Figure 8.10: *All band (∼1.5-12 keV) RS Oph ASM light curve. The vertical dotted line is the time of the first optical detection of the outburst.*

In order to know if the "outburst points" are real, a Kolmogorov Smirnov test (K-S test) was made. Taking into account two different distributions, the K-S test is based on the maximum distance between two normalised integral distributions. The K-S test assesses if the difference between them is likely to have been caused by chance fluctuation or not. In this case two different distributions of the values of the significances relative to the error estimate of the points from the all band lightcurve (∼1.5 - 12 keV) at different epochs were constructed. The first set was composed of the significances of all the points in the range $-2 < t < 6$ days (outburst epoch) whereas the second one covered the range $-103 < t < -2$ and $6 < t < 108$ (quiescent epoch).

The two distributions are shown in the lower panel Figure 8.11: the red curve correspond to the outburst, the green to the quiescent epoch. The upper panel shows the relative integral distributions and their difference (in black).

It can be found that the probability that the maximum difference between the two curves occurs by chance is 0.02% (see Figure 8.11). This is another confirmation of the reality of the outburst.

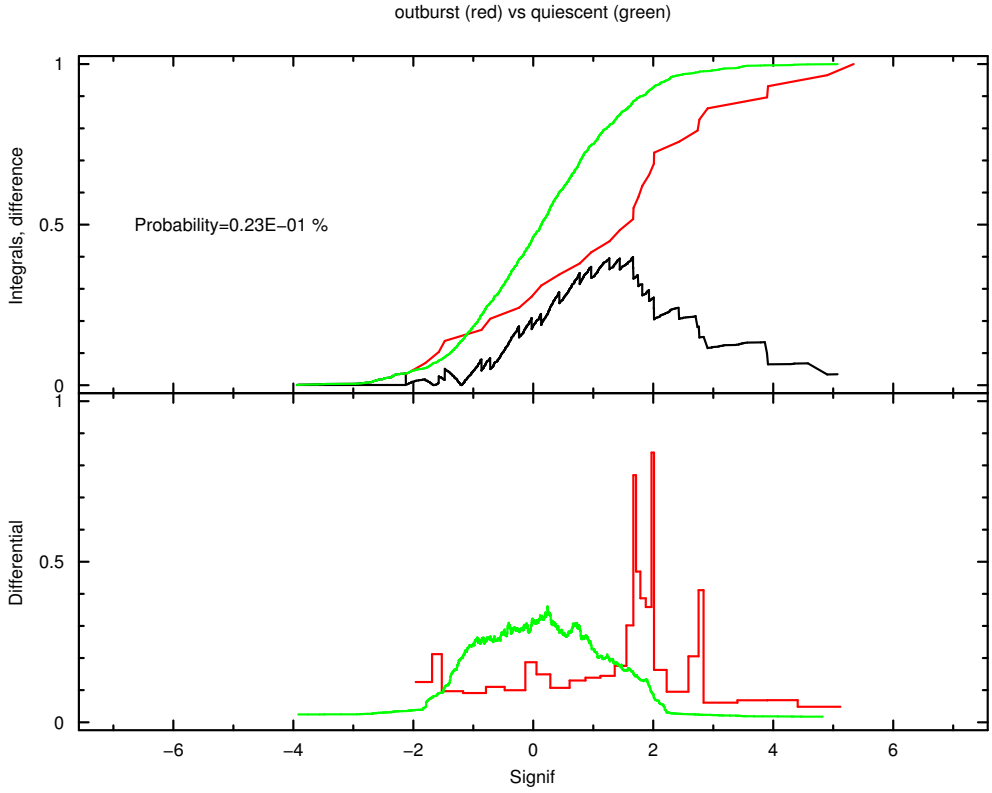

Figure 8.11: *Kolmogorov Smirnov test for two distributions of significance values from the 'all' band (∼1.5 - 12 keV) light curve obtained with the RXTE/ASM. The lower panel shows the distributions of significances relevant to the outburst epoch ($-2 < t < 6$ days, red curve) and to the quiescent epoch ($-103 < t < -2$ and $6 < t < 108$ days, green curve). The upper panel shows the normalised integral distributions. The black curve is the difference between them.*

A second test was performed in order to see if there was a low continuum emission after the outburst. In this case, the two distributions compared were the $-103 < t < -2$ days set of points (before outburst) and the $11 < t < 108$ days set of points (after outburst). It was found that the probability that the maximum difference between the two curves occurs by chance is 18% (see Figure 8.12). One can conclude that ASM data do not provide convincing evidence of any longer term low continuum emission after the outburst.

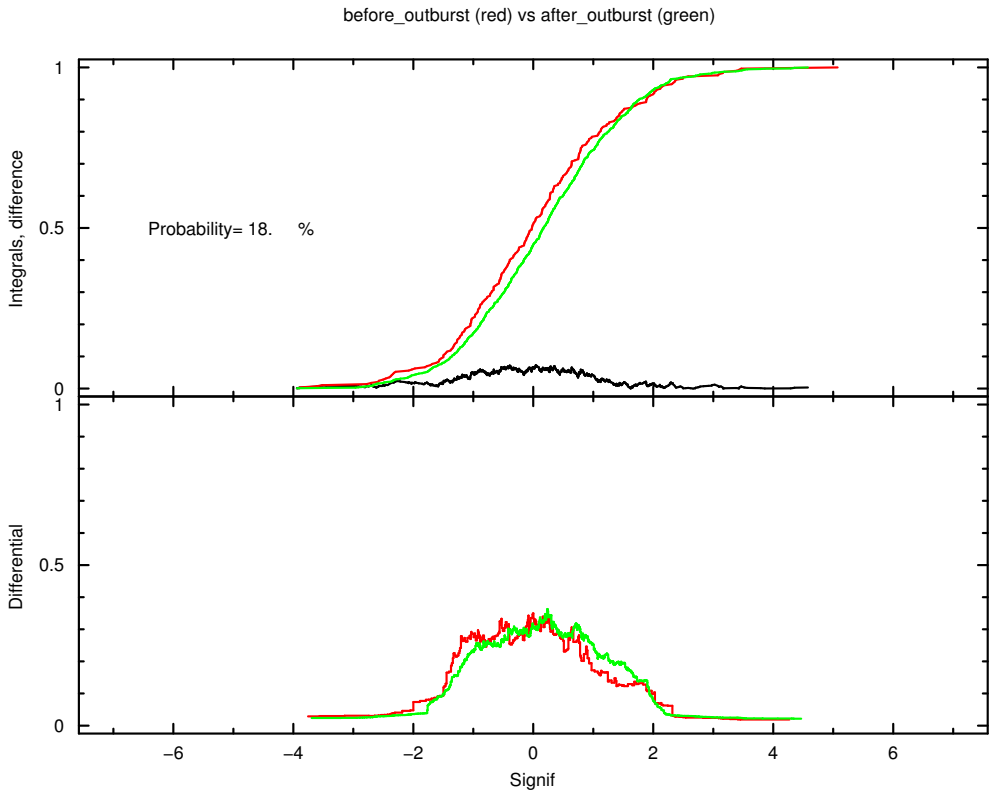

Figure 8.12: *Kolmogorov Smirnov test for pre-outburst* ($-103 < t < -2$) *and post-outburst* ($11 < t < 108$) *periods (see Figure 8.11 for details). The 'all' energy band light curve was used.*

Interpretation

As explained in section 8.1.3, a nova eruption causes the outwards ejection at supersonic velocities of a fraction of the material accreted since the previous outburst. When the companion star of the binary system is a red giant, such as the case of RS Oph, very fast ejecta run into a dense circumstellar medium: the red giant wind. Under such circumstances a double shock system is established, with a forward shock being driven into the stellar wind and a reverse shock being driven into the otherwise unshocked ejecta[224]. The typical gas temperatures is $\sim 2.2 \times 10^8$ K for velocities of the forward shock of v_s= 4000 km s^{-1}. The evolution of a nova remnant can be divided in 3 phases. Phase I is a free expansion stage during which the contribution of the ejecta in supplying energy to the shocked stellar wind is dominant. For strong shocks, the post-shock temperature T_s is related to the shock wave velocity by the equation

$$T_s = \frac{3}{16}\frac{\mu m_H v_s^2}{k} \tag{8.12}$$

where k is Boltzmann's constant and $\mu m_H = 10^{-24} g$ is the mean particle mass, including electrons. During Phase II a blast wave is driven into the wind. The newly shocked gas is so hot that only an insignificant amount of energy is lost by radiation. During such adiabatic phase, known as Sedov-Taylor phase, the explosion can be modelled by the instantaneous release of energy at a point. Phase III begins when the shocked material starts to be cooled by radiation. Assuming a spherically symmetric model in which high-velocity ejecta interact with a slow moving pre-outburst wind, Bode & Kahn[225] showed that at the time the first X-ray observation of the 1985 RS Oph outburst began (t = 55d; made by EXOSAT), the remnant was in transition between Phase II and III. Using the same model and assuming the parameters derived by O'Brien *et al.*[226], a value of $t \simeq 6.2$d for the duration of Phase I can be derived.

The 2006 RS Oph outburst was observed since its very early stage. The XRT and PCA observations presented here (see Tables 8.4 and 8.5) provide a very much better coverage than that of EXOSAT in the 1985. In fact they cover the period of the expected Phase I/II transition and extend into that of Phase II/III. From the above, it can be seen that the XRT and PCA spectra are well described by a model of emission from a high temperature thermal plasma, which is consistent with the emission produced by the shock-system described above. The observed X-ray emission comes mainly from electron bremsstrahlung, and the detected H-like and He-like Fe lines confirm the high ionization state of the plasma. Values of unabsorbed X-ray fluxes of post-shock material in the 0.7-10 keV energy band, taken from Table 8.4, are shown in Figures 8.13 as a function of time. To compare XRT and PCA data, the fluxes of the observations of Table 8.5 were calculated in the same energy band as for XRT and overplotted.

The plot shows an initial rise to peak at around t = 5d, a time consistent with the expected Phase I/II transition. The flux then decays as $t^{-1.5}$, as

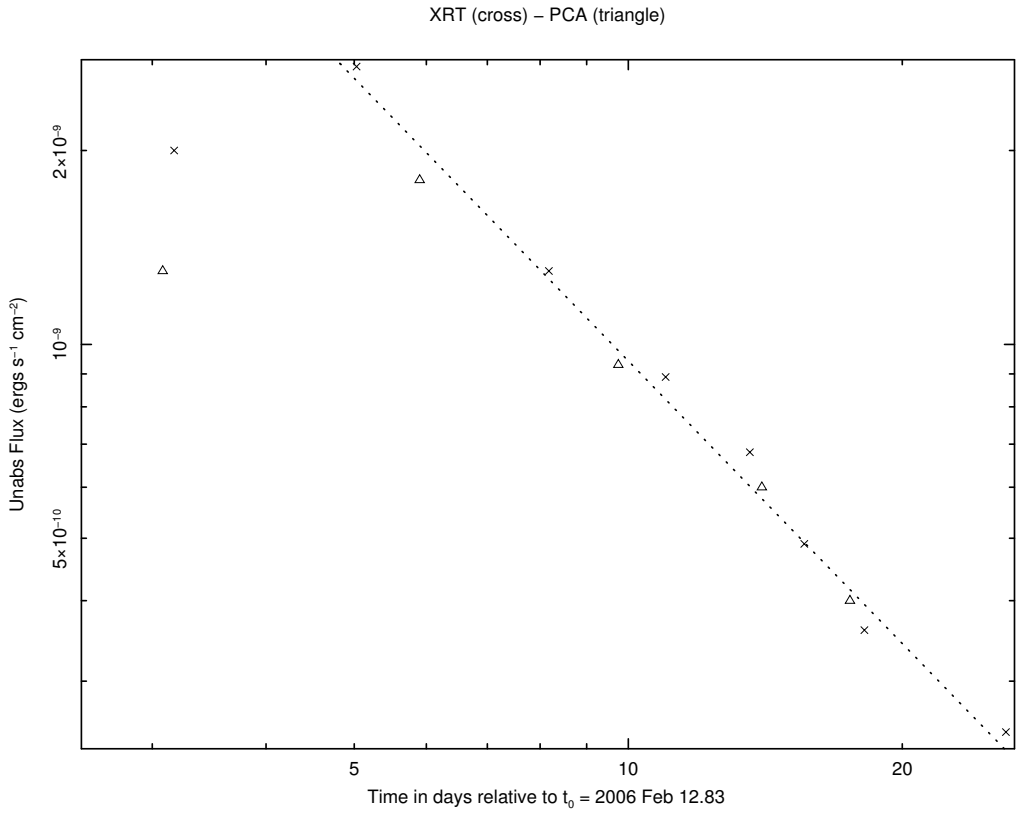

Figure 8.13: *XRT fluxes in the 0.7-10 keV band. PCA fluxes in the same energy band are also plotted. The flux increases for the first 5 days, then decays as a power law with index* $\alpha = 1.5$

expected from a well-cooled shock. The shock velocities v_s derived by putting the temperature values of table 8.4 and 8.5 into equation 8.12 range from $\sim$ 2500 km s^{-1} for t=3d down to $\sim$ 1000 km s^{-1} for t=21d. The values derived from optical spectroscopy are of the same order[227,228,229]. After $t \simeq$10 days, a $t^{-\alpha}$ dependence for v_s can be seen, with $\alpha \simeq 0.6$. As pointed out by Bode *et al.*[222], such value is closer to the expected value of 0.5 for Phase III than to the expected value of 0.33 for Phase II[225]. During the first few days after outburst the gas is too thick for soft X-ray emission to escape, so a large fraction of such photons are absorbed. Such absorption is added to the interstellar absorption ($N_H = (2.4 \pm 0.6) \times 10^{21} cm^{-2}$ as measured by Hjellming *et al.*[210]) resulting in a total absorbing column of $\sim$5.5$\times$ 10^{22} cm^{-2} on day 3. Such absorbing column decreased progressively to normal values after few days. By considering the time dependence (for $t \gtrsim$10 days) of the absorption column from the overlaying red giant wind, Bode *et al.*[222] obtained a similar indication as above: the value of such dependence is closer to that predicted for Phase II. Therefore, such results lead to the conclusion that the remnant moved rapidly into Phase III in the 2006 outburst.

The hard X-ray emission detected by BAT occurred before the first XRT and PCA observations. The fact that the detection is contemporaneous with the discovery time of the outburst suggests a radioactive decay origin for the observed gamma-ray emission. Nevertheless, as discussed by Hernanz[230], such an emission does not correspond either temporally or spectrally with that expected for radioactive decay. As explained above, the prompt gamma-ray emission from novae is expected to happen most probably some days before the maximum in visual magnitude, the time interval depending on the speed class (see also Gomez-Gomar *et al.*[200]). In this case, RS Oph was discovered in outburst in 2006 February 12.83UT. The previous recorded optical observation, performed $\sim$ 1 day before, showed the source still in a quiescent state. Even assuming that the visual maximum occurred during this optical observational gap, hard X-rays were detected after it, differently from what expected. Moreover, such an emission was detected in the 14-25 keV energy band, whereas one expects it to be detectable at higher energies. All these indications seem to point to shocks as the possible origin of the detected emission. However, such a detection provides a demonstration of the efficacy of the approach adopted in this search.

8.3.4 Classical Novae

In this section the results obtained for all the classical novae of the sample shown in Table 8.3 are presented. The analysis method described in section 8.3.2 was adopted.

Detections and Upper limit evaluation

For each nova, all BAT data having the nova in the FOV and covering the interval $t_{discovery} - 20$ days $< t < t_{discovery} + 20$ days were selected. Such data were analysed with the pipeline described in section 3.2 using Table 8.3 as catalog of sources to be fitted. Since the pipeline can analyse many sources at a time, when analysing the data selected for a particular nova, all other novae from Table 8.3 that were in the FOV were included in the analysis. The very large BAT FOV often includes many such novae at a time because these are mainly concentrated in the galactic plane. Since the discovery time of such novae are spread over ∼2 y, for a given nova, results are often available even long before or after its discovery. Following the third item described in section 8.3.2, many triggers above 4σ in at least one energy band and above 2.5σ in at least two energy bands were found, some of which supported by a detection above the signal-to-noise threshold of 3.8 with the *batcelldetect* algorithm. The distribution of the significances obtained in all energy bands for all the novae is compatible with a Gaussian distribution with a mean of zero and a standard deviation of 1.1 (see Figure 8.14), significantly wider than the ideal value of 1.0 and indicating that the error estimates from the fitting process are slightly low. Assuming a Gaussian distribution with mean of zero and a standard deviation of 1.1, the probability that a trigger greater than $>5\sigma$ occurs by chance is $\sim 10^{-6}$. By multiplying such value by the total number of elements of the real distribution (~ 750000), ~ 1 trigger above 5σ is expected to occur by chance. Following the third item described in section 8.3.2, a total of eight triggers above 5σ was found, but none of these was supported by a detection with *batcelldetect*. To obtain a detection, *batcelldetect* tool requires the peak in the image to have the form of the point spread function (PSF), otherwise poor χ^2 is obtained as in the case of the eight triggers above. Thus, such triggers cannot be considered as real.

As regarding the triggers obtained for a given nova following the third item described in section 8.3.2, the ones obtained below 5σ and supported by a *batcelldetect* detection are compatible with the above Gaussian distrbution and generally found outside the 40 days temporal range selected for that nova. Moreover, none of such *batcelldetect* detections of a given nova is either temporally close to another detection or found in at least two energy bands for a given time, thus suggesting the non reality of the detections.

The following step was the search for a positive mean level. Even in this case no significant results were found, only upper limits.

Comparison of the results with theoretical expectations

Because no confirmed detection was found for any of the 17 classical novae analysed, it is interesting to estimate the flux upper limits and to compare them with the expected fluxes given in section 8.2.2. For this purpose a smaller dataset for each nova was selected (5 days before and after $t_{discovery}$) and

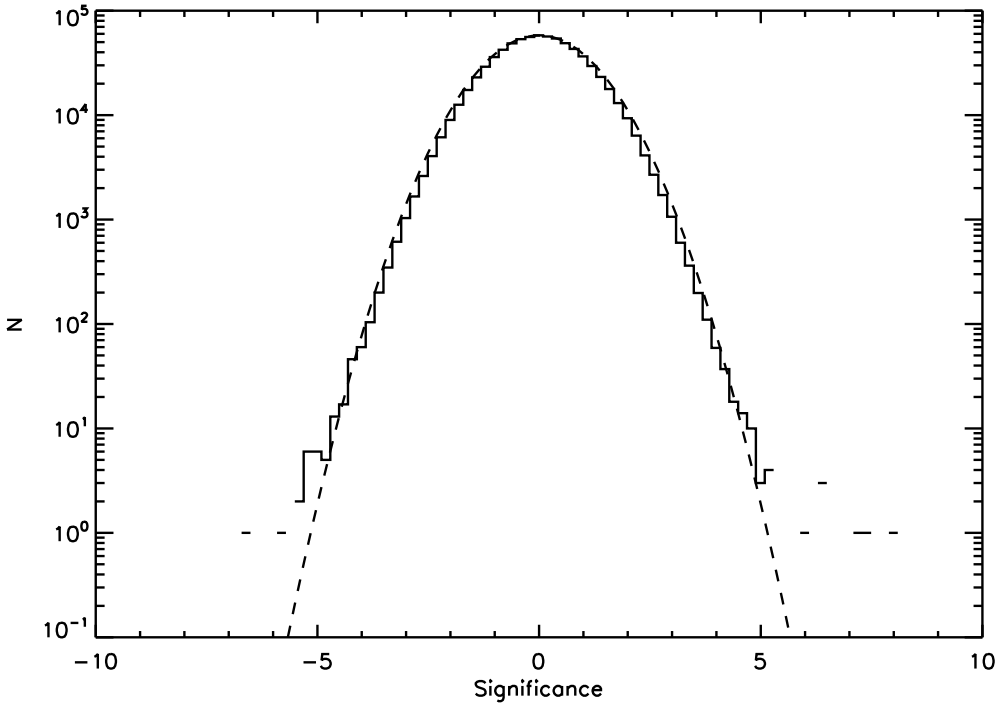

Figure 8.14: *Distribution of the significances in all energy bands for all the novae of Table 8.3 (751655 points). For the analysis, the pipeline described in section 3.2 was used on the dataset described in section 8.3.2). The dashed line represents a Gaussian distribution with standard deviation of 1.1. Assuming such distribution,* ~ 1 *trigger above* 5σ *is expected to occur by chance. The eight triggers found above* 5σ *are not confirmed by the* batcelldetect *algorithm (see text for details).*

lightcurves for each one of the four energy bands described above with different bintimes (1h, 3h, 6h, 12h, 24h) were produced. Then, in every lightcurve, the negative points were discarded. A correction factor due to systematic effects on BAT images was applied to all errors (err) of the other points. The origin of this correction lies mainly in two reasons: first, when constructing the lightcurve of a particular source, the other strong sources in the FOV might be not well subtracted. This is due to the fact that the model used to fit these sources was not completely in agreement with the real distribution. Second, the background is neither uniform nor random. Once again the disagreement between reality and the Poissonian noise models assumed for analysing data introduces some systematic error. The value of this correction factor was roughly estimated for each of the 17 novae using the square root of the reduced χ^2 from the relevant lightcurve. A mean value of 1.57 was found. Each point of the lightcurves was converted into a 3σ upper limit using the formula $uplim = amp + (err * 3 * 1.57)$, where amp is the amplitude in arbitrary units obtained by the pipeline described in section 3.2. In order to convert the upper limits into physical units one can use a reference source for which this conversion is known and the flux and spectral behaviour do not change with time. The Crab nebula was chosen for this purpose. Assuming the same spectral form as for the Crab (a powerlaw with photon index ~ 2.14 and normalization at 1 keV ~ 12), the upper limit amplitudes were converted in real fluxes (ph/cm^2/s) for each of four energy bands. As suggested in a previous section, the BAT coverage is not continuous and the total coverage time within the selected 10 days around $t_{discovery}$ is not the same for each nova. Thus, in order to compare the upper limits found for different novae, the lightcurves were put in a standard form by progressively removing the least constraining limits until a specific temporal coverage (50% and 10%) was obtained. Then, for each lightcurve (i.e. for each nova, energy band and timescale), all the remaining flux upper limits were averaged to obtain a single upper limit.

The expected fluxes were also estimated, for comparison with the measured averaged upper limits. Starting from the values of Table 8.2, the mean expected flux according to those models was calculated both for a CO and for a ONe type nova, using the same timescales and energy bands as for the upper limits. The fluxes of the last energy band of Table 8.2 were rescaled to the 100-195 keV energy band assuming a flat spectrum (reasonable if considering the spectral shape above 100 keV of Figure 8.4). Considering the expected lightcurves of a nova (see Figure 8.4) it is evident that, whichever timescale is selected, the first time bin after the onset of the emission will have the highest flux. Thus, for each nova type, timescale and energy band, the expected flux in this timebin was considered to be compared with the above upper limits. The results for the nova V2362 Cyg are summarised in Figure 8.15 (all other novae lead to similar results).

BAT upper limits are indicated with an arrow. Black symbols show the limits which can be placed on the flux for 10% of the time over the 5 days before

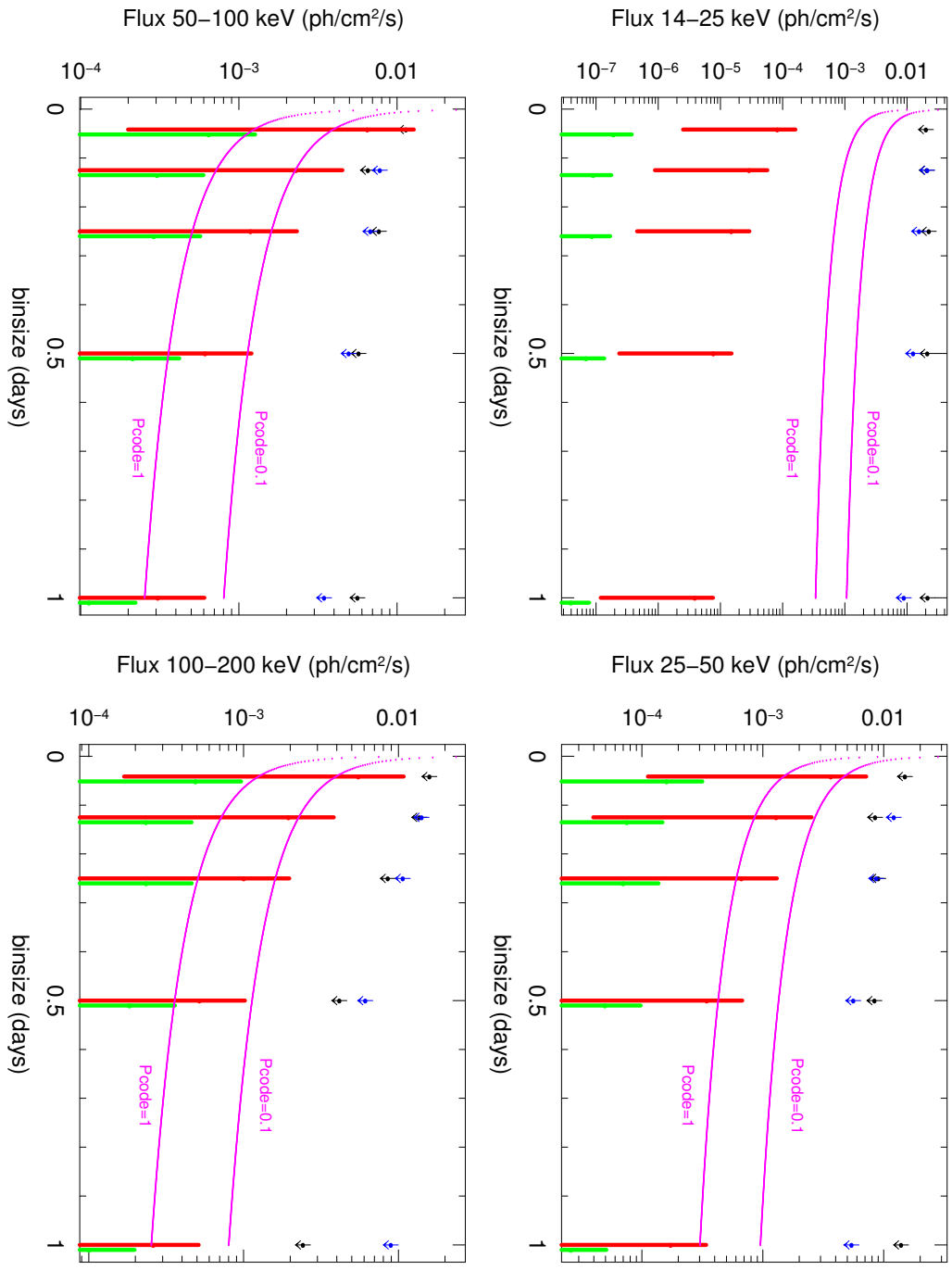

Figure 8.15: *Flux versus timebin duration diagram for the nova V2362 Cyg. BAT upper limits are indicated with arrows (black for a 10%, blue for a 50% dataset temporal coverage). Red lines (CO type) and green lines (ONe type) are the theoretical fluxes: the error bars represent the uncertainty on the distance suggested by the literature. The lower and upper purple curves represent the ideal 3σ BAT sensitivity if the source were seen continously at $n_{c.f.}$=1 and $n_{c.f.}$=0.1 respectively.*

and after the discovery time. Blue show the corresponding limits for 50% of the time. Red lines (CO type) and green lines (ONe type) are the expected flux ranges for a classical nova located at distances taken from literature[217,218]. The lower and upper purple curves represent the predicted 3σ BAT sensitivity if the source were seen at $n_{c.f.}$=1 and $n_{c.f.}$=0.1 respectively according to formula 8.11. Mean values of $r_B(E)$ and $\eta(E)$ for the 4 energy bands were adopted. Figure 8.15 shows a big difference between the ideal BAT sensitivity and measured upper limits. The factor ~ 10 seen in the plot can be entirely explained by the fact that the observed novae are often near the edge of the FOV and that their total integration time for each selected timebin is normally a fraction of the timebin itself, because the BAT coverage is not continuous. From relation 8.11 it is clear that a difference of factor ~ 10 both in $n_{c.f.}$ and in Δt with respect to the lower purple curve in Figure 8.15 translates directly in a difference of threshold flux of $\sqrt{n_{c.f.}\Delta t} \sim 10$. It is clear from Figure 8.15 that the probability of detection is significantly greater for a CO nova than for a ONe nova, but it is important to remember that the expected flux for these two nova types were calculated for different values of WD masses (see section 8.2.2). As expected, the chances of detecting a gamma-ray emission from a nova are greatest for energies greater than 25 keV. For these energies, the expected 3σ BAT sensitivity at $n_{c.f.}$=1 curves are lower than the expected fluxes if the distance of V2362 Cyg would have been 1.5 kpc (as estimated by Czart *et al.*[217]): in this case and given the above assumptions, the nova would have been detected. Table 8.6 shows, among the limits obtained for each nova and percentage of coverage, whichever one is the most constraining (i.e. the upper limit closest to the expected flux in that energy bin and over that timescale, given the likely distance; strictly it is the ratios that are compared). For all novae, the most constraining upper limit ($uplim_{best}$) was always found in the 50-100 keV energy band and generally for shorter timescale (Δt_{best} in Table 8.6). Therefore, when searching for gamma-rays from a nova eruption, the first and stronger peak (related to the ^{13}N decay, see section 8.2.2) is the most probable to be detected.

In order to quantify the distance below which a nova in the BAT FOV at $n_{c.f.}$=1 might be seen, for each energy band, the relevant threshold fluxes for a 1h integration time was compared with the expected fluxes of a type CO and ONe nova as a function of the distance (Figure 8.16).

The intersection between the expected fluxes of a CO (red) or ONe (green) nova with the 3σ BAT sensitivity for a source on-axis (purple line) is the distance out to which one would expect the nova to be detectable: gamma-rays are detectable if the nova is located within $\sim$ 3-4 kpc (CO nova) or $\sim$ 1-2 kpc (ONe nova). But this assumes an ideal situation, while BAT cannot observe the same object on-axis for 1h consecutively. A more realistic situation is given by intersecting, for each energy band, $uplim_{best}$ with the theoretical fluxes of a CO and ONe nova. In Figure 8.16 $uplim_{best}$ values for V2362 Cyg are shown (black lines labeled with arrows). The tightest constraints for

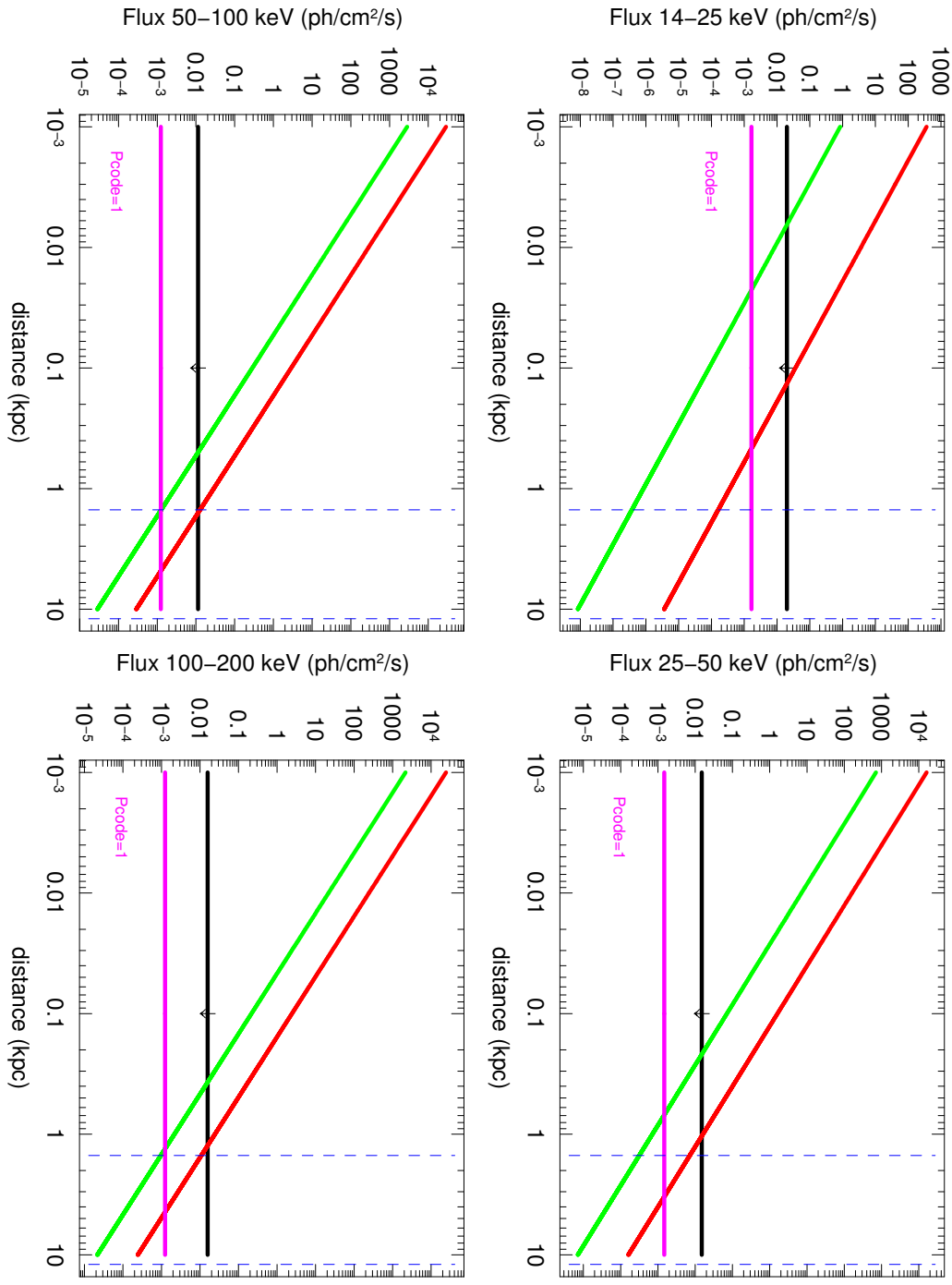

Figure 8.16: *Expected flux versus assumed distance diagram for the nova V2362 Cyg. Red lines (CO type) and green lines (ONe type) are the theoretical fluxes, whereas the purple bar is the predicted 3σ BAT sensitivity for a source on-axis. The upper limit is the best constraint among the different binsizes of Figure 8.15 ($uplim_{best}$), which happens for a detection probability of 10%. Dashed blue lines represent the distances estimated in the literature (see Table 8.3).*

each one of the 17 analysed novae are shown in Table 8.6. For comparison, Table 8.6 also gives the distances estimated from the AAVSO publicly available lightcurves (see *http://www.aavso.org/* website). To obtain these, m_V, t_2 and t_3 were estimated from the AAVSO lightcurves and put into equations 8.4 and 8.7. Where available, the $E(B-V)$ values were taken from IAU Circulars (see Table 8.3), otherwise from a precalculated extinction galactic map[231]. The derived distances must be treated with some caution, because of the large uncertainty in the values of m_V, t_2, t_3 and $E(B-V)$, and in the empirical equation 8.4.

It can be established from Table 8.6 that typically BAT should be able to detect gamma-ray emission from classical novae if these are located at distances smaller than $\sim$ 2 kpc for a CO nova and rather less for a ONe nova. Several factors may contribute to modify this limiting distance. These falls into two categories: theoretical factors and instrumental factors. In section 8.2.2 the predicted fluxes for a CO and ONe type nova at 1 kpc and for a WD mass of 1.15 and 1.25 $M_\odot$ respectively are shown. As discussed in section 8.1.2 the maximum luminosity is an increasing function of the WD mass (see equation 8.2). Therefore the theoretical curves shown in Figures 8.16 can be shifted up if the WD mass is greater than the values indicated above, leading to an increase of the limiting distance.

It is important to bear in mind that rates of the nuclear reactions that occur during a nova explosion are still uncertain: a better knowledge of these rates will give a more precise estimates on the predicted gamma-ray fluxes from novae. Instrumental factors include the temporal coverage and the sensitivity of BAT. The former is not continuous. BAT monitors most of the sky every day but has a FOV of only $\sim$2 steradians, not 4π:therefore it cannot observe continuously the same region of the sky, leading to a possible complete or partial missing of the nova explosion if the detectable emission occurs over very short timescales. The BAT sensitivity falls as the square root of the partial coding fraction $n_{c.f.}$. As a consequence, if the nova is in the fully coded region the distance upper limit will increases. However, assuming that the theories about the emission from novae are correct, the maximum distance at which a nova must be located in order to be detected in the most favorable case is $\sim$ 3-4 kpc (see above).

Nova	m_V	t_2 (days)	t_3 (days)	E(B-V)	M_V	D_{AAVSO} (kpc)	10% coverage time Δt_{best} (hours)	10% coverage time $uplim_{best}$ (ph cm^2 s^{-1})	10% coverage time D_{best} (kpc)	50% coverage time Δt_{best} (hours)	50% coverage time $uplim_{best}$ (ph cm^2 s^{-1})	50% coverage time D_{best} (kpc)
V2361 Cyg	10	5.5 ± 0.5	7 ± 0.5	1.2	$-8.89^{+0.52}_{-0.52}$	$10.80^{+2.29}_{-2.92}$	1	4.4×10^{-3}	2.5	3	3.2×10^{-3}	1.8
V382 Nor	9.7	14.5 ± 2.5	35.5 ± 6.5	1.50-1.51 (*)	$-8.41^{+0.69}_{-0.67}$	$4.8^{+1.8}_{-1.2}$	3	7.0×10^{-3}	1.2 (0.4)	24	4.3×10^{-3}	0.6 (0.3)
V378 Ser	11.6	52 ± 18	95 ± 19	0.74	$-7.07^{+0.59}_{-0.74}$	$18.88^{+5.48}_{-5.91}$	1	7.5×10^{-3}	2.0	12	4.6×10^{-3}	0.8
V5115 Sgr	7.75	4 ± 2	10.5 ± 1.5	0.53	$-8.94^{+0.57}_{-0.57}$	$10.22^{+2.37}_{-3.09}$	1	4.7×10^{-3}	2.5 (0.8)	12	4.2×10^{-3}	0.8 (0.5)
V1663 Aql	10.7	14 ± 6	28.5 ± 8.5	2	$-8.44^{+0.96}_{-0.84}$	$3.88^{+1.24}_{-2.15}$	1	2.0×10^{-3}	3.8 (1.2)	6	1.8×10^{-3}	1.7 (0.9)
V5116 Sgr	7.2	7 ± 4	17 ± 5	0.34-0.57 (*)	$-8.83^{+0.69}_{-0.65}$	$8.3^{+5.1}_{-3.1}$	3	4.1×10^{-3}	1.6 (0.6)	24	4.3×10^{-3}	0.4 (0.1)
V1188 Sco	8.9	12 ± 5	24 ± 7	1.09-1.49 (*)	$-8.57^{+0.85}_{-0.75}$	$4.4^{+4.8}_{-1.9}$	1	4.7×10^{-3}	2.5 (0.8)	3	3.4×10^{-3}	1.7 (0.6)
V1047 Cen	7.4	4.5 ± 1.5	14 ± 3	1.28-1.38 (*)	$-8.92^{+0.56}_{-0.55}$	2.8 ± 0.5	1	6.4×10^{-3}	2.1 (0.7)	3	9.0×10^{-3}	1.1 (0.4)
V477 Sct	10.75	7.5 ± 2.5	12.5 ± 3.5	1.3	$-8.81^{+0.62}_{-0.60}$	$12.74^{+3.07}_{-4.20}$	1	1.2×10^{-2}	1.5 (0.5)	3	7.8×10^{-3}	1.1 (0.4)
V2575 Oph	11	31 ± 2	58 ± 15	1.5	$-7.40^{+0.56}_{-0.57}$	$5.63^{+1.30}_{-1.65}$	1	7.5×10^{-3}	2.0	3	7.9×10^{-3}	1.1
V5117 Sgr	9.9	59 ± 11	84.5 ± 6.5	0.5 ± 0.15	$-7.03^{+0.55}_{-0.58}$	$11.91^{+2.78}_{-3.42}$	1	1.1×10^{-2}	1.6 (0.5)	6	9.7×10^{-3}	0.7 (0.4)
V2362 Cyg	7.75	7 ± 2.5	18 ± 2	0.59	$-8.83^{+0.61}_{-0.60}$	$8.90^{+2.14}_{-2.91}$	1	1.1×10^{-2}	1.6	3	7.8×10^{-3}	1.1
V2576 Oph	9.2	25.5 ± 2.5	45.5 ± 8.5	0.62	$-7.63^{+0.62}_{-0.65}$	$9.58^{+2.47}_{-3.15}$	1	1.2×10^{-2}	1.6	3	5.5×10^{-3}	1.4
V1065 Cen	8.7	19.5 ± 1	30.5 ± 1	?	$-8.02^{+0.57}_{-0.58}$		1	6.5×10^{-3}	2.1 (0.7)	3	7.1×10^{-3}	1.2 (0.4)
V1280 Sco	4	13 ± 1	14.5 ± 1	?	$-8.51^{+0.57}_{-0.56}$		1	5.6×10^{-3}	2.3 (0.7)	3	7.0×10^{-3}	1.2 (0.4)
V1281 Sco	8.8	8 ± 4	22.5 ± 3.5	?	$-8.78^{+0.71}_{-0.66}$		1	5.1×10^{-3}	2.3 (0.7)	3	5.2×10^{-3}	1.4 (0.5)
V2467 Cyg	7.6	8 ± 2	17 ± 4	0.31	$-8.78^{+0.59}_{-0.59}$	$12.13^{+3.78}_{-2.88}$	1	5.8×10^{-3}	2.2 (0.7)	6	6.4×10^{-3}	0.9 (0.5)

Table 8.6: *Summary of the results obtained from BAT data for 17 Classical novae. The values of* m_V, t_2 *and* t_3 *are estimated by AAVSO lightcurves. The extinction is taken from IAU Circulars where indicated, from a precalculated extinction galactic map otherwise (* ;*[231]*). The derived AAVSO distances (*D_{AAVSO}*), calculated with 8.7 formula, must be threated with some caution. For a detection probability of both 10% and 50% the best constraining timescale (*Δt_{best}*), the measured upper limit on the flux (*$uplim_{best}$*) and the limit distance (*D_{best}*) is given (see text for details). If the nova type is unknown, the value of this intersection for a ONe nova is indicated into brackets. The best constraining energy band was 50-100 keV in all the cases.*

Expected rate of detections from a simulated sample of novae

An IDL procedure was written that uses a Monte Carlo approach to quantify the probability of detecting a nova during the *Swift* operating lifetime. It gives the rate of detection expected by BAT by comparing the real BAT observations with a sample of novae generated with a Monte Carlo simulation. Three different models of the spatial distribution in the Galaxy of the simulated novae were used in producing the samples of supposed novae. The same models as for the Jean *et al.*[10] paper were adopted except the oldest one which was described by Higdon & Fowler[232]. Details on the three adopted models are given in Table 8.7.

Model 1[233]: $\rho_h = 3.0$ kpc and $z_h = 0.170$ kpc. K_0 is the modified Bessel function		
Disc $n(z,\rho)$	$= n_d exp\Big(-\frac{\lvert z\rvert}{z_h} - \frac{\rho}{\rho_h}\Big)$	
Bulge $n(R)$	$= n_s 1.04\times 10^6 \Big(\frac{R}{0.482}\Big)^{-1.85}$	$R \leq 0.938 kpc$
	$= n_s 3.53 K_0\Big(\frac{R}{0.667}\Big)$	$R \geq 0.938$
	$= 0$	$R \geq 5kpc$
Model 2[234]: $\rho_h = 5.0$ kpc and $z_h = 0.30$ kpc		
Disc $n(z,\rho)$	$= n_d exp\Big(-\frac{\lvert z\rvert}{z_h} - \frac{\rho}{\rho_h}\Big)$	
Bulge $n(R)$	$= n_s 1.25\Big(\frac{R}{R_\odot}\Big)^{-6/8} exp\Big[-10.093\Big(\frac{R}{R_\odot}\Big)^{1/4} + 10.093\Big]$	$R \leq R_\odot$
	$= n_s\Big(\frac{R}{R_\odot}\Big)^{-7/8}\Big[1 - \frac{0.0867}{\Big(\frac{R}{R_\odot}\Big)^{1/4}}\Big] exp\Big[-10.093\Big(\frac{R}{R_\odot}\Big)^{1/4} + 10.093\Big]$	$R \geq R_\odot$
Model 3[235]: $\rho_h = 5.0$ kpc and $z_h = 0.35$ kpc		
Disc $n(z,\rho)$	$= n_d exp\Big(-\frac{\lvert z\rvert}{z_h} - \frac{\rho}{\rho_h}\Big)$	
Bulge $n(R)$	$= \frac{n_s}{R^3 + 0.343}$	$R \leq 3kpc$
	$= 0$	$R \geq 3kpc$

Table 8.7: *Models of the nova spatial distribution in the Galaxy used for the Monte Carlo simulation[10]. R is the distance to the Galactic Center, z is the distance perpendicular to the Galactic plane and ρ is the galactocentric planar distance. The distance from the Galactic Center to the Sun is* $R_\odot = 8kpc$, n_s *and* n_d *are the normalisation factors for the bulge and the disc respectively (in* kpc^{-3}*). The proportions of novae in the bulge are 0.179 (Model 1), 0.105 (Model 2) and 0.111 (Model 3).*

Each model assumes a different proportion between the novae in the bulge and in the disk. For each model a total of $N_{sim} = 350000$ novae were simulated, choosing for each one a distance from the Sun, a position in the sky (RA and DEC coordinates) and a time ranging from 0 to 10000 years (hereafter such time is referred to as the "explosion time", not the "discovery time"). For each model, the distribution of the distances from the Sun of the simulated novae is shown in Figure 8.17.

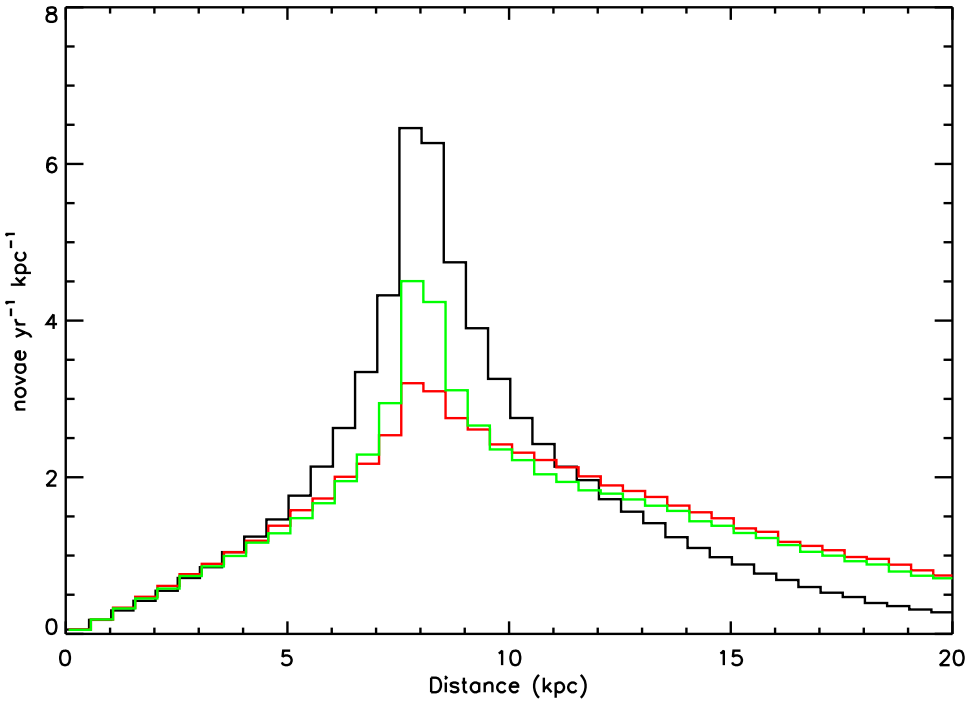

Figure 8.17: *Distribution of the distances from the Sun of the simulated novae. Black, red and green histograms correspond to samples of novae with spatial distribution in the Galaxy as for model 1, 2 and 3 respectively (see Table 8.7).*

The next step was to test whether BAT would have seen the novae given a typical observational scenario. The actual first 2.28 years period of BAT observations were adopted and the 10000 years simulated were mapped onto it assuming a rate of novae in the Galaxy of $r_{expected} = 35 yr^{-1}$[183]. In this way the time of the simulated novae is constrained to fit in the selected 2.28 years of BAT observations for which we have a real observing sequence. Thus the detection rate $r_{detected}$ was estimated by the relationship

$$r_{detected} = r_{expected} * \frac{N_{detected}}{N_{sim}} \tag{8.13}$$

where $N_{detected}$ is the number of detected simulated novae. A nova was assumed to have been detected if all the following conditions were satisfacted:

- the time interval since the nova explosion to the following 48 hours was even partially covered by at least one BAT observation.

- the nova was in the FOV.

- the 5σ sensitivity at the position of the nova in the FOV and for an exposure time equal to that of a given observation was less than the expected flux from the nova in at least one energy band. The expected fluxes were estimated by integrating the lightcurves presented in section 8.2.2 in the given observed time.

The lightcurves presented in section 8.2.2 were produced assuming typical values of WD mass for the ONe and CO nova. In this scenario CO novae release more flux than ONe novae and so the probability of detection is higher for the former. Since the expected gamma-ray flux from a nova depend critically on its WD mass, different results can be achieved using lightcurves of novae with WD masses different from those assumed here. When such lightcurves become available, it will be interesting to perform an update of the work presented below. In any case, it is crucial to know the real ratio of the number of ONe and CO novae. This ratio is usually deduced from the observations of abundances in nova ejecta and it is still largely uncertain. Livio & Truran[236] estimated a fraction of Galactic ONe novae between 11 and 33 percent. The results presented below are given by assuming a reasonable mix of 25% ONe and 75% CO novae in the whole sample (equal proportions both in the disc and in the bulge). Results for a distribution of 100% ONe and 100% CO novae are also shown.

BAT observational time windows of entire DPHs were adopted. For such a choice, the integration time has an average duration of 13 minutes with no gaps. The results for model 1 of Table 8.7 are given in Table 8.8. The other two models led to similar results.

Nova type proportions	Detection rate (yr^{-1}) 14-25 keV	25-50 keV	50-100 keV	100-195 keV
		Model 1		
100% ONe	0	0.0069	0.0393	0.0291
100% CO	0.0024	0.2759	0.6466	0.4459
25% ONe + 75% CO	0.0013	0.2168	0.5155	0.3542

Table 8.8: *Expected detection rates of novae with BAT in four energy bins. A sample of simulated novae assuming a spatial distribution as for model 1 of Table 8.7 and the actual first 2.28 years period of BAT observations were used (see text for details).*

It is clear that in the most favorable case (CO-type nova and 50-100 keV energy band) the chances of detecting a nova during the *Swift* lifetime (predicted to be $\sim$ 10 years) are low but not zero. It is important to note that such rates were obtained assuming $r_{expected} = 35yr^{-1}$: as pointed out in section 8.1.2, although the true occurrence rate is very uncertain, the maximum rate of discoveries obtained up to date ($\sim$ 10 y^{-1}) is much lower. Optically undiscovered novae cannot be retrospectively searched for gamma-ray emission with BAT because their positions and explosion times are unknown, so the values shown in Table 8.8 are upper limits. The origin of the difference between the expected rate of novae in the Galaxy and the observed one can be ascribed to three factors:

1. Some novae erupt when their angular separation from the Sun with respect to the Earth is too small for them to be observable at optical wavelengths (i.e. they are 'daytime' objects). To estimate the fraction of novae which cannot be discovered for such a reason, the distribution of the angular separation from the Sun at the discovery time for the novae of the samples based on model 1, 2 and 3 of Table 8.7 was examined. The threshold angle below which a nova cannot be discovered was fixed by considering the angular separation from the Sun of the novae of Table 8.3 at the time of their discovery: the minimum value is that of RS Oph which was discovered very low at the horizon ($\sim 50^\circ$ from the Sun). Taking this value as a limit, the fraction of novae expected to be missed for this reason is about $\sim$10% for all the three models.

2. A large fraction of novae are too far to be visible because of the interstellar extinction. As one can see in Figure 8.17, the distribution of the distances from the Sun of the simulated novae is peaked at $\sim 8kpc$ with the right tail larger than the left one. Thus, the number of the farthest and more absorbed novae is greater than that of the closer ones.

3. It is possible that some novae have been missed by the astronomers because of a lack of observations. As pointed out at the beginning of this chapter, the rate of discoveries has greatly improved in the last years thanks to the amateurs activity. Figure 8.3 shows that the general trend of discoveries as a function of time is rising and is quite promising if maintained in the future.

Because of the above considerations, it is difficult to evaluate more precisely the values shown in Table 8.8. However, a rough estimate can be done by normalizing each value to the observed rate of 10 novae per year, which gives in the most favorable case a detection rate of $\sim 0.15yr^{-1}$. This procedure is not completely correct because the expected spatial distribution of galactic novae is different from the observed one. However, the observed novae will tend to be preferentially those that are closest, so the detection rate $\sim 0.15yr^{-1}$

is underestimated. Under such assumptions, there is still a non-negligible probability that a nova could be detected during the *Swift* lifetime.

In conclusion, it is useful to estimate from the simulated novae the distribution of the distances from us of the novae that, according to the Monte Carlo simulations, might be detected. Figure 8.18 shows such distribution assuming model 1, the others leading to similar results.

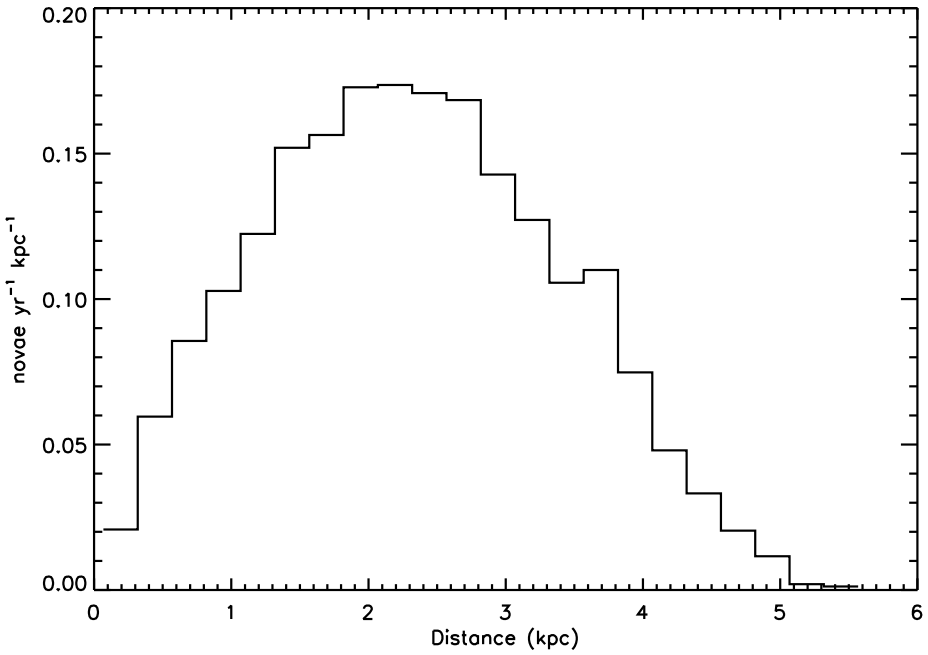

Figure 8.18: *Distribution of the distances from us of the novae detected in gamma-rays in the Monte Carlo simulation. Model 1 was assumed.*

As one can see, the distribution has a peak at ∼2-3 kpc and it extends up to ∼5 kpc. Generally, the probability of detecting a nova decreases monotonically as a function of its distance. The presence of a peak is due to a geometrical factor: since the Earth is at the edge of the galactic disk, the number of sources increase when seeing deeper in the Galaxy. Thus, best probabilities of detecting gamma-rays from novae with BAT are for those located at less than ∼2-3 kpc, although detection of novae at distances up to ∼5 kpc are not completely excluded.

8.4 Future prospects

The search for prompt gamma-ray emission from novae is still an intriguing challenge. As outlined above, many unsuccessful efforts were done in the past to detect the predicted gamma-ray lines or the continuum. The reason of

such negative results mainly lies in the instruments used for the search which were not sufficiently sensitive and complete in coverage. Instead, BAT is a good instrument to search for gamma-ray emission from novae in the energy range 14-195 keV. Its large FOV and good sensitivity will allow few novae to be detected, as described in section 8.3.4. No positive detections were found up to date, but, if *Swift* will be operating for 10 years as predicted and the general assumptions made in previous sections are true, the chances to detect gamma-rays from novae are quite promising.

In the next future, the EXIST mission[237], designed to study the black holes, is expected to provide a breakthrough in the search for gamma-rays from novae. Thanks to its very large collecting area (10 times larger than that of BAT) and pointing strategy it will be able to perform a complete hard X-ray survey every 95 minutes. With such a coverage, it is very difficult to miss the first and stronger peak of gamma-rays from novae. Thus the chances to detect them will greatly increase. Moreover, EXIST will operate in a wider energy range than BAT (10-600 keV) with good sensitivity, covering the 511 keV line and all the continuum down to few keV.

Conclusions

Swift/BAT, owing to its good sensitivity, huge field of view as well as almost uniform coverage of the sky along the mission, is a very useful tool for hard X/gamma-ray astronomy. Due to its characteristics, BAT can be exploited to monitor known, bright X-ray sources with a very good temporal coverage, as well as to serendipitously catch and study interesting transient sources. Moreover, thanks to the huge amount of data collected from the *Swift* launch, it is also possible to perform retrospective searches in the BAT data archive.

No procedures for analysing BAT data have been made available to date from the NASA/GSFC team. In this thesis, a detailed description of new data analysis procedures aimed at exploiting BAT data is given, together with the first astrophysical results on galactic accreting sources.

The main results may be summarized as follows:

1. A new, complete pipeline for BAT survey data analysis, entirely based on public software tools, was created (Pipeline 1). It was designed to provide good-quality spectra and light curves in physical units (i.e. ergs/cm^2/s) for a given source. A "step by step" description of the procedure logic and functionality is given in Chapter 2. Another procedure, composed of public tools and non-standard products, is also described (Pipeline 2). It was designed to provide light curves in arbitrary units of many sources at a time with no contamination from the bright sources in the FOV. Pipeline 2 was developed and tested by Prof. Skinner at the CESR of Toulouse (France). Both the pipelines contain an initial filtering procedure to select a good-quality, reliable dataset.

2. A detailed description of the tests performed on Pipeline 1 to verify the reliability of the results was presented in Chapter 3. A large number of observations ($\sim$7 months) of the steady, very bright Crab was first analysed. It was found that both the flux and photon index values of the spectra are very stable as a function of the source location within the BAT FOV and in good agreement with the values assumed for the BAT instrument calibration. Moreover, the requirements to combine different BAT datasets were estimated. The results suggest that significant flux

losses ($> 5\%$) may occur, especially for target position at low coded fractions, when stacking different data with a pointing offset larger than 2 arcmin. Then, the BH binary GRO J1655-40 during its 2005, 9-months long outburst was used to test the results of Pipeline 1 in the case of a fainter, strongly variable source. The well calibrated *RXTE* was also observing the outburst, allowing the BAT results to be cross-checked against those independently obtained by *RXTE*. The spectral and flux evolution of the outburst was in very good agreement: BAT reproduces *RXTE*/HEXTE fluxes within a 10-15% uncertainty with a 3σ sensitivity of $\sim$20 mCrab for an on-axis source, thus establishing its capabilities to monitor the evolution of relatively bright hard X-ray sources. It is worth noting that the detection of the source activity by *RXTE*/HEXTE and PCA was due to planned observational campaign of the Galactic center region, while BAT caught the outburst since the very beginning simply owing to its good sensitivity over a very large FOV. Had GRO J1655-40 be located outside the galactic bulge region scanned by *RXTE*, its outburst would have been detected by ASM with >15 day delay with respect to BAT.

3. The spectra and light curves obtained with Pipeline 1 for GRO J1655-40 were used to follow its evolution during the rising phase of the 2005 outburst (Chapter 5). Data from *INTEGRAL*/SPI and *RXTE* were also used, but only the BAT ones were decisive: due to the wide temporal coverage of the source serendipitously obtained by BAT, it was possible to clearly observe the transition from the Low Hard State to the High Soft State. An evolution of the high energy component of the emission was noticed during the Low Hard State : it decreased from a value above 200 keV down to 130 keV when the source reached the maximum of luminosity in the gamma-ray domain (above 23-600 keV). During the HSS, the high energy cutoff disappeared. This decrease corresponds to a decrease in the radio flux, and the cutoff disappeared along with the radio jet.

4. The third recorded outburst of the source IGR J08408-4503, not observed by *INTEGRAL* satellite, was studied on BAT data using Pipeline 1. Together with the second outburst, discovered in the *INTEGRAL* data archive, it provided a clear proof that IGR J08408-4503 is a new Super Fast X-ray Transient. In Chapter 6 a detailed study of all the three outbursts was performed. From timing analysis, it was found that a periodicity of the flaring activity from this source can be excluded. By analysing the spectra of all the three events, a spin period of the order of hours with a long orbital period, and a 10^{13} G magnetic field for the NS were inferred. The typical scenario in which outbursts from SFXTs occur because of the clumpy nature of the donor wind, cannot be applied to the case of IGR J08408-4503. The low intrinsic absorption measured during

the flares points towards a sudden accretion onto the magnetic poles of matter previously stored in the magnetosphere during the quiescent phase.

5. Thanks to the huge amount of BAT survey data serendipitously collected in more than ∼1 year, it was possible to unveil the nature of the flaring X-ray binary 4U 1954+319, composed of a Neutron Star and a late type star (Chapter 7). Pipeline 1 was used to extract a light curve from which timing analysis allowed a periodic signal to be determined (∼5.17 hr) as well as a clear spin-up trend with spin-up time scale ($P/\dot{P}$) of $\sim$ 25 years. An orbital origin of such periodicity was ruled out. The inferred magnetic field of the NS is of the order of $B \sim 10^{12}$ G and, from the standard binary pulsar evolutionary picture, it allows the NS to be spun down (via an ejector and a propeller phase) to a few hours on a timescale compatible with the age of the companion star in 4U 1954+319 ($\sim 10^8$-10^9 yr). The spectral and timing characteristics indicate that we are dealing both with the slowest established wind-accreting X-ray pulsar and with the second confirmed member of the emerging class dubbed "symbiotic low mass X-ray binaries" that hosts a neutron star.

6. BAT was also used to search for prompt gamma-ray emission from novae (Chapter 8). A detailed description of the main properties of such systems was given, focusing on the short-lived gamma-ray emission due to downgraded decay of radioactive elements which is predicted to be produced by these objects. Such an emission is hard to detect for many reasons and, in spite of many efforts performed in the past using different instruments, it was never found. BAT is a suitable instrument for this kind of research because of its wide field of view, good sensitivity and pointing strategy. A retrospective search using Pipeline 2 was made in the BAT data for evidence for gamma-ray emission from the direction of 18 novae at around the time of their explosion. The main result was a clear detection in the 14-25 keV band of the RS Ophiuchi 2006 outburst. However, the origin of such emission can be ascribed to the shock between the material ejected from the nova and the dense stellar wind of the companion red giant star. No positive detections were found for all the other novae. The probability of detecting a nova during the *Swift* operating lifetime was estimated using a Monte Carlo approach. Assuming three different models of the spatial distribution in the Galaxy of the simulated novae, and typical gamma-ray fluxes from novae based on the most recent estimations of nuclear reaction rates, it was found that the chance of detecting gamma-rays from novae is low but not null, with highest probability for the novae located at less than ∼2-3 kpc.

The results presented in this thesis are only a small sample of those which can be obtained with BAT survey data. In the next future a more extensive and systematic utilisation of the very good performance of Pipeline 1 will be

carried out, focusing on the monitoring of the spectral and temporal behaviour of bright, Galactic hard-X ray sources. The amount of data collected by the BAT will largely increase as long as the *Swift* mission will be operating, thus providing a huge archive of sensitive data containing information of the sky as observed in the 14-195 keV energy range. Such a database, together with Pipeline 1, is an excellent instrument to study in detail the evolution of different types of sources. For example, they will be widely exploited to observe new and old outbursts of Galactic microquasars. The advantageous possibility, provided by the BAT, to almost continuously observe a given celestial direction will yield a very good coverage of such sources during their transitional states, and, therefore, it will allow a better characterisation of such states to be performed. A multi-wavelength campaign of observations coordinated with the BAT ones could be of great interest to understand the role played by the high energy cutoff and the mechanism that powers the radio jets in microquasars.

Then, given the good temporal coverage of the sources and the good sensitivity of the BAT, Pipeline 1 can be easily used to search for old and new outbursts of interesting hard X-ray transients such as the SFXTs. Our knowledge of these sources is very poor, thus the discovery of new outbursts is of crucial importance to improve it. It is still not clear if the ouburst periodicity is a common characteristic of the SFXTs or IGR J11215-5952 is a unique/rare case. The periodic nature of some known SFXTs could probably have been occulted because *INTEGRAL* missed some short outbursts. BAT may help in this direction, as its coverage is more complete than the *INTEGRAL* one and a possible periodic nature of such sources could be unveiled. Moreover, the good spectral performance of Pipeline 1 can be well exploited in this case to study the spectral properties of the SFXTs during their short flares. This information may help to constrain a reasonable model which can explain such short and bright emissions.

Another interesting study that can be deepened thanks to BAT is a long-term characterisation of the evolution of the NS spin period of some peculiar X-ray binaries. As for the case of 4U 1954+319, the timing analysis of this kind of sources, performed over a long time period, could yield crucial information about the spin period evolution of the NSs in accreting binary systems as well as their magnetic field. Moreover, very recently *INTEGRAL* discovered a large amount of new X-ray binaries, many of which have periodicities not yet understood. A good temporal coverage of such sources is again of crucial importance to clearly determine the period variations (if any) and possibly to infer the nature of such periodicities.

Finally, following the encouraging estimations of detecting gamma-rays from novae with BAT, a systematic search for such an emission will continue for the novae which will explode in the next years. The estimated rate of detection of the order of ~ 0.5 y$^{-}1$ is quite promising as compared with the expectations made for previous gamma-ray instruments. Moreover, if the rate of discoveries at optical wavelengths will increse in the following years, as expected, due to

the increasing activity of amateurs observers, it can be concluded that good chances to detect for the first time gamma-rays from novae are guaranteed before the end of the *Swift* mission. Such a detection would provide strong constraints on the theoretical models which can be adopted to successful describe such a kind of explosion. The discovery of a nova close enough to us should allow this intriguing challenge to be won.

Bibliography

1. Bildsten, L. *et al.* Observations of Accreting Pulsars. ApJS **113**, 367–+ (1997).

2. Shaposhnikov, N. *et al.* GRO J1655-40: Early Stages of the 2005 Outburst. ApJ **655**, 434–446 (2007).

3. Hernanz, M. Classical nova explosions. In *ASP Conf. Ser. 330: The Astrophysics of Cataclysmic Variables and Related Objects* (eds. Hameury, J.-M. & Lasota, J.-P.), 265–+ (2005).

4. Tauris, T. M. & van den Heuvel, E. Formation and Evolution of Compact Stellar X-ray Sources. *ArXiv Astrophysics e-prints* (2003).

5. Gehrels, N. *et al.* The Swift Gamma-Ray Burst Mission. ApJ **611**, 1005–1020 (2004).

6. Lamers, H. J. G. L. M., Snow, T. P. & Lindholm, D. M. Terminal Velocities and the Bistability of Stellar Winds. ApJ **455**, 269–+ (1995).

7. Darnley, M. J. *et al.* Classical novae from the POINT-AGAPE microlensing survey of M31 - I. The nova catalogue. MNRAS **353**, 571–588 (2004).

8. Coc, A., Hernanz, M., José, J. & Thibaud, J.-P. Influence of new reaction rates on ^{18}F production in novae. A&A **357**, 561–571 (2000).

9. Hernanz, M., José, J., Coc, A., Gómez-Gomar, J. & Isern, J. Gamma-Ray Emission from Novae Related to Positron Annihilation: Constraints on its Observability Posed by New Experimental Nuclear Data. ApJ **526**, L97–L100 (1999).

10. Jean, P., Hernanz, M., Gómez-Gomar, J. & José, J. Galactic 1.275-MeV emission from ONe novae and its detectability by INTEGRAL/SPI. MNRAS **319**, 350–364 (2000).

11. Giacconi, R., Gursky, H., Paolini, F. R. & Rossi, B. B. Evidence for x Rays From Sources Outside the Solar System. *Physical Review Letters* **9**, 439–443 (1962).

12. Schreier, E. *et al.* Evidence for the Binary Nature of Centaurus X-3 from UHURU X-Ray Observations. ApJ **172**, L79+ (1972).

13. Webster, B. L. & Murdin, P. Cygnus X-1–a Spectroscopic Binary with a Heavy Companion? Nature **235**, 37–+ (1972).

14. Bolton, C. T. Identification of Cygnus X-1 with HDE 226868. Nature **235**, 271–273 (1972).

15. Giacconi, R., Gursky, H., Kellogg, E., Schreier, E. & Tananbaum, H. Discovery of Periodic X-Ray Pulsations in Centaurus X-3 from UHURU. ApJ **167**, L67+ (1971).

16. Grindlay, J. *et al.* Discovery of intense X-ray bursts from the globular cluster NGC 6624. ApJ **205**, L127–L130 (1976).

17. Mirabel, I. F. & Rodriguez, L. F. A Superluminal Source in the Galaxy. Nature **371**, 46–+ (1994).

18. Barziv, O., Kaper, L., Van Kerkwijk, M. H., Telting, J. H. & Van Paradijs, J. The mass of the neutron star in Vela X-1. A&A **377**, 925–944 (2001).

19. van der Klis, M. *et al.* Discovery of Submillisecond Quasi-periodic Oscillations in the X-Ray Flux of Scorpius X-1. ApJ **469**, L1+ (1996).

20. Miller, J. M. *et al.* Resolving the Composite Fe Kα Emission Line in the Galactic Black Hole Cygnus X-1 with Chandra. ApJ **578**, 348–356 (2002).

21. Pringle, J. E. & Rees, M. J. Accretion Disc Models for Compact X-Ray Sources. A&A **21**, 1–+ (1972).

22. Henrichs, H. F. *Accretion-Driven Stellar X-ray Sources* (ed. W.H.G. Lewin and E.P.J. van den Heuvel (Cambridge and New York: Cambridge University Press), 1983).

23. Frank, J., King, A. & Raine, D. *Accretion Power in Astrophysics* (Accretion Power in Astrophysics, ISBN 0521408636, Cambridge University Press, 1992., 1992).

24. King, A. *X-ray Binaries* (eds. W.H.G. Lewin, J. van Paradijs, E.P.J. van den Heuvel. Cambridge Univ. Press, 419, 1995).

25. Shapiro, S. L., Lightman, A. P. & Eardley, D. M. A two-temperature accretion disk model for Cygnus X-1 - Structure and spectrum. ApJ **204**, 187–199 (1976).

26. Petterson, J. A. On the occurrence of streams and disks in massive X-ray binary systems. ApJ **224**, 625–630 (1978).

27. Vasyliunas, V. M. Theories of magnetospheres around accreting compact objects. *Space Science Reviews* **24**, 609–634 (1979).

28. Davidson, K. & Ostriker, J. P. Neutron-Star Accretion in a Stellar Wind: Model for a Pulsed X-Ray Source. ApJ **179**, 585–598 (1973).

29. Illarionov, A. F. & Sunyaev, R. A. Why the Number of Galactic X-ray Stars Is so Small? A&A **39**, 185–+ (1975).

30. Stella, L., White, N. E. & Rosner, R. Intermittent stellar wind accretion and the long-term activity of Population I binary systems containing an X-ray pulsar. ApJ **308**, 669–679 (1986).

31. Maraschi, L., Traversini, R. & Treves, A. A model for A 0538-066 - The fast flaring pulsar. MNRAS **204**, 1179–1184 (1983).

32. Shapiro, S. L. & Teukolsky, S. A. *Black holes, white dwarfs, and neutron stars: The physics of compact objects* (Research supported by the National Science Foundation. New York, Wiley-Interscience, 1983, 663 p., 1983).

33. Kato, S., Fukue, J. & Mineshige, S. (eds.). *Black-hole accretion disks* (1998).

34. Ghosh, P. & Lamb, F. K. Accretion by rotating magnetic neutron stars. III - Accretion torques and period changes in pulsating X-ray sources. ApJ **234**, 296–316 (1979).

35. Lamb, F. K. & Ghosh, P. *Interaction of accretion disks with magnetospheres*, 37–+ (Particle Acceleration Near Accreting Compact Objects, 1991).

36. van Paradijs, J. On the Accretion Instability in Soft X-Ray Transients. ApJ **464**, L139+ (1996).

37. King, A. R., Kolb, U. & Burderi, L. Black Hole Binaries and X-Ray Transients. ApJ **464**, L127+ (1996).

38. van der Klis, M. Millisecond Oscillations in X-ray Binaries. ARA&A **38**, 717–760 (2000).

39. Miller, M. C., Lamb, F. K. & Psaltis, D. Sonic-Point Model of Kilohertz Quasi-periodic Brightness Oscillations in Low-Mass X-Ray Binaries. ApJ **508**, 791–830 (1998).

40. Mirabel, I. F. *et al.* Accretion instabilities and jet formation in GRS 1915+105. A&A **330**, L9–L12 (1998).

41. Corbel, S. *et al.* Coupling of the X-ray and radio emission in the black hole candidate and compact jet source GX 339-4. A&A **359**, 251–268 (2000).

42. Lewin, W., van Paradijs, J. & Taam, R. *X-ray binaries* (Cambridge University Press, 1995., 1996).

43. Kato, M. Neutron star wind. PASJ **35**, 33–46 (1983).

44. Kuulkers, E. *et al.* Photospheric radius expansion X-ray bursts as standard candles. A&A **399**, 663–680 (2003).

45. Cornelisse, R., Heise, J., Kuulkers, E., Verbunt, F. & in't Zand, J. J. M. The longest thermonuclear X-ray burst ever observed?. A BeppoSAX Wide Field Camera observation of 4U 1735-44. A&A **357**, L21–L24 (2000).

46. Psaltis, D. Accreting Neutron Stars and Black Holes: A Decade of Discoveries. *ArXiv Astrophysics e-prints* (2004).

47. Winkler, C. *et al.* The INTEGRAL mission. A&A **411**, L1–L6 (2003).

48. Ubertini, P. *et al.* IBIS: The Imager on-board INTEGRAL. A&A **411**, L131–L139 (2003).

49. Bodaghee, A. *et al.* A description of sources detected by INTEGRAL during the first 4 years of observations. A&A **467**, 585–596 (2007).

50. Bird, A. J. *et al.* The Third IBIS/ISGRI Soft Gamma-Ray Survey Catalog. ApJS **170**, 175–186 (2007).

51. Bird, A. J. *et al.* The Second IBIS/ISGRI Soft Gamma-Ray Survey Catalog. ApJ **636**, 765–776 (2006).

52. McClintock, J. E. & Remillard, R. A. *Black hole binaries*, 157–213 (Compact stellar X-ray sources, 2006).

53. Narayan, R. & Yi, I. Advection-dominated Accretion: Underfed Black Holes and Neutron Stars. ApJ **452**, 710–+ (1995).

54. George, I. M. & Fabian, A. C. X-ray reflection from cold matter in active galactic nuclei and X-ray binaries. MNRAS **249**, 352–367 (1991).

55. Gallo, E., Fender, R. P. & Pooley, G. G. A universal radio-X-ray correlation in low/hard state black hole binaries. MNRAS **344**, 60–72 (2003).

56. Homan, J. & Belloni, T. The Evolution of Black Hole States. Ap&SS **300**, 107–117 (2005).

57. Corbel, S., Fender, R. P., Tomsick, J. A., Tzioumis, A. K. & Tingay, S. On the Origin of Radio Emission in the X-Ray States of XTE J1650-500 during the 2001-2002 Outburst. ApJ **617**, 1272–1283 (2004).

58. Esin, A. A., McClintock, J. E. & Narayan, R. Advection-dominated Accretion and the Spectral States of Black Hole X-Ray Binaries: Application to Nova MUSCAE 1991. ApJ **489**, 865–+ (1997).

59. Narayan, R. & Yi, I. Advection-dominated accretion: A self-similar solution. ApJ **428**, L13–L16 (1994).

60. Quataert, E. & Narayan, R. Spectral Models of Advection-dominated Accretion Flows with Winds. ApJ **520**, 298–315 (1999).

61. Negueruela, I., Smith, D. M., Reig, P., Chaty, S. & Torrejón, J. M. Supergiant Fast X-ray Transients: a new class of high mass X-ray binaries unveiled by INTEGRAL. In *The X-ray Universe 2005* (ed. Wilson, A.), vol. 604 of *ESA Special Publication*, 165–170 (2006).

62. Sguera, V. *et al.* INTEGRAL observations of recurrent fast X-ray transient sources. A&A **444**, 221–231 (2005).

63. in't Zand, J. J. M. Chandra observation of the fast X-ray transient IGR J17544-2619: evidence for a neutron star? A&A **441**, L1–L4 (2005).

64. Negueruela, I., Smith, D. M., Harrison, T. E. & Torrejón, J. M. The Optical Counterpart to the Peculiar X-Ray Transient XTE J1739-302. ApJ **638**, 982–986 (2006).

65. Smith, D. M. *et al.* XTE J1739-302 as a Supergiant Fast X-Ray Transient. ApJ **638**, 974–981 (2006).

66. Sidoli, L., Paizis, A. & Mereghetti, S. IGR J11215-5952: a hard X-ray transient displaying recurrent outbursts. A&A **450**, L9–L12 (2006).

67. Verbunt, F. & van den Heuvel, E. *X-ray Binaries* (eds. W.H.G. Lewin, J. van Paradijs and E.P.J. van den Heuvel (Cambridge: Cambridge Univ. Press), 457, 1995).

68. Kalogera, V. & Webbink, R. F. Formation of Low-Mass X-Ray Binaries. I. Constraints on Hydrogen-rich Donors at the Onset of the X-Ray Phase. ApJ **458**, 301–+ (1996).

69. Davidsen, A., Malina, R. & Bowyer, S. The optical counterpart of GX 1 + 4 - A symbiotic star. ApJ **211**, 866–871 (1977).

70. Iben, I. J. & Tutukov, A. V. On the Evolution of Symbiotic Stars and Other Binaries with Accreting Degenerate Dwarfs. ApJS **105**, 145–+ (1996).

71. Garcia, M. *et al.* Identification and properties of the M giant/X-ray system HD 154791 = 2A 1704+241. ApJ **267**, 291–300 (1983).

72. Piran, T. The physics of gamma-ray bursts. *Reviews of Modern Physics* **76**, 1143–1210 (2005).

73. Levine, A. M. *et al.* The HEAO 1 A-4 catalog of high-energy X-ray sources. ApJS **54**, 581–617 (1984).

74. Markwardt, C. B. *et al.* The Swift/BAT High-Latitude Survey: First Results. ApJ **633**, L77–L80 (2005).

75. Barthelmy, S. D. *et al.* The Burst Alert Telescope (BAT) on the SWIFT Midex Mission. *Space Science Reviews* **120**, 143–164 (2005).

76. Caroli, E., Stephen, J. B., di Cocco, G., Natalucci, L. & Spizzichino, A. Coded aperture imaging in X- and gamma-ray astronomy. *Space Science Reviews* **45**, 349–403 (1987).

77. Dicke, R. H. Scatter-Hole Cameras for X-Rays and Gamma Rays. ApJ **153**, L101+ (1968).

78. Skinner, G. K., Ponman, T. J., Hammersley, A. P. & Eyles, C. J. Techniques for the analysis of data from coded-mask X-ray telescopes. Ap&SS **136**, 337–349 (1987).

79. Burrows, D. N. *et al.* The Swift X-Ray Telescope. *Space Science Reviews* **120**, 165–195 (2005).

80. Roming, P. W. A., Hunsberger, S. D., Nousek, J. A., Mason, K. O. & Breeveld, A. A. The Swift Ultra-Violet/Optical Telescope. In *Bulletin of the American Astronomical Society*, vol. 35 of *Bulletin of the American Astronomical Society*, 765–+ (2003).

81. Krimm, H. *et al.* Announcement of the Swift/BAT Hard X-ray Transient Monitor. *The Astronomer's Telegram* **904**, 1–+ (2006).

82. Senziani, F. *et al.* Using GRO J1655-40 to test Swift/BAT as a monitor for bright hard X-ray sources. A&A **476**, 1297–1305 (2007).

83. Groh, G., Hayat, G. S. & Stroke, G. W. X-ray and gamma -ray imaging with multiple-pinehole cameras using a posteriori image synthesis. Appl. Opt. **11**, 931–933 (1972).

84. Brown, C. Multiplex imaging with multiple-pinhole cameras. *Journal of Applied Physics* **45**, 1806–1811 (1974).

85. Cannon, T. M. & Fenimore, E. E. Coded aperture imaging - many holes make light work. *Opt. Eng.* **19**, 283–289 (1980).

86. Markwardt, C. B. & Swank, J. H. New Outburst of GRO J1655-40? *The Astronomer's Telegram* **414**, 1–+ (2005).

87. Ulrich-Demoulin, M.-H. & Molendi, S. The ROSAT-PSPC Spectrum of Bright Low-z Quasars. ApJ **457**, 77–+ (1996).

88. Zhang, S. N. *et al.* Broadband High-Energy Observations of the Superluminal Jet Source GRO J1655-40 during an Outburst. ApJ **479**, 381–+ (1997).

89. Hynes, R. I. *et al.* The 1996 outburst of GRO J1655-40: the challenge of interpreting the multiwavelength spectra. MNRAS **300**, 64–82 (1998).

90. Zhang, S. N., Harmon, B. A., Paciesas, W. S., Wilson, C. A. & Fishman, G. J. X-Ray Nova in Scorpius. IAU Circ. **6106**, 1–+ (1994).

91. Kuulkers, E. *et al.* Turmoil on the accretion disk of GRO J1655-40. A&A **358**, 993–1000 (2000).

92. Mendez, M., Belloni, T. & van der Klis, M. "Canonical" Black Hole States in the Superluminal Source GRO J1655-40. ApJ **499**, L187+ (1998).

93. Bailyn, C. D. *et al.* The Optical Counterpart of the Superluminal Source GRO:J1655-40. Nature **374**, 701–+ (1995).

94. Greene, J., Bailyn, C. D. & Orosz, J. A. Optical and Infrared Photometry of the Microquasar GRO J1655-40 in Quiescence. ApJ **554**, 1290–1297 (2001).

95. Hjellming, R. M. & Rupen, M. P. Episodic Ejection of Relativistic Jets by the X-Ray Transient GRO:J1655-40. Nature **375**, 464–+ (1995).

96. Foellmi, C., Depagne, E., Dall, T. H. & Mirabel, I. F. On the distance of GRO J1655-40. A&A **457**, 249–255 (2006).

97. Tingay, S. J. *et al.* Relativistic Motion in a Nearby Bright X-Ray Source. Nature **374**, 141–+ (1995).

98. Brocksopp, C. *et al.* The 2005 outburst of GRO J1655-40: spectral evolution of the rise, as observed by Swift. MNRAS **365**, 1203–1214 (2006).

99. Vedrenne, G. *et al.* SPI: The spectrometer aboard INTEGRAL. A&A **411**, L63–L70 (2003).

100. Torres, M. A. P., Steeghs, D., Jonker, P. & Martini, P. A NIR Observation of GRO J1655-40. *The Astronomer's Telegram* **417**, 1–+ (2005).

101. Joinet, A. *et al.* State Transition and Flaring Activity of IGR J17464-3213/H1743-322 with INTEGRAL SPI. ApJ **629**, 1008–1016 (2005).

102. Bradt, H. V., Rothschild, R. E. & Swank, J. H. X-ray timing explorer mission. A&AS **97**, 355–360 (1993).

103. Rothschild, R. E. *et al.* In-Flight Performance of the High-Energy X-Ray Timing Experiment on the Rossi X-Ray Timing Explorer. ApJ **496**, 538–+ (1998).

104. Tomsick, J. A., Corbel, S. & Kaaret, P. X-Ray Observations of XTE J1550-564 during the Decay of the 2000 Outburst. I. Chandra and RXTE Energy Spectra. ApJ **563**, 229–238 (2001).

105. Arnaud, K. A. XSPEC: The First Ten Years. In *Astronomical Data Analysis Software and Systems V* (eds. Jacoby, G. H. & Barnes, J.), vol. 101 of *Astronomical Society of the Pacific Conference Series*, 17–+ (1996).

106. van der Hooft, F., Heemskerk, M. H. M., Alberts, F. & van Paradijs, J. The quiescence optical light curve of Nova Scorpii 1994 (=GRO J1655-40). A&A **329**, 538–550 (1998).

107. Mitsuda, K. *et al.* Energy spectra of low-mass binary X-ray sources observed from TENMA. PASJ **36**, 741–759 (1984).

108. Díaz Trigo, M., Parmar, A. N., Miller, J., Kuulkers, E. & Caballero-García, M. D. XMM-Newton and INTEGRAL spectroscopy of the microquasar GRO J1655-40 during its 2005 outburst. A&A **462**, 657–666 (2007).

109. Magdziarz, P. & Zdziarski, A. A. Angle-dependent Compton reflection of X-rays and gamma-rays. MNRAS **273**, 837–848 (1995).

110. Titarchuk, L. Generalized Comptonization models and application to the recent high-energy observations. ApJ **434**, 570–586 (1994).

111. Sunyaev, R. A. & Titarchuk, L. G. Comptonization of X-rays in plasma clouds - Typical radiation spectra. A&A **86**, 121–138 (1980).

112. Zdziarski, A. A., Poutanen, J., Paciesas, W. S. & Wen, L. Understanding the Long-Term Spectral Variability of Cygnus X-1 with Burst and Transient Source Experiment and All-Sky Monitor Observations. ApJ **578**, 357–373 (2002).

113. Belloni, T. *et al.* The evolution of the timing properties of the black-hole transient GX 339-4 during its 2002/2003 outburst. A&A **440**, 207–222 (2005).

114. Remillard, R. A. & McClintock, J. E. X-Ray Properties of Black-Hole Binaries. ARA&A **44**, 49–92 (2006).

115. Zdziarski, A. A., Gierliński, M., Rao, A. R., Vadawale, S. V. & Mikołajewska, J. GRS 1915+105: the distance, radiative processes and energy-dependent variability. MNRAS **360**, 825–838 (2005).

116. Poutanen, J. & Fabian, A. C. Spectral evolution of magnetic flares and time lags in accreting black hole sources. MNRAS **306**, L31–L37 (1999).

117. Malzac, J. *et al.* Bimodal spectral variability of <ASTROBJ>Cygnus X-1</ASTROBJ> in an intermediate state. A&A **448**, 1125–1137 (2006).

118. Titarchuk, L., Mastichiadis, A. & Kylafis, N. D. X-Ray Spectral Formation in a Converging Fluid Flow: Spherical Accretion into Black Holes. ApJ **487**, 834–+ (1997).

119. Beloborodov, A. M. Electron-positron outflows from gamma-ray emitting accretion discs. MNRAS **305**, 181–189 (1999).

120. Fender, R. *et al.* Quenching of the Radio Jet during the X-Ray High State of GX 339-4. ApJ **519**, L165–L168 (1999).

121. Grove, J. E. *et al.* Gamma-Ray Spectral States of Galactic Black Hole Candidates. ApJ **500**, 899–+ (1998).

122. McConnell, M. L. *et al.* A High-Sensitivity Measurement of the MeV Gamma-Ray Spectrum of Cygnus X-1. ApJ **543**, 928–937 (2000).

123. McConnell, M. L. *et al.* The Soft Gamma-Ray Spectral Variability of Cygnus X-1. ApJ **572**, 984–995 (2002).

124. Beloborodov, A. M. Plasma Ejection from Magnetic Flares and the X-Ray Spectrum of Cygnus X-1. ApJ **510**, L123–L126 (1999).

125. Malzac, J., Beloborodov, A. M. & Poutanen, J. X-ray spectra of accretion discs with dynamic coronae. MNRAS **326**, 417–427 (2001).

126. Walter, R. *et al.* XMM-Newton and INTEGRAL observations of new absorbed supergiant high-mass X-ray binaries. A&A **453**, 133–143 (2006).

127. Sguera, V. *et al.* Unveiling Supergiant Fast X-Ray Transient Sources with INTEGRAL. ApJ **646**, 452–463 (2006).

128. Gotz, D. *et al.* Outburst of a new source IGR J08408-4503 detected by INTEGRAL. *The Astronomer's Telegram* **813**, 1–+ (2006).

129. Masetti, N. *et al.* Emission-line early-type stars as possible optical counterparts of INTEGRAL hard X-ray sources IGR J08408-4503 and IGR J15539-6142. *The Astronomer's Telegram* **815**, 1–+ (2006).

130. Walborn, N. R. The space distribution of the O stars in the solar neighborhood. AJ **78**, 1067–1073 (1973).

131. Humphreys, R. M. Studies of luminous stars in nearby galaxies. I. Supergiants and O stars in the Milky Way. ApJS **38**, 309–350 (1978).

132. Schröder, S. E., Kaper, L., Lamers, H. J. G. L. M. & Brown, A. G. A. On the Hipparcos parallaxes of O stars. A&A **428**, 149–157 (2004).

133. Kennea, J. A. & Campana, S. Swift/XRT observation of IGR J08408-4503. *The Astronomer's Telegram* **818**, 1–+ (2006).

134. Barba, R., Gamen, R. & Morrell, N. HD 74194, a new binary supergiant fast X-ray transient?, possible optical counterpart of INTEGRAL hard X-ray source IGR J08408-4503. *The Astronomer's Telegram* **819**, 1–+ (2006).

135. Pellizza, L. J., Chaty, S. & Negueruela, I. <ASTROBJ>IGR J17544-2619</ASTROBJ>: a new supergiant fast X-ray transient revealed by optical/infrared observations. A&A **455**, 653–658 (2006).

136. Conti, P. S., Leep, E. M. & Lorre, J. J. Spectroscopic studies of O-type stars. VIII - Radial velocities and the K-term. ApJ **214**, 759–772 (1977).

137. Mereghetti, S., Sidoli, L., Paizis, A. & Gotz, D. IGR J08408-4503 is a recurrent transient. *The Astronomer's Telegram* **814**, 1–+ (2006).

138. Ziaeepour, H. *et al.* IGR J08408-4503 (= v* LM vel): Swift detection of a transient. *GRB Coordinates Network* **5687**, 1–+ (2006).

139. Götz, D. *et al.* IGR J08408-4503: A New Recurrent Supergiant Fast X-Ray Transient. ApJ **655**, L101–L104 (2007).

140. Lebrun, F. *et al.* ISGRI: The INTEGRAL Soft Gamma-Ray Imager. A&A **411**, L141–L148 (2003).

141. Lund, N. *et al.* JEM-X: The X-ray monitor aboard INTEGRAL. A&A **411**, L231–L238 (2003).

142. Lutovinov, A. *et al.* INTEGRAL insight into the inner parts of the Galaxy. High mass X-ray binaries. A&A **444**, 821–829 (2005).

143. White, N. E., Swank, J. H. & Holt, S. S. Accretion powered X-ray pulsars. ApJ **270**, 711–734 (1983).

144. Rubin, B. C. *et al.* Observations of 4U 1700-37 with BATSE. ApJ **459**, 259–+ (1996).

145. Dickey, J. M. & Lockman, F. J. H I in the Galaxy. ARA&A **28**, 215–261 (1990).

146. Heap, S. R. & Corcoran, M. F. Properties of the massive X-ray binary 4U 1700 - 37 = HD 153919. ApJ **387**, 340–346 (1992).

147. Lamers, H. J. G. L. M. & Cassinelli, J. P. *Introduction to Stellar Winds* (Introduction to Stellar Winds, by Henny J. G. L. M. Lamers and Joseph P. Cassinelli, pp. 452. ISBN 0521593980. Cambridge, UK: Cambridge University Press, June 1999., 1999).

148. Filliatre, P. & Chaty, S. The Optical/Near-Infrared Counterpart of the INTEGRAL Obscured Source IGR J16318-4848: An sgB[e] in a High-Mass X-Ray Binary? ApJ **616**, 469–484 (2004).

149. Blondin, J. M. The shadow wind in high-mass X-ray binaries. ApJ **435**, 756–766 (1994).

150. Bondi, H. & Hoyle, F. On the mechanism of accretion by stars. MNRAS **104**, 273–+ (1944).

151. La Barbera, A., Santangelo, A., Orlandini, M. & Segreto, A. A pulse phase-dependent spectroscopic study of Vela X-1 in the 8-100 keV band. A&A **400**, 993–1005 (2003).

152. Falanga, M. *et al.* On the maximum efficiency of the propeller mass-ejection mechanism. A&A **464**, 807–810 (2007).

153. Masetti, N., Orlandini, M., Palazzi, E., Amati, L. & Frontera, F. M-type giants as optical counterparts of X-ray sources 4U 1700+24 and 4U 1954+319. A&A **453**, 295–299 (2006).

154. Corbet, R. *et al.* Swift/BAT Detection of a 5 hour Period in 4U 1954+31. *The Astronomer's Telegram* **797**, 1–+ (2006).

155. Warwick, R. S. *et al.* The Ariel V /3 A/ catalogue of X-ray sources. I - Sources at low galactic latitude /absolute value of B less than 10 deg/. MNRAS **197**, 865–891 (1981).

156. Forman, W. *et al.* The fourth Uhuru catalog of X-ray sources. ApJS **38**, 357–412 (1978).

157. Cook, M. C., Warwick, R. S. & Watson, M. G. *X–ray Astronomy* (ed. M. Oda, & R. Giacconi (Komaba: Institute of Space and Astronautical Science), 1984).

158. Warwick, R. S., Norton, A. J., Turner, M. J. L., Watson, M. G. & Willingale, R. A survey of the galactic plane with EXOSAT. MNRAS **232**, 551–564 (1988).

159. Tweedy, R., Warwick, R. & Remillard, R. *Two Topics in X–Ray Astronomy. Volume 1: X–Ray Binaries* (ed. J. Hunt, & B. Battrick, ESA SP-296, 1989).

160. Voges, W. *et al.* The ROSAT all-sky survey bright source catalogue. A&A **349**, 389–405 (1999).

161. Chakrabarty, D. & Roche, P. The Symbiotic Neutron Star Binary GX 1+4/V2116 Ophiuchi. ApJ **489**, 254–+ (1997).

162. Gaudenzi, S. & Polcaro, V. F. The peculiar M giant HD 154791. Optical counterpart of the X-ray source 4U1700+24. A&A **347**, 473–477 (1999).

163. Masetti, N. *et al.* X-ray and optical monitoring of the peculiar source 4U 1700+24/V934 Her. A&A **382**, 104–117 (2002).

164. De Luca, A., Caraveo, P. A., Mereghetti, S., Tiengo, A. & Bignami, G. F. A Long-Period, Violently Variable X-ray Source in a Young Supernova Remnant. *Science* **313**, 814–817 (2006).

165. Mattana, F. *et al.* A new symbiotic low mass X-ray binary system: 4U 1954+319. A&A **460**, L1–L4 (2006).

166. Parmar, A. N. *et al.* The low-energy concentrator spectrometer on-board the BeppoSAX X-ray astronomy satellite. A&AS **122**, 309–326 (1997).

167. Boella, G. *et al.* The medium-energy concentrator spectrometer on board the BeppoSAX X-ray astronomy satellite. A&AS **122**, 327–340 (1997).

168. Levine, A. M. *et al.* First Results from the All-Sky Monitor on the Rossi X-Ray Timing Explorer. ApJ **469**, L33+ (1996).

169. Hickox, R. C., Narayan, R. & Kallman, T. R. Origin of the Soft Excess in X-Ray Pulsars. ApJ **614**, 881–896 (2004).

170. Leahy, D. A. Searches for pulsed emission - Improved determination of period and amplitude from epoch folding for sinusoidal signals. A&A **180**, 275–277 (1987).

171. Lang, K. R. *Astrophysical Data: Planets and Stars* (New York: Springer-Verlag, 1992).

172. Claret, A. New grids of stellar models including tidal-evolution constants up to carbon burning. I. From 0.8 to 125 $M_{\odot}$ at Z=0.02. A&A **424**, 919–925 (2004).

173. Joss, P. C. & Rappaport, S. A. Neutron Stars in Interacting Binary Systems. ARA&A **22**, 537–592 (1984).

174. Paul, B., Dotani, T., Nagase, F., Mukherjee, U. & Naik, S. High-Resolution X-Ray Spectrum of the Accreting Binary X-Ray Pulsar GX 1+4. ApJ **627**, 915–919 (2005).

175. Tiengo, A. *et al.* Discovery of a redshifted X-ray emission line in the symbiotic neutron star binary 4U 1700+24. A&A **441**, 283–287 (2005).

176. Schid, H. M. *Physical Processes in Symbiotic Binaries* (ed. J. Mikołajewska, Copernicus Foundation for Polish Astronomy, Warsaw, 1997).

177. Davies, R. E. & Pringle, J. E. Spindown of neutron stars in close binary systems. II. MNRAS **196**, 209–224 (1981).

178. Warner, B. *Cataclysmic variable stars* (Cambridge Astrophysics Series, Cambridge, New York: Cambridge University Press, |c1995, 1995).

179. Fujimoto, M. Y. A Theory of Hydrogen Shell Flashes on Accreting White Dwarfs - Part Two - the Stable Shell Burning and the Recurrence Period of Shell Flashes. ApJ **257**, 767–+ (1982).

180. Livio, M. & Truran, J. W. Type I supernovae and accretion-induced collapses from cataclysmic variables? ApJ **389**, 695–703 (1992).

181. Livio, M. Classical novae and the extragalactic distance scale. ApJ **393**, 516–522 (1992).

182. Della Valle, M. & Livio, M. The Calibration of Novae as Distance Indicators. ApJ **452**, 704–+ (1995).

183. Shafter, A. W. On the Nova Rate in the Galaxy. ApJ **487**, 226–+ (1997).

184. Downes, R. A. *et al.* A Catalog and Atlas of Cataclysmic Variables: The Living Edition. PASP **113**, 764–768 (2001).

185. Hatano, K., Branch, D., Fisher, A. & Starrfield, S. On the spatial distribution and occurrence rate of Galactic classical novae. MNRAS **290**, 113–118 (1997).

186. Della Valle, M. & Livio, M. The Spectroscopic Differences between Disk and Thick-Disk/Bulge Novae. ApJ **506**, 818–823 (1998).

187. Starrfield, S., Truran, J. W. & Sparks, W. M. CNO abundances and hydrodynamic studies of the Nova outburst. V - 1.00-solar-mass models with small mass envelopes. ApJ **226**, 186–202 (1978).

188. Starrfield, S. *in Classical Novae* (Chichester: Wiley, 1989), m.f. bode & a. evans edn.

189. Starrfield, S., Truran, J. W., Sparks, W. M. & Kutter, G. S. CNO Abundances and Hydrodynamic Models of the Nova Outburst. ApJ **176**, 169–+ (1972).

190. Kovetz, A. & Prialnik, D. The Composition of Nova Ejecta from Multicycle Evolution Models. ApJ **477**, 356–+ (1997).

191. Alexakis, A. *et al.* On Heavy Element Enrichment in Classical Novae. ApJ **602**, 931–937 (2004).

192. José, J., Hernanz, M., García-Berro, E. & Gil-Pons, P. The Impact of the Chemical Stratification of White Dwarfs on the Classification of Classical Novae. ApJ **597**, L41–L44 (2003).

193. Clayton, D. D. & Hoyle, F. Gamma-Ray Lines from Novae. ApJ **187**, L101+ (1974).

194. Hernanz, M. & José, J. Gamma-rays from classical nova explosions: theory and observations. *Nuclear Physics A* **758**, 721–724 (2005).

195. Hernanz, M. & José, J. Radioactivities from novae. *New Astronomy Review* **50**, 504–508 (2006).

196. Bardayan, D. W. *et al.* Strength of the ^{18}F(p,α)^{15}O Resonance at E$_{c.m.}$=330 keV. *Physical Review Letters* **89**, 262501–+ (2002).

197. De Séréville, N. *et al.* ^{2}H(^{18}F,pα)^{15}N reaction applied to nova γ-ray emission. Phys. Rev. C **67**, 052801–+ (2003).

198. Fox, C. *et al.* Explosive Hydrogen Burning of ^{17}O in Classical Novae. *Physical Review Letters* **93**, 081102–+ (2004).

199. Chafa, A. *et al.* Hydrogen Burning of ^{17}O in Classical Novae. *Physical Review Letters* **95**, 031101–+ (2005).

200. Gomez-Gomar, J., Hernanz, M., Jose, J. & Isern, J. Gamma-ray emission from individual classical novae. MNRAS **296**, 913–920 (1998).

201. Hernanz, M., Gómez-Gomar, J. & José, J. The prompt gamma-ray emission of novae. *New Astronomy Review* **46**, 559–563 (2002).

202. Leising, M. D., Share, G. H., Chupp, E. L. & Kanbach, G. Gamma-ray limits on Na-22 production in novae. ApJ **328**, 755–762 (1988).

203. Harris, M. J., Leising, M. D. & Share, G. H. A search for the 478 keV line from the decay of nucleosynthetic Be-7. ApJ **375**, 216–220 (1991).

204. Iyudin, A. F. *et al.* COMPTEL search for ^{22}Na line emission from recent novae. A&A **300**, 422–+ (1995).

205. Hernanz, M. J. *et al.* BATSE Observations of Classical Novae. In *American Institute of Physics Conference Series* (eds. McConnell, M. L. & Ryan, J. M.), vol. 510 of *American Institute of Physics Conference Series*, 82–+ (2000).

206. Harris, M. J. *et al.* Transient Gamma-Ray Spectrometer Observations of Gamma-Ray Lines from Novae. II. Constraining the Galactic Nova Rate from a Survey of the Southern Sky during 1995-1997. ApJ **542**, 1057–1063 (2000).

207. Smith, D. M. Gamma-Ray Line Observations with RHESSI. In *5th INTEGRAL Workshop on the INTEGRAL Universe* (eds. Schoenfelder, V., Lichti, G. & Winkler, C.), vol. 552 of *ESA Special Publication*, 45–+ (2004).

208. Hernanz, M. & José, J. Updated Prospects for Detectability of Classical Novae with INTEGRAL. In *5th INTEGRAL Workshop on the INTEGRAL Universe* (eds. Schoenfelder, V., Lichti, G. & Winkler, C.), vol. 552 of *ESA Special Publication*, 95–+ (2004).

209. Band, D. L. Postlaunch Analysis of Swift's Gamma-Ray Burst Detection Sensitivity. ApJ **644**, 378–384 (2006).

210. Hjellming, R. M. *et al.* Radio observations of the 1985 outburst of RS Ophiuchi. ApJ **305**, L71–L75 (1986).

211. Hachisu, I. & Kato, M. Recurrent Novae as a Progenitor System of Type Ia Supernovae. I. RS Ophiuchi Subclass: Systems with a Red Giant Companion. ApJ **558**, 323–350 (2001).

212. Narumi, H. *et al.* RS Ophiuchi. IAU Circ. **8671**, 2–+ (2006).

213. Boyd, D. & Poyner, G. CCD photometry and visual observations of V1663 Aquilae (Nova Aquilae 2005). *Journal of the British Astronomical Association* **116**, 320–323 (2006).

214. Lane, B. F., Retter, A., Eisner, J. A., Thompson, R. R. & Muterspaugh, M. W. Interferometric observations of explosive variables: V838 Mon, Nova Aql 2005, and RS Oph. In *Advances in Stellar Interferometry. Edited by Monnier, John D.; Schöller, Markus; Danchi, William C.. Proceedings of the SPIE, Volume 6268, pp. (2006).* (2006).

215. Poggiani, R. An analysis of early spectroscopic observations and the light curve of the nova V1663 Aql (Nova Aql 2005). *Astronomische Nachrichten* **327**, 895–+ (2006).

216. Munari, U., Siviero, A., Navasardyan, H. & Dallaporta, S. BVI photometry and the spectroscopy of Nova Scuti 2005 N.2. A&A **452**, 567–569 (2006).

217. Czart, K. *et al.* Optical observations of Nova V2362 Cyg. *The Astronomer's Telegram* **792**, 1–+ (2006).

218. Steeghs, D. *et al.* The progenitor of Nova Cygni 2006 (=V2362 Cyg). *The Astronomer's Telegram* **795**, 1–+ (2006).

219. Swank, J. H. RXTE PCA Upper Limit on X-Ray Flux from V1280 Sco. *The Astronomer's Telegram* **1010**, 1–+ (2007).

220. Osborne, J. P. *et al.* Swift X-ray flux limits for the recent novae V1280 and V1281 Sco. *The Astronomer's Telegram* **1011**, 1–+ (2007).

221. Steeghs, D. *et al.* The progenitor of Nova Cygni 2007 (=V2467 Cyg). *The Astronomer's Telegram* **1031**, 1–+ (2007).

222. Bode, M. F. *et al.* Swift Observations of the 2006 Outburst of the Recurrent Nova RS Ophiuchi. I. Early X-Ray Emission from the Shocked Ejecta and Red Giant Wind. ApJ **652**, 629–635 (2006).

223. Sokoloski, J. L., Luna, G. J. M., Mukai, K. & Kenyon, S. J. An X-ray-emitting blast wave from the recurrent nova RS Ophiuchi. Nature **442**, 276–278 (2006).

224. Berman, N. M. & Kahn, F. D. Soft X-rays from very young supernova remnants. MNRAS **205**, 303–308 (1983).

225. Bode, M. F. & Kahn, F. D. A model for the outburst of nova RS Ophiuchi in 1985. MNRAS **217**, 205–215 (1985).

226. O'Brien, T. J., Bode, M. F. & Kahn, F. D. Models for the remnants of recurrent novae. III - Comparison with the X-ray observations of RS Ophiuchi (1985). MNRAS **255**, 683–693 (1992).

227. Buil, C. RS Ophiuchi. *Central Bureau Electronic Telegrams* **403**, 1–+ (2006).

228. Evans, A. *et al.* RS Ophiuchi. IAU Circ. **8682**, 2–+ (2006).

229. Ness, J.-U. *et al.* RS Ophiuchi. *Central Bureau Electronic Telegrams* **415**, 1–+ (2006).

230. Hernanz, M. . In *RS Ophiuchi 2006* (eds. Evans, A., Bode, M. & O'Brien, T.), vol. in press of *ASP Conference Series*, x (2007).

231. Hakkila, J., Myers, J. M., Stidham, B. J. & Hartmann, D. H. A Computerized Model of Large-Scale Visual Interstellar Extinction. AJ **114**, 2043–+ (1997).

232. Higdon, J. C. & Fowler, W. A. Gamma-ray constraints on Na-22 yields in nova explosions. ApJ **317**, 710–716 (1987).

233. Kent, S. M., Dame, T. M. & Fazio, G. Galactic structure from the Spacelab infrared telescope. II - Luminosity models of the Milky Way. ApJ **378**, 131–138 (1991).

234. King, I., Gilmore, G. & van der Kruit, P. C. *The Milky Way As Galaxy* (The Milky Way As Galaxy, by Ivan King, Gerald Gilmore, and Pieter C. van der Kruit. Published by University Science Books, ISBN 0-935702-62-8, 392pp, 1990., 1990).

235. Dawson, P. C. & Johnson, R. G. The Visibility of Galactic Supernovae. JRASC **88**, 369–+ (1994).

236. Livio, M. & Truran, J. W. On the interpretation and implications of nova abundances: an abundance of riches or an overabundance of enrichments. ApJ **425**, 797–801 (1994).

237. Grindlay, J. E. EXIST: All-sky hard X-ray imaging and spectral-temporal survey for black holes [review article]. *New Astronomy Review* **49**, 436–439 (2005).

AUTHOR : Fabio SENZIANI
TITLE : Monitoring of X-ray binaries and novae with the Burst Alert Telescope on board the *Swift* satellite

---

Abstract :

The Burst Alert Telescope (BAT) on board the Swift satellite is a very useful tool for hard X/gamma-ray astronomy. Thanks to its good sensitivity, huge field of view, and pointing strategy covering all the sky, BAT is a suitable instrument to monitor known hard X-ray sources as well as to catch and study new transients. In this thesis, new procedures to analyse the BAT survey data are described with details and the first astrophysical results on galactic accreting sources discussed. Three X-ray binaries were observed and studied: the microquasar GRO J1655-40 during its 2005 outburst, the SFXT IGR J08408-4503 during its third recorded outburst and the symbiotic LMXB 4U 1954+319. A search for prompt gamma-ray emission due to downgraded decay of radioactive elements from novae was also performed. The emission of RS Oph, possibly due to shock heating, led to a detection. The probability of detecting a nova during the Swift lifetime was estimated using a Monte Carlo approach.

Keywords :
Astrophysics; Instrumentation; Hard X-rays / Gamma-rays; *Swift*/BAT; Data analysis; X-ray binaries; Novae

AUTEUR	:	Fabio SENZIANI
TITRE	:	Monitoring of X-ray binaries and novae with the Burst Alert Telescope on board the *Swift* satellite
DIRECTEUR DE THESE	:	Giovanni Fabrizio BIGNAMI
	:	Gerald Keith SKINNER
DATE DE SOUTENANCE	:	1 Février 2008
LIEU DE SOUTENANCE	:	Universitá degli Studi di Pavia (ITALY)

Résumé :

Le Burst Alert Telescope (BAT) à bord du satellite Swift est un instrument très performant pour l'astronomie des rayons X-durs/gamma. L'énorme champ de vue, la bonne sensibilité et la stratégie de pointage couvrant tout le ciel font de BAT un instrument adapté pour observer des sources connues et pour étudier les nouveaux objets variables. Dans cette thèse une description détaillée des nouvelles procédures pour analyser les données de survey de BAT est fournie et les premiers résultats astrophysiques de sources galactiques en accrétion sont discutés. Trois binaires X ont été étudiées : le microquasar GRO J1655-40, le SFXT IGR J08408-4503 et le LMXB symbiotique 4U 1954+319. L'émission gamma due à la décroissance des éléments radioactifs des novae a été aussi recherchée. L'émission de RS Oph, probablement liée au chauffage par choc, a été détectée. La probabilité de détecter une nova durant le temps de vie de Swift a été estimée en utilisant une approche Monte Carlo.

Mots-clés :

Astrophysique; Instrumentation; Rayonnement X-durs / gamma; *Swift*/BAT; Traitement de données; Binaires X; Novae

Discipline : Astrophysique des hautes énergies

Laboratoire d'accueil :

Centre d'Etude Spatiale des Rayonnements
9, avenue du Colonel Roche - BP 4346 - 31028 Toulouse Cedex 4 (FRANCE)

Universitá degli Studi di Pavia, Dipartimento di Fisica Nucleare e Teorica
Via Bassi 6, 27100 Pavia (ITALY)